Development of portable low field NMR magnet : Design and construction

Hung Dang Phuc

N° d'ordre : 2015ISAL0007 Année 2015

Thèse

Développement d'aimant bas champ pour RMN Portable: Conception et construction

Présentée devant

L'Institut National des Sciences Appliquées de Lyon

Pour obtenir

Le Grade de Docteur

École Doctorale : Électronique, Électrotechnique, Automatique

Spécialité : Micro et nanotechnologies, Instrumentation

Laboratoire : CREATIS, CNRS UMR 5220 – INSERM U1044 – INSA Lyon

Par

DANG PHUC Hung

Soutenue le 29 janvier 2015 devant la commission d'examen

JURY :

Directeur de thèse:	Mme. Latifa FAKRI-BOUCHET, Maitre de Conférences, HDR. CREATIS, INSA de Lyon.
Co-directeurs:	M. Patrick POULICHET, Professeur Associé, ESIEE Paris.
	M. Huan PHAN DINH, Professeur Associé, Institut Polytechnique d'Ho Chi Minh Ville, Vietnam.
Rapporteurs:	M. Kosai RAOOF, Professeur des Universités, LAUM, ENSIM, Université du Maine.
	M. Jean-Paul YONNET, Directeur de recherches CNRS, G2Elab, ENSE3, INP, Grenoble.
Examinateurs:	M. Daniel BARBIER, Professeur des Universités, INL, INSA de Lyon.
Invité:	M. Abdennasser FAKRI, Professeur Associé, ESIEE Paris

SIGLE	ECOLE DOCTORALE	NOM ET COORDONNEES DU RESPONSABLE
CHIMIE	**CHIMIE DE LYON** **http://www.edchimie-lyon.fr** Sec :Renée EL MELHEM Bat Blaise Pascal 3e etage Insa : R. GOURDON	M. Jean Marc LANCELIN Université de Lyon – Collège Doctoral Bât ESCPE 43 bd du 11 novembre 1918 69622 VILLEURBANNE Cedex Tél : 04.72.43 13 95 directeur@edchimie-lyon.fr
E.E.A.	**ELECTRONIQUE, ELECTROTECHNIQUE, AUTOMATIQUE** http://edeea.ec-lyon.fr Secrétariat : M.C. HAVGOUDOUKIAN eea@ec-lyon.fr	M. Gérard SCORLETTI Ecole Centrale de Lyon 36 avenue Guy de Collongue 69134 ECULLY Tél : 04.72.18 60.97 Fax : 04 78 43 37 17 Gerard.scorletti@ec-lyon.fr
E2M2	**EVOLUTION, ECOSYSTEME, MICROBIOLOGIE, MODELISATION** http://e2m2.universite-lyon.fr Insa : H. CHARLES	Mme Gudrun BORNETTE CNRS UMR 5023 LEHNA Université Claude Bernard Lyon 1 Bât Forel 43 bd du 11 novembre 1918 69622 VILLEURBANNE Cédex Tél : 06.07.53.89.13 e2m2@ univ-lyon1.fr
EDISS	**INTERDISCIPLINAIRE SCIENCES-SANTE** http://www.ediss-lyon.fr Sec : Insa : M. LAGARDE	Mme Emmanuelle CANET-SOULAS INSERM U1060, CarMeN lab, Univ. Lyon 1 Bâtiment IMBL 11 avenue Jean Capelle INSA de Lyon 696621 Villeurbanne Tél : 04.72.68.49.09 Fax :04 72 68 49 16 Emmanuelle.canet@univ-lyon1.fr
INFOMATHS	**INFORMATIQUE ET MATHEMATIQUES** **http://infomaths.univ-lyon1.fr** Sec :Renée EL MELHEM Bat Blaise Pascal 3e etage infomaths@univ-lyon1.fr	Mme Sylvie CALABRETTO LIRIS – INSA de Lyon Bat Blaise Pascal 7 avenue Jean Capelle 69622 VILLEURBANNE Cedex Tél : 04.72. 43. 80. 46 Fax 04 72 43 16 87 Sylvie.calabretto@insa-lyon.fr
Matériaux	**MATERIAUX DE LYON** **http://ed34.universite-lyon.fr** Secrétariat : M. LABOUNE PM : 71.70 –Fax : 87.12 Bat. Saint Exupéry Ed.materiaux@insa-lyon.fr	M. Jean-Yves BUFFIERE INSA de Lyon MATEIS Bâtiment Saint Exupéry 7 avenue Jean Capelle 69621 VILLEURBANNE Cedex Tél : 04.72.43 83 18 Fax 04 72 43 85 28 Jean-yves.buffiere@insa-lyon.fr
MEGA	**MECANIQUE, ENERGETIQUE, GENIE CIVIL, ACOUSTIQUE** **http://mega.universite-lyon.fr** Secrétariat : M. LABOUNE PM : 71.70 –Fax : 87.12 Bat. Saint Exupéry **mega@insa-lyon.fr**	M. Philippe BOISSE INSA de Lyon Laboratoire LAMCOS Bâtiment Jacquard 25 bis avenue Jean Capelle 69621 VILLEURBANNE Cedex Tél :04.72 .43.71.70 Fax : 04 72 43 72 37 Philippe.boisse@insa-lyon.fr
ScSo	**ScSo*** **http://recherche.univ-lyon2.fr/scso/** Sec : Viviane POLSINELLI Brigitte DUBOIS Insa : J.Y. TOUSSAINT	M. OBADIA Lionel Université Lyon 2 86 rue Pasteur 69365 LYON Cedex 07 Tél : 04.78.77.23.86 Fax : 04.37.28.04.48 Lionel.Obadia@univ-lyon2.fr

*ScSo : Histoire, Géographie, Aménagement, Urbanisme, Archéologie, Science politique, Sociologie, Anthropologie

Acknowledgements

I would never have been able to finish my dissertation without the guidance of my committee members, help from friends, and support from responsible peoples in laboratory CREATIS.

I would like to express my deepest gratitude to my supervisor, Mrs. Latifa FAKR-BOUCHET, for her excellent guidance, caring, patience, and providing me with an excellent atmosphere for doing research. I would like to thank my co-supervisor, Mr. Patrick POULICHET, who let me experience the research of portable NMR devices, patiently corrected my writing. I would also like to thank another co-supervisor, Mr. PHAN DINH Huan, who gave me valuable suggestions for my works. Special thank goes to Mr. Christian Jardin, who introduced me to study in France and Mr. Abdennasser FAKRI for his help during I had studied in ESIEE, Paris.

I would like to be thankful to Mr. Kosai RAOOF and Mr. Jean-Paul YONNET, who accepted to be reviewers and gave many useful comments for my work. I would like to express my thankfulness to Mr. Daniel BARBIER, who accepted to be president of the jury.

Finally, I would also like to thank my parents, young sisters. They were always supporting me and encouraging me with their best wishes. This thesis will be dedicated for my grandmother, who passed away during I had studied in France.

Synthèse

Les travaux menés au cours de cette thèse ont porté essentiellement sur le développement d'un aimant pour système de Résonance Magnétique Nucléaire (RMN) portable : conception, modélisation et simulation puis réalisation et validation.

Chapitre 1 : Introduction à la RMN

Nous présentons dans ce premier chapitre les bases nécessaires pour comprendre les points clés de l'expérience de RMN. Depuis sa découverte en 1945, la résonance magnétique nucléaire (RMN) est devenue un outil précieux pour la physique, la chimie, la biologie et la médecine. La RMN se décline sous forme de deux techniques d'investigation non-invasives spectroscopie de résonance magnétique nucléaire (SRM) et l'imagerie par résonance magnétique (IRM).

Ces techniques exploitent le fait que certains noyaux atomiques possèdent un moment cinétique intrinsèque « le spin ». Placés dans un champ magnétique statique B_0, les moments magnétiques associés aux spins s'orientent parallèlement et antiparallèlement au champ B_0 selon deux niveaux d'énergie tout en maintenant leurs mouvements de précession.

Le phénomène de la RMN consiste à faire passer les spins d'un niveau d'énergie à l'autre. Pour ce faire on a recours à une impulsion de champ radiofréquence B_1, un champ électromagnétique qui oscille à la même fréquence de précession des spins. Les noyaux absorbent l'énergie radiofréquence qu'ils restituent sous forme d'onde donnant naissance, selon le cas à un spectre ou une image RMN dont les caractéristiques dépendent du type de noyau et de son environnement chimique.

A l'arrêt de l'impulsion radiofréquence, les spins continuent leur précession autour d'un axe perpendiculaire au champ B_0, puis l'aimantation globale (résultante de tous les moments magnétiques) revient à son état d'équilibre. Le temps de retour à l'équilibre est appelé temps de relaxation longitudinale T_1. Il est caractéristique des tissus et dépend des molécules en présence.

Il existe aussi un temps de relaxation dit T_2, temps de relaxation transversale correspondant à la constante de temps de décroissance de la tension électrique correspondante à l'onde restituée, lors de la détection, par les spins. T_2 dépend essentiellement de la nature de l'atome et de son environnement magnétique immédiat.

A l'état macroscopique le phénomène de précession et de relaxation est décrit par les équations de Bloch :

$$\frac{dM}{dt} = \gamma M \wedge B_0 - A[M - M_0]$$

$$A = \begin{pmatrix} 1/T_2 & 0 & 0 \\ 0 & 1/T_2 & 0 \\ 0 & 0 & 1/T_1 \end{pmatrix}$$

La RMN portable permet d'accéder à l'enveloppe du signal et ainsi à l'amplitude qui permet d'extrapoler la quantité de proton en présence. Les constantes de temps T_1 et T_2 donnent des informations sur les interactions entre - par exemple - les noyaux d'hydrogène et leur environnement.

Dans ce chapitre nous avons aussi discuté les techniques de mesure des temps de relaxation T_1 et T_2, plus particulièrement la mesure de T_2. L'intérêt est que cette mesure peut être effectuée en champ magnétique non uniforme en utilisant plusieurs impulsions créant ainsi un train d'échos. Il existe deux techniques bien connues pour la mesurer du T_2 : Échos de spin ou Echo de Hahn et la séquence d'impulsions CPMG.

Dans ce chapitre, nous avons terminé notre revue des bases de RMN par des considérations concernant l'influence de l'homogénéité du champ magnétique sur la spectroscopie RMN. Il est nécessaire d'effectuer les expériences de RMN dans un champ magnétique B_0 le plus homogène possible. L'homogénéité de B_0 reste un critère important dont il faut tenir compte lors de la conception d'un dispositif de RMN portable.

Chapitre 2 : Conception de système de RMN Portable : Etat de l'art

Ce deuxième chapitre est un récapitulatif de l'état de l'art concernant les appareils de RMN portables. Le développement de ces dispositifs portables est exposé de manière exhaustive afin d'avoir un aperçu de ce domaine de recherche et pouvoir choisir la solution la plus adéquate pour nos applications.

La question qui se pose est pourquoi une RMN portable ? Alors que la plupart des chercheurs s'orientent vers des champs de plus en plus élevés et des protocoles de mesure de plus en plus complexes. En effet, les systèmes de RMN classiques produisent des champs magnétiques très intenses homogènes et stables avec cependant des aimants volumineux, coûteux en maintenance et en énergie. De plus, ils limitent la taille maximale de l'échantillon à leurs dimensions internes, alors qu'un système de RMN portable - dans sa configuration *ex-situ* par exemple - peut être positionné à la surface des objets d'étude sans limitation de taille.

La RMN portable trouve un intérêt dans de nombreuses applications y compris dans des milieux extrêmes. Un exemple significatif est les systèmes de la société Magritek (Nouvelle-Zélande), pour l'analyse des changements des propriétés mécaniques des glaces arctiques avec le réchauffement climatique.

Le développement de la technologie des aimants permanents tels que des aimants de « terre rare » a permis aux chercheurs de les utiliser pour des applications RMN. Ces aimants peuvent produire un champ fort et homogène, deux critères importants pour les exigences expérimentales en RMN. Autres caractéristiques attrayantes d'aimants permanents sont évidemment l'absence de la source d'énergie électrique extérieure et pas de maintenance. Ainsi, ils remplissent les conditions pour la conception de dispositifs portables RMN.

Les dispositifs RMN portables sont divisés en deux groupes en raison des applications visées. Un premier groupe appelé *ex-situ* avec des échantillons d'étude placés à l'extérieur de l'aimant. Un second groupe appelé *in situ* où les échantillons sont analysés à l'intérieur de l'aimant.

Les appareils de RMN portables *ex-situ* ont une configuration simple avec le volume sensible (région d'intérêt: ROI) à proximité de leur surface. Ces systèmes sont appropriés pour des investigations de surface. Ainsi, ils peuvent être utilisés pour des objets aux dimensions illimitées.

Les aimants *in situ* ont, quant à eux, la particularité de renforcer le champ en leur centre et par conséquent nul en dehors du champ de la structure. Dans ce cas, leur champ magnétique est homogène à l'intérieur de la structure en comparaison avec aimants *ex situ*. Un autre avantage d'aimants *in situ*, il est moins sensible aux influences environnementales externes en raison du confinement du champ.

Dans ce chapitre, nous nous sommes intéressés aussi aux techniques d'optimisation de l'homogénéité du champ magnétique et leurs applications aux aimants portables. Fondamentalement, deux méthodes répandues ont été utilisées pour augmenter l'homogénéité du champ magnétique. La première méthode est l'optimisation de l'écart entre les deux anneaux de la configuration. Cependant, cette méthode n'améliore pas suffisamment l'homogénéité pour spectroscopie. Le « Shim » est la seconde méthode c'est la plus utilisée pour augmenter l'homogénéité du champ magnétique des appareils de RMN en général et les RMN portables en particulier. La technique du « Shim » est non seulement utilisée pour augmenter l'homogénéité du champ magnétique, mais aussi utilisé pour compenser l'hétérogénéité causée par les imperfections du matériau, les tolérances de fabrication et les imprécisions d'assemblage.

Chapitre 3 : Aimant pour RMN Portable: Conception et Modélisation

Ce chapitre est consacré à la discussion sur les propriétés des matériaux magnétiques et les méthodes numériques.

Les propriétés des matériaux magnétiques ont été discutées dans la première section de ce chapitre. Nous avons examiné différentes familles de matériaux magnétiques les plus utilisés ces quinze dernières années afin de choisir le matériau le plus approprié pour notre application.

Les méthodes numériques de simulation mises en œuvre ont également été détaillées dans ce chapitre. Nous présentons le calcul de champ magnétique sur la base de la méthode des éléments finis, sous-jacente au logiciel ANSYS (nous avons utilisé ce logiciel pour les calculs et la simulation). En outre, les matériaux de l'élément de la bibliothèque d'éléments d'ANSYS sont décrits dans notre procédure de simulation.

Les méthodes numériques et la simulation jouent un rôle important à la conception de l'aimant et le processus d'optimisation. La géométrie de l'instrument doit être définie par les utilisateurs et les paramètres spécifiques peuvent être alors optimisés. Les stratégies analytiques fournissent des solutions précises pour la distribution du champ magnétique dans la région d'intérêt (ROI) et le profil de champ magnétique. Dans la littérature, il existe différentes méthodes numériques que nous avons décrites aussi dans ce chapitre.

Les éléments utilisés pour la simulation dans la bibliothèque de logiciel ANSYS ont été décrits. Selon le problème à résoudre, les utilisateurs peuvent choisir les éléments appropriés. Par exemple, l'élément PLANE53 est utilisé pour la simulation 2-D tandis que l'élément SOLID98 est considéré pour des solutions 3-D. Dans ce travail, deux éléments sont utilisés pour la simulation. L'élément PLANE13 et SOLID97 est respectivement utilisé pour la 2-D et 3-D simulation.

Nous nous sommes intéressés aussi aux matériaux permanents, matériaux qui maintiennent une aimantation en l'absence de champ extérieur. Ces matériaux sont souvent anisotropes (ils admettent un axe d'aimantation) et suivent une courbe d'hystérésis après leur première aimantation. Dans ce chapitre, nous discutons, par ailleurs, certains de leurs paramètres essentiels à ce travail. Ainsi plusieurs propriétés magnétiques initiales d'un matériau peuvent être déterminées:

- La rémanence d'un matériau (Br) mesurée en Tesla (T) est sa capacité à maintenir une magnétisation lorsqu'un champ magnétique externe est retiré après avoir atteint la saturation, avec $Br = \mu 0 Mr$ où Mr est l'aimantation rémanente.

- Le coercivité d'un matériau (Hc) mesurée en Oersted (Oe) ou ampères/mètre (A/m) est l'intensité du champ magnétique extérieur *H* opposé à l'aimantation rémanente, nécessaire pour que l'induction magnétique dans le matériau soit annulée ($\overrightarrow{B} = \mu_0 \overrightarrow{H} + \overrightarrow{M}$).

Il existe une variété de matériaux pour aimants permanents, nous avons donné un bref résumé sur des matériaux de qualité généralement utilisés dans la fabrication d'aimants, leurs avantages et désavantages respectifs. Plus particulièrement les aimants permanents utilisant un matériau ~~moderne~~ tel que le NdFeB, que nous avons retenu pour sa meilleure rémanence et coercivité ainsi que son prix bas.

Chapitre 4 : Conception, construction de poids léger RMN portables de type Halbach de barres identiques aimants

Ce chapitre présentera une conception simple pour dispositif de RMN portable. La configuration est basée sur le type Halbach. Il a deux anneaux principaux alignés pour compenser le champ magnétique à l'extérieur des anneaux. Chaque anneau est composé de 12 aimants identiques de forme cylindrique. Pour prédire les propriétés de cette configuration, l'intensité du champ magnétique et l'homogénéité sont calculées et simulées par deux logiciels qui sont ANSYS et RADIA. Ces deux méthodes sont complémentaire: RADIA est utilisé pour l'optimisation et de simulation. ANSYS est utilisé pour la vérification des résultats obtenus par RADIA. Les résultats obtenus par les deux logiciels sont en bonne corrélation à la fois pour la simulation et l'optimisation. La valeur maximale de B_0 calculée avec RADIA est 0,103 T alors que la valeur correspondante dérivée de l'analyse ANSYS est de 0,11 T. La différence de calcul entre RADIA et ANSYS est 6,79%. Cette différence a été discutée dans ce chapitre. Une nouvelle méthode de shim pour augmenter l'homogénéité et corriger les imperfections du champ B_0 a été aussi introduite. La position des aimants de shim a fait l'objet d'une optimisation avec le logiciel RADIA et vérifié par le logiciel ANSYS.

Sur la base de ces résultats, nous avons réalisé un nouveau prototype. Ses propriétés ont été vérifiées par simulation et mesurée également. Ce prototype est constitué de deux anneaux de 12 aimants. Ces aimants sont placés en cercle de 30 mm de rayon et insérés dans douze trous de deux couronnes en aluminium. Les deux anneaux du prototype, fixés par des vis sur les couronnes en aluminium, peuvent coulisser sur trois tiges pour obtenir la position souhaitée des aimants.

Le champ magnétique est mesuré à l'aide d'un gaussmètre numérique Hirst GM08 avec une limite de sensibilité de 10-4 T dans une gamme variant de 0 à 0,299 T. Le Micro-positionneur Signatone S-926 est utilisé pour contrôler le mouvement de la sonde dans les trois directions. La résolution est de 254 µm « per knob révolution ». Les différences constatées entre la mesure et la simulation sont expliquées à la fin de ce chapitre.

Chapitre 5: Modélisation et conception de la configuration Mandhalas pour des applications biomédicales et agro-alimentaire.

Un autre aimant basé sur la configuration Mandhalas (**M**agnet **A**rrangement for **N**ovel **D**iscrete **H**albach **La**yout) a fait l'objet d'une étude comparative, portant sur deux configurations utilisant des aimants de formes circulaires et de formes carrés, effectuée par simulation 2D (sur la base de trois critères: la masse, l'homogénéité et l'intensité du champ magnétique). Les Mandhalas fabriqués à partir d'aimants circulaires permettent d'avoir de meilleurs résultats (0.32 T, 178 ppm). Sur la base du résultat de la simulation 2D, la configuration avec 16 aimants permanents de formes circulaires a été choisie pour la construction de notre prototype. La simulation 3D a permis d'évaluer le système dans sa globalité.

Tenant compte des résultats obtenus, un système de shim passif a été aussi utilisé dans ce cas et a permis l'augmentation de la zone d'homogénéité de manière significative. Les résultats de l'optimisation indiquent que dans l'axe longitudinal, la région homogène s'étend sur 2,5 fois en comparaison de celle sans le système de shim. L'homogénéité du champ magnétique dans un volume cylindrique de diamètre de 40 mm et de 50 mm de longueur est de 178 ppm au lieu de 638 ppm dans le cas de la configuration sans les aimants de shim, soit une valeur d'homogénéité supérieure d'un facteur 3,5.

Partant des résultats de simulation, nous avons conçu un prototype d'environ 20 kg de poids total. Cet aimant de table génère un champ magnétique de 0,32 T et offre une homogénéité de 178 ppm dans un volume sensible de 40 mm de diamètre et de 50 mm de longueur.

Conclusion et perspective

En raison de nos objectifs d'applications, nous avons choisi un aimant in situ de configuration de type Halbach pour son homogénéité et sa capacité à confiner le champ à l'intérieur. Les avantages et les inconvénients des matériaux magnétiques ont été analysés. Sur la base de ces analyses, nous avons constaté que la famille des aimants NdFeB est adaptée à nos travaux. Ce matériau

magnétique a des propriétés similaires au matériau « terre rare », Samarium Cobalt (SmCo) non retenu en raison de son prix élevé (30% à 40% plus cher que le NdFeB).

Les méthodes numériques existantes ont été également examinées afin de définir la meilleure solution pour nos travaux de simulation et d'optimisation. Nous avons choisi la méthode des éléments finis, procédure sous-jacente de nombreux logiciels.

Les calculs et les simulations sont principalement basés sur ANSYS, dont les résultats ont été confrontés et vérifiés par les résultats obtenus avec le logiciel RADIA. Le principe de calcul ANSYS est basé sur la méthode des éléments finis tandis que celui de RADIA repose sur des méthodes d'intégrales aux limites. Les résultats sont en parfaite concordance aussi bien pour l'homogénéité que pour l'optimisation. Cependant, l'intensité du champ magnétique est différente entre les deux logiciels en raison du maillage choisi. Nous avons également utilisé Matlab pour les différents tracés.

Les mesures ont été effectuées avec l'gaussmètre Hirst GM08 avec une limite de sensibilité 10-4T. Le micro positionneur Signatone S-926 est utilisé pour contrôler le mouvement de la sonde dans les trois directions de l'espace.

A partir des résultats de la simulation, nous avons réalisé un prototype compact et léger avec 24 aimants « tige » identiques. Notre prototype a deux anneaux; chaque anneau est composé de 12 aimants. Chaque aimant a une longueur de 50 mm et 8 mm de diamètre. Le prototype génère un champ B_0 dans le plan transversal à 0.12T d'intensité. Son homogénéité est 4230 ppm sur un volume de 7x8x20 mm^3. Il est bien évident que cette homogénéité n'est pas suffisante pour avoir une grande résolution. Pour l'améliorer, nous avons proposé un système de shim constitué de huit petits aimants placés dans l'alésage du prototype. En ajustant le positionnement de ces aimants, nous avons obtenu une configuration optimisée. Les résultats montrent une amélioration significative de l'homogénéité. Ainsi avec ce système de shim, l'homogénéité est 18 fois meilleure : soit 230 ppm en comparaison avec 4230 ppm sur le même volume 7x8x20 mm^3. Ces résultats de simulation ont été aussi vérifiés par mesure.

Les valeurs de mesure du champ magnétique variant dans l'axe longitudinal sont en bonne corrélation avec les résultats de simulation. Cependant, l'homogénéité obtenue par mesure est différente de celle simulée en raison des caractéristiques réelles du matériau utilisé.

Nous avons également proposé une autre configuration pour des applications biomédicales et/ou agroalimentaires : la configuration Mandhalas (Magnetic Arrangement for Novel Discrete Halbach Layout). Pour parfaire notre choix, deux configurations Halbach à aimants permanents de forme cubique et cylindrique, respectivement, ont été comparés en termes de force moyenne du champ

magnétique et d'homogénéité du champ magnétique. Cette comparaison a été effectuée par simulation 2-D avec le logiciel ANSYS. Nous avons déterminé que la configuration utilisant des aimants de forme cylindrique présente de meilleures performances; sauf le cas où n = 4.

Les simulations 2-D, nous ont permis de choisir la configuration Mandhalas avec 16 aimants cylindriques pour la réalisation de notre prototype. Une Simulation 3-D a été aussi réalisée pour évaluer l'ensemble des propriétés de cette configuration. L'optimisation de l'homogénéité du champ a été réalisée en utilisant la même méthode de shim passive. Cette optimisation, a permis une amélioration considérable de l'homogénéité du champ magnétique.

Les travaux restant à faire concernent deux parties principales :

La première partie est la correction du désalignement de direction magnétique mentionné dans le chapitre 4.

La deuxième partie concerne l'usinage et l'assemblage précis d'un système de RMN Mandhalas afin obtenir des performances plus élevées.

TABLE OF CONTENTS

INTRODUCTION 1

Chapter 1: Basic of NMR 4

1.1 Introduction 4

1.2 Principle of NMR and MRI 4

1.3 Signal to noise ratio 10
1.3.1 The signal 10
1.3.2 The noise 13
1.3.3 The sensitivity 14

1.4 T_1 and T_2 measurements 14
1.4.1 T_2 measurement 14
1.4.2 T_1 measurement 16
1.4.3 Self-diffusion and field gradient 17

1.5 Influence of magnetic field homogeneity on NMR spectroscopy 18

CHAPTER 2: PORTABLE NMR SYSTEM DESIGN 21

2.1 Introduction 21

2.2 The need of portable NMR devices 21

2.3 Review of portable NMR devices 23
2.3.1 *Ex-situ* portable NMR devices 23
2.3.1.1 Well-logging sensors 24
2.3.1.2 TRAFI concept 25
2.3.1.3 NMR- MOUSE 26
2.3.1.4 NMR-MOLE 30
2.3.1.5 *Ex-situ* portable NMR devices for high resolution experiments 32
2.3.2 *In-situ* portable NMR devices 33
2.3.2.1 Yoked magnets 34

2.3.2.2 Halbach structure 35
2.3.2.3 NMR MANDHALAS 39
2.3.3 Techniques are used to improve the magnetic field homogeneity 42
2.3.3.1 Optimize the gap between two rings 42
2.3.3.2 Shimming 43

2.4 NMR systems and applications 44
2.4.1 Biomedicine 44
2.4.2 Cultural heritage 45
2.4.3 Material testing 46

2.5 The components of portable NMR devices 46

2.6 Motivation for this work 48

CHAPTER 3: MAGNETIC MATERIALS AND NUMERICAL METHODS 50

3.1 Introduction 50

3.2 Units 51

3.3 Magnetic materials 51

3.4 Numerical methods and simulation 59

3.5 ANSYS Software ..... Erreur ! Signet non défini.

3.6 Conclusions 67

CHAPTER 4: DESIGN, CONSTRUCTION OF A LIGHT WEIGHT PORTABLE NMR DEVICES WITH HALBACH TYPE FROM IDENTICAL ROD MAGNETS 69

4.1 Introduction 69

4.2 Modeling and simulation 70
4.2.1 Modeling 70
4.2.2 Simulation and results 72
4.2.2.1 Simulation 72
4.2.2.2 Results 73

4.3 Optimization 77

4.4 Prototype design and experimental set up 84
4.4.1 Prototype design 84
4.4.2 Experimental set up 85

4.5 Measurement results 85
4.5.1 Before shimming measurements 85
4.5.2 After shimming measurements 87

4.6 Discussion 89

4.7 Solution to correct the misalignment of magnetic directions 91
4.7.1 Modeling 91
4.7.2 Results of simulation 92
4.7.2.1 Before shimming 92
4.7.2.2 After shimming 94
4.7.3 Evaluation of the magnetic force between the magnets 95

4.8 Conclusion 96

CHAPTER V: MODELING AND DESIGN OF MANDHALAS CONFIGURATION FOR BIOMEDICAL AND AGRO-ALIMENTARY APPLICATIONS 99

5.1 Introduction 99

THIS APPROACH LEAD US TO REACH AN OPTIMUM CONFIGURATION 100

5.2 Modeling and simulation 101
5.2.1 Modeling 101
5.2.2 Simulation 102
5.2.2.1 2-D simulation 102
5.2.2.2 3-D simulation 108

5.3 Improvement of magnetic field homogeneity 111

5.4 Prototype design 115

5.5 Discussion and conclusions 116

CONCLUSION AND PERSPECTIVES 111

Résume en Français

Les travaux menés au cours de cette thèse portent sur le développement d'un aimant pour les systèmes de RMN portable. Une homogénéité élevée a été recherchée tout en maintenant le champ magnétique statique B_0 aussi élevé que possible (100 ppm, 0.12T). Les dimensions de l'aimant sont prédéfinies ainsi que celles de la zone d'intérêt en fonction de la taille des aimants permanents utilisés. Ce type de système est dédié à la recherche biomédicale et agroalimentaire.

Les travaux présentés ont consisté, à discuter dans un premier temps un certain nombre des paramètres des matériaux magnétiques essentiels à la construction d'aimants de RMN portables. Plus particulièrement le choix des aimants permanents à base de NdFeB, qui a été justifié.

Une combinaison entre portabilité, prix et sensibilité a abouti à la conception d'un prototype d'aimant portable à partir d'un système simple d'arrangement de 24 aimants permanents. Le champ magnétique et l'homogénéité de ce système ont été calculés et simulés à l'aide du logiciel ANSYS puis les résultats obtenus ont été vérifiés avec le logiciel RADIA. Une nouvelle méthode de shim pour augmenter l'homogénéité et corriger les imperfections du champ B_0 a été aussi introduite. La position des aimants de shim a fait l'objet d'une optimisation modélisée et simulée sous RADIA. Sur la base de ces résultats, un prototype a été réalisé. Les résultats des mesures de champ magnétique et de l'homogénéité sont en bonne corrélation avec les résultats obtenus par simulation. Les erreurs de mesure ont été estimées et une précision suffisante a été atteinte compte tenu des tolérances portant à la fois sur les caractéristiques des aimants et sur leur fabrication.

Un autre aimant basé sur la structure Mandhalas (**M**agnet **A**rrangement for **N**ovel **D**iscrete **H**albach **La**yout) a fait l'objet d'une étude comparative, portant sur deux configurations utilisant respectivement des aimants de formes circulaires et de formes carrés. Les simulations 2D ont été effectuées sur la base de trois critères : la masse, l'homogénéité et l'intensité du champ magnétique. Il est à noter que les Mandhalas fabriqués à partir d'aimants circulaires permettent d'avoir de meilleurs résultats (0.32 T, 178 ppm). D'autre part, la simulation 3D a été faite afin d'évaluer la totalité du système. A partir des résultats obtenus, un système de shim passif a été aussi utilisé dans ce cas et a permis l'augmentation de la zone d'homogénéité de manière significative.

MOTS CLÉS: Résonance magnétique nucléaire, bas champ, homogénéité, aimant permanent portable, configuration Halbach, configuration Mandhalas, shims, méthodes numériques.

Résume en Anglais

This thesis focuses on the development of a magnet system for NMR applications with high homogeneity while maintaining the static magnetic field B_0 as high as possible (100 ppm, 0.12T). Due to the application targets, the magnet dimensions are predefined as well as those of the region of interest according to the size of the used permanent magnets. Such system is dedicated to biomedical and agroalimentary applications.

The goal of this research has been firstly, the discussion of parameters of magnetic materials which are essential to the construction of portable NMR magnets, and then the choice of the permanent magnet material the "NdFeB" that was explained.

A compromise between the portability, price and the sensitivity has led to the design of a prototype of portable NMR magnet with a simple system of arrangement of 24 permanent magnets. The magnetic field and the homogeneity of the system were calculated and simulated by using ANSYS software and these results were correlated to those obtained by the RADIA software. A new shim method has been used to increase the homogeneity and correct the field B_0 imperfection.

Based on these results, a prototype was realized. The results of the magnetic field strength and homogeneity obtained by measurements are in good correlation with the results obtained by simulation. Sufficient accuracy was reached to take into account and correct errors due to manufacturing tolerances of the magnets.

Another magnet system based on Mandhalas configuration (Magnet Arrangement for Novel Discrete Halbach Layout) was studied. The comparison between two configurations made from circle and square magnets was performed by 2D simulation (using three criteria: mass, homogeneity and the magnetic field strength). The Mandhalas made from circle magnets give better results (0.32 T, 178 ppm). The 3D simulation was carried out to evaluate the total system. From these results, a passive shim system was also used in this case and the homogeneity has been increased significantly.

KEY WORDS: Nuclear Magnetic Resonance, Low field, portable permanent Magnet, Halbach, Mandhalas, Shim magnets, Homogeneity simulation.

Introduction

Since its discovery in 1945, Nuclear Magnetic Resonance (NMR) has become an analytical tool in physics, chemistry, biology and medicine. The devices for this phenomenon are also quickly developed in order to adapt to the diversity of applications. Usually, these devices are large, heavy and used inside. They are expensive, consume a lot of energy and need a high cost of maintenance. The portable NMR devices have been developed in order to overcome these difficulties. However, the drawbacks of portable NMR devices are its low field and poor homogeneity. To achieve the high homogeneity while maintaining the field and reducing material consumption are the challenge for researchers until now. Thus, increase of homogeneity and miniature the magnet sizes must achieved when designing a portable NMR device.

The objective of this thesis is to develop a magnet for NMR system with the homogeneity as high as possible while maintaining the magnetic field. Due to the objective of application, the dimensions of magnets are first defined. The mission of this PhD is to extend the region of interest (the region where the samples are detected), as large as possible for a given magnet size.

This thesis is organized into five chapters.

Chapter I: In this chapter, the nuclear magnetic resonance phenomenon will be briefly described. The techniques used to measure and detect the NMR signal are also presented.

Chapter II: The second chapter is an overview of the state of the art. The work and developments already done in relation to portable NMR devices will be presented in a systematic way. This allowed us to find out the best solution for our applications.

Chapter III: This chapter focuses on discussion about the magnetic material properties and numerical methods. The magnetic materials influence on the magnet specifications. Thus, the properties of materials will be discussed in the first section of this chapter. We will examine the different families of magnetic materials mostly used in the recent years in order to choose the most suitable material for our applications. The numerical and simulation methods of existing works have also been examined in this chapter. We will introduce the magnetic field calculation based on the Finite Element Method (FEM) which is the underlying procedure of ANSYS (The software we use for calculation and simulation). In addition, the element materials of the element library from ANSYS will be described in our method of simulation.

Chapter IV: This chapter will present a simple design for portable NMR device. The configuration is based on the Halbach type. It has two main rings arranged in alignment to

compensate the magnetic field outside of the rings. Each ring consists of 12 identical magnets of cylindrical shape. In order to predict the properties of this configuration, its magnetic field strength and homogeneity are calculated and simulated respectively by ANSYS and RADIA software~~s~~. The results obtained from both software~~s~~ are in good correlation for simulation as well as for optimization. Based on these results, we realized a new prototype. The properties of prototype have been also verified by measurement.

Chapter V: In this chapter, we propose a configuration based on the Halbach structure with discrete magnets abbreviated Mandhalas (Magnet Arrangement for Novel Discrete Halbach Layout) ~~configuration~~. The properties of Mandhalas made respectively from cube and cylindrical magnets are compared by 2D simulation. Taking into account criteria~~s~~ as magnetic field strength, homogeneity and mass, we have chosen the Mandhalas with cylindrical magnet for modeling and 3D simulation.

To increase the homogeneity, we use two shim rings placed inside the bore of this configuration. The magnetic field homogeneity has been significantly improved by optimizing the positions of these rings. In that case we also designed, realized and characterized a new prototype.

Chapter 1

Basic of NMR

Summary:

- **Introduction**
- **Principle of NMR or MRI**
- **Signal to noise ratio**
- **T_1, T_2 measurements**
- **Influence of magnetic field homogeneity on NMR spectroscopy**

Chapter 1: Basic of NMR

1.1 Introduction

Since its discovery in 1945, the Nuclear Magnetic Resonance (NMR) has become a valuable tool in physics, chemistry, biology and medicine. The Nuclear Magnetic Resonance (MRS) and the magnetic resonance imaging (MRI) are non-invasive techniques. Both of them are based on the principle of NMR. These techniques are complementary and are used in the characterization of tissue, molecules..etc.

The MRI is a medical imaging technique used to investigate inside the human body by producing high quality images. In 1952, one dimensional MRI image was reported by Herman Carr in his PhD thesis [1]. Much later, in 1973, Paul Lauterbur and his team expanded the Carr's technique and introduced the method of using magnetic field gradients to obtain the images of objects in two dimensions and three dimensions [2]. Today, it is a powerful tool for the diagnostic of human diseases and other medical applications.

The NMR spectroscopy is a technique that exploits the magnetic properties of certain atomic nuclear such as ^{1}H or ^{13}C. Since NMR experiment was first described by Rabi *et al* [3] in 1938, the field of NMR has drawn much attention of researchers. This technique has been expanded for the use on liquids and solids by Felix Bloch and Edward Mills Purcell, for which they shared the Nobel Prize in Physics in 1952. NMR spectroscopy can analyze the chemical solutions and determine the structure, environments of various molecules. It thus becomes the standard technique in chemical analysis of materials, elucidation of protein structures, drug research and production control, …etc.

As this work is concerned with the NMR spectroscopy, it is necessary to figure out the NMR phenomenon. In this chapter, we will briefly describe the principle of NMR and the techniques used to measure the NMR signal.

1.2 Principle of NMR and MRI

The nucleus of an atom consists of two particles, protons and neutrons. These particles spin about their axis. These motions produce an angular momentum. Because a proton has a mass, a positive charge and spins, it produces a small magnetic field like a tiny bar magnet (Figure 1-1).

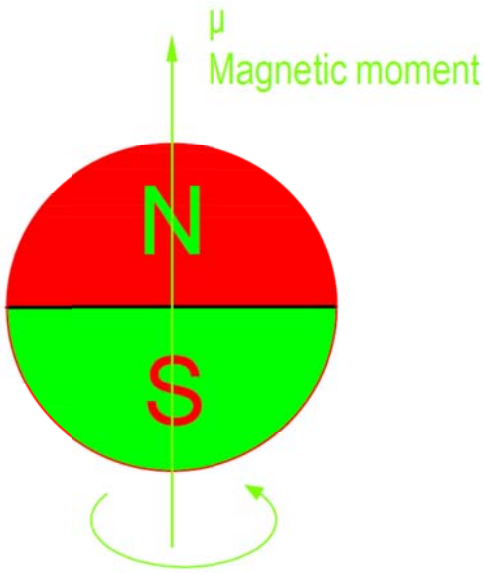

Figure 1-1: The proton rotates around its axis and produces a magnetic moment.

The magnetic field of proton produced when it spins about their axis is called magnetic moment. This magnetic moment has both magnitude and direction like the same direction of angular momentum. The ratio between magnetic moment and the angular moment is known as the gyromagnetic ratio, γ (MHz/T). Each nucleus has different gyromagnetic ratio. For example, the gyromagnetic ratio of proton (^{1}H) is 42.58 MHz/T. When a proton is placed in an external field called B_0, the magnetic moments align in either parallel or anti-parallel with the direction of B_0 (Figure 1-2).

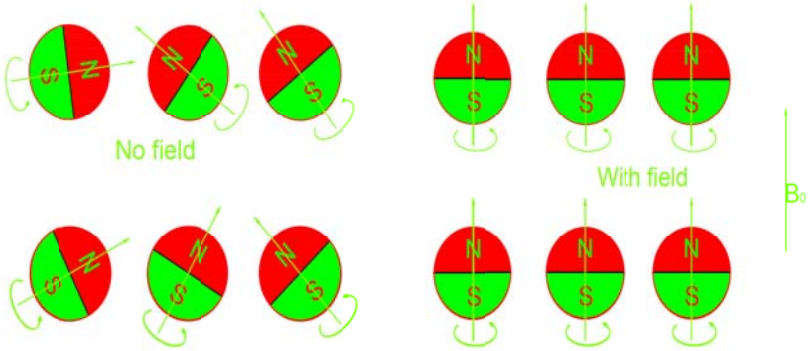

Figure 1-2: Without external magnetic field B_0, the protons are randomly oriented, resulting in zero magnetization. With B_0, they are aligned along the direction of B_0 .

There are two energy states of proton. The proton is in low energy state when its precessional axis is parallel to B_0, and in high energy state when its axis is antiparallel as shown in Figure 1-3 [4].

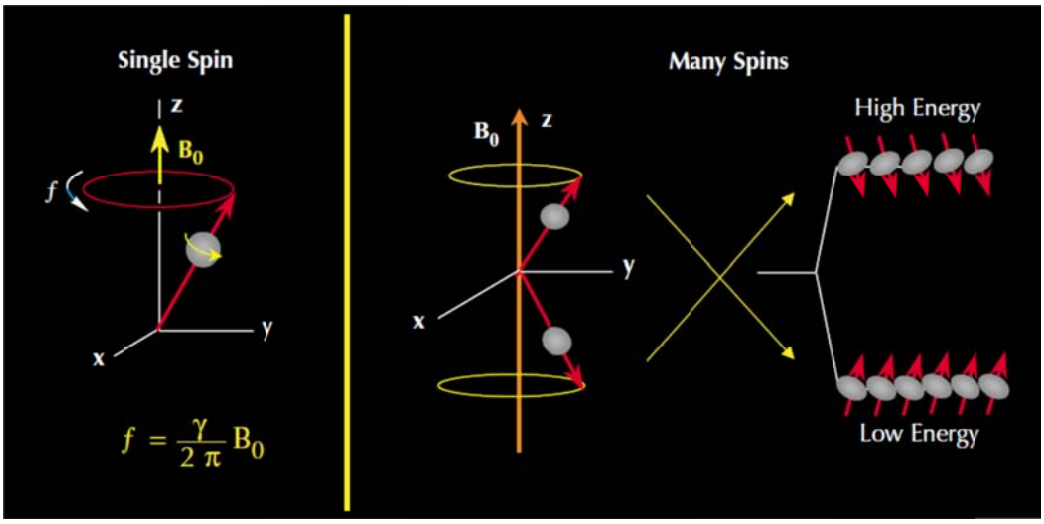

Figure 1-3: When the protons are placed in an external magnetic field B_0, they are forced into two energy states which are low and high energy state [4].

The sum of magnetic moment of each proton is called magnetization (M_0). The magnetization M_0 is given by Curie's law [5]. It is defined as the magnetic moment per unit volume. For the case of N nuclei per unit volume, M_0 is given by:

$$\boldsymbol{M_0 = N\frac{\gamma^2 h^2 I(I+1)}{3(4\pi^2)kT}\,B_0} \tag{1-1}$$

Where:

- k: Boltzman's constant,
- T: absolute temperature (Kelvin),
- h: Planck's constant,
- I: the spin quantum number of the nucleus.

When a radio frequency (RF) pulse at a frequency f is applied perpendicular to B_0, the net magnetization M_0 tilt away from the external field B_0. This frequency known as Larmor frequency, is given by:

$$\boldsymbol{f = \frac{\gamma B_0}{2\pi}} \tag{1-2}$$

The equation (1-2) shows that the Larmor frequency is proportional to the magnitude of the external field B_0 and the gyromagnetic ratio of the nucleus. Each nuclei proton has the

different Lamor frequency because of its gyromagnetic ratio.

When the RF pulse stops the nuclei return to their initial position called equilibrium, it means that M_0 is parallel again to B_0. The time that the nuclei return to equilibrium is known as relaxation time. There are two kinds of relaxation time:

- T1 (spin lattice relaxation time) is the time that the net magnetization returns to its equilibrium. At equilibrium, the vector $\overrightarrow{M_0}$ is parallel to the direction of B_0. In this status, the magnitude of longitudinal magnetization called M_z equals M_0. The M_z is a function of time t. Its change is described by equation (1-3) if the net magnetization is placed along the +Oz axis. In contrast, if the net magnetization is placed along the –Oz axis, the behavior of M_z is governed by equation 1-4 [6]. In summary, T_1 characterizes the alignment of protons with ~~the external field~~ B_0 (Figure 1-4).

$$\boldsymbol{M_z(t) = M_0(1 - e^{\frac{-t}{T_1}})} \quad (1\text{-}3)$$

$$\boldsymbol{M_z(t) = M_0(1 - 2e^{\frac{-t}{T_1}})} \quad (1\text{-}4)$$

Where:

- t is the time that the spins are exposed to the B_0.
- $M_z(t)$ is the magnitude of magnetization at time t, when the direction of B_0 is taken along the Oz axis.
- M_0 is the maximum value of magnetization in a given magnetic field.

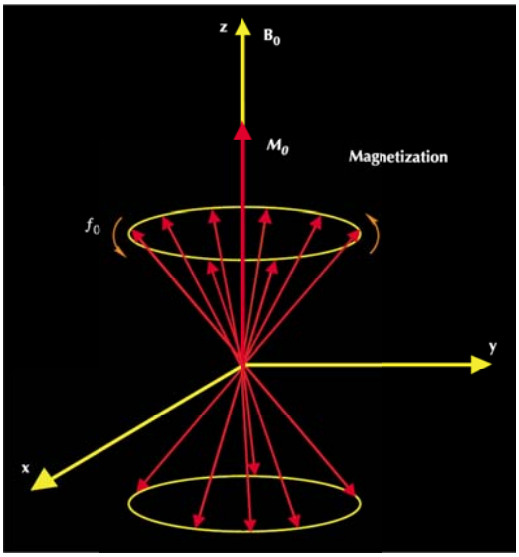

Figure 1-4: M_0 is the sum of the number of protons aligned parallel and anti-parallel to B_0 [4].

- T_2 (spin-spin lattice relaxation time) is the time that the transverse magnetization returns to its equilibrium. When the RF pulse (B_1: perpendicular to external field B_0) is applied, the net magnetization tips from the longitudinal axis to the transverse plane. It rotates around the longitudinal axis at the frequency of the protons. This frequency is called Lamor frequency. The applied field B_1 provides the energy to spins and makes them move to the high energy state. Simultaneously, it also makes spins precession in phase with each other. This phenomenon is known as NMR. The oscillating field results in the tipping of the net magnetization which rotates away from the Oz axis. The angle between the net magnetization and the Oz axis is called flip or tip angle (Figure 1-5) and given by:

$$\boldsymbol{\theta = \gamma B_1 \tau} \tag{1-5}$$

Where:

- θ is the tip angle (degrees),
- B_1 is the amplitude of the oscillating field,
- τ is the time over which the oscillating field is applied.

The equation (1-5) shows that the tip angle is proportional to the strength of B_1 and duration of τ. It means that the strength of B_1 and duration of τ determine amount of energy supplied to the proton spin system [4].

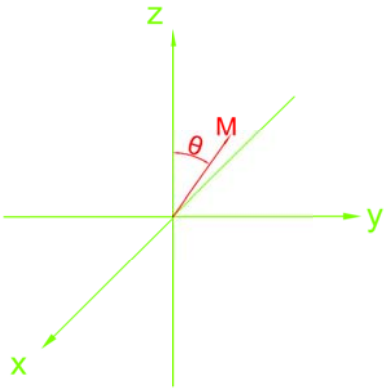

Figure 1-5: The field B1 is applied, the nuclear magnetization M tips and rotates away from the longitudinal axis. The angle between them is known as tip angle.

In NMR experiments, the RF pulse is usually applied at an angle θ=90° and θ =180°. For the angle θ=90°, the polarized protons tip and start to precess in phase in the transverse plane. When the RF pulse is turned off, the phase coherence of the spins is gradually lost because of the interactions between them. The time which describes the return to equilibrium is known as spin-spin relaxation time T_2. It is governed by equation (1-6).

$$\boldsymbol{M_{xy}(t) = M_{xyo} e^{\frac{-t}{T_2}}} \quad (1\text{-}6)$$

Where

- M_{xyo} is the magnitude of the transverse magnetization at t=0 (the time at which the 90° pulse ceases).

There are two factors that affect on T_2: the molecular interactions and the inhomogeneity of B_0. The combination of two factor above is the time constant called T_2^*. The relationship between the T_2 from molecular processes and that from inhomogeneity in the magnetic field is as follows [6]:

$$\boldsymbol{\frac{1}{T_2^*} = \frac{1}{T_2} + \frac{1}{T_{2inhomo}}} \quad (1\text{-}7)$$

When a 90° RF pulse is applied, M_0 tips to XY plane (Figure 1-6-a). It rotates about the Oz axis and this motion will produce a sine wave current which is a function of time in the coil of wire located around of Ox axis (Figure 1-6-b, Figure 1-7-a). When the RF pulse is turned off, the spins start to diphase with the time T_2^*. Therefore, the corresponding wave will decay with the time T_2^*. This decay signal is called free induction decay (FID) (Figure 1-7-b). The FID is converted into a frequency domain spectrum by Fourier transform (figure I.7-c).

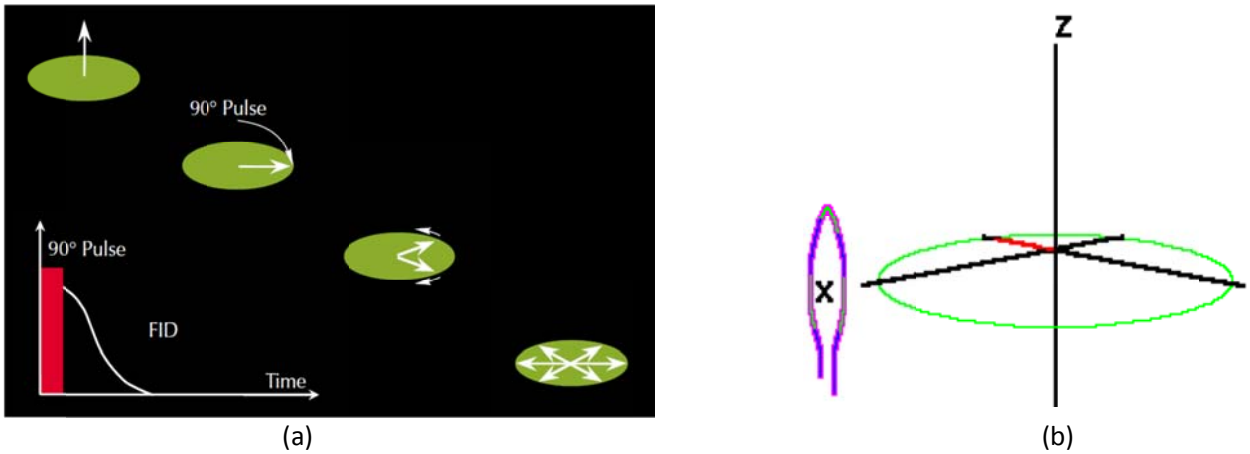

Figure 1-6:(a) After application of a 90° RF pulse, the proton spins tip to transverse plane and start to diphase when the pulse turns off. (b) The coil is placed on Ox axis to detect the decay signal [4] [6].

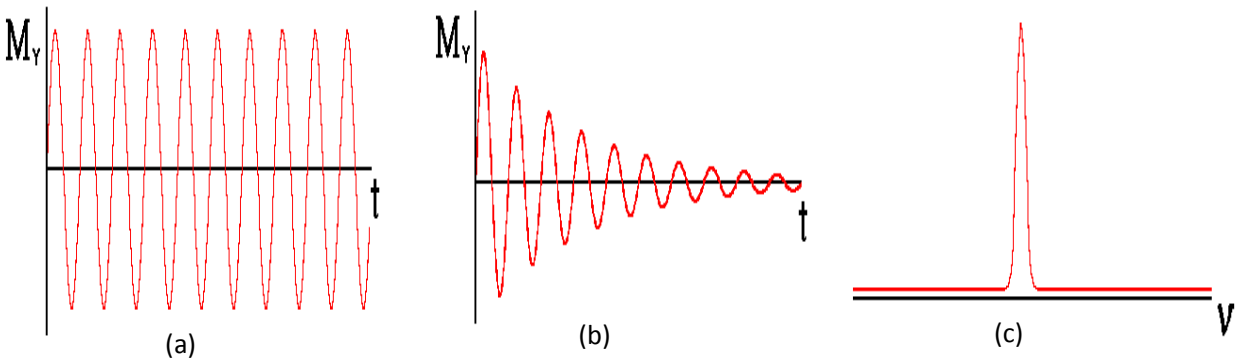

Figure 1-7: The current is plotted as a function of time and decay with the time T_2 due to the dephasing of spins. Then, the FID is converted into spectrum by Fourier transform* [6].

1.3 Signal to noise ratio

The concept of signal to noise ratio (SNR) for NMR is first proposed by Ernst et al [7] in 1966 and applied to Micro-NMR by Odelblad [8] in the same year . The SNR is defined as the ratio of the amplitude of the signal to the average value of the noise. It is an important criteria to analyze the sensitivity of detection systems [9][10] in NMR experiments. Therefore, it is necessary to compute the SNR for evaluation of the quality of the detection of the NMR signal. This evaluation involves both ability of the system to detect the signal and the influence of the noise on this system.

1.3.1 The signal

There are numerous detection devices of NMR signal proposed by previous researchers. These devices have been used in the specific experimental conditions. The Superconducting Quantum Interference Device (SQUID) [11][12] and the mixed-sensor [13][14] is only operated in a low magnetic field condition. Another method is Cantilever (force detection) [15][16] which is suitable for the samples with nano size. The most popular device used to detect NMR signal is conductive coil due to the simple use and good intrinsic sensitivity. D. I. Hoult and R. E. Richards [9] proposed an approach to calculate the signal to noise ratio of the conductive coil using the principle of reciprocity. This method considers an arbitrary loop S where a unit current circulates and an arbitrary point P locates in the free space. The unit current creates a magnetic field B1 in the loop. They are placed in the static magnetic field B_0 which is perpendicular to B_1 as shown in Figure 1-8.

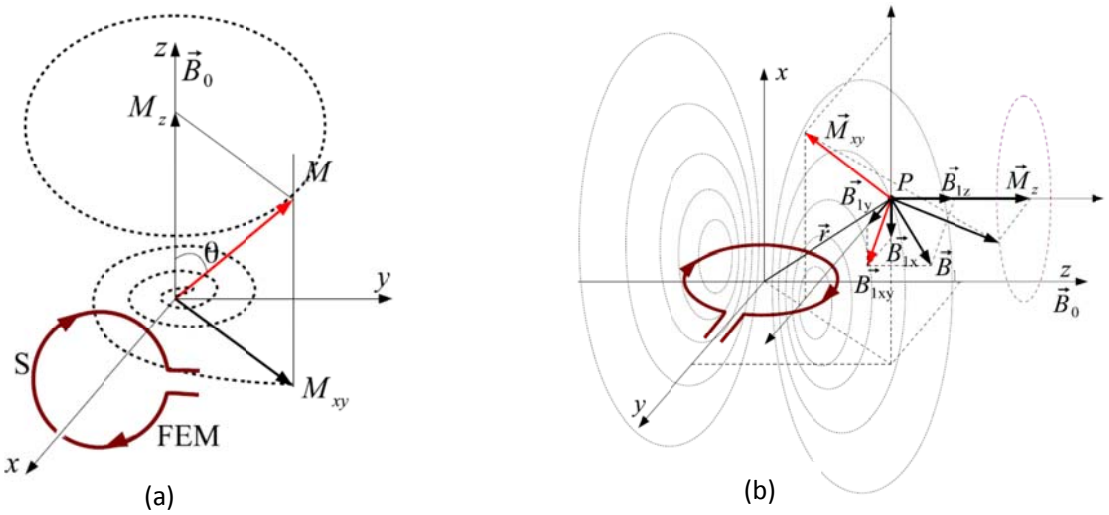

Figure 1-8: The induction principle and signal reception [9][10]. *(a) The rotation of Mxy induces on the loop S an electromotive force (EMF). (b) The signal from point P is proportional to the B1 field at that point.*

Considering that the surface S consists of elementary loops of surface dS bounded by an elementary loop of unit current. There exists a magnetic pseudo scalar potential at the point P. The potential of an elementary loop producing at the point P is:

$$d\Phi = d\vec{S}.\vec{\nabla}\left(\frac{1}{r}\right) \tag{1-8}$$

Where:

- r is the distance from P to the elementary loop
- The derivatives are taken on the coordinates of point P

The total field produced by the loop is:

$$\overrightarrow{B_1} = -\mu_0 \int_S \vec{\nabla}\left[d\vec{S}.\nabla\left(\frac{1}{r}\right)\right] \tag{1-9}$$

The element magnetic flux dF passes through the element loop generated by a dipole $\vec{m}$ located at the point P is:

$$dF = d\vec{S}.\overrightarrow{B_1} = \mu_0 d\vec{S}.\vec{\nabla}\left[\vec{m}.\vec{\nabla}\left(\frac{1}{r}\right)\right] \tag{1-10}$$

We consider that the dipole $\vec{m}$ is constant through space and d$\vec{S}$ is also constant. The equation (1-10) can be written as following:

$$dF = \mu_0 \vec{m}.\vec{\nabla}\left[d\vec{S}.\vec{\nabla}\left(\frac{1}{r}\right)\right] \tag{1-11}$$

Thus the electromotive force (EMF) induced in the loop is given by:

$$\xi = \frac{\partial F}{\partial t} = \mu_0 \frac{\partial}{\partial t}\left(\vec{m}.\int_S \vec{\nabla}\left[d\vec{S}.\vec{\nabla}\left(\frac{1}{r}\right)\right]\right) \quad (1\text{-}12)$$

We substitute the equation 1-9 to the equation 1-12. We have:

$$\xi = -\frac{\partial}{\partial t}(\overrightarrow{B_1}.\vec{m}) \quad (1\text{-}13)$$

This result is called the principle of reciprocity. The equation 1-13 was validated for the intermediate and radiation zone fields [17]. This equation is applied to calculate the signal induced by spins precession [9][10].

After the 90° pulse, the net magnetization M_0 of the sample tips to transverse plane and rotate away from the longitudinal axis at an angular velocity ω_0 (Figure 1-8) given by:

$$\omega_0 = \gamma B_0 \quad (1\text{-}14)$$

The rotation of the net magnetization M on the transverse plane produces an alternating magnetic field at the loop of conductor S (Figure 1-8-a). Using the principle of reciprocity, the EMF induced in the loop S is:

$$\partial\xi_s(t) = -\frac{\partial}{\partial t}\left(\frac{\overrightarrow{B_1}}{\iota}.\overrightarrow{M(t)}\right)dV_s \quad (1\text{-}15)$$

Where:

- $\partial\xi_s(t)$ is the electromotive force induced in the loop S by elementary volume dV_s of the sample.
- B_1 is the magnetic field created by unit current i.

Thus the electromotive force EMF induced in the loop S by the volume V of sample is:

$$\xi_s(t) = -\iiint_S \frac{\partial}{\partial t}\left(\frac{\overrightarrow{B_1}}{\iota}.\overrightarrow{M(t)}\right)dV_s \quad (1\text{-}16)$$

The behavior of the net magnetization M_0 is described by the well-known Bloch equation [18][19]:

$$\frac{\partial\vec{M}}{\partial t} = \gamma M\left(B_0 + \frac{\omega_0}{\gamma}\right)\vec{u}_z - \frac{M_z - M_0}{T_1}\overrightarrow{u_z} - \frac{M_x\overrightarrow{u_x} + M_y\overrightarrow{u_y}}{T_2} \quad (1\text{-}17)$$

Where:

- $\overrightarrow{u_x}, \overrightarrow{u_y}, \vec{u}_z$: are the unit vectors in Ox, Oy and Oz directions of $\vec{M}$ respectively.
- T_1, T_2 are the longitudinal and transversal relaxation time respectively.

The magnetic field B_1 produced by the sinusoidal current $i = Icos(\omega_0 t)$ in the loop S is:

$$\overrightarrow{B_1}(t) = \overrightarrow{B_{1x}}(t) + \overrightarrow{B_{1y}}(t) + \overrightarrow{B_{1z}}(t) \quad (1\text{-}18)$$

The NMR signal is only received on the transverse plane, thus the component $\overrightarrow{B_{1z}}(t)$ is ignored. Hence the equation 1-18 can be written as:

$$\overrightarrow{\boldsymbol{B_{1xy}}}(\boldsymbol{t}) = \overrightarrow{\boldsymbol{B_{1x}}}(\boldsymbol{t}) + \overrightarrow{\boldsymbol{B_{1y}}}(\boldsymbol{t}) = \boldsymbol{B_{1xy}}\mathbf{cos}(\boldsymbol{\omega_0 t})\overrightarrow{\boldsymbol{v_{xy}}} \quad (1\text{-}19)$$

Where:

- $\overrightarrow{v_{xy}} = \overrightarrow{v_x} + \overrightarrow{v_y}$ is the unit vector of $\overrightarrow{B_{1xy}}(t)$.
- $B_{1xy} = \sqrt{B_{1x}^2 + B_{1y}^2}$ is the magnitude of $\overrightarrow{B_{1xy}}(t)$.

We substitute the equations 1-17 and 1-19 into the equation 1-16, then, we have:

$$\boldsymbol{\xi_s(t)} = -\frac{\boldsymbol{\partial}}{\boldsymbol{\partial t}} \iiint_{\boldsymbol{s}} \left[\frac{\boldsymbol{B_{1xy}}\overrightarrow{\boldsymbol{v_{xy}}}}{\boldsymbol{I}} . \left[\boldsymbol{\gamma M} \left(\boldsymbol{B_0} + \frac{\boldsymbol{\omega_0}}{\boldsymbol{\gamma}} \right) \overrightarrow{\boldsymbol{u_z}} - \frac{\boldsymbol{M_z - M_0}}{\boldsymbol{T_1}} \overrightarrow{\boldsymbol{u_z}} - \frac{\boldsymbol{M_x}\overrightarrow{\boldsymbol{u_x}} + \boldsymbol{M_y}\overrightarrow{\boldsymbol{u_y}}}{\boldsymbol{T_2}} \right] \right] \boldsymbol{dV_s} \quad (1\text{-}20)$$

And

$$\overrightarrow{\boldsymbol{M_{xy}}} = \boldsymbol{M_x}\overrightarrow{\boldsymbol{u_x}} + \boldsymbol{M_y}\overrightarrow{\boldsymbol{u_y}} = \boldsymbol{M_0} \boldsymbol{e}^{-\frac{\boldsymbol{t}}{\boldsymbol{T_2^*}}} \mathbf{sin}(\boldsymbol{\theta})\overrightarrow{\boldsymbol{u_{xy}}} \quad (1\text{-}21)$$

$$\overrightarrow{\boldsymbol{v_{xy}}} . \overrightarrow{\boldsymbol{u_z}} = \mathbf{0} \quad (1\text{-}22)$$

$$\overrightarrow{\mathbf{v_{xy}}} . \overrightarrow{\mathbf{u_{zxy}}} = \mathbf{cos}(\boldsymbol{\omega_0 t}) \quad (1\text{-}23)$$

Where:

- M_0 and T_2^* are given by the equations 1-1 and 1-7 respectively.

Substitute the equations 1-21, 1-22 and 1-23 into the equation 1-20, the integral simplifies to:

$$\boldsymbol{\xi_s(t)} = \frac{\boldsymbol{B_{1xy}}}{\boldsymbol{I}} \boldsymbol{\omega_0 M_0 V_E} \boldsymbol{e}^{-\frac{\boldsymbol{t}}{\boldsymbol{T_2^*}}} \boldsymbol{cos}(\boldsymbol{\omega_0 t}) \boldsymbol{sin\theta} \quad (1\text{-}24)$$

If the tip angle $\theta = 90°$ and B_1 is homogeneous over the sample volume. The amplitude of NMR signal of a pulse RF is:

$$\boldsymbol{\xi_s(t)} = \frac{\boldsymbol{B_{1xy}}}{\boldsymbol{I}} \boldsymbol{\omega_0 M_0 V_E} \quad (1\text{-}25)$$

1.3.2 The noise

In NMR experiments, the noise of the detection systems mostly comes from the thermal noise associated to the resistance of the coil while other noises such as radiation, sample are negligible [20]. The thermal noise is given by formula:

$$V_N = \sqrt{4kT_p \Delta f R} \tag{1-26}$$

Where:

- $k = 1.38 * 10^{-23} [\frac{J}{K}]$ is Boltmann constant.
- T_p (K) is the temperature of the coil.
- R is the electrical resistance of the coil.
- Δf is the detection bandwidth.

1.3.3 The sensitivity

The sensitivity of detection systems refer to the signal to noise ratio (SNR). It is defined as the ratio of the NMR signal (equation 1-25) to the noise (equation 1-26).

$$SNR = \frac{\frac{B_{1xy}}{I} \omega_0 M_0 V_E}{\sqrt{4kT_p \Delta f R}} \tag{1-27}$$

$$SNR \, \alpha \, \frac{B_{1xy}}{I\sqrt{R}} \tag{1-28}$$

The equation 1-28 is used to evaluate the sensitivity of the antennas and optimize the configuration of antennas [21].

1.4 T_1 and T_2 measurements

1.4.1 T_2 measurement

Both T_1 and T_2 are important in NMR experiment. However, the measurement of T_2 relaxation is more practical because it can be obtained quicker than T_1. There are two well-known techniques which are used to measure T_2.

Firstly, Spin echoes or Hahn's echo, this technique was first discovered by Hahn in 1950 [22]. The echo is a signal which has first vanished with time and then reappears some time later. The Hahn echo consists of two pulses, the first one is 90° pulse and then followed by 180° after the delay time τ as shown in Figure 1-9.

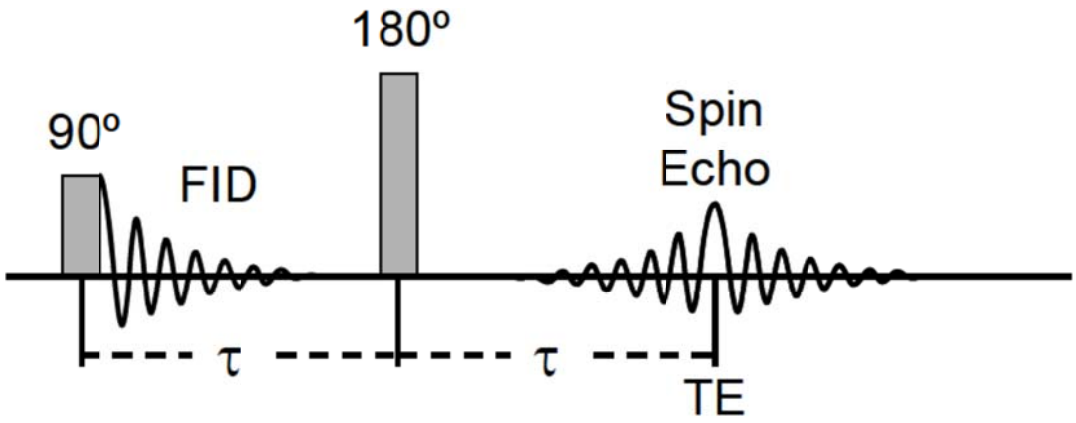

Figure 1-9: Hahn echo with two pulse sequence used to measure T_2. FID is the free induction decay; τ is the delay time between two pulse and TE is the inter-echo spacing used in the pulse sequence [22].

After the first pulse, the net magnetization is transversal to the XOY plane and lies along Oy axis. Initially, the transverse vector M_0 is a single vector because the nuclei are in phase. As the time τ after which the 90° pulse is turned off, the nuclei are loss of coherence due to the inhomogeneity of the static field. Some nuclei with higher Larmor frequency rotate faster while those with lower Larmor frequency lag behind. At a period of time τ after the first pulse, the second 180° pulse is applied along Oy axis. All the spins are mirrored around OY and continue to rotate around Oz axis. Now the phases of the spins with higher Larmor frequency transform lead into lag, in contrast, the spins with lower Larmor frequency transform lag into lead. Thus, after the period of time τ, all the spins refocus. Because the spins refocus, they generate a signal in a receive coil. This phenomenon is called spin echo.

T_2 can be determined by measuring the interpolation of the curve $e^{\frac{-t}{T_2}}$. After the second pulse, the amplitude of transverse magnetization is defined by the equation (1-29) [23].

$$\boldsymbol{M_z(2\tau) = M_0 e^{\frac{-2\tau}{T_2}}} \quad (1\text{-}29)$$

Secondly, the pulse sequence used to measure the transverse relaxation time T_2 is known as CPMG pulse sequence. The CPMG sequence was first introduced by Carr and Purcell in 1954 [24] and modified by Meiboom and Gill after four years [25]. The resulting sequence is now well-known Carr-Purcell-Meiboom-Gill (CPMG) sequence. It consist of one 90° pulse and series of 180° pulse which lead to the formation a train of echoes after the delay time τ. The time between two 180° pulse is called the echo time T_E. The decay of the amplitude of the spin echoes is used to measure the time T_2 (Figure 1-10). The amplitude of the spin echo is weaker than the initial

amplitude by a factor of $e^{\frac{-2\tau}{T_2}}$ [26].

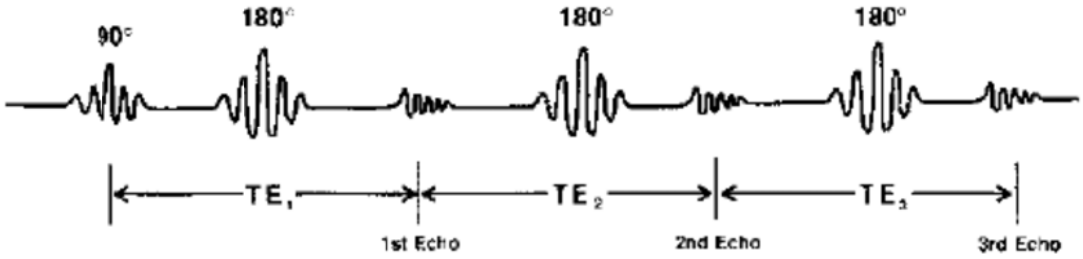

Figure 1-10: CPMG sequence: After the initial 90° pulse, a series of 180° pulse is applied to produce a train of echoes. The NMR signal is detected by the decay of T_2 **[27]**.

1.4.2 T_1 measurement

The time T_1 is decay constant for the Z component of the longitudinal magnetization (M_z) towards its equirilium value (M_0). There are two common pulse sequence used to measure T_1: The saturation recovery and the inversion recovery [26].

The saturation recovery uses a series of 90° pulses with the separation τ to cancel the M_z. The signal after each pulse is given by equation 1-30 [26]. By recording the echo signal intensity as a function of continuously increasing recovery time τ, the time T_1 can be determined. This is an efficient method for measuring T_1.

$$\boldsymbol{M_z(\tau) = M_0(1 - e^{\frac{-\tau}{T_1}})} \quad (1\text{-}30)$$

While the inversion recovery sequence initially uses the 180° pulse to invert the M_z from the positive Oz axis to the negative Oz axis as shown in Figure 1-11 and then follows by a 90° pulse. Immediately after the stimulus, the spins start to flip back at the rate of $1/T_1$, which is described by the equation 1-4. It can not be directly measured by the time which the vector M_z grow because there is no transverse component. Therefore, the subsequent 90° pulse is used to tilt the magnetization into the plane of the receiving coil where it can be measured. The time T_1 can be computed by equation 1-4.

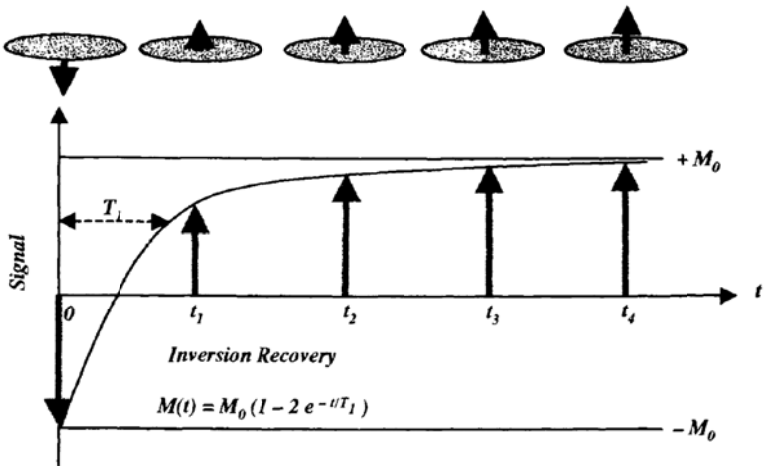

Figure 1-11: A sequence of experiment in which the recovery time are 0, t1, t2, t3 and t4 and the corresponding FID is plotted against the variable recovery time [26].

1.4.3 Self-diffusion and field gradient

In NMR experiments, the spins experience a constant steady field. This is an imperative condition for them refocus after the second pulse. However, spins in the liquid samples are not immobile and diffuse in space. Their moving is characterized by the diffusion coefficient which appears in the law governing the diffusion of the local magnetization m [28]. Self-diffusion is very important in the context of inhomogeneous field. Through an analysis of the effect of diffusion on the echo amplitude, the values of both the transverse relaxation time T_2 and the diffusion coefficient can be obtained by observing the decay of the echoes. This analysis can be found in detail in [23].

The sample is placed in a strong field gradient $G = \frac{\partial B_0}{\partial z}$ in direction Oz, the Larmor frequency is then:

$$\boldsymbol{\omega(z) = \omega_0 + Gz} \tag{1-31}$$

Neglecting the effects of relaxation and diffusion, the magnetization at the time t after the initial 90° pulse is:

$$\boldsymbol{M(z,t) = A(t)exp(iGzt)} \tag{1-32}$$

M depends only on the space component Z and the diffusion equation is:

$$\boldsymbol{\frac{\partial M}{\partial t} = D\frac{\partial^2 M}{\partial z^2}} \tag{1-33}$$

The equation 1-33 yields:

$$\frac{dA}{dt} = -DG^2t^2A \tag{1-34}$$

and

$$A(t) = A(0)\exp(\frac{-DG^2t^3}{3}) \tag{1-35}$$

The amplitude of the spin echo is weaker than the initial amplitude by a factor of $e^{\frac{-2\tau}{T_2}}$. The echo amplitude at the time 2τ is:

$$M(2\tau) = M_0\exp(\frac{-2\tau}{T_2})\exp(\frac{-2DG^2\tau^3}{3}) \tag{1-36}$$

When using a pulse train and observing the various echoes, the amplitude of the nth echo at the time 2nτ is:

$$M_n(2n\tau) = M_0\exp(\frac{-2nDG^2\tau^3}{3} + \frac{-2n\tau}{T_2}) \tag{1-37}$$

Or else, as a function of time $t = 2n\tau$, the equation 1-37 can be written:

$$M_n(t = 2n\tau) = M_0\exp\left[-\left(\frac{1}{T_2} + \frac{1}{3}DG^2\tau^2\right)t\right] \tag{1-38}$$

This is an exponential function of time, both D and T_2 are possible to retrieve with the rate constant that depends on the interval 2τ between the pulses:

$$\frac{1}{T'_2} = \frac{1}{T_2} + \frac{1}{3}DG^2\tau^2 \tag{1-39}$$

1.5 Influence of magnetic field homogeneity on NMR spectroscopy

The homogeneity of magnetic field is an important criteria which influents on the NMR signals. Therefore, it is necessary to emphasize the extremely homogeneous fields for NMR spectroscopy (MRS) when design a portable NMR device. NMR is the result of Zeeman Effect on the nucleus. The external part of the spin Hamiltonian which describes the interaction of the spins with magnetic environment is given by the equation 1-40 [18]:

$$\hat{H}_{ext}(t) = \hat{H}_{static} + \hat{H}_{grad}(r,t) + \hat{H}_{RF}(t) \tag{1-40}$$

$$\hat{H}_{static} = \sum_j \hat{H}_j^{static} \tag{1-41}$$

$$\hat{H}_{grad}(r,t) = \sum_j \hat{H}_j^{grad}(r,t) \tag{1-42}$$

$$\widehat{\boldsymbol{H}}_{\boldsymbol{RF}}(\boldsymbol{t}) = \sum_{\boldsymbol{j}} \widehat{\boldsymbol{H}}_{\boldsymbol{j}}^{\boldsymbol{gradRF}}(\boldsymbol{t}) \quad (1\text{-}43)$$

Where:

- $\widehat{H}_j^{static}$ is the interaction of each spin I_j with the external static field B_0.
- $\widehat{H}_{grad}(r,t)$ is the interaction of each spin I_j with the gradient field B_{grad}.
- $\widehat{H}_{RF}(t)$ is the interaction of each spin I_j with the RF field B_{RF} generated by the RF coil.

Some of these interactions are proportional to the external field (chemical shift), some are not (dipolar coupling), but always remain in the order of the part per million (ppm) of the main Zeeman Hamiltonian. The small changes of the static field B_0 in each point of the sample will affect on the Larmor frequency. Hence, MRS requires sub-ppm over the volume of sample in order to be useful [29], for example, $\frac{\Delta B_0}{B_0} < 10^{-7}$ across the sample for good spectroscopic resolution [30].

Chapter 2

Portable NMR system

Summary:

- **Introduction**
- **The need of portable NMR devices**
- **Portable NMR devices**
- **The applications of NMR devices**
- **The components of portable NMR devices**
- **Motivation for this work**

Chapter 2: Portable NMR system design

2.1 Introduction

The field of portable NMR devices has been rapidly developed in the past few years. In the early time, the NMR devices are large, expensive and complicated devices. They are usually used in laboratory and are not portable. They use superconducting magnet to generate the field B_0. Such devices generate the homogeneous field, consume too much energy and need high cost of maintenance.

The need of external applications of the laboratory motivates the development of portable NMR devices. There are varieties of portable NMR devices that have been done by previous researchers such as NMR-MOUSE, Mandhalas and well-logging etc... The shapes of the magnets depend on the end uses. For example, the *Ex-situ* devices are suitable for the samples with large size and placed outside the magnets while *in-situ* devices are suitable for the small samples and high resolution experiments due to high field strength and homogeneity are more easily achieved with such geometries. The portable NMR devices are used for many applications such as oil industry, medicine and materials….

The objective of this chapter is to introduce the development of portable NMR devices from the early time until now. In addition, we will present the different kinds of them and their diversity applications as state of the art.

2.2 The need of portable NMR devices

In 1952, one dimensional MRI image is reported by Herman Carr in his PhD thesis [1]. Much later on, in 1973, Paul Lauterbur and his team expanded the Carr's technique and introduced the way using magnetic field gradients to obtain the images of objects in two dimensions and three dimensions [2]. The major drawback of NMR is its lack of sensitivity. This lack of sensitivity makes difficult the study of low γ nuclei in NMR spectroscopy by increasing the experiment time. The low sensitivity is also a limitation of MRI resolution [29]. One solution to solve this difficulty is to increase the external magnetic field in order to improve the SNR. Thus, the idea of the increase of magnetic field motivated many researchers performing experiments with high magnetic field.

Rabi and his team were performed the first experiment at a field of 0.6T (about 25.6 MHz) while Lauterbur's experiment was done at a field 1.4T (60 MHz). In 1964, a superconducting magnet at 200 MHz was introduced by Nelson and Weaver [31] for the NMR spectroscopy

experiment. Since then, the field strength of NMR spectrometers continues to increase reaching 23.5T with the machine installed in the Centre de RMN "*à très hauts champs in Lyon, France*". The prominent feature of NMR spectroscopy experiments with high magnetic field is the magnetic field B_0 more homogeneous than one with low magnetic field. The high field associated the field homogeneity, weight and dimension of magnets is shown in the Figure 2-1. However, very high field also have some disadvantages. The machine is very expensive (some machines cost millions of dollars). These machines are heavy and have the large dimensions. Because of large and heavy, they need high cost of maintenance and consume much energy. Therefore, these obstacles are the limitation of high field NMR spectrometers for widely applications of this technique. In addition, their weight is also a difficulty for out of laboratory applications.

The development of permanent magnet technology such as rare-earth magnets has allowed researchers to use them for NMR applications, although they are applied for accelerators earlier. These magnets can produce a strong and homogeneous field which is two important criteria for the NMR experimental requirements. Thus, this satisfied the conditions for design of portable NMR devices. Other attractive features of permanent magnets are obviously the absence of external source of electric power and no maintenance.

For these reasons, the portable NMR devices have been developed.

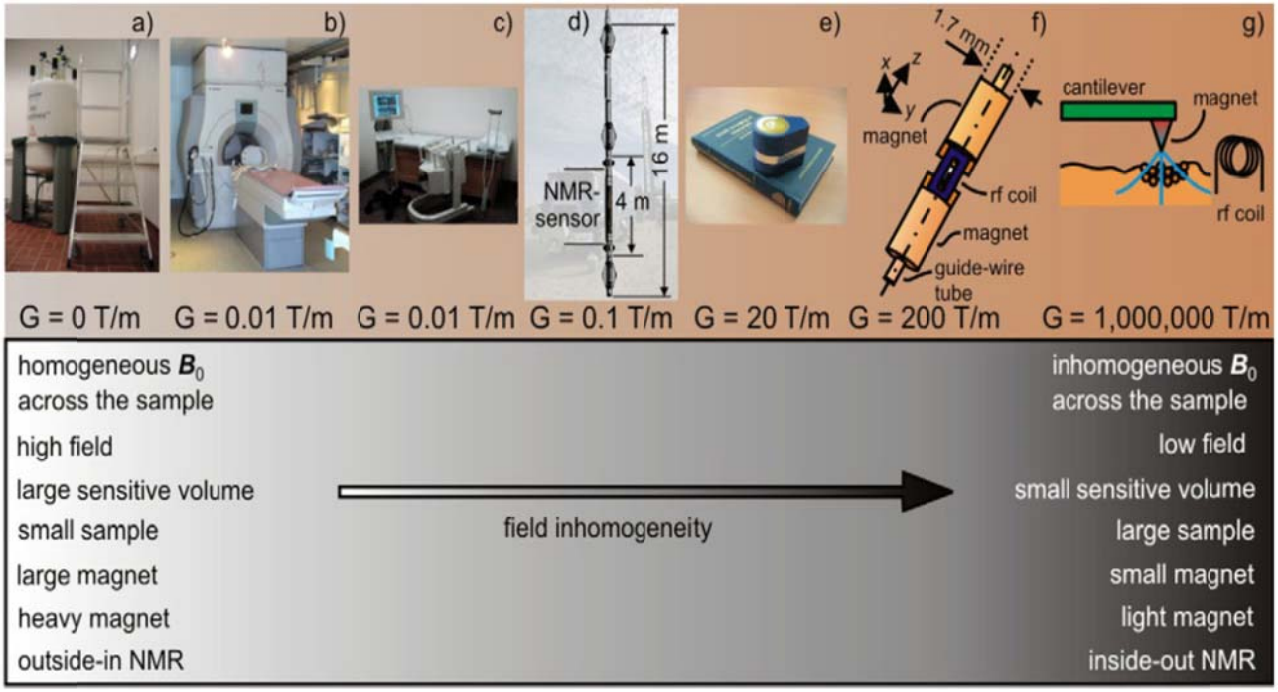

Figure 2-1: The field homogeneity relates to the field strength, weight and dimension of magnets [32].

2.3 Review of portable NMR devices

Normally, the portable NMR devices are divided into two groups due to the objectives of applications. The first group with the measured samples placed outside the magnet is called single-sided, unilateral or *ex-situ* NMR. The other group with the samples inside the magnet is called closed magnets or *in-situ* NMR. The existing ideas of two groups will be exposed briefly in order to show the progresses to be done.

2.3.1 *Ex-situ* portable NMR devices

The *ex-situ* portable NMR devices have the simple configuration with the sensitive volume (region of interest: ROI) near their surface and the samples are putted outside the magnets (Figure 2-2). Thus, they can use for the experimental object with unlimited dimensions. Such systems are suitable for surface investigation. Although the *ex-situ* magnets have the simple shape and light weight, they are difficult to achieve the homogeneity of magnetic field in the sensitive volume.

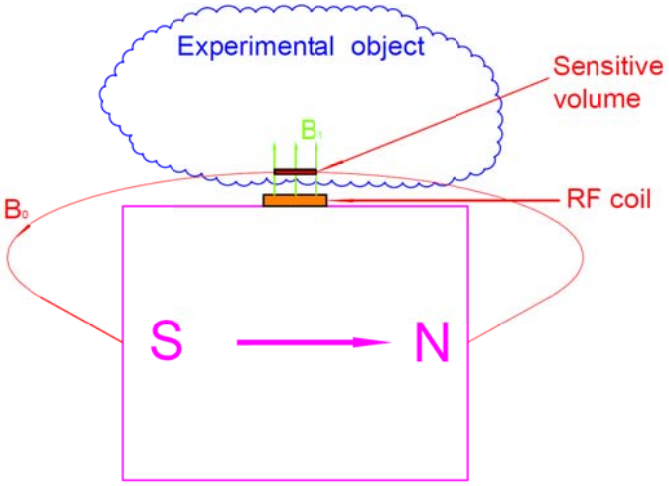

Figure 2-2: The schematic of single-sided or ex-situ magnets.

Ex-situ magnets derive from well-logging sensors. Apart from sensor geometries particularly suited to the cylindrical boreholes of oil wells, single-sided sensors suited for diverse other applications have been tested. The classical geometries of *ex-situ* magnets are usually C-shaped, U-shaped or a simple bar magnets as Figure 2-3.

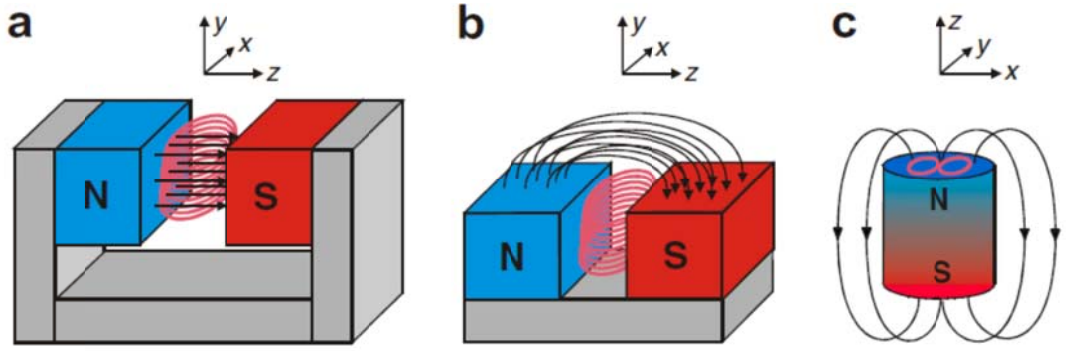

Figure 2-3: Conventional geometries of ex-situ magnets. (a) C-shaped. (b) U-shaped. (c) simple bar magnets [32].

2.3.1.1 Well-logging sensors

Well-logging sensors are examples of early outside-out NMR application. This concept has been first developed in the oil industry. The purposes of these sensors are to measure diffusion and relaxation time in rocks in order to determine the presence of water, oil and the rock's porosity. In 1952, in Varian's patent [33], he introduced an apparatus which can determine the presence of compounds or substances by virtue of their nuclear interactions with magnetic fields. This apparatus was applied to sound the presence of petroleum beneath the earth's surface. The successful of low field and low cost NMR in well-logging has motived the scientists expanding it. In 1980, Jackson *et al* [34] realize an ingenious well-logging sensor. This sensor consists of two axially aligned cylinder magnets facing each other with the same pole. These magnets produce the field B_0 in the transverse plane through the gap as in Figure 2-4-a. A simple solenoid coil placed coaxially with the magnets produces a field B_1 that is perpendicular to the field B_0. The field B_0 and B_1 create a toroidal region of homogeneous magnetic field as in Figure 2-4-b.

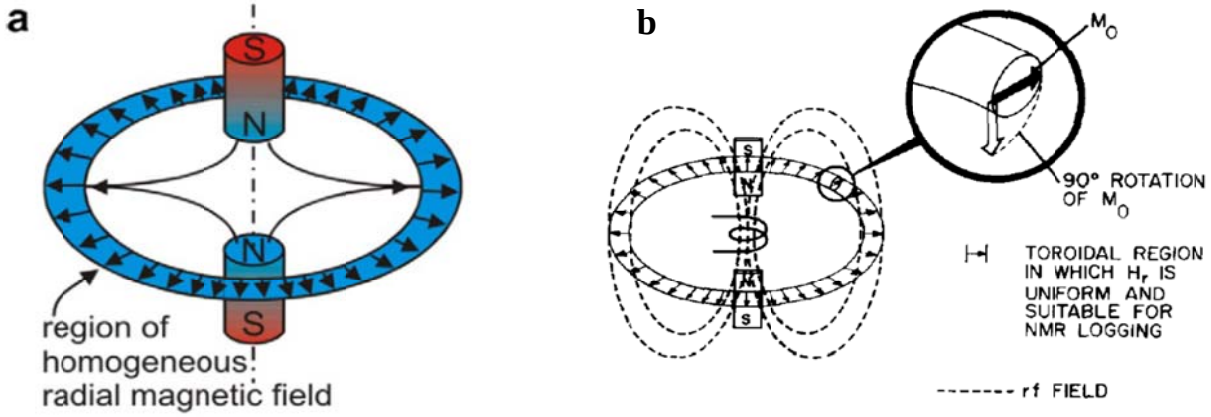

Figure 2-4: The Jackson's apparatus with the sensitive volume in the shape of an annulus [34].

In 1992, Kleinberg *et al* [35] designed a sensor with the sensitive volume localized at a given sector. This sensor contains three magnets magnetized in the same direction and a RF antenna sandwiched between these magnets in a tube as in Figure 2-5. "This sensor is far better suited for wire-line NMR as the residence time of the spins in the sensitive volume under axial motion of the sensor is far longer than with the Jackson sensor" [32].

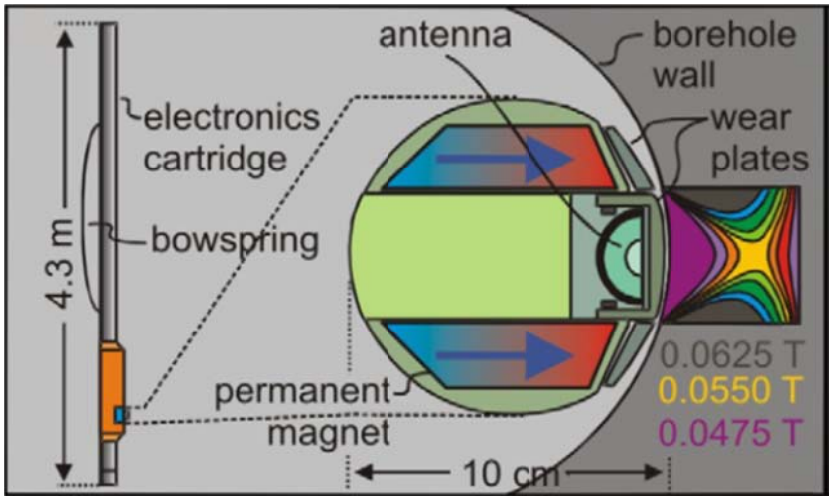

Figure 2-5: The sensor with the sensitive volume localized at the given sector but axially extended [35].

The NMR well-logging tools have been developing with the work of Goswami *et al* in 2000 [36] and the patent of Reiderman in 2007 [37].

2.3.1.2 TRAFI concept

Another kind of NMR "outside of the magnets" is the TRAFI (TRAy Field Imaging) technique. The concept of TRAFI is lately introduced in the late 1980_s and in the beginning of 1990_s. This technique uses the superconducting magnet offering a very large magnetic field gradient (from about 2 to 10T) [38] in order to obtain high resolution NMR imaging (down to the micrometer). "One of the main issues in such techniques is the SNR, which can be increased by using train of echoes such as solid echoes or spin echoes. The very stable gradient of superconducting magnets can also be used for diffusion measurements"[29]. However, the main drawback of this technique is that the TRAFI can be low acquisition method due to the time require for sample repositioning. In addition, for liquid state MRI, in which T_2 is long, STRAFI is not the method of choice because of the inflexibility of working in a fixed gradient [39]. The applications of TRAFI concept can be found in [40].

2.3.1.3 NMR- MOUSE

The NMR-MOUSE was introduced in the late 1980s and in the mid-1990s by the group of professor Blumich. The NMR-MOUSE is a system of a simple yorked magnet generating the magnetic field parallel to its surface very close to it with an integrated detection coil. The first NMR-MOUSE was developed in 1996 [41]. This sensor has the light weight of 1kg and the poor homogeneity with gradient field higher than 10 T/m at the field strength 0.5 T used for material testing as shown in Figure 2-6.

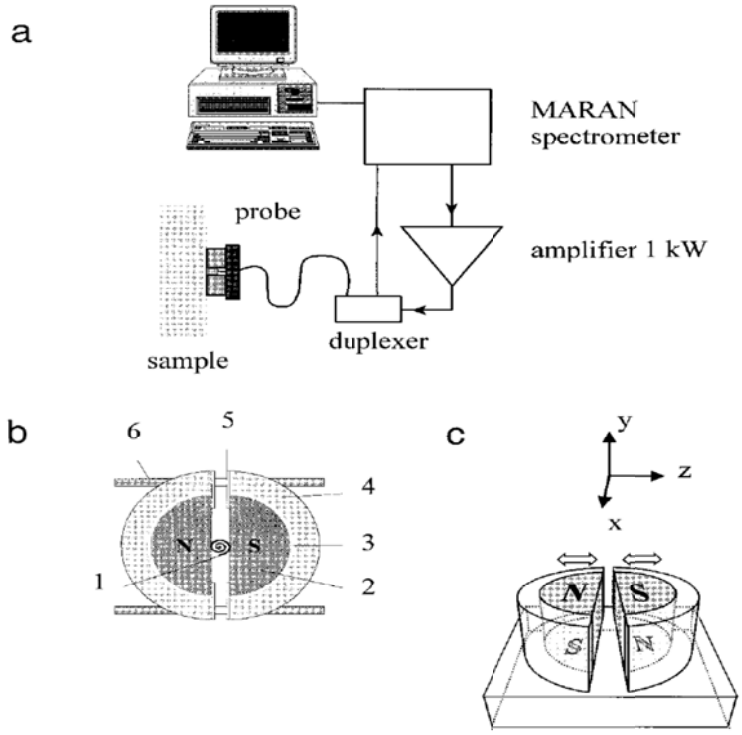

Figure 2-6: (a) The first NMR-MOUSE. (b) Spectrometer. and (c) probe design **[41]**.

The NMR-MOUSE configuration continues to develop with the U-shaped magnet. The static magnetic field is generated by two permanent magnets with opposite poles facing each other. A solenoidal radio-frequency (RF) coil is positioned in the gap between the two magnets. This coil generates a magnetic field B_1 approximately orthogonal to the field B_0 in order to create a sensitive volume above the surface of the sensor (Figure 2-7) [42].

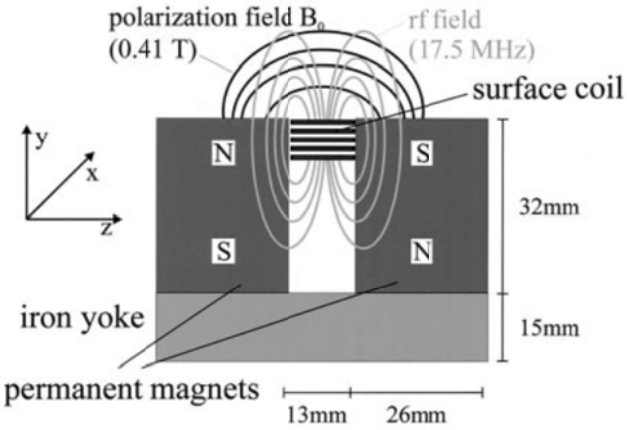

Figure 2-7: The NMR-MOUSE with the U-Shaped magnet with solenoidal RF coil[42].

Blumich *et al* [43][44] introduced a new concept of the NMR-MOUSE using a simple bar magnet instead of U-shaped magnet described above. In these sensors, the RF coils are integrated located on one of the pole faces (Figure 2-8). The new NMR-MOUSE with a bar-shaped magnet has a constant gradient of the static magnetic field $\boldsymbol{B}_0$ in the central part of the magnet. It is oriented in the *Z* direction from the pole facing the sample. The constant gradient of magnetic field of such devices is longer than that of u-shaped magnet design. Thus, it can deeply investigate inside the object better than U-shaped magnet.

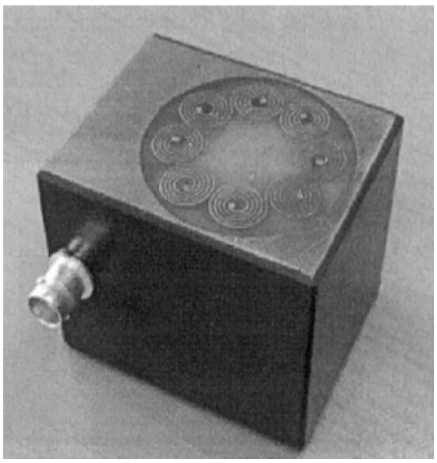

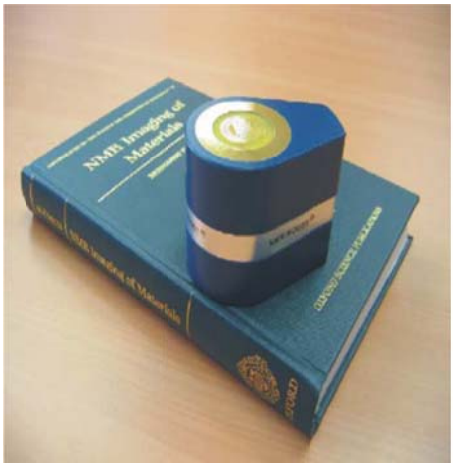

Figure 2-8: The NMR-MOUSE with the RF coil printed on the surface of the sensors [42][43].

Based on the idea of deep investigation inside the object, Anferova *et al* [45] constructed a prototype with the improvement of single-side detection (Figure 2-9). Modified versions with improved homogeneity of the NMR-MOUSE were reported and used in 2001 and 2003 [46][47].

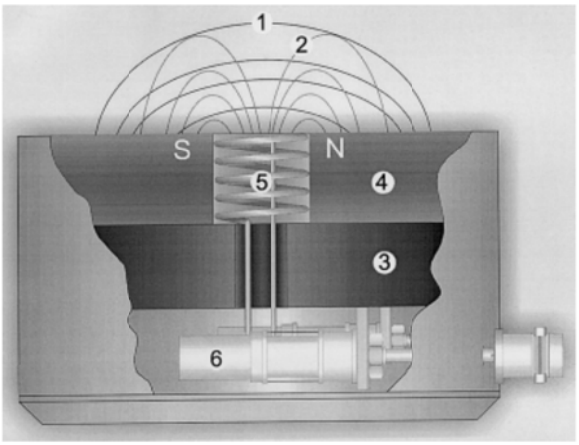

Figure 2-9: The NMR-MOUSE with the field profile of Z component of B_0 at a distance of 2.5mm above the surface of the coil **[45]**.

Other systems used for profiling outside a magnet has a single permanent magnet topped with a shaped iron pole cap [48][49]. These magnets provide higher magnetic field strength with 0.8T at the center of magnets and more homogeneity with the constant gradient of 31G/cm over an 8mm depth. However, the magnet weight is heavier about 5.7kg (Figure 2-10).

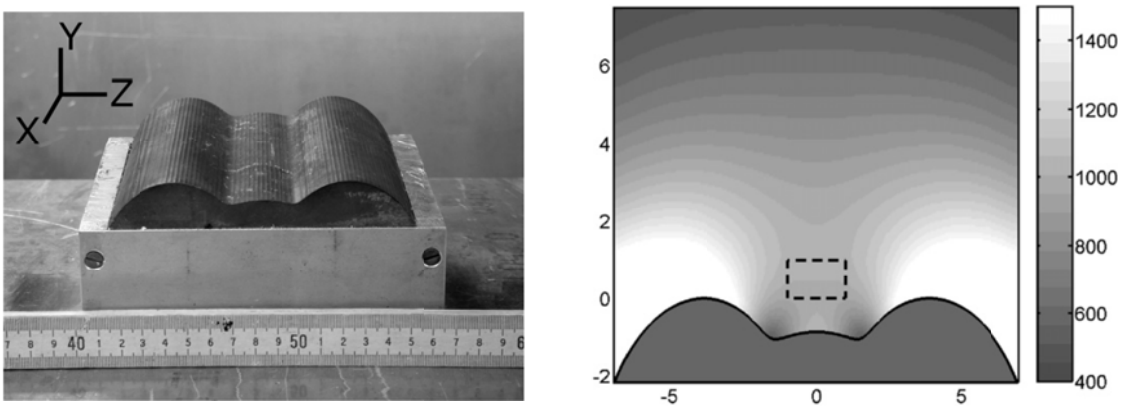

Figure 2-10: The prototype consists of a single permanent magnet topped with a shaped iron pole cap and its magnetic field distribution[48].

In 2006, Wei-Hao Chang *et al* [50] presented a lighter single-sided mobile NMR apparatus uses to detect the samples in one dimensional profiling with the weight of 2kg. This apparatus uses eight identical magnets and arranges them in Halbach type. These magnets generate the field strength 0.2T and the gradient field remains nearly constant for 2mm. The sweet spot (homogeneous region) 20x20mm was most homogeneous at about 0.5mm above the top of device (Figure 2-11).

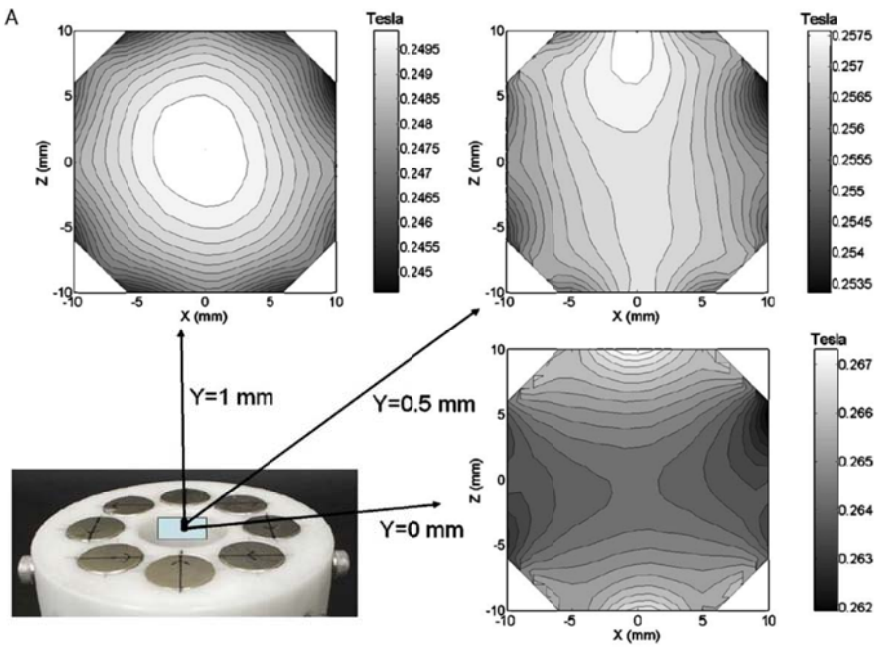

Figure 2-11: Wei- Hao Chang apparatus with the homogeneous sweet spot 20x20mm at 0.5mm above the surface of device **[50]**.

In 2010, Wei-Hao Chang group published another prototype which uses the magnetic flux parallel to the magnetization direction of a single, disc-shaped permanent magnet polarized in radial direction [51]. Such prototype weighs 1.8 kg and the magnetic field B_0 is 0.279 T. The strength of the static magnetic field gradient near the center of the apparatus surface is about 10.2 T/m. The field B_0 of this apparatus is parallel to its surface, allowing relatively flexible selection of the RF coil ~~for the apparatus~~ (Figure 2-12).

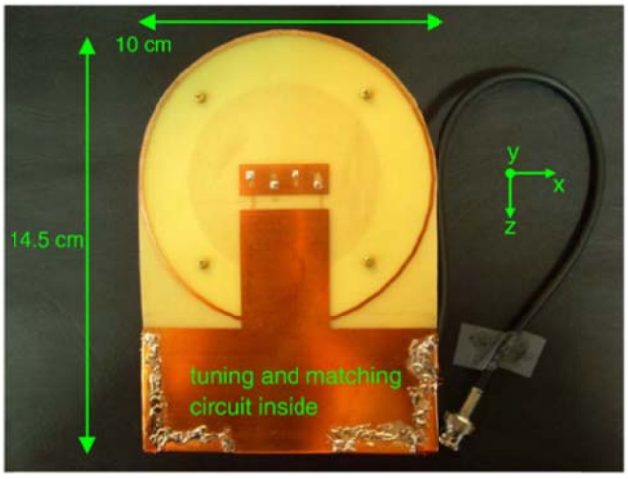

Figure 2-12: The rectangular RF coil was positioned to cover the horizontal area with relatively homogeneous B_0 field strength directly above the center of the magnet surface [51].

2.3.1.4 NMR-MOLE

NMR-MOLE (MObile Lateral Explorer) is one kind of *ex-situ* magnets and is based on barrel magnet concept. These magnets have a remote sweet spot, which can be located at different levels away from the magnet top. Fukushima *et al* in their patent [52] introduced a unilateral magnet apparatus having a remote uniform field region. In this apparatus, the magnets are arranged on the hollow cylinder. The sweet spot is created by rotating a pair of bar magnets and its position depends on the radius and the thickness of walls of the cylinder. In order to increase the sweet spot, a second magnet is placed with the same polarization of the barrel in the center of cylinder. Based on the concept of "barrel magnet", Manz *et al* [53] reported a portable NMR sensor called NMR-MOLE in 2006. This sensor created the movable sweet spot by adjusting the tilt of the magnets. The NMR-MOLE has the homogeneity of magnetic field 15,000 ppm over a region from 4 to 16mm away from the sensor with maximum sensitivity at a depth of 10 mm (Figure 2-13). Its proton NMR frequency is 3.3MHz.

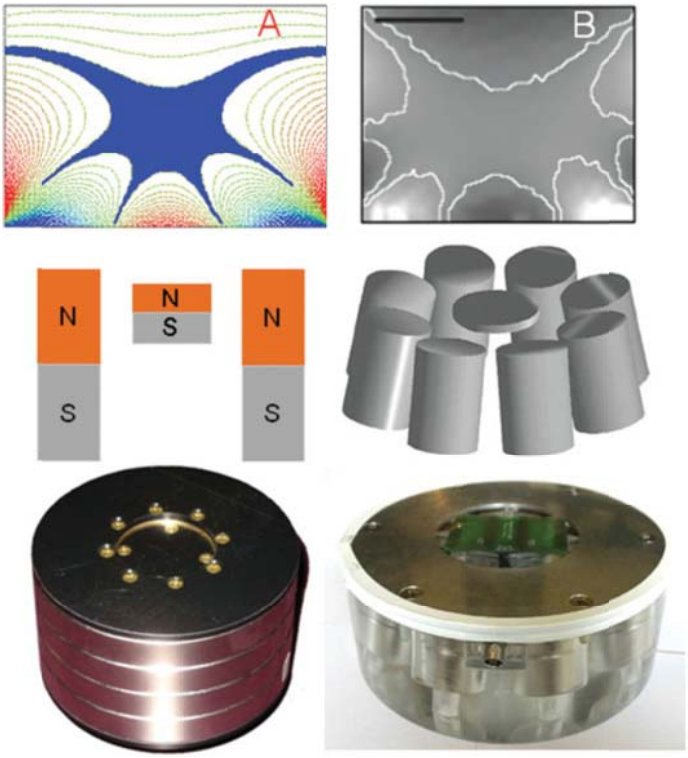

Figure 2-13: (a) the barrel magnet with remote sweet spot. (b) the sweet spot can be adjusted and increased by rotating the barrel bar magnets and placing the second magnet in the center of the cylinder **[52][53]**.

The movable sweet spot continued to develop with the proposition of Marble *et al* in 2007

[54]. The differences of Marble's apparatus in comparison to Manz's are the arrangement of magnets and the direction of the field B_0. While Manz's apparatus arranges magnets on the hollow cylinder, Marble's apparatus did that in an array with the field B_0 parallel to its surface (Figure 2-14). Such apparatus weighs approximately 5 kg and has B_0 field with a 'sweet spot" at a point 1 cm above its surface.

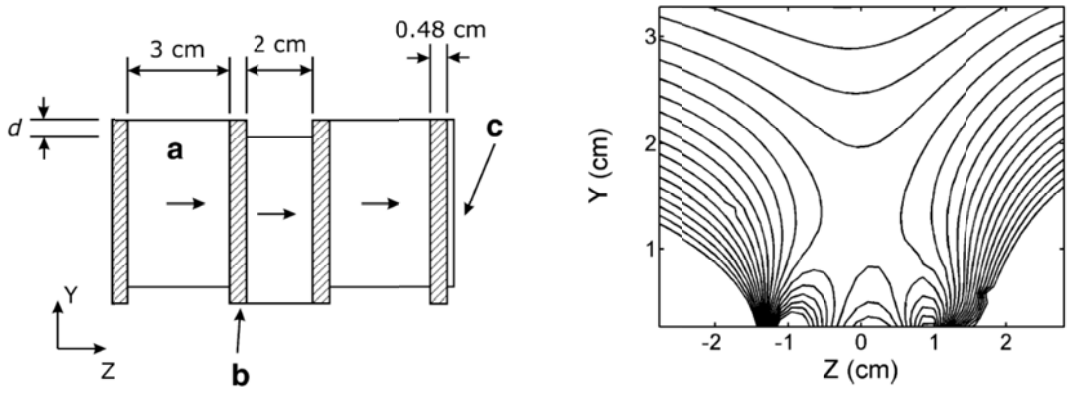

Figure 2-14: The magnet array with the movable sweet spot and its magnetic field field distribution on the surface [54].

Another array configuration which provides a movable sweet spot was presented by Paulsen *et al* [55] in 2008. The magnets consist of four cylinders with a dipole field across the cylinder (Figure 2-15). The optimum position and ratios of sizes of the different cylinders were optimized to achieve the desired goal. The sweet spot location can be changed by adjusting the direction of magnetization of these rod magnets; however, the shape of the sweet spot remains a constant.

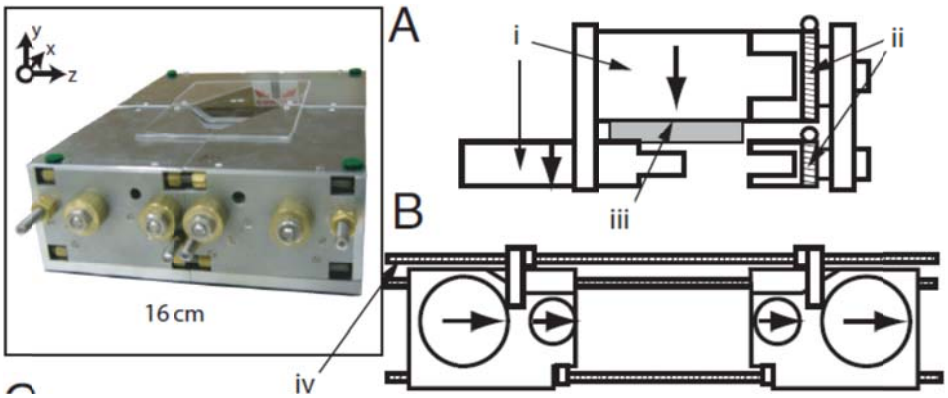

Figure 2-15: (a) the schematic of assembly of Paulsen apparatus. (b) To push the sensitive volume further out, the outer rods are turned 7.5° into the plane containing the rods[55].

2.3.1.5 *Ex-situ* portable NMR devices for high resolution experiments

The single-sided NMR community continues to improve their properties in order to adapt to the diversity of applications. The magnet derived from the U-shaped concept was broken down into several magnets in order to use for deep resolution [56][47]. In this method, the gaps between magnet segments can be adjusted to achieve the desired field profile. Spatial resolution is also attained by generating flat surfaces of constant field with a solid magnet [46]. These systems can perform 3D imaging with transverse gradient of static field [57]. These prototypes are displayed in (Figure 2-16).

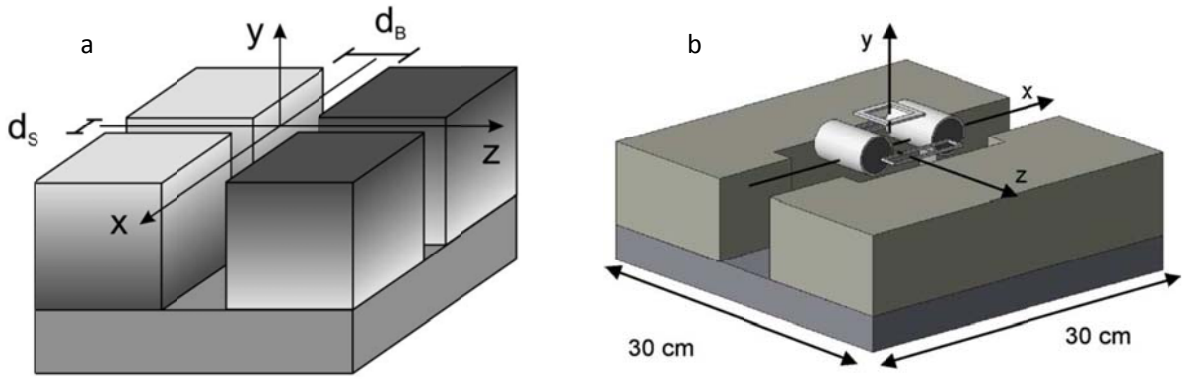

Figure 2-16: (a) U-shaped concept was broken down into several magnets in order to use for deep resolution [56]. (b) The open magnet with the two perpendicular pulsed gradient fields, 3D spatial resolution [57].

The limited spatial inhomogeneity of the static magnetic field generated by the single-sided magnets has precluded their use for high-resolution NMR spectroscopy. In order to overcome this difficulty, some techniques were introduced for high-resolution applications. To regain the resolution that is lost during a classical spin echo, the methodology of matching the inhomogeneity of static and radio frequency field was reported in [58].

Based on previous design and that concept, Perlo *et al* [59][60] presented a portable single-sided sensor with a resolution that is much higher than previous systems in 2006. These sensors achieve a spectral resolution of about 8 ppm and allow to measure wide range of chemical shift spectra (fluorinated liquids). The total magnet assembly generates a static field of about 0.2 T in the region of interest and weighs about 36 kg (Figure 2-17).

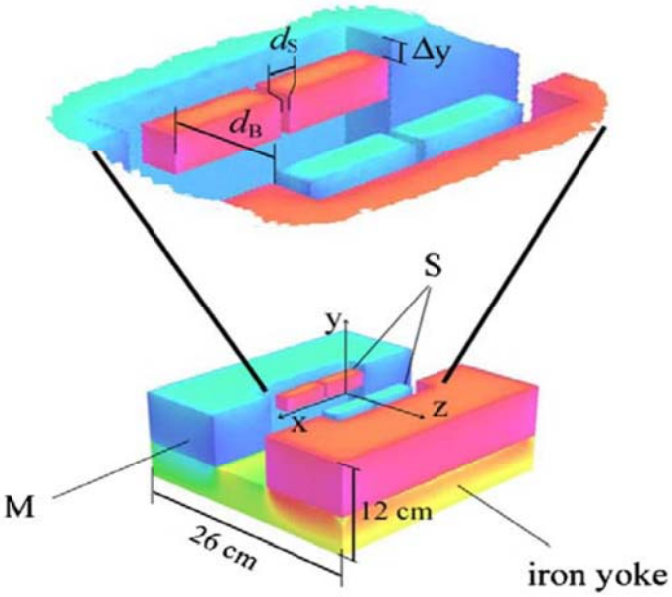

Figure 2-17: The single-side sensor using shim magnets so that increase the magnetic field homogeneity for high resolution spectroscopy **[60]**.

In 2007, Perlo *et al* [61] continued to develop this sensor with the sub-ppm resolution by using a passive shimming system (Figure 2-18). The sensor can achieve a resolution of 0.25 ppm on a volume of 5x5x0.5 mm with the magnet size 28x28x12 cm. The resolution of 0.25 ppm achieved by this prototype is the highest resolution for a single-sided configuration until now.

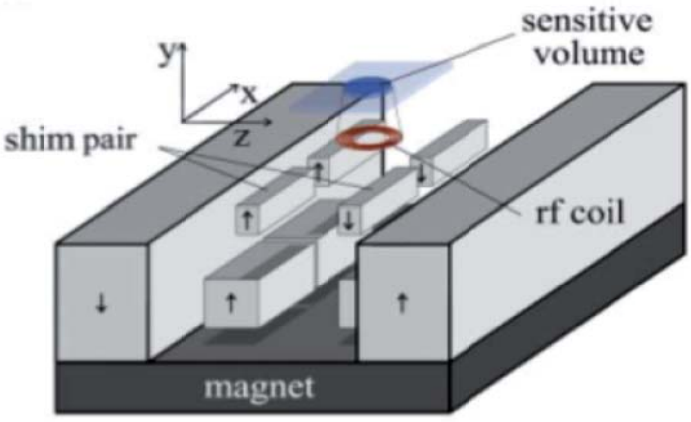

Figure 2-18: High resolution single-sided magnet with a passive shimming sysytem **[61]**.

2.3.2 *In-situ* portable NMR devices

While the *Ex-situ* magnets have to face the inhomogeneity of magnetic field, the *in-situ*

magnets reinforce the field in their center and cancel the field outside of the structure. Therefore, their magnetic field is homogeneous inside the structure in comparison to *Ex-situ* magnets. Another advantage of *In-situ* magnets is less sensitive to external environmental influences because such structures can confine the field. The schematic of such structure is shown on the Figure 2-19.

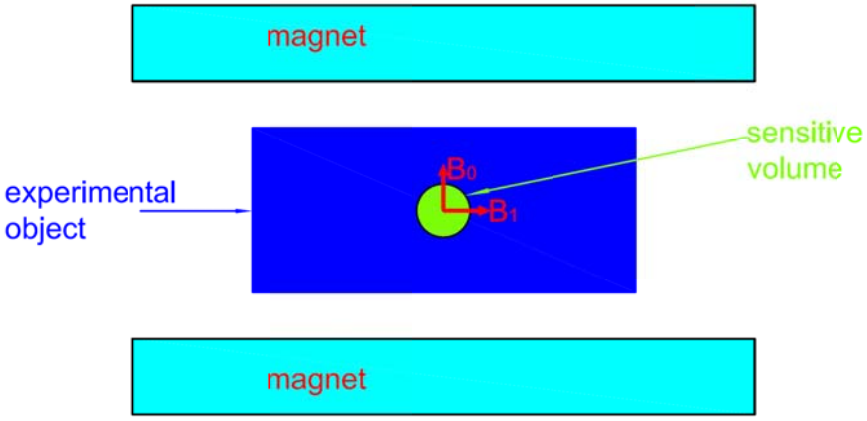

Figure 2-19: The schematic of ex-situ devices.

Basically, the *in-situ* systems have two kinds of structure. The first structure relies on the use of a ferromagnetic yoke (yoked magnets) [62]. The second one bases on the Halbach's structure [63].

2.3.2.1 Yoked magnets

The yoked magnets are not widely used in NMR applications in comparison to Halbach's structure and still use in accelerators. Such structures usually have the C-shaped and H-shaped.

An example of C-shaped has been done by Abele *et al* [64] in 2006. In this system, the magnetic field homogeneity can be controlled with pole pieces placed at the end of yoke and facing to the region of interest. The magnet of such structure can generate a field of 0.55T within its center gap as shown in the Figure 2-20.

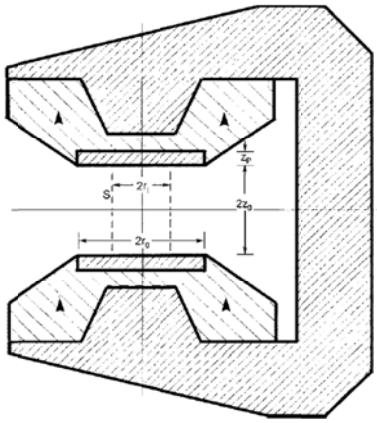

Figure 2-20: The C-shaped structure with two cylindrical disks is used to control the magnetic field homogeneity **[64]**.

In 2008, a H-shaped yoked magnet has been realized for portable NMR by McDowell and Fukushima [65]. McDowell's apparatus has the field B_0 of 1T in the region of interest and homogeneity of 0.24 ppm over very small volume 21 nanoliters (Figure 2-21).

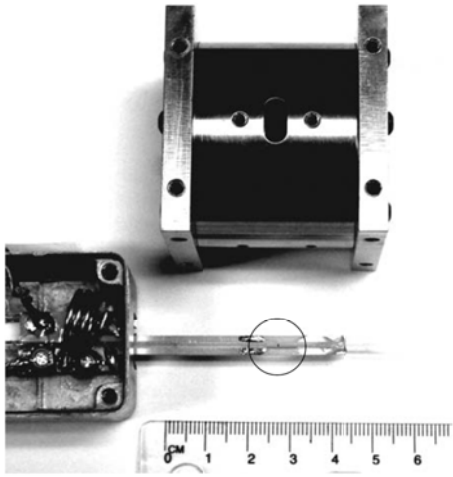

Figure 2-21: Yoked magnet achieving sub-ppm resolution on micrometric samples with a field of 1T [65]

2.3.2.2 Halbach structure

One of the most notable permanent magnet system is Halbach ring [63], although the primary purpose of such system is not used for NMR applications. However, this design has become increasingly popular in the community portable NMR device in recent years. This ring was proposed by Klaus Halbach in 1980. The Halbach ring consists of segments of permanent magnets joined together in an array to create the homogenous field in transverse plane as shown in Figure 2-22.

This advantage allows the use of a solenoid coil for NMR experiments. Other advantages of Halbach ring are low stray field, optimal field efficiency, high homogeneity associated with internal-flux. Several adaptations of the Halbach ring have been implemented using wedge elements, square block, cylinders and hexagons. The Halbach structures reinforce the field in their center and cancel the field outside of the structure [29].

The homogeneous field of the infinite long ring depends on the angular position Φ_1 of the ring and the angular orientation of magnetization Φ_2 as Figure 2-22-a. The relationship between them is described by equation 2-1:

$$\Phi_2 = k\Phi_1 \tag{2-1}$$

When k=2, the Halbach ring reinforces the field in its center and cancels the field outside the structure as shown in Figure 2-22-b. In this case, the magnetic field in the bore of the ring is completely homogeneous. In addition, the static field B_0 at the center of the ring is given by equation 2-2 [63]:

$$B_0 = B_r ln\left(\frac{r_2}{r_1}\right) \tag{2-2}$$

Where:

- B_0 is the static field at the center.
- B_r is remanence of material.
- r_1, r_2 are the inner and outer radius of the ring respectively.

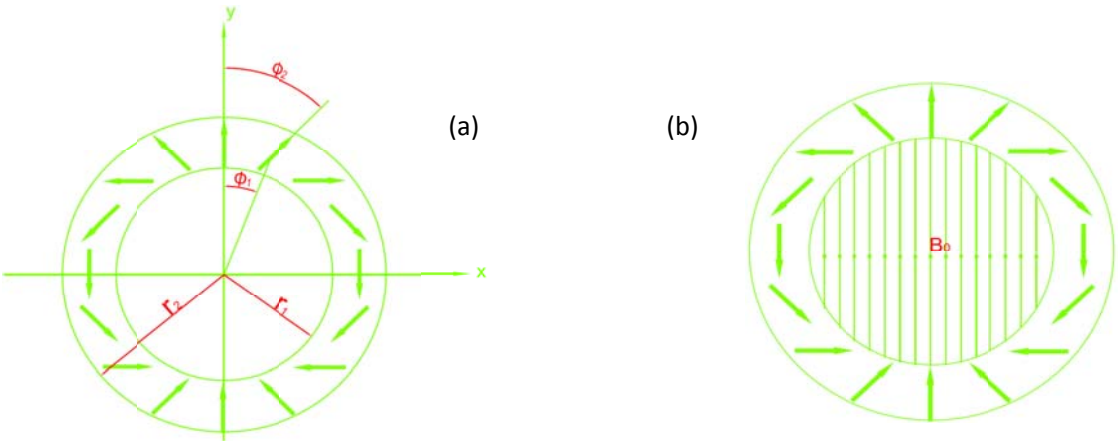

Figure 2-22: The original Halbach structure with 16 segments of permanent magnets. (a) The field strength at the center depends on the magnetization amplitude, the inner and outer radius of the ring while its homogeneity depends on the ratio of Φ_2 to Φ_1. (b) The Halbach ring reinforces the field in its center and cancels the field outside of the structure. The field at the center is completely homogeneous with k=2 [29].

One of the advantages of the Halbach structure in comparisons to yoked magnets is that such structure requires less material to generate the same field. This advantage allows one increase the field strength [66].

In 2003, Moresi *et al* [67] introduced a miniature Halbach system for high resolution. This compact system consists of 8 cylindrical permanent magnets that generated the static field 0.6T with the homogeneity of 20 ppm over an elliptical volume of 3x3x5 mm^3. The static field of the system could be increased to 3T by adding a second layer of magnetic material (Figure 2-23).

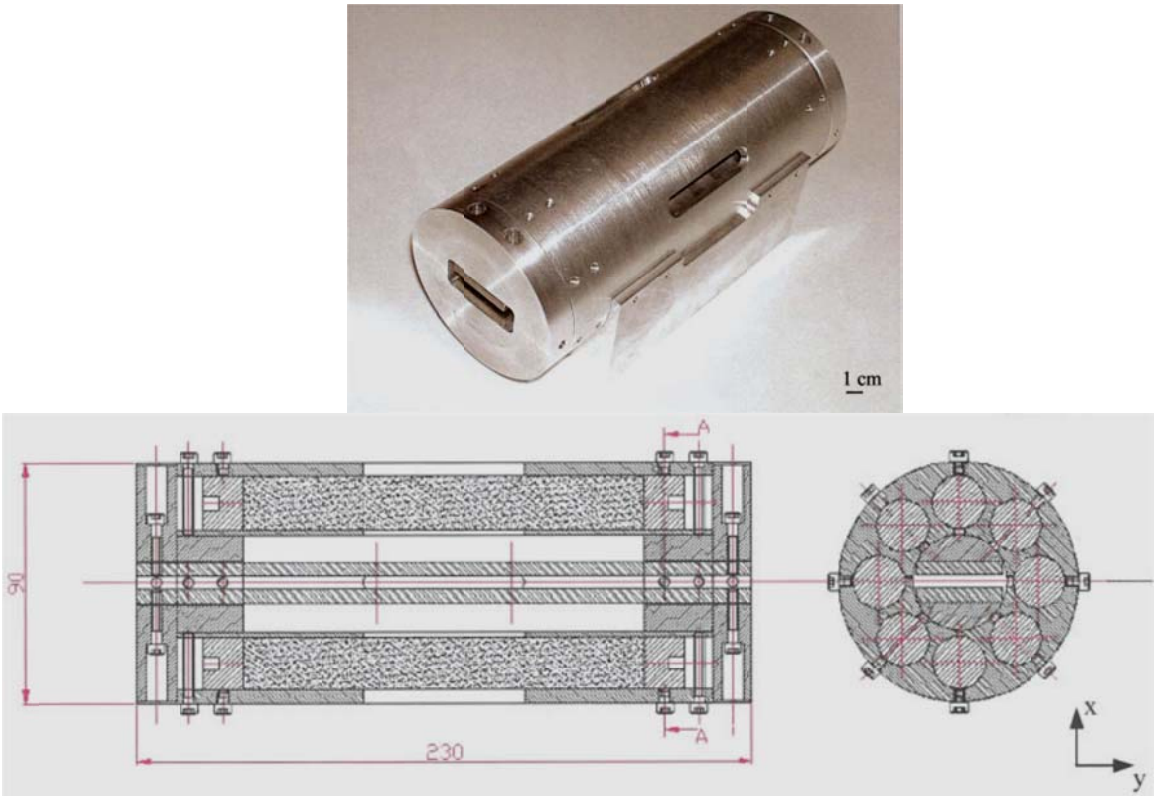

Figure 2-23: The prototype consists of 8 cylindrical magnets arranged in Halbach structure **[67]**.

Another prototype based on this concept was proposed by Hill *et al* [68] in 2005. Such prototype has a simple structure with poor homogeneity and low field (about 90 mT). It just consists of four rectangular magnets which provide a sensitive volume easy to access (Figure 2-24).

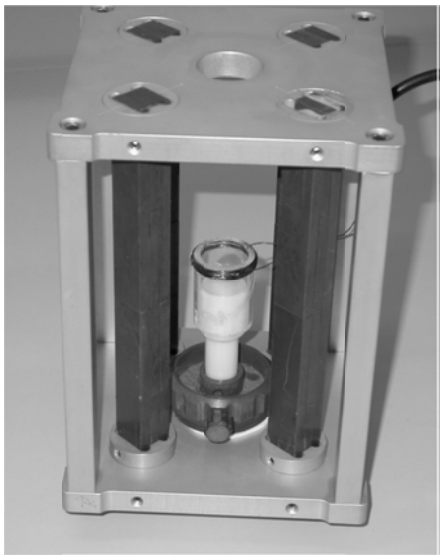

Figure 2-24: Simple Halbach structure with poor homogeneity and low field provides a sensitive volume easy to access **[68]**.

A Halbach structure with the high field strength was proposed by Xiaofeng Zhang et al [69] in the same year with Hill proposition. This configuration can generate high field up to 1T with a compact magnets. It consists of an array of 36 cylindrical magnets positioned hexagonally in two layers (Figure 2-25). Halbach magnet fabricated with stacked rings of magnet rods.

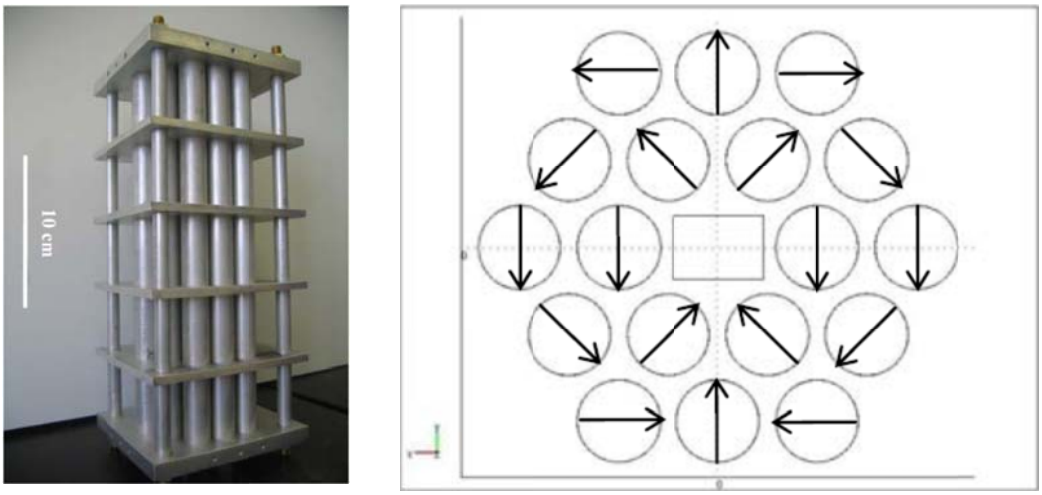

Figure 2-25: The photograph of Xiaofeng Zhang apparatus and the orientations of each magnet element [69].

Unlike most of the *in-situ* portable NMR devices produce the homogeneous field in the transverse plane, a prototype producing a homogeneous and strong magnetic field and having an

arbitrary inclination with respect to the axis of the cylinder has been published by the group of Sakellariou [70] in 2010. The structure has been constructed by using small cube magnets. Its magnetic field amplitude and homogeneity can be fully controlled by using the analytical theory of 3D magnetostatics [71][72] (Figure 2-26).

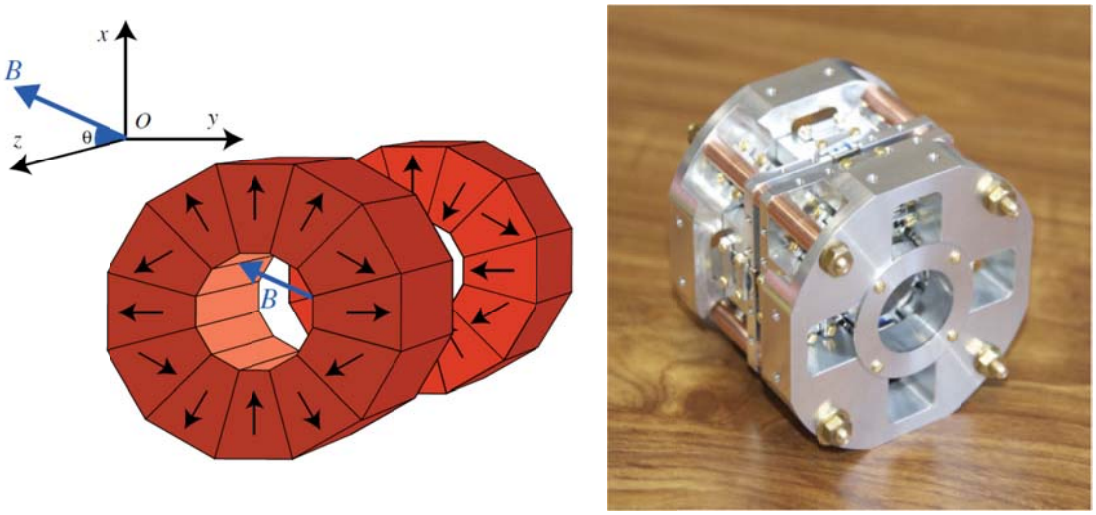

Figure 2-26: The prototype with the orientation of the field B_0 can be controlled and its assembly [70].

2.3.2.3 NMR MANDHALAS

However, one drawback of Halbach ring is the assembly of the magnets and their polarization which still complicated to realize. The inaccuracy of the magnets in the array and their directions of magnetization will affect on the field strength and the homogeneity of the ring. The influence of the tile permanent magnets on the field properties have been studied by Ravaud *et al* [73].

In order to overcome this problem, the Halbach structure with discrete magnets abbreviated Mandhalas (**Ma**gnet **A**rrangement for **N**ovel **D**iscrete **Ha**lbach **La**yout) was proposed. It is based on an arrangement of identical bar magnets, described by the analytical equations. These magnets arranged on a restricted space on a circle to obtain the strongest magnetic field and the highest homogeneity in the center. This type of configuration is not only inherits the advantages of Halbalch ring but are also easy to assembly, cheap to produce because it is constructed from identical bar magnets.

The concept of Mandhalas was first proposed by Raich and Blümler in 2004 [74]. Such system has reasonable field strength with 0.3T; however, its homogeneity is quite poor with

700ppm over a volume 18x18x30mm (Figure 2-27).

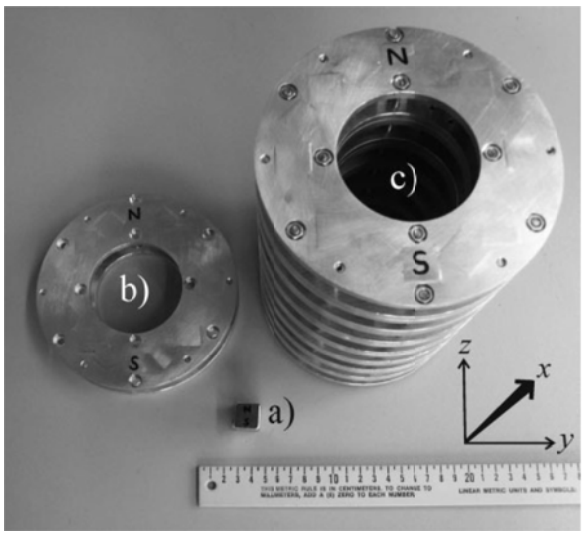

Figure 2-27: Photograph of (a) a single bar-magnet, (b) a finished "sandwich" subunit, and (c) the final magnet made from a stack of eight "sandwich" subunits [74].

This concept has been then extensively used to construct variations of the initial systems. Anferova *et al* has proposed a Mandhalas used to measure the moisture and porosity [75][76] in the same year with Raich and Blümler. Its homogeneity is poor with the gradient field 0.3T/m within the sensitive volume of 60mm diameter and 60mm length.

A recent work based on the Mandhalas concept has been published by Danieli *et al* [77] in 2009 with the better performance than previous versions. They proposed a larger magnet (33cm diameter, 27cm length, 20cm bore diameter) with a field of 0.22T and a homogeneity of 0.85ppm over $1cm^3$. However, while the performance is much better than previous Mandhalas systems, the sample is still very small compared to the magnet volume.

An extension of the Mandhalas system is the NMR-CUFF (cut open, uniform, force free) designed to open and close the ring around a test object [78] in 2010. The system uses only 4 magnets and generates the field of 0.57T and achieves homogeneity better than 200 ppm over a spherical volume of 5 mm in diameter without shimming.

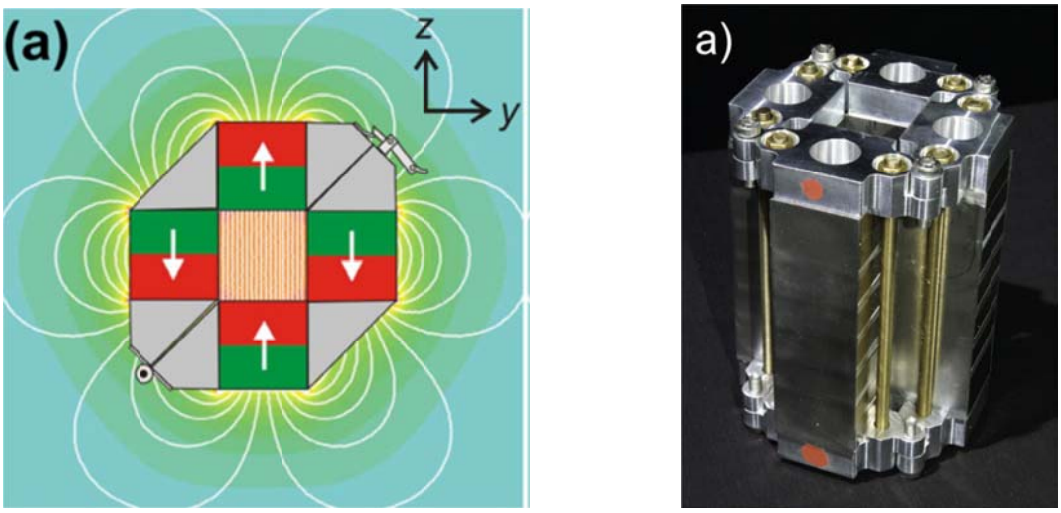

Figure 2-28: The NMR Mandhalas with four magnets is designed to open and close the ring around a test object [78].

In 2010, based on the publication of Raich and Blümler in 2004, Soltner and Blümler [79] extended the notion of Mandhalas from cube-shaped magnets to polygonal and cylindrical ones and present construction guidelines for the stacking of such rings to generate homogeneous magnetic fields over larger volumes. This publication uses the dipole approach to improve the design in three dimensions. Based on these results, they construct a prototype with polygon magnets. However, their prototype is too cumbersome with total mass of the system is about 300 kg (Figure 2-29).

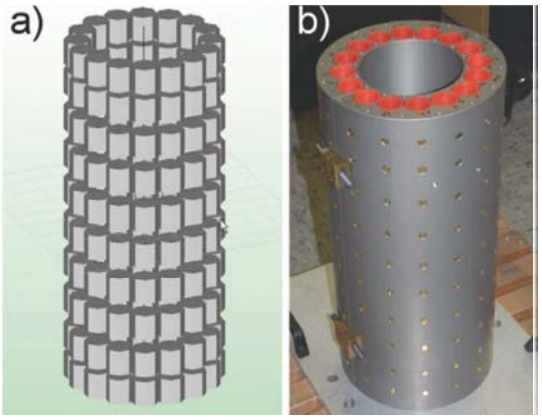

Figure 2-29: The large system consisting of a stack with m=10 Mandhalas. Each Mandhala is composed of n=16 octagon magnets, which had been characterized concerning their magnetic moments to identify their optimum positions in the Mandhalas [79].

In 2014, based on the works of [74][79], Qiaoyan Chen et al [80] compare a cube and an octagonal Halbach permanent magnet array in equal quantity of the material consumption with Maxwell software simulation. They found that the octagonal shape magnet has better performance than the cube one. By analysis of magnetic field strength, the best homogeneity in 5 mm DSV (Diameter of Spherical Volume) with 133.4 ppm was achieved when the height of magnetic blocks is 16.25 mm. However, the prototype has not been constructed yet.

To conclude, although the Halbach structure is less homogeneity, they indicate that they are tremendous cheaper than homogeneous standard NMR spectrometers.

2.3.3 Techniques are used to improve the magnetic field homogeneity

One of the drawbacks of portable NMR devices is their inhomogeneity for high resolution spectroscopy. In order to overcome this difficulty, there are some techniques have been used to increase the homogeneity. Basically, two popular methods have been used.

2.3.3.1 Optimize the gap between two rings

In the Halbach structure, the homogeneity is homogeneous with the infinite magnets (2D). However, with the finite height magnets 3D), the magnetic field homogeneity is much smaller than the 2D case. In the 3D case, the homogeneity is homogeneous at the center of configuration and becomes worse towards at the end. Thus, in order to compensate this distortion, the Halbach structure is divided into many rings. By optimizing the gaps between these rings, the homogeneity of the magnet along the cylinder axis is improved. Based on this concept, Anferova et al [75] splits the sensor made by [76] into the stack of six magic rings. These six magic rings are combined into two identical arrays, each of them consisting of three magic rings. The magnetic field profile along the cylinder axis becomes more homogeneous as the distance between the two arrays increases from zero as shown in the Figure 2-30. Although this method is easy to perform, it does not improve too much the homogeneity for high resolution spectroscopy.

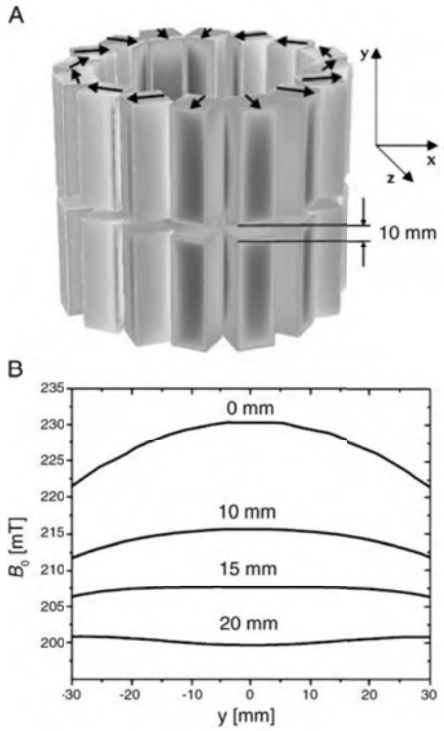

Figure 2-30: (a) the structure consists of two identical arrays with three magic rings. (b)the homogeneity is achieved with the certain gaps between the arrays [75].

2.3.3.2 Shimming

Shimming is the most popular method used to increase the magnetic field homogeneity of portable NMR devices both *ex-situ* and *in-situ* magnets. Shimming is not only used to increase the magnetic field homogeneity but also used to compensate the inhomogeneity caused by the imperfection of material, inaccuracy of assembly and the tolerance of fabrication.

The concept of shim units built from movable permanent magnet blocks which can be implemented to control the homogeneity of stray magnetic field in single-sided NMR was presented by Perlo *et al* [59][61]. In 2005, Jachmann *et al* [81] introduced the two dimensional shimming method based on harmonic corrector rings which can provide arbitrary multipole order shimming corrections. In this method, they used two pairs of corrector rings to compensate the inhomogeneity of magnetic field in transverse plane of the configuration.

In 2009, Danieli *et al* [77] proposed a shim strategy for a Mandhalas configuration based on the concept of movable magnet blocks. This strategy uses eight small magnets placed in the bore of configuration. The homogeneity increases due to the match of the magnetic field of shim magnets and the magnetic field of the main magnets. By optimizing of the position of these shim

magnets, the homogeneity significantly increases. The results shows that the homogeneity is achieved 0.85 ppm over a cylindrical volume 10 mm in diameter and 10 mm long after shimming (Figure 2-31).

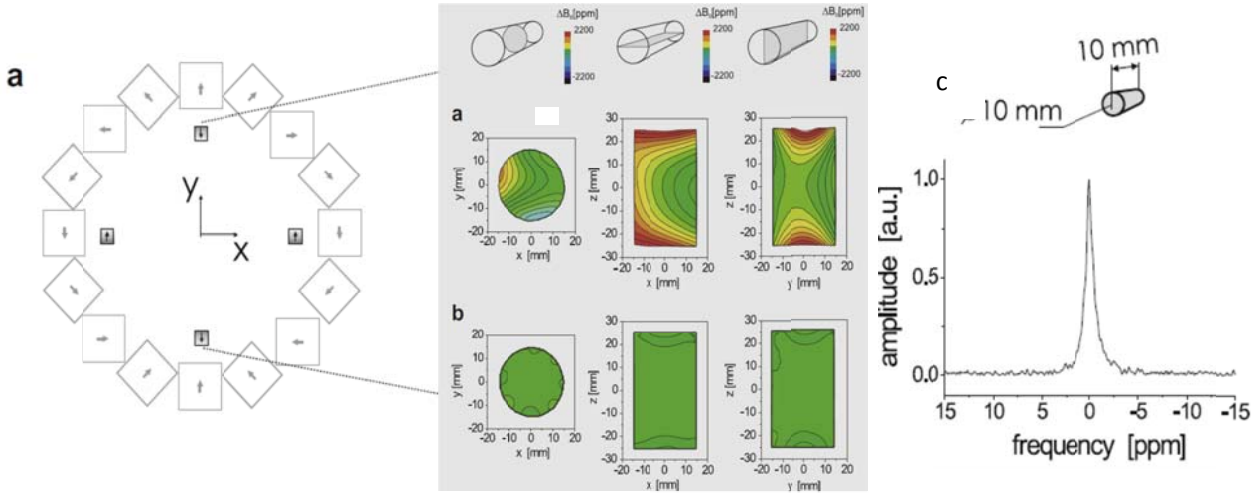

Figure 2-31: (a) The Mandhalas with shim magnets. (b) The field distribution in region of interest before shim and after shim. (c) The homogeneity is achieved 0.85 ppm in the volume of 10 mm in diameter and 10mm long [77].

2.4 NMR systems and applications

The NMR spectroscopy can analyze the chemical solutions and determine the structure, environments of various molecules; thus becomes the power tool for chemists, biologists and physicists. This technique is nowadays used for variety of applications.

2.4.1 Biomedicine

One area of applications for portable NMR devices which comes to mind first is biomedicine. The NMR-MOUSE employed to investigate the anisotropy of T_2 in Achilles tendon in vivo is reported by [82][83]. "In the case of the Achilles tendon, the anisotropic behavior of T_2 and the magic-angle value can be a measure to assess the condition of tendon and to detect degenerative changes. The NMR-MOUSE provides a convenient tool for analyzing the correlation of T_2 and the physical condition of tendon"[82].

Another biomedical application is human skin. GARField magnets are used to explore skin hydration [84][85]. These methods provide a map of hydrogen density in the sample with an intensity weighted by molecular motion.

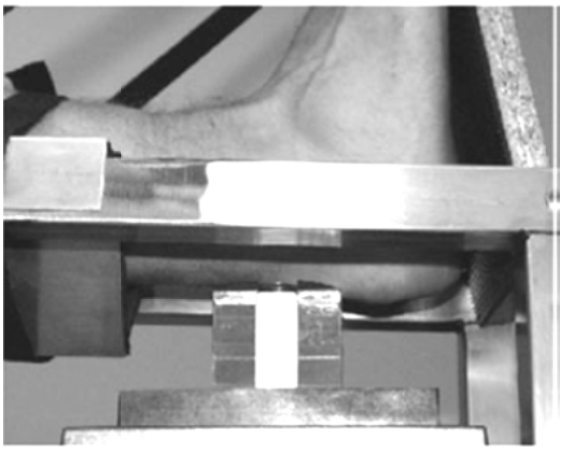

Figure 2-32: The NMR-MOUSE measures T_2 in human Achilles tendon in vivo **[82]**.

2.4.2 Cultural heritage

Old paper and wood contain bound and free water. Thus, these materials can be measured by ^{1}H NMR. The *ex-situ* NMR devices can be used to investigate the state of conservation of wood and paper. An example of this is NMR-MOUSE with a short dead time employed to observe the solid cellulose signal in historical books [45]. Other successful applications of NMR-MOUSE in wood and paper have been published in [86][87][88].

Mummies are another subject of interest for non-destructive analysis by NMR-MOUSE. Computer tomography (CT) is the popular method to study the ancient mummies. However, CT scanners cannot easily be moved to the object, and the ability of CT to discriminate dry soft-tissue is limited. The mobile NMR sensors provide an excellent solution for this. NMR-MOUSE used to visualize historic human tissues have been reported in [89][90].

Figure 2-33: The NMR-MOUSE analyzes the Iceman (3300 BC) in situ in the cold storage room of the South Tyrol Museum of Archaeology, Bozen [89].

2.4.3 Material testing

The early NMR device was employed to study the moisture in bridge decks [91] used an electro-magnet and weighted about 300 kg. Later on, a barrel-type portable NMR sensor called NMR-MOLE has been designed with a sweet spot for moisture measurement [53]. The portable NMR devices used to scan moving sample was built. Such devices were employed to analyze moisture transport in building materials with paramagnetic impurities at spatial resolution of better than 1 mm in a gradient of 0.4 T/m, the water absorption and drying of bricks [92][93][94].

Another mobile NMR scanner has been designed with a Halbach magnet for measurements of porosity and pore-size distributions of water-saturated cylindrical geological cores with diameters up to 60 mm [76][75]. This sensor provides the homogeneous magnetic field in a large and accessible cylindrical volume. It slides on a table and automatically scans the cylindrical samples. The Halbach tool is more sensitive, and porosities can be determined down to 3%. Thus, the measurements with the Halbach system yield higher accuracy for porosity values than those of the NMR-MOUSE.

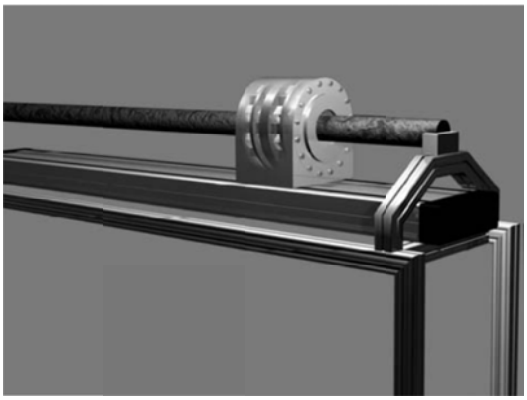

Figure 2-34: The sliding sensor automatically scans the sample **[75]**.

Portable NMR devices still have other applications such as plant [95], food [96] and measurement of the oil/water ratio in fruit [97]. Because it is not interest of this works, we only briefly examine the popular application fields of portable NMR devices. The curious readers can be found the detail applications of them in [32].

2.5 The components of portable NMR devices

Basically, Portable NMR devices consist of three main components that are magnet system, RF coil and spectrometer as Figure 2-35 [98].

(a)

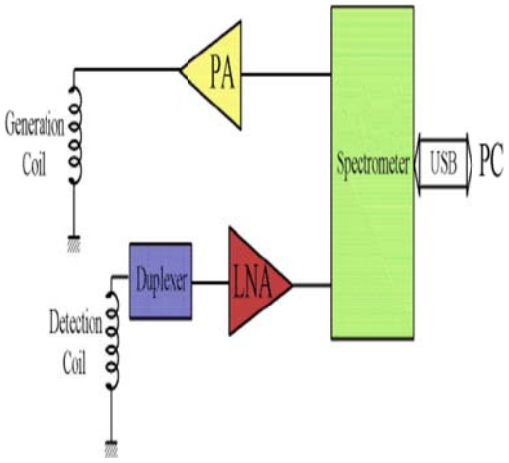

(b)

(c)

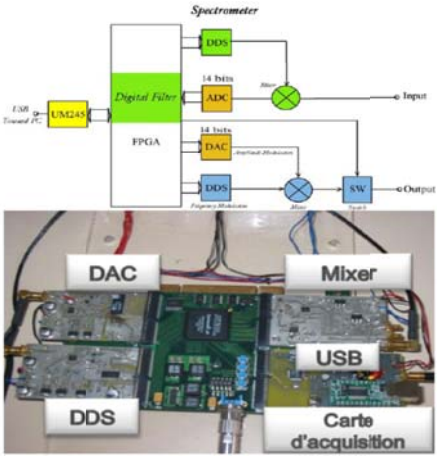

Figure 2-35: Three main components of a portable NMR device. (a) Magnets and the coils connect to the duplexer. (b) Functional schematic of the connection between the coils and spectrometer. (c) Functional schematic of spectrometer.

The function of magnet system (Figure 2-35-a) is to generate the static field B_0 which polarizes the nuclear magnetic moments. Its strength determines the degree of polarization and thus defines the sensitivity of measurement. Furthermore, it determines the measurement frequency as well as the spread in resonance frequencies.

The coils (Figure 2-35-b) are employed to emit and receive the RF radiation to and from the sample. The generation coil generates the field B_1 which is perpendicular to the static field B_0 of the magnets, while the detection coil detects the FID. These coils are connected to the spectrometer.

The spectrometer (Figure 2-35-c) is used to control the FID generation, acquisition and processing. It is connected to the PA (power amplifier), the LNA (low noise amplifier) and the

duplexer. The duplexer is a circuit which consists of two diodes to ensure a good isolation when a signal is applied to the generation coil. The information of FID, acquisition time, sequence repetition time are transferred to PC via USB port.

2.6 Motivation for this work

The homogeneity of magnetic field is an important criterion in NMR experiments. Thus, the increase of homogeneity is necessary in the design of portable NMR devices. Most of the portable NMR devices do not provide the sufficient homogeneity for NMR spectroscopy and high-resolution MRI over a macroscopic volume. Some previous design achieved such homogeneity on a very small sample size (5x5x0.5mm [61] or 21 nanoliter [65]). This is difficult to precisely position the sample and limit the signal to noise ratio. Moreover, the magnetic field is perfectly homogeneous for a perfect Halbach geometry and infinite long magnets. However, the magnets must have a finite length in reality, thus, the strength and homogeneity of magnetic field gradually decreases from the center to the edge of the cylinder. In order to get an enough homogeneous magnetic field region for NMR experiments, the magnet length must be extended. This results in the increase of magnetic materials, the weight of device and the cost of production. This work is devoted to maximize the region of interest (ROI) as large as possible with the given magnet dimensions (due to the objective of applications) while maintaining the high magnetic field. Based on the need of applications, the *in-situ* configuration has been chosen for design the prototypes. The calculations and simulation are performed with the help of two different software packages for the magnetic field modeling brought similar results, then; these results are verified by measurement with gaussmeter. The results shows that the prototypes generate the sufficient homogeneity and field strength for biomedical and agroalimentary applications.

Chapter 3

Magnetic materials and simulation methods

Summary:

- **Introduction**
- **Magnetic materials**
- **Numerical and simulation methods**
- **ANSYS software**
- **Conclusions**

Chapter 3: Magnetic materials and numerical methods

3.1 Introduction

In magnetic resonance, there are two sources of magnetic field required for. The first source can be produced by a current through a superconducting or resistive wire, typically in a solenoid shape. The benefits of using a superconductor are easy to achieve the homogeneity of magnetic field and the high field strength. Its field strength is not influenced by external environment. The superconductors is not compact, thus limit the widely applications. In addition, they need too much energy to operate and high cost for maintenance. Unlike the first source, the second source is produced by permanent magnets. They are the most suitable material for compact MR instruments. The drawbacks of permanent magnets are low field, inhomogeneity and their field is instable with external environment such as temperature. However, they are compact, low cost and no maintenance. Their field strength and homogeneity depend on the quality and kind of magnetic materials. Therefore, in order to proceed with magnet design, it is necessary to bear in mind some elementary aspects of the materials used.

In order to achieve the optimum configuration, numerical methods and simulation play an important role to magnet design and optimization process. The geometry of instrument needs to be defined by the users and specific parameters can be then optimized. Analytical strategies provide accurate solutions for the magnetic field distribution in the region of interest (ROI) and magnetic field profile. There are various numerical methods have been published. The dipole approach was proposed by Soltner *et al* [79]. This method is used to optimize the gap between two rings of magnet stack in order to increase the homogeneity in longitudinal axis of instrument. Hugon *et al* [71][72] bases on the spherical harmonics expansion of the field to design homogeneous magnets systems for NMR and MRI. This approach for magnet design gives a method to control magnetic field of arbitrarily magnet systems. A method of designing 2D magnets based on scalar potential proposed by Marble *et al* in 2005 [49]. Based on this method, they built a prototype with a constant gradient field near its surface [48]. They also developed a method of designing 3D magnets with the scalar potential approach [99]. However, no prototype has been built with this method. Sometime, some designs and optimization are based on software packages such as COMSOL [69], RADIA [71].

This chapter gives a short description of magnetic materials, their properties. We also describe the numerical method based on the finite element method (FEM) which is the underlying

procedure of ANSYS (the software we used for simulation in this project). Finally, we give an overview and the procedures of magnetic field simulations of ANSYS software [100].

3.2 Units

There are three systems of units that are commonly used in the magnetism. These are the CGS or Gaussian system, and two MKS or SI systems that are referred to as the Kennelly and Sommerfeld conventions, respectively. The CGS system is based on the fundamental units of Centimeter, Gram and Second, and the SI systems are based on the MKSA units of Meter, Kilogram, Second, and Ampere. The units for the SI (Sommerfeld) and CGS systems are as follows the Table 3-1:

Symbols	Description	SI	CGS
H	Magnetic field strength	A/m	Oe
B	Flux density	Tesla	Gauss
M	Magnetization	A/m	emu/cm^3
$\boldsymbol{\Phi}$	Flux	Weber	Maxwell

Table 3-1: Fields and units in the SI and CGS systems

To convert between the SI and CGS systems, we use the Table 3-2

SI	To	CGS
H in A/m	* $4\pi/10^3$ =	**H** in Oe
B in Tesla	* 10^4 =	**B** in Gauss
M in A/m	* 10^{-3} =	**M** in emu/cm^3
$\boldsymbol{\Phi}$ in Webers	* 10^8 =	$\boldsymbol{\Phi}$ in Maxwells
$(BH)_{max}$ in J/m^3	* 40π =	$(BH)_{max}$ in GOe
$(BH)_{max}$ in kJ/m^3	* $4\pi/10^2$ =	$(BH)_{max}$ in MGOe

Table 3-2: Conversation from SI to CGS units

3.3 Magnetic materials

The fundamental element in magnetism is the magnetic dipole. A magnetic dipole has a magnetic dipole moment $\boldsymbol{m}$ measured in $A.m^2$. The magnetization M measured in $A.m^{-1}$ is a measure of the net magnetic dipole moment per unit volume. It is given by equation 3-1 [101][102].

$$\boldsymbol{M} = \lim_{\Delta V \to 0} \frac{\sum_i \boldsymbol{m_i}}{\Delta V} \tag{3-1}$$

Where the $\sum_i m_i$ is a vector sum of the dipole moments contained in the elemental volume ΔV.

From the relationship between magnetic moment and flux, the relationship between B and M can be found. A bar magnet with flux density Φ at the center, the dipole *length l* and with the cross sectional area *A* has a magnetic moment *m* given by $m = \frac{\Phi.l}{\mu_0}$ [103]. The magnetization can be written as equation 3-2:

$$\boldsymbol{M} = \frac{\boldsymbol{m}}{\boldsymbol{A.l}} = \frac{\boldsymbol{\Phi}}{\boldsymbol{\mu_0.A}} = \frac{\boldsymbol{B}}{\boldsymbol{\mu_0}} \tag{3-2}$$

The equation 3-2 hence:

$$\boldsymbol{B} = \boldsymbol{\mu_0 M} \tag{3-3}$$

Where $\mu_0 = 4\pi \,.\, 10^{-7} \frac{T.m}{A}$ is the permeability of free space.

Another indispensable auxiliary field when dealing with magnetism is H field known as the magnetic field strength. The distinction between B and H is trivial in free space. Their relationship is described by equation 3-4:

$$\boldsymbol{B} = \boldsymbol{\mu_0 H} \tag{3-4}$$

The magnetic induction consists of two contributions: one from the magnetic field as equation 3-4, the other from the magnetization as equation 3-3. The magnetic induction is then simply the vector sum of these.

$$\boldsymbol{B} = \boldsymbol{\mu_0}(\boldsymbol{H} + \boldsymbol{M}) \tag{3-5}$$

B is the magnetic induction, expressed in Tesla (T). H is the magnetic field, expressed in Amperes per meter (A/m).

The magnetic polarization or intensity (in Tesla) might also be used. In the Kennelly [101] convention, the constitutive relation is:

$$\boldsymbol{B} = \boldsymbol{\mu_0 H} + \boldsymbol{J} \tag{3-6}$$

Where $J = \mu_0 M$ is called the magnetic polarization.

The magnetization is defined by a constitutive equation of material. This constitutive equation simplifies for linear, homogeneous and isotropic media. For such materials, both *B* and *M* are proportional to *H*. The permeability and susceptibility of the material μ and $\boldsymbol{\chi}$ respectively can

be defined as:

$$\boldsymbol{B} = \boldsymbol{\mu}\mathbf{H} \tag{3-7}$$

$$\boldsymbol{M} = \boldsymbol{\chi}\mathbf{H} \tag{3-8}$$

These coefficients are related to one another. From the equations 3-5, 3-7 and 3-8, the permeability of material is:

$$\boldsymbol{\mu} = \boldsymbol{\mu_0}(\boldsymbol{\chi} + \mathbf{1}) \tag{3-9}$$

The relative permeability μ_r is a dimensionless quantity defined as:

$$\boldsymbol{\mu_r} = \frac{\boldsymbol{\mu}}{\boldsymbol{\mu_0}} = (\boldsymbol{\chi} + \mathbf{1}) \tag{3-10}$$

In inhomogeneous materials, the permeability and susceptibility are function of coordinate variables, $\mu = \mu(x, y, z)$, $\chi = \chi(x, y, z)$. A material is said to be isotropic if μ depends on direction. In this case, the equation 2-7 can be written:

$$\boldsymbol{B_x} = \boldsymbol{\mu_{11}H_x} + \boldsymbol{\mu_{12}H_y} + \boldsymbol{\mu_{13}H_z} \tag{3-11}$$

$$\boldsymbol{B_y} = \boldsymbol{\mu_{21}H_x} + \boldsymbol{\mu_{22}H_y} + \boldsymbol{\mu_{23}H_z} \tag{3-12}$$

$$\boldsymbol{B_x} = \boldsymbol{\mu_{31}H_x} + \boldsymbol{\mu_{32}H_y} + \boldsymbol{\mu_{33}H_z} \tag{3-13}$$

The expansion for equation 2-8 is similar. Permeability is usually discussed in relation to soft ferromagnetic materials, where μ_r can take very large values, up to 10^4 or more [102]. The quantities discussed above are very important when using magnetic materials. There are two types of materials are pertinent to our discussion: Soft and hard magnetic materials. They are classified as either soft or hard depending on their coercivity H_c. The coercivity of a material is its capacity to maintain its magnetization in an opposing external magnetic field.

- Soft magnetic materials are characterized by a high permeability and a low coercivity (Hc < 1000 A/m), which makes them easy to magnetize and demagnetize. However, the soft magnetic materials easily loose memory of their field. They are used to enhance and channel flux produced by an electric current or permanent magnet. The most commonly used soft magnetic materials are soft iron, alloy of iron-silicon, nicken-iron and soft ferrites. They are applied in variety of devices such as relays, motors, inductors…
- Hard magnetic materials are characterized by a low permeability and high coervicity (H_c > 10000 A/m). Such materials are referred to as permanent magnets that retain their magnetism after being magnetized. Permanent magnets are widely used as a field source in

data storage devices, computers, biomedical apparatus. In mobile NMR devices, permanent magnets are materials of interest due to the stability of the field and ability to maintain their field. The hysteresis loops shown on Figure 3-1 describe the difference of these materials.

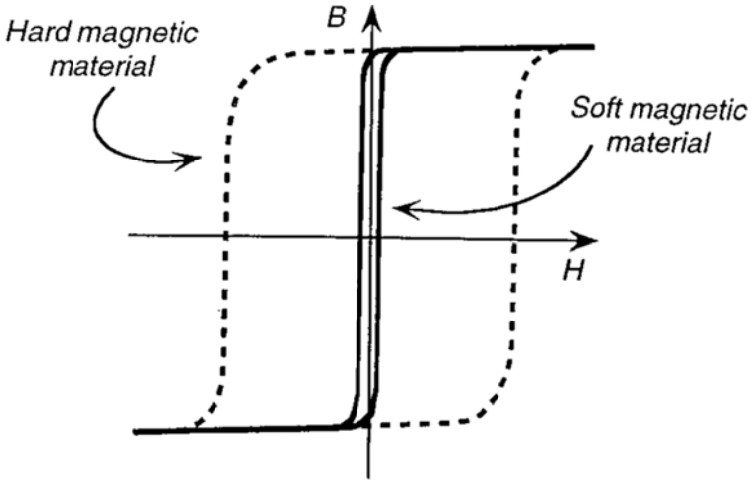

Figure 3-1: The B-H loops for soft and hard materials [101].

The magnetic hysteresis loop is used while designing a magnet. It shows the behavior of a ferromagnetic core graphically as the relationship between B and H is non-linear. The principle of the hysteresis loop is displayed in the Figure 3-2.

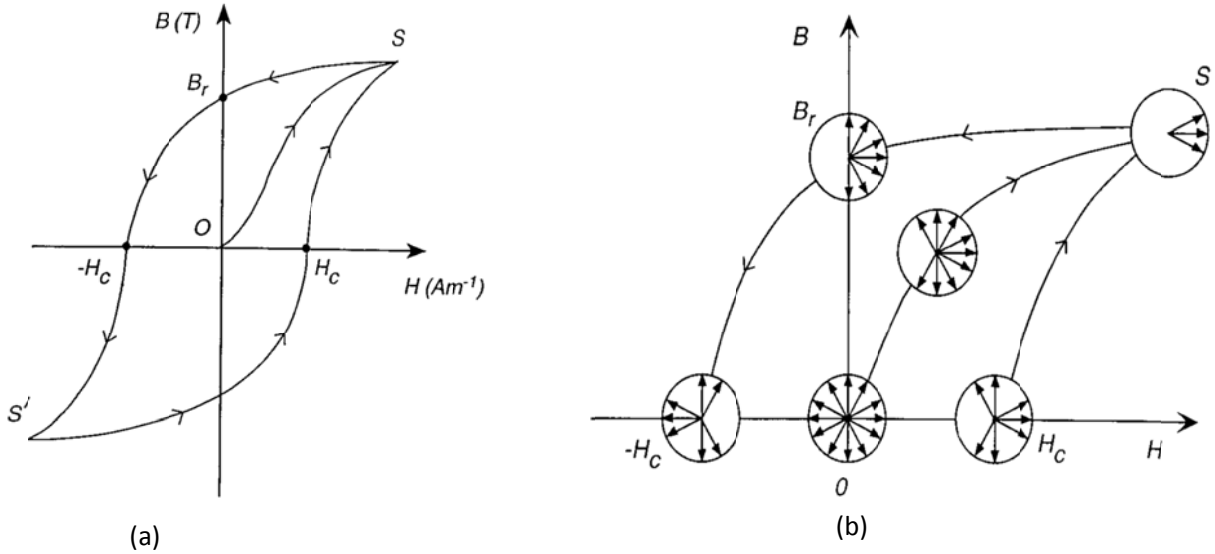

Figure 3-2: The principle of hysteresis loop [99]. (a) Hysteresis loop. (b) The orientations of magnetic domains at various points along a hysteresis loop.

Initially, a ferromagnetic material has never been previously magnetized or demagnetized, thus, the orientations of magnetic domains is isotropic as shown at the point O in Figure 3-2-b.

When the H field is applied and increased, the magnetic domains are aligned with H grow and reaching the point of magnetic saturation at the point S. This process is illustrated by the OS curve. At the saturation point S, the magnetic moments are in alignment with the positive direction of H and the material has achieved its saturation induction B_r. When H is reduced to zero, some magnetic moments in domains rotate away from H and the others still remain alignment with H, even when H achieves zero value. This is referred to as the retentive point on the Figure 3-2-b and indicates a remanent (residual) induction B_r. Now, as H is reversed to the negative direction, the magnetic moments in domains rotate from the positive direction to the negative direction of H. The reversed magnetic force which has flipped enough of the domains so that the net induction within the material is zero (B=0) is called the coercive force. It is denoted H_c.

As H increases in the negative direction, the material will become magnetically saturated but in the opposite direction (point S'). The point S$'$ is symmetrical to the point S. From the point S', H is decreased again to zero, the residual magnetism in the material will be equal to the previous value but in reverse $-B_r$. Again increasing H back in the positive direction, B will return to zero (H=H_c). As H increases further in the positive direction, the magnetic moments in domains again align themselves with H until the saturation is achieved. This path is called the major hysteresis loop as shown in Figure 3-2-a. The minor hysteresis loops are formed by cycling H within the range $-H_c < H < H_c$ illustrated in ***Figure 3-3***[101].

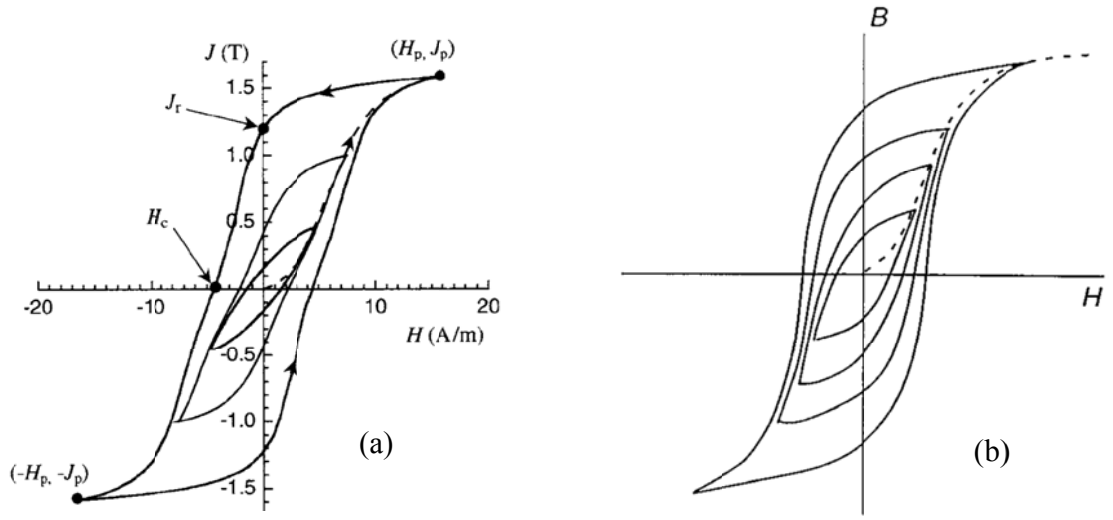

Figure 3-3: The major and minor hysteresis loops **[101]**.*(a) Hysteresis shows the dependence of magnetic polarization J on the exciting field H. (b) Hysteresis shows the dependence of flux density B on the exciting field H.*

From the hysteresis loop, a number of primary magnetic properties of a material can be

determined:

- The saturation magnetization corresponds to the maximum magnetization achieved when increasing the external magnetic field. In this status, the magnetic moments in material are aligned with the external field (the value at point S on the hysteresis loop).
- The remanence of a material (B_r) measured in Tesla (T) is its ability to maintain a magnetization when an external magnetic field is removed after achieving saturation. The relationship between the remanence induction and the remanence magnetization is described by equation 3-14:

$$\mathbf{B}_r = \boldsymbol{\mu_0 M_r} \tag{3-14}$$

- The coercivity of a material (H_c) measured in Oersted or Ampere/meter is the intensity of applied magnetic field that is required to reduce the magnetization of the material to zero.

All the properties of magnetic material are highly dependent on temperature. Each of magnetic materials has the temperature called Curie temperature or Curie point where a material's permanent magnetism changes to induced magnetism. Below the Curie temperature, the magnetic moments of magnetic material align in a ferromagnet in the absence of an applied magnetic field. On the other hand, above its Curie temperature T_c, a ferromagnet becomes paramagnetic [104]. It means that the magnetic moments are randomly aligned in a paramagnet and the magnetic material does not maintain its magnetization when the external magnetic field is removed. The Curie temperature is an important quantity must be considered when designing portable NMR devices for out of laboratory applications. The material should be selected as to be far from the Curie temperature.

There exists a variety of materials for permanent magnets. We will give the brief summary of top grade materials typically used in magnet manufacturing and their respective advantages and drawbacks.

Lodestones are known as the first magnetic material. Lodestones contain magnetite, an oxide iron. They are a naturally occurring magnet having the composition Fe_3O_4. Lodestone has low magnetic field, but high resistance to demagnetization.

Magnetic carbon steels were developed in the 18th century. They have high magnetic saturation, but are prone to demagnetization, thus can be used in limited designs [105].

Ferrite magnets are the most common commercial magnets due to their low cost. They have excellent corrosion resistance. They are very hard and brittle. Thus, this makes them difficult to machine and drill holes. Ferrite magnets have high coercivity corresponding to resistance to

demagnetization which makes them suitable for use in complex shapes. Ferrite magnets are used in electronic sensing devices, electric motors, loudspeakers and lifting devices….

Alnico magnets were developed in the 1930_s. They are alloys of iron, cobalt, nickel and aluminum (Al) along with lesser amount of other metals such as copper (Cu). Alnico magnets can be either isotropic or anisotropic, depending on whether or not the magnetic particles are oriented during their formation. Alnicos are hard as well as too brittle for cold working. They provide considerable magnetic hardness based on shape anisotropy. Alnico's remanence (B_r) may exceed 12.000 gauss. They have an excellent Curie temperature which is approximate 850°C. Alnico magnets have impressive magnetic properties. Unfortunately, they also have poor physical properties. They are extremely hard and brittle. Thus, in order to achieve a finished magnet with tight tolerances, it requires tedious and costly machining [101].

Samarium cobalt magnets (SmCo) were developed in the late 1960_s. They are a type of rare-earth magnet and strong permanent magnet made from an alloy of samarium and cobalt. The two most common SmCo materials are $SmCo_5$ and Sm_2Co_{17}. They are generally ranked similarly in strength to Neodymium magnets, but have higher Curie temperature. The maximum operating temperatures for cobalt magnets are between 250 and 550°C; Curie temperatures range from 700 to 800°C. SmCo materials offer high coercivity up to 10.500 Oersted. These materials have good thermal stability and high energy product make them popular specifically for MR applications, despite their high production cost. In addition, a samarium cobalt magnet is less subject to corrosion than a neodymium magnet, and usually does not need coating and plating. Samarium cobalt magnets are widely used in high temperature and poor working conditions.

Neodymium iron boron magnets (NdFeB) was developed in the 1980_s. They are another type of rare-earth magnet made from an alloy of neodymium, iron and boron. This material has similar properties as the samarium cobalt except that it does not have the same temperature resistance. NdFeB offers the highest energy product approaching 50MGOe. They have the highest magnetic field strength and have a higher coercivity in comparison to samarium cobalt magnets. However, their Curie temperature (310°C) is lower than the Curie temperature of samarium cobalt magnets. This prohibits them from being used in high temperature applications. While today neodymium magnets with higher quality grades have eliminated an oxidization chain reaction in the surface of the magnets, a protective coating is still necessary to protect them from the atmosphere. In addition, NdFeB is lighter and less brittle than SmCo.

The mass density of NdFeB is about $7g/cm^{-3}$ while the correspondent value of SmCo is about 8.4

g/cm^{-3}. Moreover, NdFeB is cheaper than SmCo due to Neodymium is much more abundant than Samarium [101].

Samarium iron nitride bonded magnets is a new material under development. It has high resistance to demagnetization, high magnetization and increased resistance to corrosion and temperature when compared to NdFeB. Demas and Prado [105] summarized the information of magnetic materials mentioned in this section as in Table 3-3.

Material	Remanence (Gauss)	Coercivity (Oe)	BH_{max} (MGOe)	T_{Curie} (°C)	T_c (%/°C)
SmCo	11.600	10.500	30	800	-0.035
NdFeB	12.800	12.300	40	310	-0.12
Alnico	12.500	640	5.5	860	-0.02
Ceramic	3.900	3.200	3.5	750	-0.2
Flexible	1.600	1.370	0.6	100	-0.12

Table 3-3: Summary of top grade materials typically used in magnet manufacturing **[105]**.

The desired materials for designing portable NMR devices must have high remanence, coercivity and energy product. In the Table 3-3, it is obvious that the family of NdFeB and SmCo satisfy the conditions mentioned above. From the analyses above, we will choose NdFeB for this work because they are cheaper while it has similar properties as SmCo. The Figure 3-4 shows the different families of materials and the progress in expanding the range of coercivity of magnetic materials during twentieth century [102].

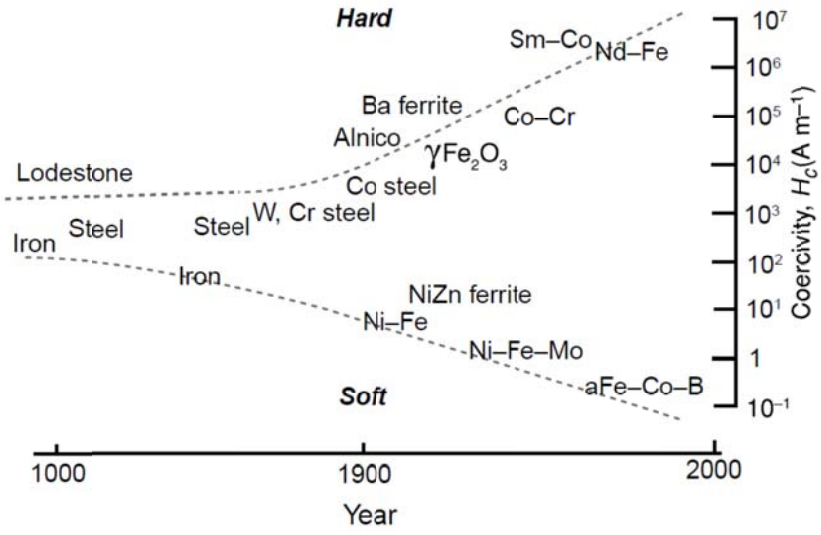

Figure 3-4: The progress in expanding the range of coercivity of magnetic materials during twentieth century **[102]**.

3.4 Numerical methods and simulation

In order to analyze the magnetic field of portable NMR devices and their homogeneity, a variety of numerical and simulation approaches can be used. The popular method is dipole approach. In this approach, each magnet is considered as a simple dipole. The magnetic field of a magnetic dipole can be calculated by formula 3-15.

$$\vec{B}(x,y,z) = \frac{\mu_0}{4\pi}\frac{3(\vec{m}.\vec{n})\vec{n}-\vec{m}}{R^3} \tag{3-15}$$

Thus, the flux density in the bore of the Halbach cylinder can be written as the formula 3-16. The Figure 3-5 shows the component definitions of this formula.

$$B = \frac{\mu_0}{4\pi}\sum_{i=0}^{n-1}\frac{3(m_i.n_i)n_i-m_i}{R^3} \tag{3-16}$$

Where:

- m_i are the magnetic moment vectors of the n^{th} magnets, for i = 0,1,…,n-1.

$$m_i = \begin{bmatrix} 0 \\ msin(\beta) \\ mcos(\beta) \end{bmatrix} \tag{3-17}$$

- P is the measurement field point.

$$P = \begin{bmatrix} P_x \\ P_y \\ P_z \end{bmatrix} \tag{3-18}$$

- M_p is the positions of magnets on the array.

$$M_p = \begin{bmatrix} 0 \\ rsin(\alpha) \\ rcos(\alpha) \end{bmatrix} \tag{3-19}$$

- n_i are unit vectors from the field points.

$$n_i = \begin{bmatrix} \frac{P_x}{\sqrt{P_x^2+(P_y-rsin(\alpha))^2+(P_z-rcos(\alpha))^2}} \\ \frac{P_y-rsin(\alpha)}{\sqrt{P_x^2+(P_y-rsin(\alpha))^2+(P_z-rcos(\alpha))^2}} \\ \frac{P_z-rcos(\alpha)}{\sqrt{P_x^2+(P_y-rsin(\alpha))^2+(P_z-rcos(\alpha))^2}} \end{bmatrix} \tag{3-20}$$

- R is the distance between the measurement field point P and the dipole as shown on

Figure 3-5.

$$\boldsymbol{\alpha_i = \frac{2\pi i}{N}} \tag{3-21}$$

$$\boldsymbol{\beta_i = \frac{4\pi i}{N}} \tag{3-22}$$

- N is the number of magnets.

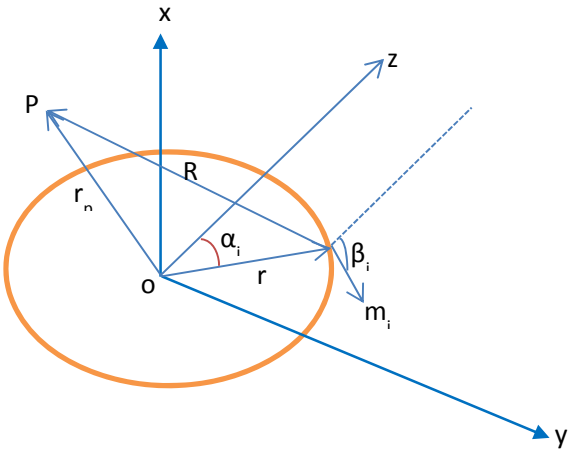

Figure 3-5: Definition of parameters in equation 3-16.

Substitute the parameters m_i, n_i, M_p, R and P into the equation 3-16, the flux density can be written as:

$$\boldsymbol{B = \sqrt{B_x^2 + B_y^2 + B_z^2}} \tag{3-23}$$

Where:

$$B_x = \frac{mcos(\beta)P_x\big(P_z - rcos(\alpha)\big) + msin(\beta)P_x(P_y - rsin(\alpha))}{\big((P_x^2 + (P_y - rsin(\alpha))^2 + (P_z - rcos(\alpha))^2\big)^{\frac{5}{2}}}$$

$$B_y = -\frac{m(\sin(\beta)\left[(P_x^2 + (P_x^2 + (P_y - rsin(\alpha))^2 + (P_z - rcos(\alpha))^2\right] + msin(\beta)\left[\left(P_z - rcos(\alpha)\right)^2\right] - mcos(\beta)[P_y - rsin(\alpha)][P_z - rcos(\alpha)]}{\big((P_x^2 + (P_y - rsin(\alpha))^2 + (P_z - rcos(\alpha))^2\big)^{\frac{5}{2}}}$$

$$B_z = -\frac{m(\cos(\beta)\left[(P_x^2 + (P_x^2 + (P_y - rsin(\alpha))^2 + (P_z - rcos(\alpha))^2\right] + mcos(\beta)\left[\left(P_y - rsin(\alpha)\right)^2\right] - msin(\beta)[P_y - rsin(\alpha)][P_z - rcos(\alpha)]}{\big((P_x^2 + (P_y - rsin(\alpha))^2 + (P_z - rcos(\alpha))^2\big)^{\frac{5}{2}}}$$

The equation 3-16 is very useful for calculating the flux density in the bore of a Halbach cylinder from the given B_r of the magnet materials. It is a good approximation method (because in this method, the size of the magnets is neglected) to model first the element of a design by dipoles and then move toward a specific geometry. Based on this method, Soltner and Blümler [79] proposed formulas and numerical values to calculate the flux density of single rings and composed 3D system.

Another method based on the spherical harmonic expansions (SHE) of the scalar potential and the magnetic field. Based on this method, Hugon *et al* [71][29] proposed an approach to design an axisymmetric magnet achieving a specific homogeneity ΔB_0 in a given sphere of diameter R_0 with the homogeneity condition:

$$\left(\frac{r}{R_0}\right)^{n_0} \leq \Delta B_0 \tag{3-24}$$

Marble *et al* [54] proposed the 2D calculation of magnetic field for a bar magnet. Based on this calculation, they were built a prototype with the remote homogeneous field. Their calculation considered the permanent magnet as two sheets of thin wires. However, this approach neglected inhomogeneity in the magnetization or saturation effects from the magnets in close proximity. Thus, it is not a solution for the finite magnet.

Finite element methods (FEM) are currently the most popular method for the solution of electromagnetic and magnetostatic problems because of two reasons. Firstly, FEM is a powerful method widely used in a variety of applications. Secondly, There exists numerous commercially FEM software packages such as ANSYS, COMSOL…These software packages enable users to solve complex problems without developing their own application specific algorithms. For these reasons, we chose the finite element methods which are underlying principles of ANSYS (the commercial software package we use for simulation and optimization in this work).

The calculation of ANSYS for electromagnetic and magnetostatic problems are based on the Maxwell's equations. Electromagnetic fields governed by Maxwell's equations can be written as:

$$\nabla \times \{H\} = \{J\} + \left\{\frac{\partial D}{\partial t}\right\} = \{J_s\} + \{J_e\} + \{J_V\} + \left\{\frac{\partial D}{\partial t}\right\} \tag{3-25}$$

$$\nabla \times \{E\} = -\left\{\frac{\partial B}{\partial t}\right\} \tag{3-26}$$

$$\nabla . \{B\} = 0 \tag{3-27}$$

$$\boldsymbol{\nabla}.\{\boldsymbol{D}\} = \boldsymbol{\rho} \tag{3-28}$$

Where:

- $\nabla \times$ is curl operator.
- $\nabla.$ is divergence operator.
- $\{H\}$ is magnetic field intensity vector.
- $\{J\}$ is total current density vector.
- $\{J_s\}$ is the applied source current density vector.
- $\{J_e\}$ is the induced eddy current density vector.
- $\{J_V\}$ is the velocity current density vector.
- $\{D\}$ is the electric flux density vector.
- t is time.
- $\{E\}$ is the electric field intensity vector.
- $\{B\}$ is the magnetic density vector.
- ρ is the electric charge density.

The solution of magnetic field problems is commonly obtained by using potential functions. Depend on the chosen element type and element option, the magnetic vector potential or the scalar potential is considered to use. There are three applicable regions refer to the solutions for electromagnetic or magnetostatic problems as shown on the Figure 3-6.

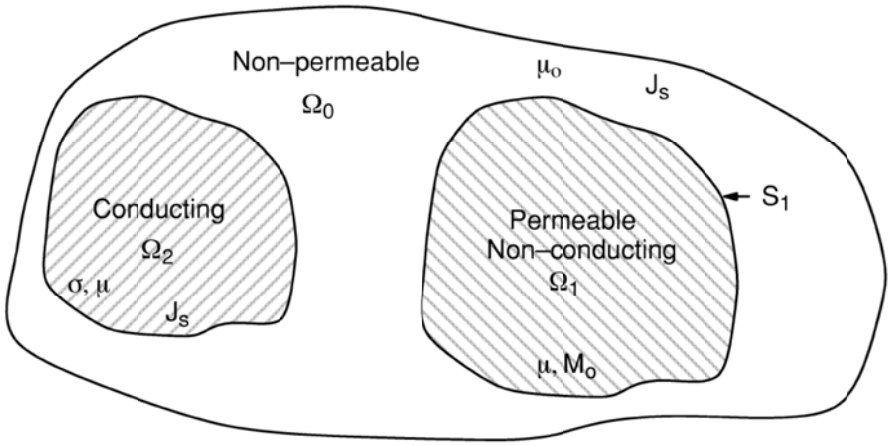

Figure 3-6: Electromagnetic field regions[106].

Where:

- Ω_0 is the free space region.
- Ω_1 is the non-conducting permeable region.

- Ω_2 is the conducting region.
- μ is the permeability of iron.
- μ_0 is the permeability of air
- M_0 is permanent magnets.
- S_1 is boundary of Ω_1.
- σ is conductivity.

The domain Ω_2 does not concern with magnetostatics. It is considered for electromagnetic problem. Thus, the readers can find the detail in reference [106]. Here, we discuss the domains Ω_0 and Ω_1 which refer to permanent magnets. When permanent magnets are considered, the constitutive relation becomes [106]:

$$\{\boldsymbol{B}\} = [\boldsymbol{\mu}]\{\boldsymbol{H}\} + \boldsymbol{\mu_0}\{\boldsymbol{M_0}\} \tag{3-29}$$

Where $\{M_0\}$ is the remanent intrinsic magnetization vector. The equation 3-29 can be rewritten as:

$$\{\boldsymbol{H}\} = [\boldsymbol{\nu}]\{\boldsymbol{B}\} - \frac{\mathbf{1}}{\boldsymbol{\nu_0}}[\boldsymbol{\nu}]\{\boldsymbol{M_0}\} \tag{3-30}$$

Where:

- $[\nu] = [\mu]^{-1}$ is the reluctivity matrix.
- $[\nu_0] = \frac{1}{\mu_0}$ is the reluctivity of free space.

The constitutive relations for the related electric field are:

$$\{\boldsymbol{J}\} = [\boldsymbol{\sigma}]\,[\{\boldsymbol{E}\} + \{\boldsymbol{V}\} \times \{\boldsymbol{B}\}] \tag{3-31}$$

$$\{\boldsymbol{D}\} = [\boldsymbol{\epsilon}]\{\boldsymbol{E}\} \tag{3-32}$$

Where:

- $[\sigma] = \begin{bmatrix} \sigma_{xx} & 0 & 0 \\ 0 & \sigma_{yy} & 0 \\ 0 & 0 & \sigma_{zz} \end{bmatrix}$ is the electrical conductivity matrix.
- $[\epsilon] = \begin{bmatrix} \epsilon_{xx} & 0 & 0 \\ 0 & \epsilon_{yy} & 0 \\ 0 & 0 & \epsilon_{zz} \end{bmatrix}$ is the permittivity matrix.
- $\{V\} = \begin{Bmatrix} V_x \\ V_y \\ V_z \end{Bmatrix}$ is the velocity vector.

The quantities $\sigma_{xx}, \epsilon_{yy}, \epsilon_{zz}, \epsilon_{xx}, \epsilon_{yy}, \epsilon_{zz}$ are respectively conductivity and permittivity in three directions x, y and z. These directions can be assigned for materials by MP command in ANSYS.

In ANSYS, the values of H and B can be obtained by two solutions, which are the magnetic scalar potential and the magnetic vector potential. The second solution is described here because it is implemented in PLANE13, SOLID97 and SOLID117. The elements PLANE13 and SOLID97 are respectively used for 2D and 3D simulation in this work. The detail of the first solution can be found in the reference [106].

Unlike the scalar potential formulations are restricted to static field analysis, the vector potential formulation can be applied to both static and dynamic fields with partial orthotropy nonlinear permeability. The basic equation to be solved is [106]:

$$\left[\overline{\boldsymbol{C}}\right]\{\dot{\boldsymbol{u}}\} + \left[\overline{\boldsymbol{K}}\right]\{\boldsymbol{u}\} = \{\overline{\boldsymbol{J}}_{\boldsymbol{i}}\} \tag{3-33}$$

Degrees of freedom:

$$\{\boldsymbol{u}\} = \begin{Bmatrix}\{\boldsymbol{A_e}\}\\ \{\boldsymbol{v_e}\}\end{Bmatrix} \tag{3-34}$$

Where:

- $\{A_e\}$ is magnetic vector potential (AX, AY, AZ).
- $\{v_e\}$ is time integrated electric scalar potential $v = \int V\, dt$.

Coefficient matrices:

$$\left[\overline{\boldsymbol{K}}\right] = \begin{bmatrix}[\boldsymbol{K^{AA}}] & [\boldsymbol{0}]\\ [\boldsymbol{K^{VA}}] & [\boldsymbol{0}]\end{bmatrix} \tag{3-35}$$

$$[\boldsymbol{K^{AA}}] = [\boldsymbol{K^{L}}] + [\boldsymbol{K^{N}}] + [\boldsymbol{K^{G}}] \tag{3-36}$$

$$[\boldsymbol{K^{L}}] = \int_{\boldsymbol{vol}} (\boldsymbol{\nabla} \times [\boldsymbol{N_A}]^{\boldsymbol{T}})^{\boldsymbol{T}}\, [\boldsymbol{\nu}] \left(\boldsymbol{\nabla} \times [\boldsymbol{N_A}]^{\boldsymbol{T}} - [\boldsymbol{N_A}][\boldsymbol{\sigma}](\{\boldsymbol{v}\} \times \boldsymbol{\nabla} \times [\boldsymbol{N_A}]^{\boldsymbol{T}})\right) \boldsymbol{d(vol)} \tag{3-37}$$

$$[\boldsymbol{K^{G}}] = \int_{\boldsymbol{vol}} (\boldsymbol{\nabla}.\ [\boldsymbol{N_A}]^{\boldsymbol{T}})^{\boldsymbol{T}}\, [\boldsymbol{\nu}] (\boldsymbol{\nabla}.\ [\boldsymbol{N_A}]^{\boldsymbol{T}}) \boldsymbol{d(vol)} \tag{3-38}$$

$$[\boldsymbol{K^{N}}] = \boldsymbol{2} \int_{\boldsymbol{vol}} \frac{\boldsymbol{d\nu_h}}{\boldsymbol{d(|B|^2)}} (\{\boldsymbol{B}\}^{\boldsymbol{T}} (\boldsymbol{\nabla} \times [\boldsymbol{N_A}]^{\boldsymbol{T}})^{\boldsymbol{T}}) \left(\{\boldsymbol{B}\}^{\boldsymbol{T}} (\boldsymbol{\nabla} \times [\boldsymbol{N_A}]^{\boldsymbol{T}})\right) \boldsymbol{d(vol)} \tag{3-39}$$

$$[\boldsymbol{K^{VA}}] = -\int (\boldsymbol{\nabla}[\boldsymbol{N_A}]^{\boldsymbol{T}})^{\boldsymbol{T}}\, [\boldsymbol{\sigma}]\{\boldsymbol{v}\} \times \boldsymbol{\nabla} \times [\boldsymbol{N_A}]^{\boldsymbol{T}} \boldsymbol{d(vol)} \tag{3-40}$$

$$\left[\overline{\boldsymbol{C}}\right] = \begin{bmatrix} [\boldsymbol{C^{AA}}] & [\boldsymbol{C^{AV}}] \\ [\boldsymbol{C^{AV}}] & [\boldsymbol{C^{VV}}] \end{bmatrix} \tag{3-41}$$

$$[\boldsymbol{C^{AA}}] = \int_{\boldsymbol{vol}} [\boldsymbol{N_A}]\,[\boldsymbol{\sigma}][\boldsymbol{N_A}]^{\boldsymbol{T}}\boldsymbol{d(vol)} \tag{3-42}$$

$$[\boldsymbol{C^{AV}}] = \int_{\boldsymbol{vol}} [\boldsymbol{N_A}]\,[\boldsymbol{\sigma}]\{\boldsymbol{N}\}^{\boldsymbol{T}}\boldsymbol{d(vol)} \tag{3-43}$$

$$[\boldsymbol{C^{VV}}] = \int_{\boldsymbol{vol}} (\boldsymbol{\nabla}\{\boldsymbol{N}\}^{\boldsymbol{T}})^{\boldsymbol{T}}[\boldsymbol{\sigma}]\boldsymbol{\nabla}\{\boldsymbol{N}\}^{\boldsymbol{T}}\,\boldsymbol{d(vol)} \tag{3-44}$$

Applied loads:

$$\left\{\overline{\boldsymbol{J}}_{\boldsymbol{i}}\right\} = \begin{Bmatrix} \{\boldsymbol{J^A}\} \\ \{\boldsymbol{I^t}\} \end{Bmatrix} \tag{3-45}$$

$$\{\boldsymbol{J^A}\} = \{\boldsymbol{J^S}\} + \{\boldsymbol{J^{pm}}\} \tag{3-46}$$

$$\{\boldsymbol{J^S}\} = \int_{\boldsymbol{vol}} \{\boldsymbol{J_s}\}\,[\boldsymbol{N_A}]^{\boldsymbol{T}}\boldsymbol{d(vol)} \tag{3-47}$$

$$\{\boldsymbol{J^{pm}}\} = \int_{\boldsymbol{vol}} (\boldsymbol{\nabla} \times [\boldsymbol{N_A}]^{\boldsymbol{T}})^{\boldsymbol{T}}\{\boldsymbol{H_c}\}\,\boldsymbol{d(vol)} \tag{3-48}$$

$$\{\boldsymbol{I^t}\} = \int_{\boldsymbol{vol}} \{\boldsymbol{J_t}\}\,[\boldsymbol{N_A}]^{\boldsymbol{T}}\boldsymbol{d(vol)} \tag{3-49}$$

Where:

- $[N_A]$ is the matrix of element shape functions for $\{A\}$

$$\{\boldsymbol{A}\} = [\boldsymbol{N_A}]^{\boldsymbol{T}}\{\boldsymbol{A_e}\};\ \{\boldsymbol{A_e}\}^{\boldsymbol{T}} = \left|\{\boldsymbol{A_{Xe}}\}^{\boldsymbol{T}}\ \{\boldsymbol{A_{Ye}}\}^{\boldsymbol{T}}\ \{\boldsymbol{A_{Ze}}\}^{\boldsymbol{T}}\right| \tag{3-50}$$

- $\{N\}$ is the vector element shape functions for $\{V\}$ ($V = \{N\}^T\{V_e\}$).
- $\{J_s\}$ is the source current density vector.
- $\{J_t\}$ is the total current density vector.
- vol id the volume of element.
- $\{H_c\} = \frac{1}{\nu_0}[\nu]\{M_0\}$ is the coercive force vector.
- $\frac{d\nu_h}{d(|B|^2)}$ is the derivative of reluctivity with respect to the magnitude of magnetic flux squared (derived from input material property curve B versus H).

Magnetic vector potential results:

The magnetic flux density is defined as the curl of the magnetic vector potential as equation 3-51.

$$\{\boldsymbol{B}\} = \boldsymbol{\nabla} \times [\boldsymbol{N_A}]^{\boldsymbol{T}}\{\boldsymbol{A_e}\} \tag{3-51}$$

Where:

- $\{B\}$ is the magnetic flux density.
- $\nabla \times$ is the curl operator.
- $[N_A]$ is the shape functions.
- $\{A_e\}$ is the nodal magnetic vector potential.

From the flux density results, the magnetic field intensity is then calculated by equation 3-52.

$$\{\boldsymbol{H}\} = [\boldsymbol{\nu}]\{\boldsymbol{B}\} \tag{3-52}$$

Where:

- $\{H\}$ is the magnetic field intensity.
- $[\nu]$ is the reluctivity matrix.

3.5 ANSYS

ANSYS multiphysics [100] is the general purpose finite element analysis software. It can solve complex problems which concern with variety of engineering field such as heat transfer, fluid problems, magnetic field…It is a powerful tool for simulation and optimization. The analysis process of ANSYS consists of three steps: pre-process, FEM analysis and post-process.

Pre-process is the processes of geometry modeling, setting up material properties, meshing and setting boundary condition. The ANSYS program has a large library of element types. Depending on the solved problem, the users can choose the suitable elements. For example, the element PLANE53 is used for 2-D simulation while the element SOLID98 is considered for 3-D solutions. In this work, two elements are used for simulation. The element PLANE13 and SOLID97 is respectively used for 2-D and 3-D simulation.

The element PLANE13 models (planar and axis-symmetric) 2-D static magnetic field analysis. It is defined by four nodes with up to four degrees of freedom per node. This element has nonlinear capability for modeling B-H curves or permanent magnet demagnetization curves. PLANE13 is based on the magnetic vector potential formulation. In this element, the MGXX, MGYY represent vector components of the coercive force for permanent magnet materials in two directions X and Y. The magnitude of the coercive force is the square root of the sum of the squares of the components. The direction of polarization of permanent magnets is assigned in whether X or Y direction through the command MP [106].

The element SOLID97 models 3-D magnetic fields. The element is defined by eight nodes and has up to five degrees of freedom per node. SOLID97 is also based on the magnetic vector

potential formulation with the Coulomb gauge and it is applicable to the low-frequency magnetic field analysis such as magnetostatic, Eddy current… This element has nonlinear capability for modeling B-H curves or permanent magnet demagnetization curves. In this element, the MGXX, MGYY and MGZZ represent vector components of the coercive force for permanent magnet materials in three directions X, Y and Z. The magnitude of the coercive force is the square root of the sum of the squares of the components. The direction of polarization of permanent magnets is assigned in the same command with the element PLANE13 [106].

Post-process is the processes of display results and data extraction after building the model and obtaining the solution. Via the post processor of ANSYS, the results can be plotted or visualized. Data extraction is an important process for our work. In our work, the homogeneity of magnetic field in the region of interest is the most important criteria need to be calculated. Thus, the magnetic field nodes in this region of interest are extracted and treated by Matlab. The region of interest is first defined in the pre-process step.

3.6 Conclusions

The desired properties of the magnetic materials used for portable NMR devices are highly required such as high remanence, high coercivity… In order to achieve the highest magnetic field possible. There exists a variety of magnetic material families which have been discovered through history. Each of magnetic material has different advantages and drawbacks. The users can choose the suitable magnetic material depend on their objective of applications. In addition, the properties of magnetic materials are influenced by the external environment such as temperature. Therefore, it is necessary to figure out the properties of magnetic materials in order to exactly choose for applications. In this chapter, we briefly described the magnetic material properties which is the desired materials used in recent years. From these descriptions, we have chosen the best material for our applications.

The simulation plays an important role to the design of portable NMR devices. It is a tool to predict the properties of magnet systems. From the results of simulation, the designers can give the solutions to improve or optimize them. In this chapter, we have examined the numerical and simulation methods of previous researchers and chosen the finite element method which is the underlying procedure of ANSYS for our calculation and simulation. Finally, we also examined the field calculation based on the magnetic vector potential and gave the short description about the two elements used in our work.

Chapter 4

Design, construction of light weight portable NMR with Halbach type from identical bar magnets

Summary:

- **Introduction**
- **Modeling and simulation**
- **Optimization**
- **Measurement and experiments**
- **Discussion and conclusions**

Chapter 4: Design, construction of a light weight portable NMR devices with Halbach type from identical rod magnets

4.1 Introduction

Halbach type magnet has been developed extensively for use in a variety of applications because of their homogeneity and confinement of magnetic field inside the bore. Starting with the proposition of Klaus Halbach in 1980 [63], the Halbach ring consists of segments of permanent magnets joined together in an array to create the homogeneous field in transverse plane. This allows using the solenoid coil for NMR experiments. However, its assembly and polarization of magnets are the problems which can be affected to their homogeneity and performances. Based on the principle of Halbach ring, the Halbach structure with discrete magnets for NMR portable known as NMR Mandhalas was given by Raich and Blümler [74]. It is based on an arrangement of identical bar magnets, described by the analytical equations reported in literature [79]. This concept has been widely used for building prototypes because they are easy to assembly and their region of interest is easy to access. Despite the lowest homogeneity of Halbach type, it still better in comparison to ex situ magnets, but poor compared to magnet volume. For measurement of the relaxation time T_2 and T_1 or the spectrum, the fraction of inhomogeneity $\frac{\Delta B_0}{B_0}$ is approximate 10ppm. T_1 and T_2 represent the relaxation of the nuclear spin magnetization, respectively parallel and perpendicular, to the external magnetic field. In order to provide the sufficient field homogeneity for NMR experiments, a popular method to improve this inhomogeneity is shimming. The concept of movable permanent magnets in the shim unit of a Halbach array is reported by Ernesto Danieli *et al* [77]. Another method of shimming based on the spherical harmonic expansion proposed a complete procedure for permanent magnet design, fabrication, and characterization [72]. In this chapter, we introduce the light weight (3kg), low cost (200euros) and simple design NMR apparatus which consists of 24 identical rod magnets arranged in Halbach array. This apparatus generates a B_0 field strength about 0.12T. Its characteristics are described by simulating and calculating the field strength and homogeneity in three dimensions (3D). These simulations and calculation were performed by two softwares RADIA and ANSYS Multiphisics. The results of simulation which refer to the field strength B_0 and homogeneity of device were compared to those obtained with a digital gaussmeter. The results of verification show that the

homogeneity in the longitudinal axis of apparatus and the field strength B_0 were found to be similar. However, the homogeneity in transverse plane differs from simulation and measurement because of the quality of the magnets. To overcome this difficulty, we propose a new shim method to compensate the imperfection of the magnets. The homogeneity of magnetic field significantly improves with 18 times in comparison to one without shim magnets.

4.2 Modeling and simulation

4.2.1 Modeling

In order to design and construct the prototype, we chose the Halbach type. This prototype has two rings placed alignment to compensate the magnetic field outside of the rings, each ring consist of 12 identical magnets in cylindrical shape. The direction of magnetization of static field B_0 is defined parallel to the Ox axis. The homogeneous region is expected in the middle length of the prototype. The geometric parameters are displayed in Figure 4-1 and Table 4-1.

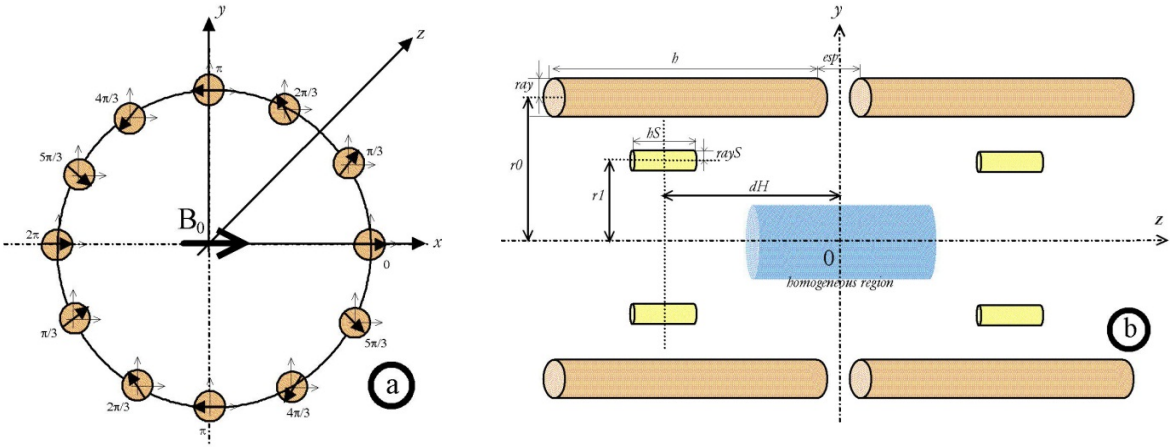

Figure 4-1: The position of magnets and their directions of magnetization.

The Table 4-1 shows the geometric parameters of apparatus, their definitions and dimensions.

Names of the parameters	Definitions	Dimensions
r0	Radius of the ring	30 mm
h	Height of the ring	50 mm
ray	Radius of magnets	4 mm
hS	Height of shim magnets	6 mm
rays	Radius of shim magnets	2 mm
esp	Gap between two rings	to be optimized
r1	Radius of the shim rings	to be optimized
dH	Distance from the middle length of shim magnets to z = 0	to be optimized

Table 4-1: *The geometric parameters and their dimensions.*

In most of Halbach configuration, the static field B_0 transverses to the cylindrical axis. The direction of magnetization of each magnet is defined by two angles α_i and β_i as shown in Figure 4-2.

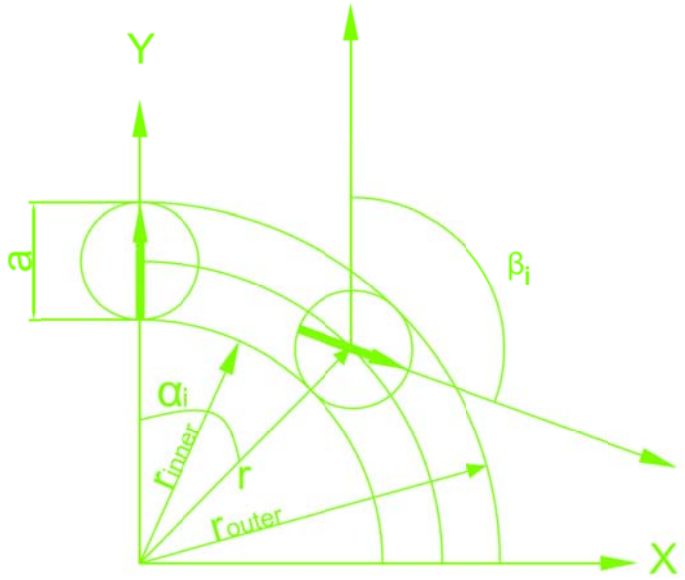

Figure 4-2: The geometric parameters of Halbach configuration.

Where:

- a is the diameter of magnets.
- r_{inner} is the inner radius of the ring.
- r_{outer} is the outer radius of the ring.
- r is the radius of the ring.
- α_i is the angle between the Oy axis and the i_{th} magnet.
- β_i is the angle between the Ox axis and the direction of magnetization of i_{th} magnet.

The i_{th} magnet is placed on a circle at an angle $\alpha_i = \frac{2\pi.i}{n}$ and its magnetization is defined by an angle $\beta_i = 2\alpha_i$. Where, n is the number of magnets, i = 0, 1, 2… n-1. In our case, the apparatus has 12 magnets placed on a circle of radius $r_0 = 30$ mm. As shown on Figure 4-1-a, each magnet is placed at an angle $\alpha_i = \frac{\pi}{6}$ and its magnetization is rotated by $\beta_i = \frac{\pi}{3}$.

4.2.2 Simulation and results

4.2.2.1 Simulation

In order to calculate and simulate the magnetic field and the homogeneity, two softwares RADIA and ANSYS Multiphisics were used. They are two different methods of calculation. RADIA was developed to design the Insertion Devices for Synchrotron light sources. It uses boundary integral methods. Each volume created to represent the magnets is subdivided in a number of sub elements to solve the general problem in terms of magnetization. The solution is performed by building a large matrix in memory which represents mutual interactions between the object. RADIA does not need to mesh the vacuum. On the other hand, ANSYS is a multiphysics software and it uses FEM (Finite Element Modeling) modeling. Each volume is sub divided with some elements. Even the air between and around the magnets has to be meshed. Flux conditions have to be placed outside the global volume in order to apply parallel or normal condition. These two methods are used complementary: RADIA is used for optimization and simulation. ANSYS is used for verification of the results obtained by RADIA The size of the meshing is reduced until the simulation results do not change.

The properties of the material used for simulation that represent magnets were chosen to represent magnets from “HCKM MAGNETS from STOCK” [107]. The magnet material is Neodinium NdFeB with the following characteristics.

- a saturation magnetization of 1.37 T
- a coercively of H_c = 1000 kA/m
- The diameter and the length of the magnet are respectively 8 mm and 50 mm
- The magnetization is oriented along the diameter
- The maximal operating temperature is 120 °C
- And the temperature coefficient is 0.11 %.°C^{-1}.

In order to calculate the homogeneity, the values of the magnetic field (mesh nodes) are selected in the homogeneous region, then exported to and treated by Matlab Software. The homogeneity is calculated by the formula 4-1.

$$\boldsymbol{Homogeneity} = \frac{\sum_i^n \frac{\boldsymbol{Abs(B_i - B)}}{\boldsymbol{B}} \boldsymbol{10^6}}{\boldsymbol{m}} \quad (4\text{-}1)$$

Where:

- B_i is the value of magnetic field at the i_{th} position in the homogeneous region.
- B is the value of magnetic field at the center of homogeneous region.
- m is the number of mesh nodes in the homogeneous region.

4.2.2.2 Results

A NMR device constitute with 24 magnets placed as shown in the Figure 4-1 is considered during the simulation with ANSYS and RADIA. The magnetic field B_0 is oriented along Ox axis. First, *esp = 0* is considered. The maximal value of B_0 calculated with RADIA is 0.103 T while the correspondent value derived from ANSYS Analysis is 0.11 T. The difference of calculation between RADIA and ANSYS is 6.79 %. This difference can be accounted for by the problem of mesh size convergence. It means that the results of fine meshes are higher than coarse meshes. This difference can be accounted for by the problem of mesh size convergence. It means that the results of fine meshes are higher than coarse meshes. In order to mesh the volumes, the command SMRTSIZE, n was used in this simulation. Where, n is the mesh size level ranging from 1 (fine mesh) to 10 (coarse mesh). We used the default mesh size level with n=6 for this simulation. Furthermore, the difference can be acceptable. Although the magnetic field strength calculated by two softwares is slightly different, the magnetic field distribution in the homogeneous region is similar as shown in Figure 4-4-a,b. This results in the similarity of the magnetic field homogeneity.

The Figure 4-3-a displays the variation of magnetic field B_0 along Ox axis. The value of magnetic field is almost constant for 1.8mm < x < 4.2mm or in the distance of 2.4mm at the center of configuration. The Figure 4-3-b represents the distribution of magnetic field in the XOY plane. Each shades of color represent a variation of the inhomogeneity $\frac{\Delta B_0}{B_0}$ of 50 ppm. In a rectangle of 5 × 6.4 mm, the inhomogeneity $\frac{\Delta B_0}{B_0}$ is larger than 450 ppm (RADIA) while the correspondent value determined by ANSYS is 380 ppm. For an inhomogeneity lower than 100 ppm, the expected volume for experiment is 3 x 3 x 3 mm^3.

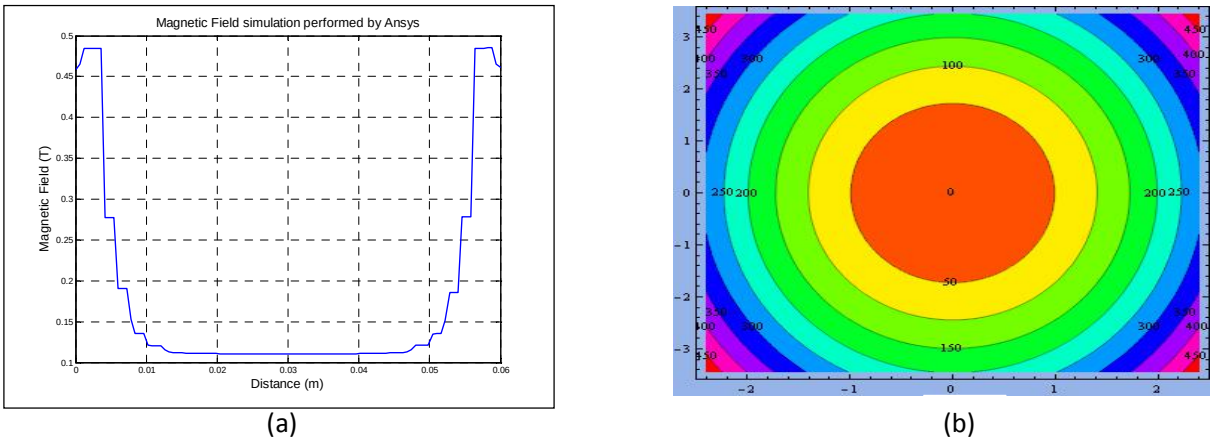

Figure 4-3: The magnetic field Bx distribution in the XOY plane (at Z=0). (a) the variation of magnetic field B_x versus Ox axis. (b) the inhomogenity of the magnetic field Bx versus X and Y.

The variation of magnetic field B_x on the XOZ plane is shown on the Figure 4-4. The homogeneity of magnetic field is 300ppm in the region of 5 x 6.4mm as determined by RADIA, while ANSYS gives a result of 200ppm. The Figure 4-4 shows the similarity of magnetic field distribution obtained by ANSYS and RADIA. However, the homogeneity calculated by ANSYS is always smaller than those of RADIA because of the method of calculation. It can be explained that the RADIA determines the homogeneity on the different region of the plane while ANSYS calculates the mean value of magnetic field on the whole plane.

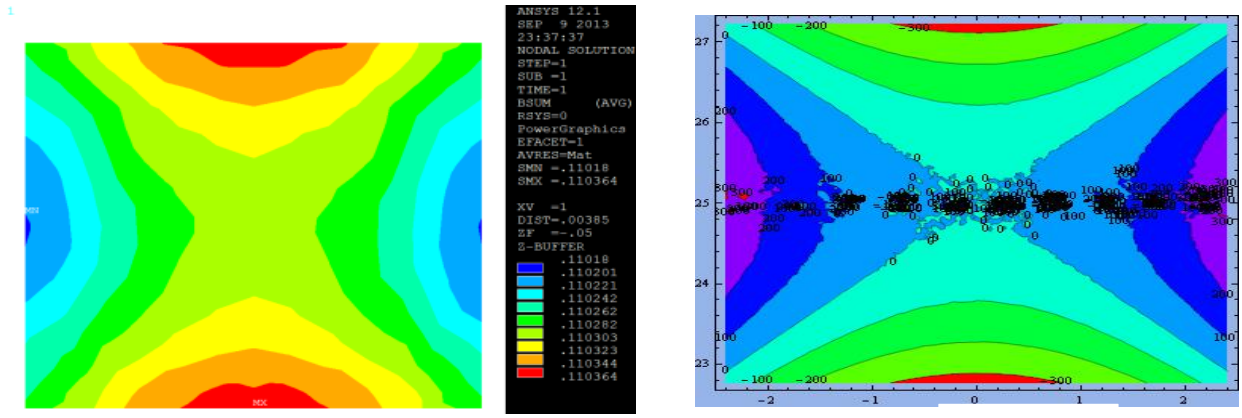

(a) ANSYS (b) RADIA

Figure 4-4: Magnetic Field Bx distribution in the region of 5 x 6.4 mm in xOz plane. (a) the variation of magnetic field B_x simulated by ANSYS. (b) the variation of magnetic field B_x simulated by RADIA.

The variation of the magnetic field Bx profile along Oz axis depends on the gap *esp* between the two rings. The best homogeneity is achieved at a certain distance. In order to optimize this gap, we increased the value of *esp* by the steps of 0.1mm. The Figure 4-5 shows the B_x profiles versus the Oz axis for four values of *esp*. When esp = 0, the magnetic field outside one ring does not compensate the magnetic field for the other ring. For *esp* = 0.9 mm, the compensation is optimum and the magnetic field at the center almost constant. The magnetic field at the center of apparatus significantly decreases at the gap *esp* = 1.3mm.

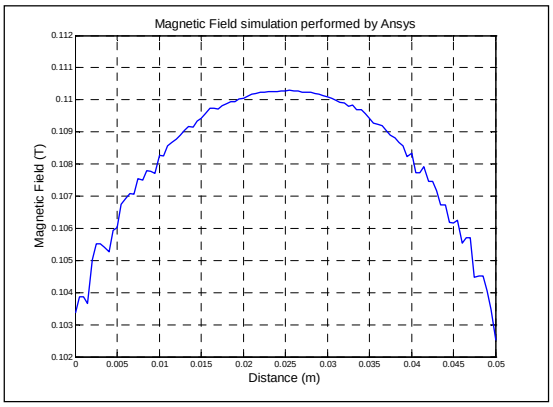

(a)= 0 mm

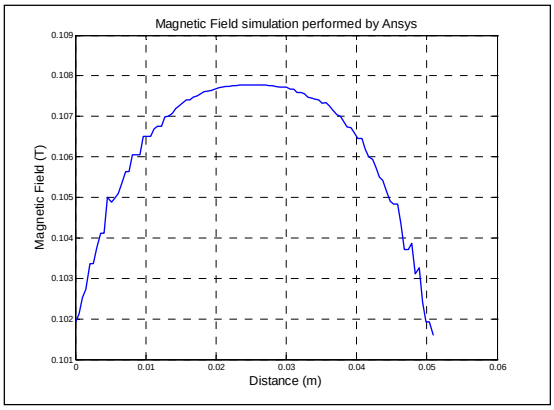

(b)= 0.5 mm

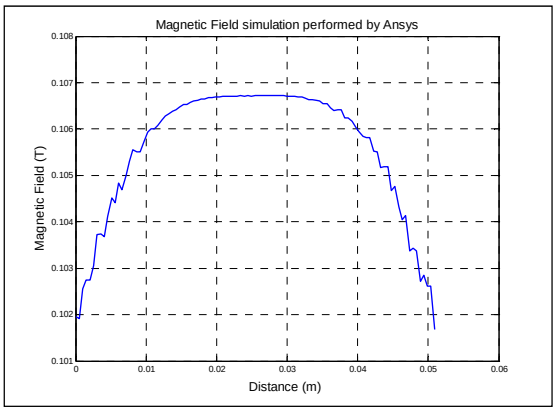

(c)= 0.9 mm

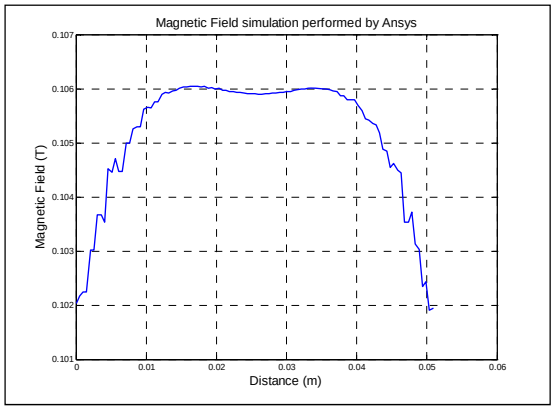

(c)= 1.3 mm

Figure 4-5: The variation of magnetic field in Z direction at different gaps.

The useful volume for NMR sample is determined from the coordinates (x,y,z) of the point where Bx is maximal. Then, the volume is calculated with the 3 coordinates that generate a variation of $\frac{\Delta B_0}{B_0}$ of 100 ppm. The Figure 4-6 shows that the volume of the homogeneous region is a function of the *esp*. The optimal value of *esp* determined by RADIA is around 0.77 mm and the useful volume is about 2640 mm^3. The volume is increased by a ratio of around 80 when the space between the two rings is improved. This is caused by the decrease of the magnetic field outside one ring is similar to the other ring. There's an optimum space between the two rings where the sum of the variations of the magnetic field outside the rings are canceled.

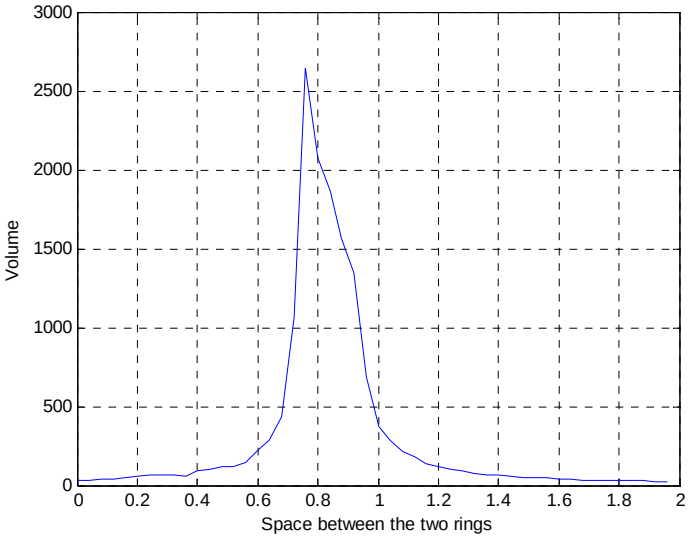

Figure 4-6: Volume of homogeneous region is a function of the gap esp.

4.3 Optimization

Although the homogeneity of magnetic field increases by adjusting the gap between the two rings, the inhomogeneity of magnetic field also comes from magnetic material (dispersion of the value of magnetization, variation of the orientation of the magnetization), errors in fabrication process and positions of the magnets in the array. These factors cannot be corrected by adjustment of *esp*. To overcome these difficulties, the shim magnets are considered to compensate the inhomogeneity of magnetic field [77][72][81]. In our case, we use eight small magnets placed inside the bore of the two rings as shown on the Figure 4-7.

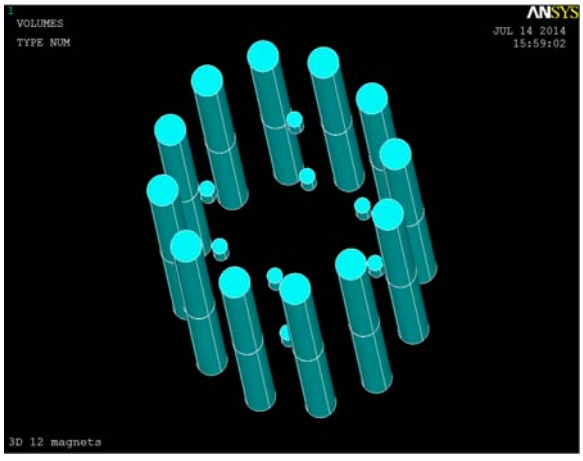

(a) With ANSYS

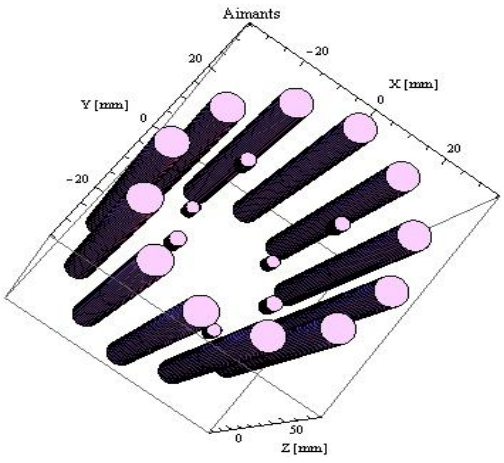

(b) With RADIA

Figure 4-7: Halbach magnets with 8 shim magnets modeled with ANSYS and RADIA.

The direction of magnetization of the shim magnets is defined as shown in Figure 4-8.

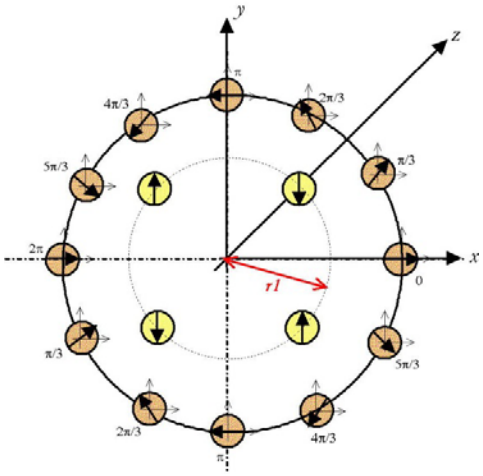

Figure 4-8: Direction of magnetization of the shim magnets.

There are three variables that need to be optimized: *esp, r1* and *dH*. The optimization objective is to determine the values for *esp, r1* and *dH* that maximized the volume for a given inhomogeneity, in our case 100 ppm. The flow chart shown in Figure 4-9 describes the optimization process implemented with the software Mathematica for the algorithm of the optimization and RADIA for the calculus of the magnetic field. To avoid the superposition of the main magnets and the shim magnets, we set the range of *r1* from 15 to 23 mm and *esp* ranging from 0.1 to 0.6 mm. The optimal value for *esp* considered here is different from the value considered before because the shim magnets modified the magnetic field.

Each step of increase of *r1* is 1 mm while correspondent value of *esp* is 0.1 mm. Each possible values of *r1* are placed in a matrix. For all these values, the magnetic field is determined and then the three coordinates x,y,z for an homogeneity lower than 100 ppm. For each value of *r1*, a value of the volume is obtained. A selection of the value of *r1* that correspond to the highest value of the volume is saved. The same process is repeated with *esp* and *dH*. After a variation of one parameter, the variation is refined around the best value previously obtained. It's very important to choose good initial condition and begin the variation of one parameter with plausible value for the others parameters. This method was preferred than the use of optimization function of Mathematica like *FindMaximum*.

The optimization objective performed by RADIA is to determine the values for *esp, r1* and *dH* that maximized the volume for a given inhomogeneity. For ANSYS, on the other hand, the

optimization objective is to determine the values for *esp, r1* and *dH* that achieve the best homogeneity of magnetic field for a given volume. The flow chart shows in figure Figure 4-10 describes the optimization process performed by ANSYS.

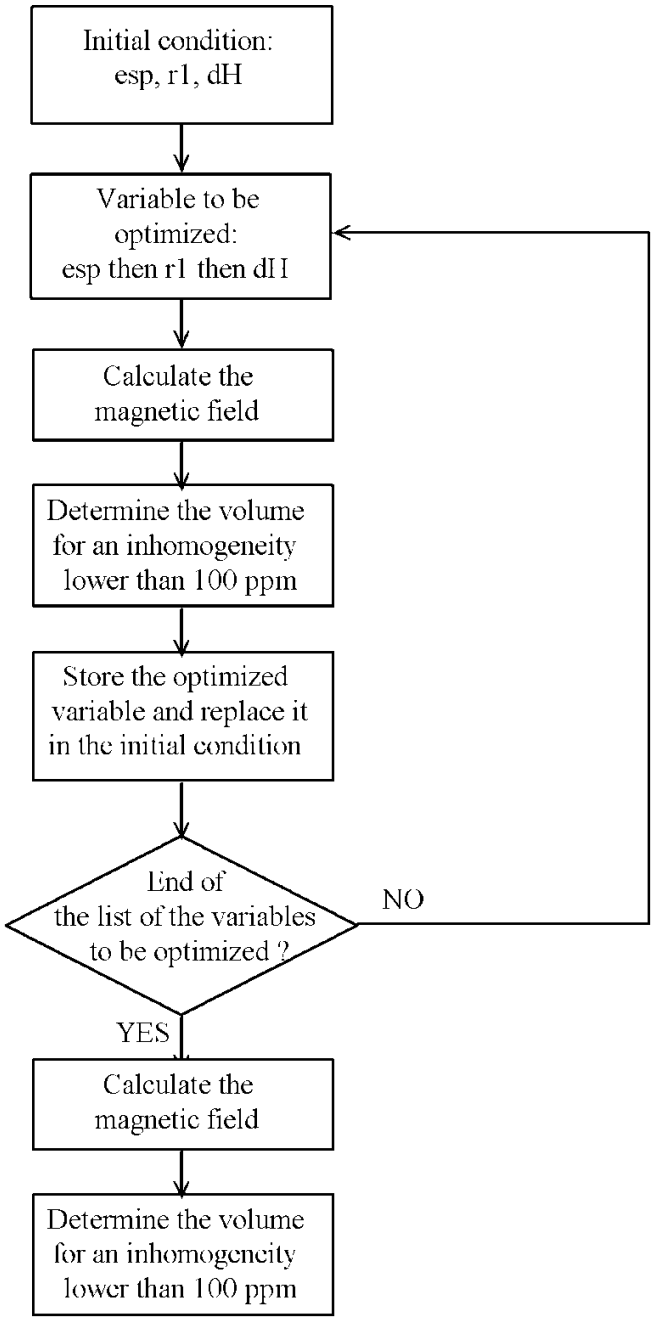

Figure 4-9: Optimum flow chart of our configuration with 24 main magnets and 8 shim magnets performed by RADIA.

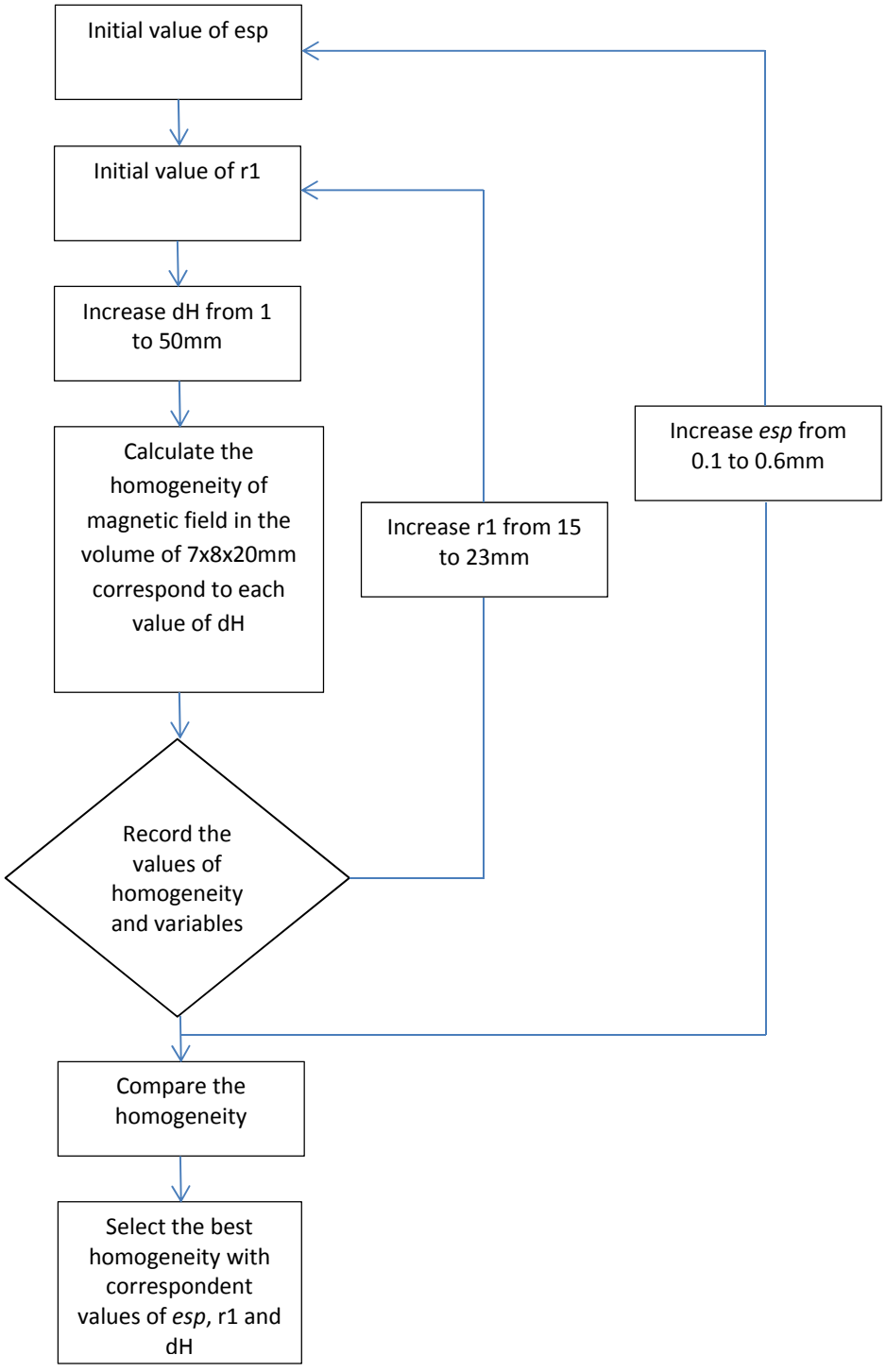

Figure 4-10: Optimum flow chart of our configuration with 24 main magnets and 8 shim magnets performed by ANSYS.

The optimum positions of shim magnets found by two softwares RADIA and ANSYS is the same. Their values are presented in the Table 4-2.

Name of the parameters	Dimensions
esp	0.2 mm
r1	20 mm
dH	26 mm

Table 4-2: Optimum positions of shim magnets.

The results of optimization give a great improvement of homogeneity, as can be seen in the Figure 4-11. It shows that the inhomogeneity of the magnetic field calculated in the region of 7 x 8 mm is 90 ppm after shim while the value before shim is 370 ppm.

The inhomogeneity of magnetic field calculated by RADIA is in good agreement with ANSYS. However, in the larger region, the results of ANSYS are always smaller than those obtained by RADIA because of the method of calculation. It can be explained that the results of RADIA is the highest value at the border of the region while that of ANSYS are the mean value for the overall region.

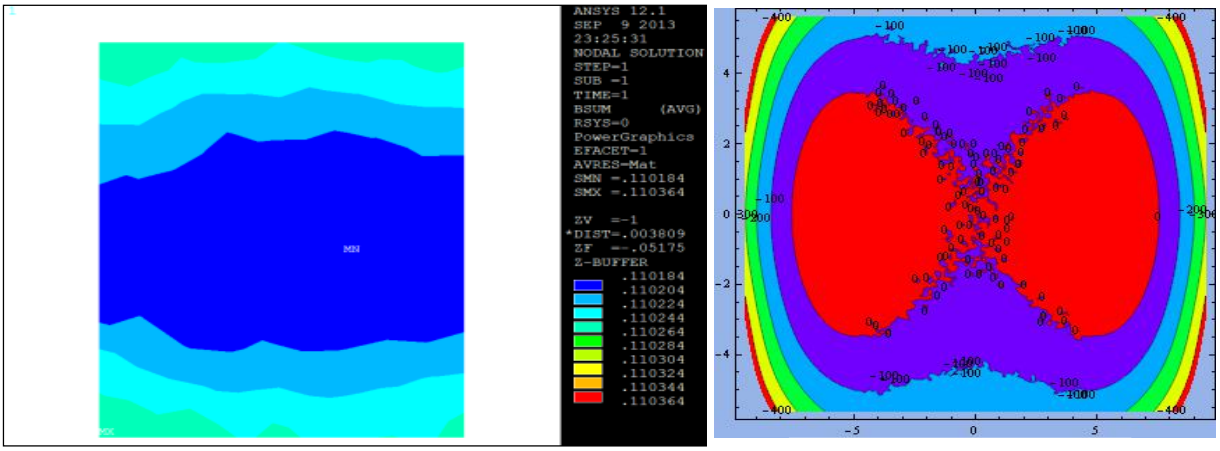

(a) Before shim (b) After shim

Figure 4-11: Magnetic field homogeneity in xOy plane and z = 0.

The Figure 4-12 shows the great improvement of homogeneity along Oz axis. The size of homogeneous region drastically increases in length from 8 mm to 25 mm. This is confirmed by the stability of the magnetic field profile of the Figure 4-13. The inhomogeneity of magnetic field in the volume of 7 x 8 x 20 mm is 230 ppm with the shim magnets in comparison to 4320 ppm in the

case without shim magnets as shown in the Figure 4-14.

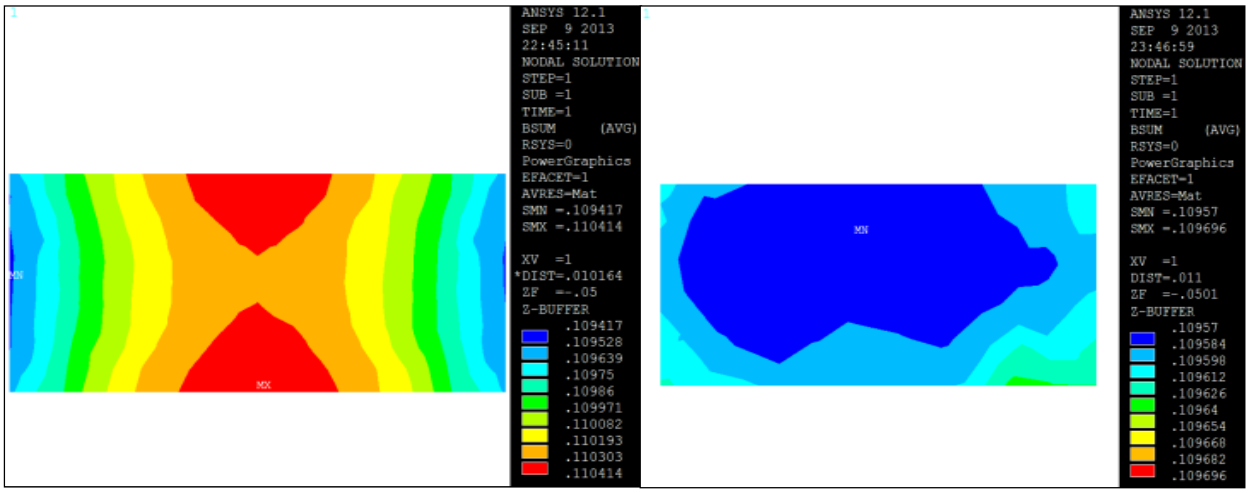

(a) Before shim (b) After shim

Figure 4-12: Magnetic field homogeneity in the region 8 x 20 mm along Oz axis.

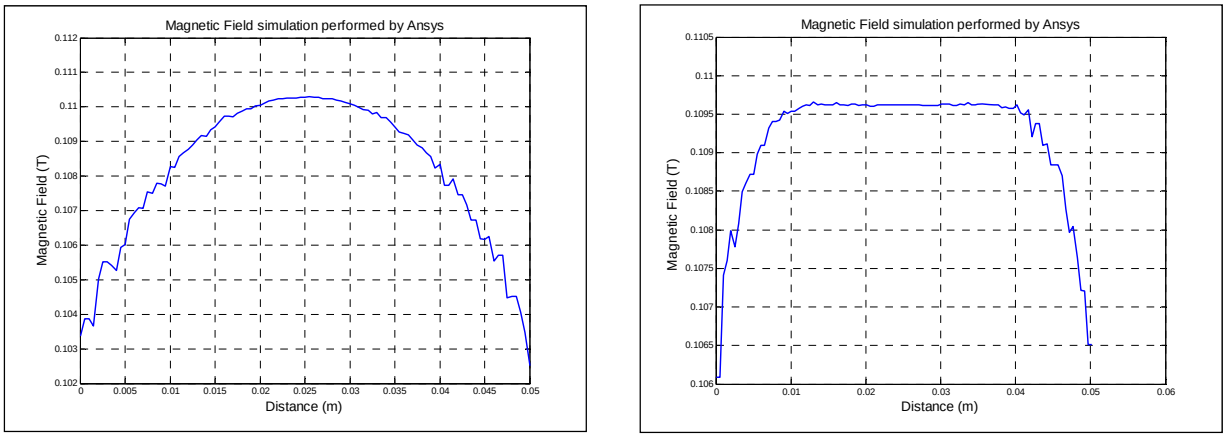

(a) Before shim with the gap *esp* = 0.9 mm (b) After shim

Figure 4-13: Magnetic field profile at the center of the center of the assembly of magnets.

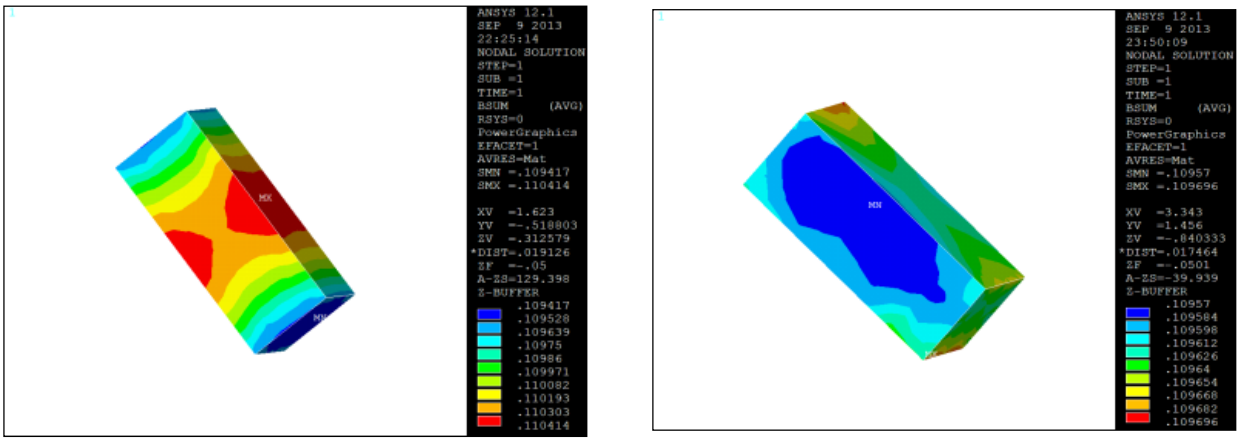

(a) Before shim (b) After shim

Figure 4-14: Magnetic field distribution in the sensitive volume 7 x 8 x 20 mm^3 in 3D.

4.4 Prototype design and experimental set up

4.4.1 Prototype design

The prototype consists of two rings of 12 magnets. These magnets are placed on a circle with a radius of 30 mm radius and insert into twelve holes of two aluminum frames. Two rings of the prototype, fixed by some screws on the aluminum frames, can slide on three rods to achieve the desired position. The highest value of the magnetic field magnets measured at the center of the frame, allow us to determine their rotation angles and to fix them by the dedicated screws as shown on Figure 4-15.

(a) Shim magnets that can move along three degrees of freedom

(b) Halbach prototype with the slide-blocks that is used to move the shim magnets in radial

Figure 4-15: View of the prototype with shim magnets

Each shim magnet shown on the Figure 4-15 is glued in a nonmagnetic cylinder. These cylinders can rotate, move along the longitudinal axis and slide along the radius of the prototype in order to find the optimal position of the shim magnets. These cylinders are placed in the holes of sliding-blocks that slide on the four apertures of an aluminum frame which is concentric with the prototype.

4.4.2 Experimental set up

The magnetic field is measured by the digital gaussmeters Hirst GM08 with the sensibility limit of 10^{-4} T in the range 0 – 0.299 T. The micropositioner Signatone S-926 is used to control the probe movement in three directions as shown in the Figure 4-16. The resolution is 254 µm per knob revolution. Matlab software carries out plotting the measurable values.

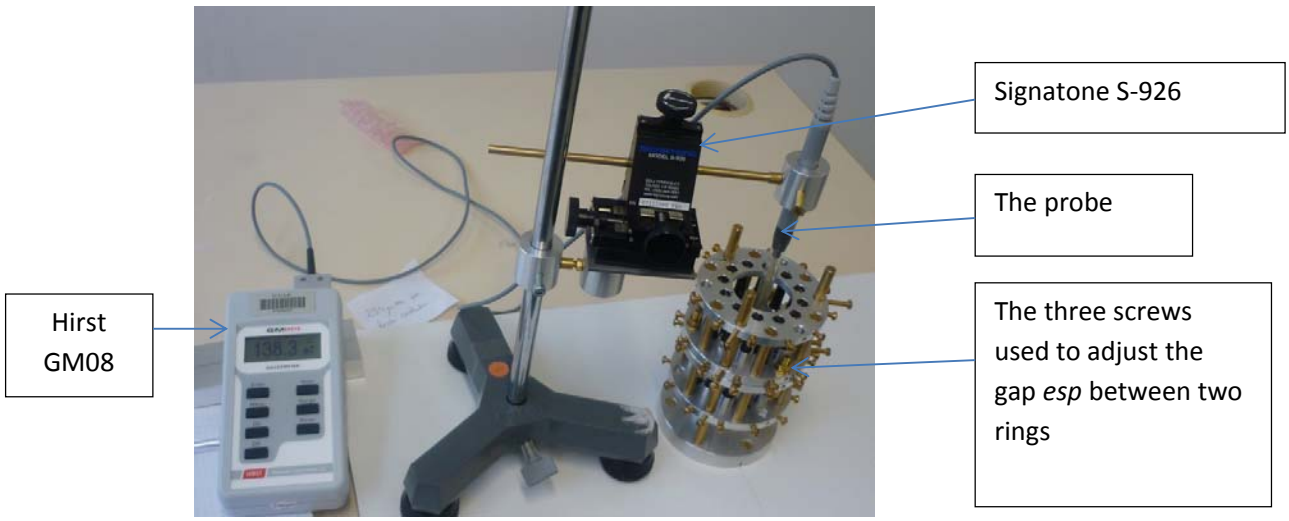

Figure 4-16: Equipment is used to measure the magnetic field of the prototype.

4.5 Measurement results

4.5.1 Before shimming measurements

To optimize the gap *esp* between two rings, at the beginning, it was set at 0mm, and was progressively increased by turning the screws on the frame of the device (Figure 4-16).

The Figure 4-17 shows the magnetic field profiles in OZ direction for four different gaps *esp* between the rings. The optimal gap is displayed in Figure 4-17-c where the magnetic strength is equal to 0.138 T remains constant for the distance of 10 mm. The shapes of the curves plotted on the Figure 6-16 are similar to those obtained by simulation on the Figure 4-5.

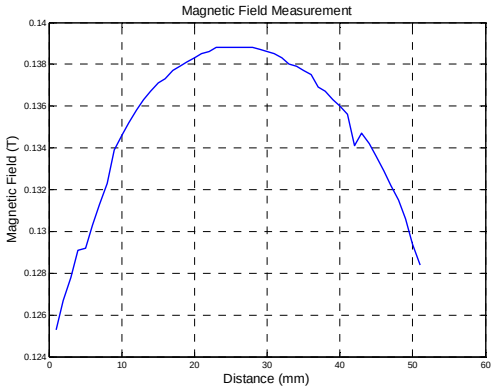

(a) esp = 0mm

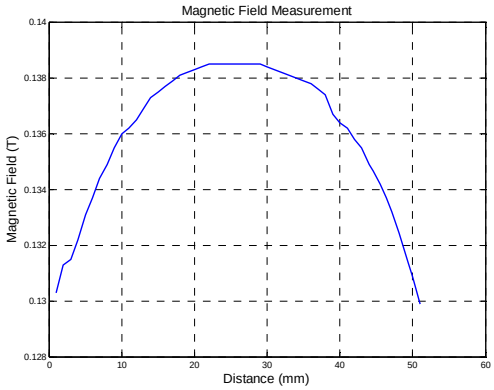

(b) esp = 1.6mm

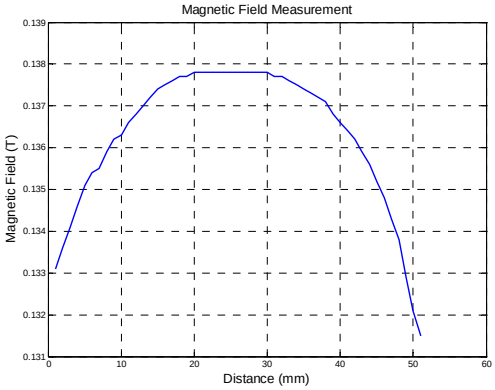

(c)esp =2.4mm

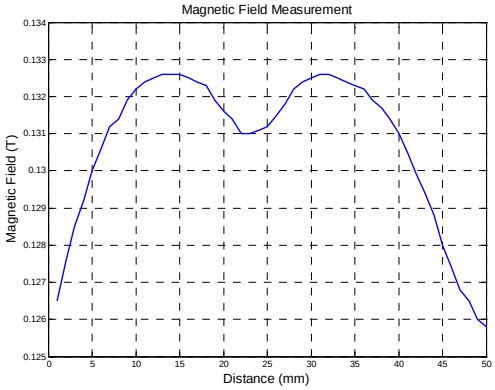

(d)esp = 6.4mm

Figure 4-17: Magnetic field profiles in OZ direction for different esp values

The magnetic field distribution shows in Figure 4-18, is measured at z = 0, in the region 6 x 6.5 mm² (xOy). In this region, the homogeneity value is respectively 1399 ppm calculated by formula (1) and 380 ppm obtained by simulation. It means that the measurable homogeneity is approximately 3.5 times worse than that simulated (Figure 4-3-b).

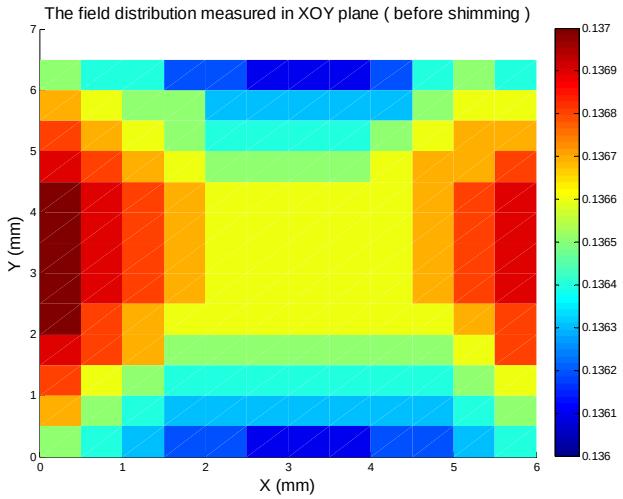

Figure 4-18: The magnetic field distribution in xOy plane obtained by measurement before shimming

Figure 4-19 shows the magnetic field distribution measurement in xOz plane in the region of 7 x 20 mm^2. In this region the homogeneity calculated by formula (4-1) is equal to 1426 ppm. This homogeneity is of 4415 ppm in the volume of 6 x 7 x 20 mm^3.The magnetic field distribution is similar to the simulation as shown in the Figure 4-4.

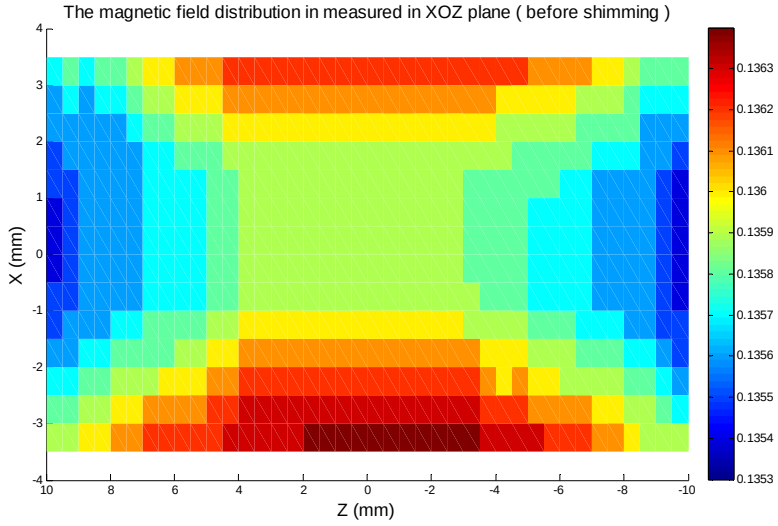

Figure 4-19: The measured magnetic field distribution in xOz plane before shimming

4.5.2 After shimming measurements

Figure 4-20 shows the improvement of the magnetic field homogeneity in xOy plane in the same region 6 x 6.5 mm^2. The homogeneity is respectively, 1399 ppm before shimming calculated by formula (4-1) and 817 ppm after shimming.

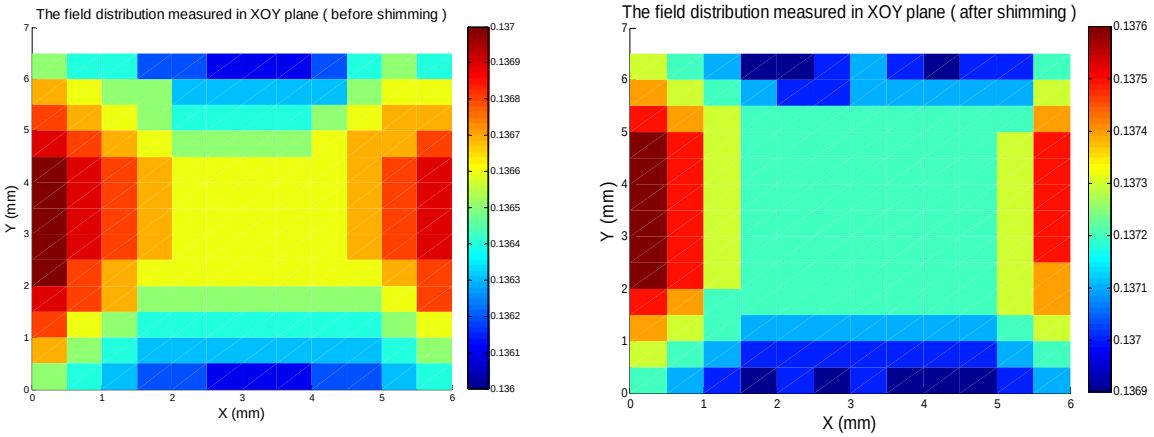

(a) Before shimming (b) After shimming

Figure 4-20: Magnetic field homogeneity at z = 0 in xOy plane

In the region of 7 x 20 mm^2 (xOz plane), the homogeneity calculated by formula (4-1) is 894 ppm while it is 1426 ppm without shim magnets. The magnetic field homogeneity with shim magnets shows in Figure 4-21, achieved in the volume 6 x 7 x 20 mm^3 is 1335 ppm in comparison to 4415 ppm obtained without shim magnets. The magnetic field homogeneity is 3.3 times. Figure 4-21 shows the improvement of the homogeneity that is approximate 5.8 times worse than simulation. The measured and simulated field distribution in xOz plane is similar as shown in the Figure 4-4.

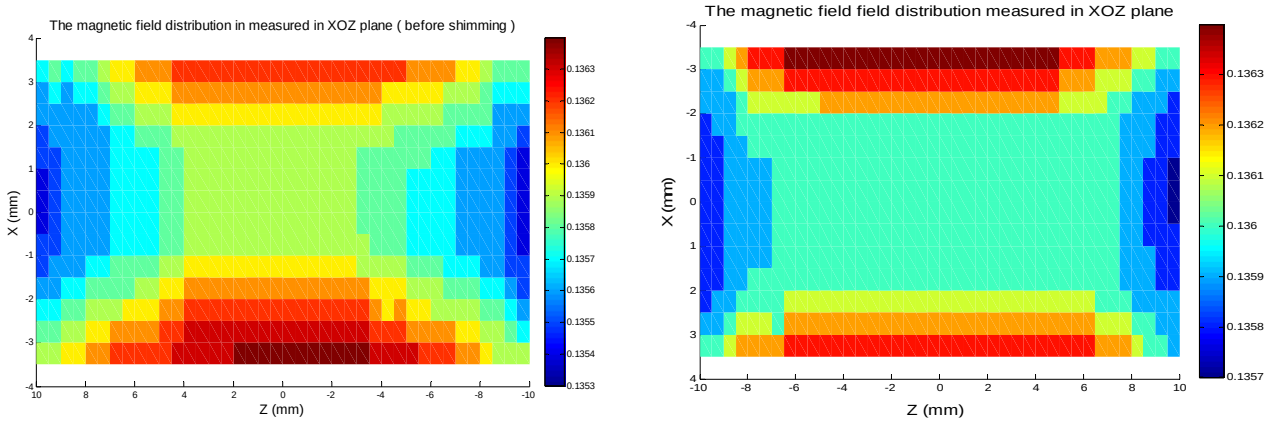

(a) Before shimming (b) After shimming

Figure 4-21: The magnetic field homogeneity in xOz plane

4.6 Discussion

The difference between the simulated and measured values of the magnetic field homogeneity is due to the poor quality of the magnets. There is a large dispersion of the magnets properties. For our prototype we selected 24 magnets among 27 having a similar magnetic field strength and the magnets 5, 22 and 23 was rejected. This was done with the measurement of the magnetic field on each tip of the magnet cylinder. Table 4-3 shows the value of B_1 and B_2 for 27 magnets and the misalignment angle α. B_1 and B_2 are respectively the magnetic field in the vicinity of the two faces of the magnet cylinder as shown on the Figure 4-22 **Erreur ! Source du renvoi introuvable.**. The average value of the magnetic field is around 27.3 mT. The misalignment angle represents the error of orientation of the radial direction of the magnetic field on each face. In ideal case, this angle value is zero but for some magnets this value can reach 17 degrees and the consequence, is an error of homogeneity of the magnetic field.

Magnet	1	2	3	4	5	6	7	8	9	10
B_1 (mT)	27.3	27.2	27.3	27.2	27.3	27.2	27.1	27.0	26.9	27.0
B_2 (mT)	27.2	27.1	27.5	27.1	27.0	27.1	27.2	26.9	27.0	27.2
α (degree)	0	0	8	9	17	8	0	0	0	12
Magnet	11	12	13	14	15	16	17	18	19	20
B_1 (mT)	27.4	27.2	27.2	27.2	27.3	27.3	27.3	27.4	27.4	27.4
B_2 (mT)	27.5	27.0	27.2	27.4	27.4	27.3	27.5	27.4	27.5	27.2
α (degree)	0	10	0	12	0	0	12	0	0	8
Magnet	21	22	23	24	25	26	27	28	29	30
B_1 (mT)	27.3	27.2	27.6	27.3	27.4	27.4	27.3			
B_2 (mT)	27.3	27.5	27.5	27.4	27.3	27.5	27.4			
α (degree)	0	16	4	6	9	7	8			

Table 4-3: Magnetic field and misalignment angle measured on each tip of the 27 magnets.

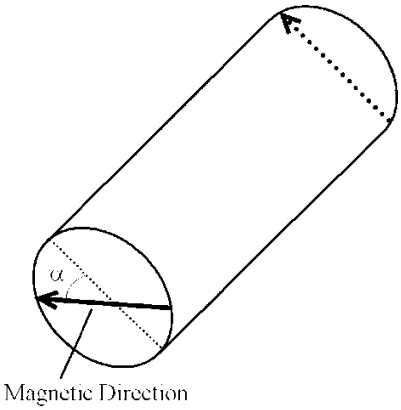

(a) Magnet cylinder with B_1 and B_2 the magnetic field in the vicinity of its two faces and the misalignment angle α.

(b) Picture of Magnet cylinder.

Figure 4-22: A prototype of Magnet cylinder

In the following, we will study the impact of the error of the misalignment of magnetic directions and the reducing of the homogeneity. During the simulation, an angle error of 3 degrees of the magnetic directions for four magnets is considered as shown on the Figure 4-23.

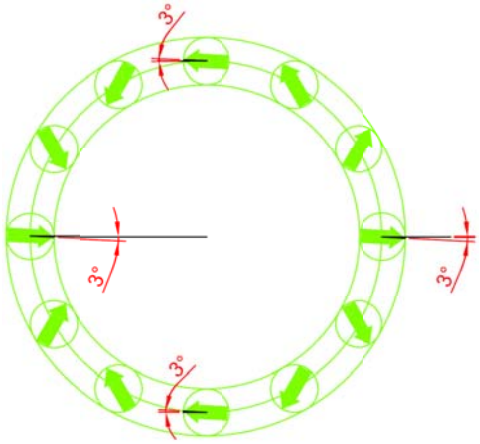

Figure 4-23: Misalignment of the magnetic direction for four magnets

The results of simulation show that the inhomogeneity of magnetic field drastically increases to 2750 ppm in the region of 6 x 6.5 mm^3 (xOz plane) in comparison to 380 ppm, the value without misalignment error. As shown on the Figure 4-24, the magnetic field distribution is found to be similar to the measurement.

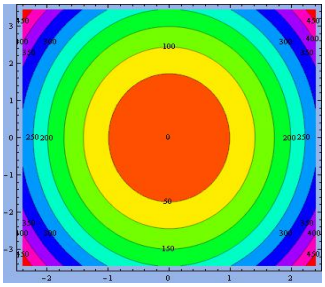

(a) Simulation without misalignment error of the direction of the magnetic field

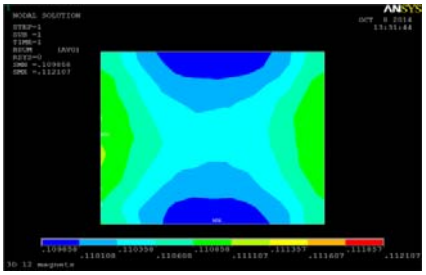

(b) Simulation with 3 degree misalignment error

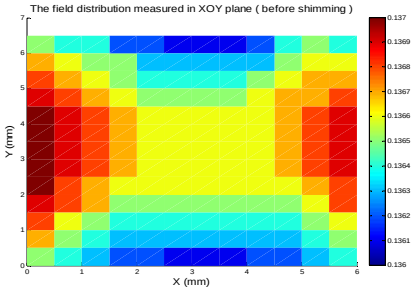

(c) Field distribution measurement of the prototype

Figure 4-24: The magnetic field distribution in xOz plane for ideal case and with error of misalignment of the direction of the magnetic field

4.7 Solution to correct the misalignment of magnetic directions

4.7.1 Modeling

In the discussion part, we mentioned about the influence of misalignment of magnetic directions on the homogeneity. In order to correct this error, we divide the long magnet (50mm) into five small magnets. The diameter and length of each magnet are respectively 8 and 10mm. These magnets are placed in an aluminum cylinder to constitute a magnet with 8mm of diameter and length of 50mm. Such magnets can be rotated in cylinder so that their magnetic directions are in alignment with those of adjacent magnets as in the Figure 4-25.

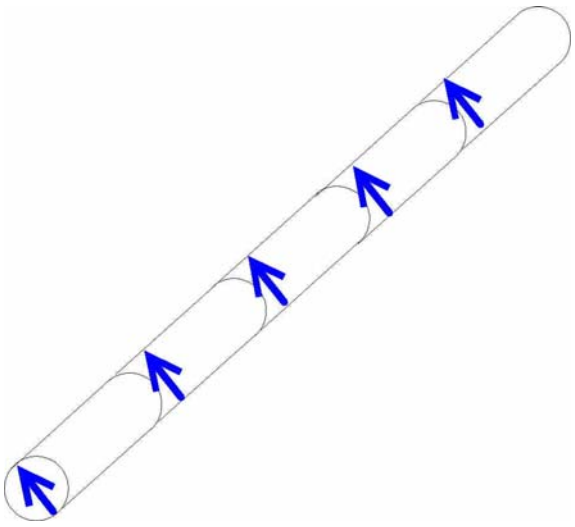

Figure 4-25: The five small magnets are placed in an aluminum cylinder to constitute a long magnet

With the new configuration, the magnetic field strength and homogeneity need to be re-

simulated to see whether they change or not. The configuration with divided magnets is modeled by ANSYS shown on Figure 4-26. The properties of small magnets are same to that of long magnet.

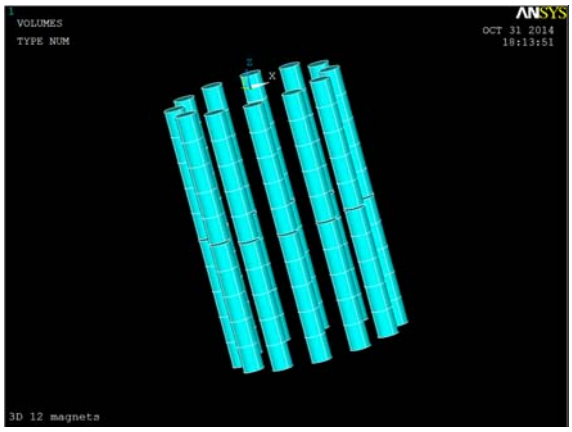

Figure 4-26: The configuration is constituted by small magnets

4.7.2 Results of simulation

4.7.2.1 Before shimming

With the gap esp=0mm, the magnetic field strength does not change in comparison to the case of long magnets with 0.11T. The magnetic profile (Figure 4-27-a) represents the variation of the magnetic field B_0 along the Ox axis; the value of the magnetic field is almost constant for 1.8mm < x < 4.2mm. In the rectangle region of 5 x 6.4mm (Figure 4-27-b), the homogeneity calculated by formula (4-1) is 326ppm in comparison to 380ppm of long magnets.

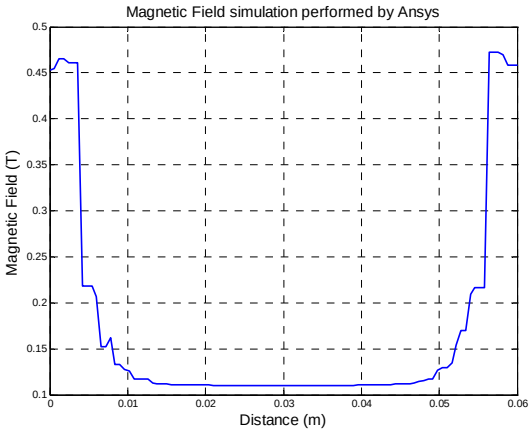

(a) Magnetic field varies in X direction

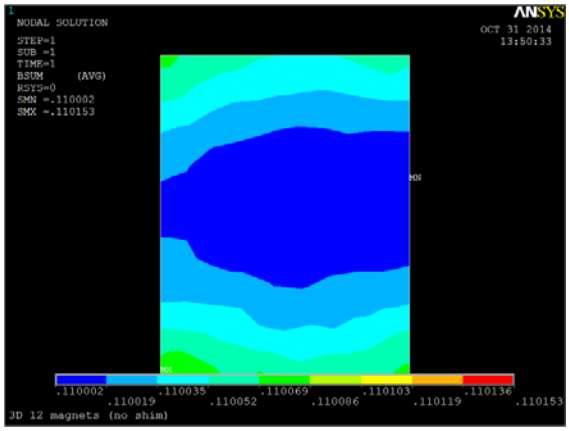

(b) Magnetic field distribution in XOY plane (5 x 6.4mm)

Figure 4-27: The variation of magnetic field B_x versus X and Y

The Figure 4-28 shows the variation of magnetic field in XOZ plane. In the region of 5 x 6.4mm, the homogeneity is 230ppm while the case of long magnets is 200ppm. The magnetic field distribution is found to be similar shape to the Figure 4-4.

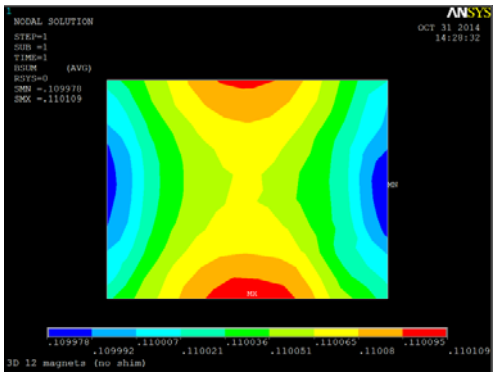

Figure 4-28: The field distribution in the rectangle region of 5 x 6.4mm (XOZ plane)

The Figure 4-29 shows the dependence of magnetic field homogeneity on the gap esp. In this case, the optimal gap is also 0.9mm as displayed in Figure 4-29-c

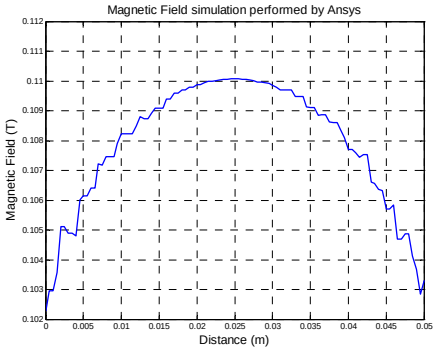

(a) esp = 0mm

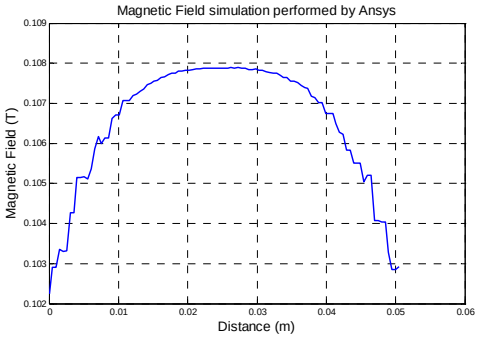

(b) esp = 0.5mm

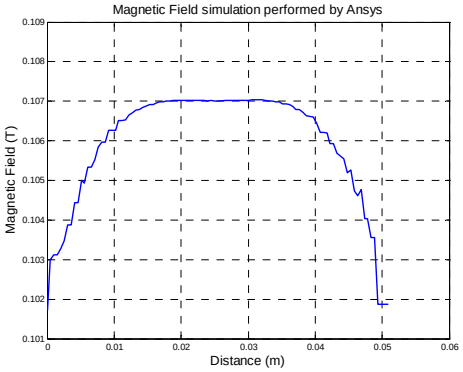

(c) esp = 0.9mm

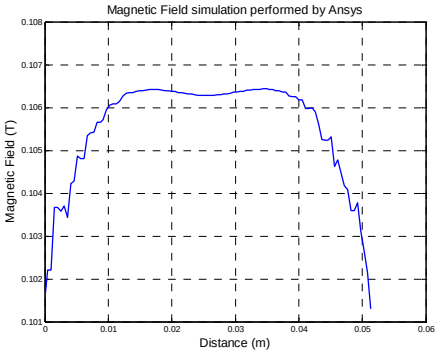

(d) esp = 1.3mm

Figure 4-29: The change of magnetic field profile in Z direction at four distance of gap esp

4.7.2.2 After shimming

In this case, we also use eight small shim magnets with the same characteristics as the shim magnets used in the configuration with the long magnets. This configuration with shim magnets is shown on the Figure 4-30.

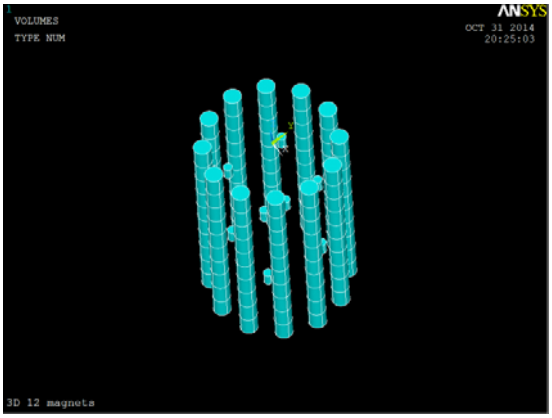

Figure 4-30: The configuration and its shim magnets is modeled by ANSYS.

The process of optimization used in this case follows the flow chart as in the Figure 4-10. The optimal geometric parameters are presented in Table 4-4.

Name of the parameters	Dimensions
esp	0.2 mm
r1	20 mm
dH	24.5 mm

Table 4-4: The optimum positions of the shim magnets

In the region of 7 x 8mm (XOY), the magnetic field homogeneity calculated by formula (4-1) is 100pmm. It slightly increases in comparison to 90ppm of the configuration of long magnets. In Z direction, the homogeneity significantly increases from 10mm (Figure 4-29-c) to 20mm (Figure 4-31-a). This increase is confirmed by the field map (Figure 4-31-b).

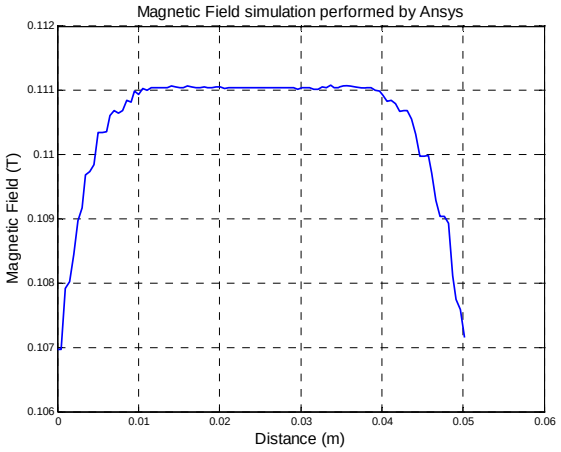

(a) The magnetic field profile in Z direction after shimming

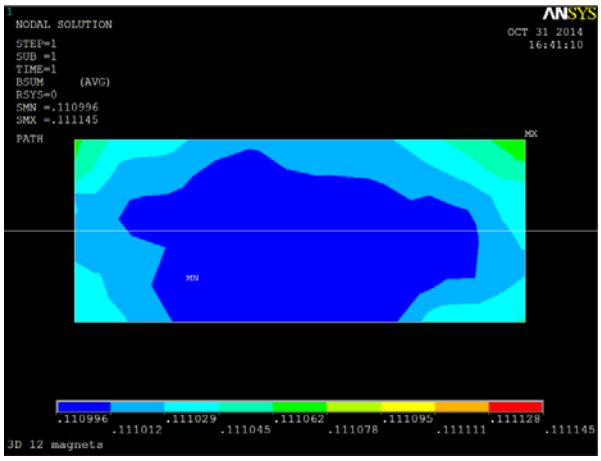

(b) The magnetic field distribution in the region of 7 x 20mm (XOZ) after shimming

Figure 4-31: The variation of magnetic field in XOZ plane

The homogeneity of magnetic field in the volume of 7 x 8 x 20 mm^3 after shimming is 254ppm while the correspondent value of configuration with long magnets is 230ppm. The Figure 4-32 shows the distribution of magnetic field in this volume.

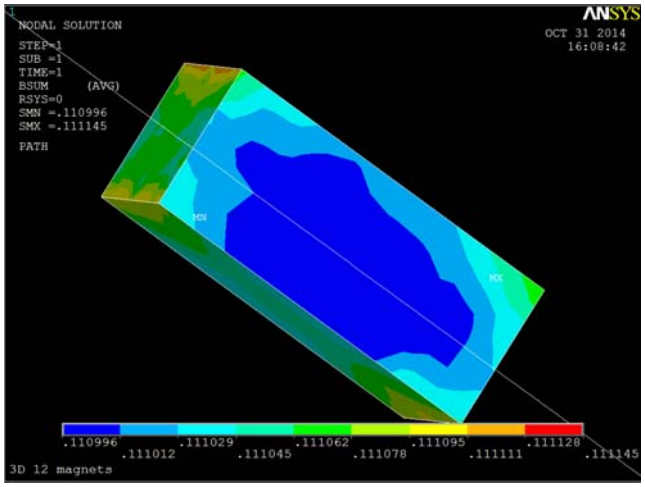

Figure 4-32: Magnetic field distribution in the volume of 7 x 8 x 20 mm^3

4.7.3 Evaluation of the magnetic force between the magnets

Because the long magnets are divided into five small magnets, the magnetic force of these magnets causes the difficulty for the assembly process. Therefore, it is necessary to determine the magnitude and direction of this force. The long magnet with 8mm of diameter and length of 50mm divided into five magnets with length of 10mm for each one is modeled by ANSYS (Figure 4-33).

The magnetic direction of these magnets is assigned in Y direction.

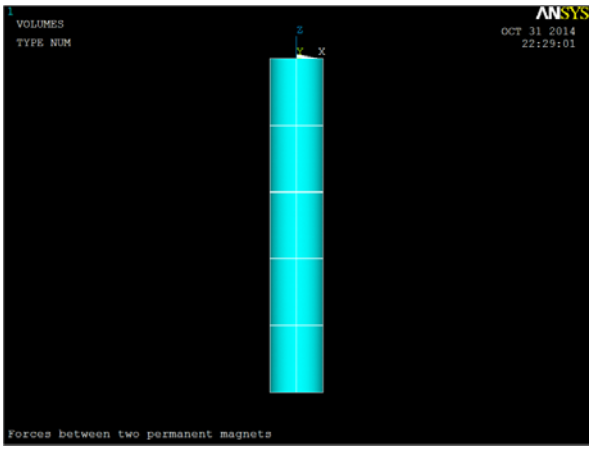

Figure 4-33: Long magnet is divided into five magnets

The result of simulation shows that the magnitude of magnetic force distribution in the magnets is around 0.03kN. The magnetic force direction of magnets turns about the longitudinal of magnets (Z direction) as shown in the Figure 4-34.

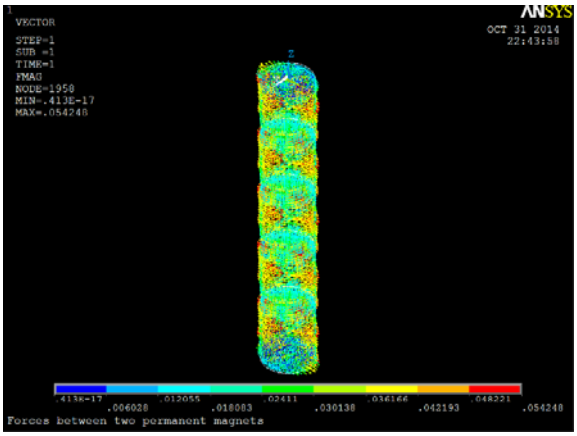

Figure 4-34: Magnetic force distribution in the magnets

4.8 Conclusion

The study presented herein depicts two methods of simulation and the main measurements results of a light weight NMR portable Halbach type. We described the optimization process of this permanent magnet designed with two rings of 12 magnets each one, that provide a magnetic field B_0 around 0.1 T. The simulation results have been published in [108]. The study describes the used based on the RADIA software process, for calculate and simulate the magnetic field B_0 and its homogeneity. We verified also those results with the finite element software ANSYS multiphysics. The obtained results with the two softwares are in good agreement. Based on the

software analysis, we simulated the homogeneity of magnetic field and optimized the gap *esp* of the two consecutive rings to increase the size of the homogeneous region. The optimum gap length is around *esp*= 0.8 mm. The measurement of the magnetic field profile for different values of the gap *esp* between the two rings give a similar value of the optimal gap.

To compensate for the magnetic field inhomogeneity caused by the errors of fabrication process and the dispersion of the magnetic properties of the magnets, we used eight small shim magnets placed at the center of the device. By optimizing their position, the homogeneity had been significantly improved. The results of optimization show that the homogeneity for a given volume (7 x 8 x 20 mm^3) is improved 18 times in comparison to the same configuration without shim magnets. Thus the value of the homogeneity decreases from 4320 ppm to 230 ppm.

For a given volume of 6 x 7 x 20 mm^3, the measurement of the magnetic field variation, shows the same homogeneity improvement, using the shim magnets. Thus the homogeneity is of 1335 ppm while it was of 4415 ppm for the case without shim magnets. The magnetic field homogeneity was enhanced of a 3.3 factor. However, there is still a difference between the simulation and the measurement, which could be explained by the poor quality of the magnets. For each used magnets for the NMR device design, the magnetic field on the tip of the cylindrical magnet and the misalignment angle of the radial magnetic field were measured. The misalignment angle could be as high as 17 degrees. The simulations with some misalignment angle error of 3 degree on four magnets were performed and the same shape of the magnetic field distribution was obtained. Thus we attribute the difference between the simulation and the measurement to the misalignment angle of the magnets.

We also propose a solution to correct the misalignment of magnetic directions. The long magnets are divided into five magnets placed in an aluminum cylinder. These five magnets can rotate in the cylinder so that their magnetic directions are parallel to each other. The magnetic field strength and homogeneity have been re-simulated. The results of simulation show that the magnetic field strength does not change. The magnetic field homogeneity slightly changes in the same volume of 7 x 8 x 20mm^3 with 230ppm and 254ppm respectively. The difference is 10.4%. It can be accepted. The magnetic force of magnets for the assembly process has been simulated. The magnitude of magnetic force is determined approximately 0.03N and its direction turns about the longitudinal of the magnets. Despite these results, there's a good agreement between the simulation results and the measurement.

Chapter 5

Modeling and design of Mandhalas configuration Magnet for Biomedical and Agroalimentary applications

Summary:

- **Introduction**
- **Modeling and simulation**
- **Improvement of magnetic field homogeneity**
- **Prototype design**
- **Discussion and conclusions**

Chapter V: Modeling and design of Mandhalas configuration for biomedical and agro-alimentary applications

5.1 Introduction

In 1979, Klaus Halbach proposed a novel type of permanent magnet [63] constructed entirely by rare earth permanent magnet material. The initial purpose of this type called Halbach ring was not used for the NMR applications. The Halbach ring reinforces the field in its center and cancels the field outside of its structure. This structure provides a generous volume for sample positioning (large bore/magnet size ration) and generates the field in transverse plane which allows the use of sensitive solenoid radio frequency coil to detect the NMR signal. Due to these prominent features, it is widely used for the NMR applications. However, the ideal Halbach ring is a continuously polarized material as shown in the Figure 5-1-a. It is hard to polarize exactly the direction of magnetization of material in practice in comparison to theory. In order to overcome this difficulty, the Halbach ring is divided into the same magnet blocks or replaced by the identical magnets in number n. To achieve the highest homogeneity of magnetic field in the center, the angle between each block is $\alpha = \frac{2\pi}{n}$ and the magnetizing direction of the next adjacent magnet is set by an angle $\beta = \frac{4\pi}{n}$ as the principle of Halbach ring.

Based on this idea, the Halbach structure with discrete magnets abbreviated Mandhalas (Magnet Arrangement for Novel Discrete Halbach Layout) configuration (Figure 5-1-b, Figure 5-1-c) was proposed by Raich and Blümler [74]. It is based on an arrangement of identical bar magnets, described by the analytical equations reported in literature [79]. These magnets arranged on a restricted space on a circle to obtain the strongest magnetic field and the highest homogeneity in the center. There are some prototypes of Mandhalas have been published in different magnet shapes such as squares [74][109], polygons [79][80]. These types of configuration are not only inherits the advantages of Halbalch ring but are also easy to assembly, cheap to produce because they are constructed from identical bar magnets.

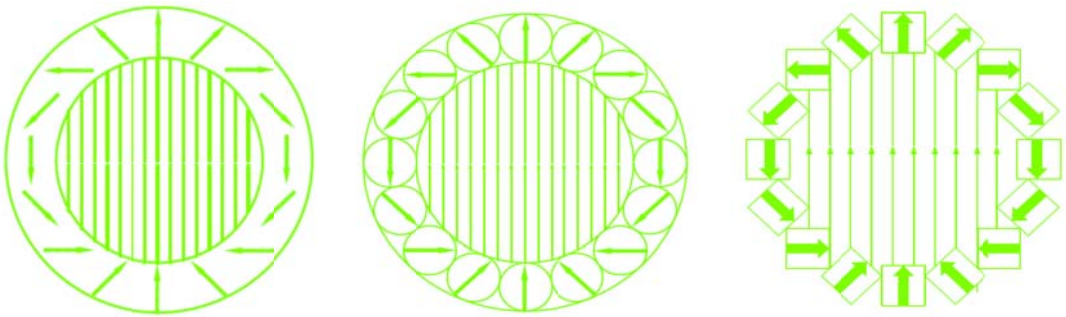

Figure 5-1: Halbach ring and two kinds of Mandhalas. (a) Halbach ring. (b) Mandhalas with cylindrical magnets. (c) Mandhalas with cube magnets

The advantages of NMR Mandhalas mentioned above motivate us to choose them for construction of our prototype. In this work, based on the principle design of Mandhalas proposed by [74][79], we describe the modeling of NMR portable Mandhalas Magnets built from, respectively n= 4, 8, 16, and 32 identical magnets, generating magnetic field from 0.13 T to 0.74T. The performance factors are calculated to compare the properties of Mandhalas built from cylindrical and square magnets.

The three criteria chosen for evaluation of the NMR devices are mass, field strength and magnetic field homogeneity. Based on these criteria and the results of 2D simulations, one of them is selected for three dimensions (3D) simulations. The Finite Element software ANSYS multiphysics was chosen for simulation and modeling. It allows us to study different configurations with different shape of magnets; rings number and optimize the gap between two consecutive rings. In order to compensate the field decay in the longitudinal axis, two rings of shim magnets are placed inside the bore of configuration. By optimizing the position of these rings, the homogeneity of magnetic field significantly increases with 3.5 times in comparison to before shim.

This approach lead us to reach an optimum configuration consist of two main rings placed in alignment with 16 cylindrical magnets for each ring and two shim rings with 8 magnets for each one. The configuration has the length of 300 mm and 70 mm diameter in use separated by a gap of 0.5 mm. The total weight is approximate 20 kg. This mobile magnet generates a magnetic field B_0 strength about 0.32 T and the homogeneity estimated 96 ppm in transverse plane (40 mm diameter), 178 ppm in the large cylindrical sensitive volume (40 mm diameter, 50 mm length).

5.2 Modeling and simulation

5.2.1 Modeling

The basic concept of a Mandhalas is described by [74],[79] and the geometric parameters illustrated on the Figure 5-2. To precisely calculate the geometry of magnet arrangement, two parameters are predetermined: Radius of the ring r and the number of magnets n as shown in the Figure 5-2-a,b.

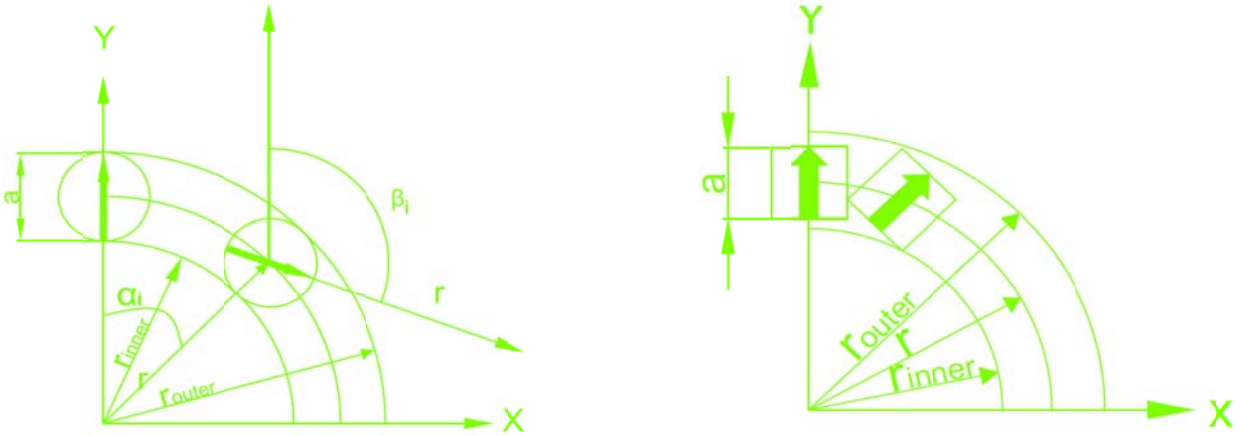

(a) Parameters of cylindrical magnets (b) Parameters of square magnets

Figure 5-2: Geometric parameter of Mandhalas in circle and square shape magnets.

In this figures:

- a: diameter of cylindrical shape magnets, width of square magnets.
- r_{inner}: the inner radius of configuration.
- r_{outer}: the outer radius of configuration.
- $\alpha_i = \frac{2\pi i}{n}$, $\beta_i = \frac{4\pi i}{n}$, n number of magnets and i ranges from 1 to n - 1.
- r: distance from center of configuration to center of magnets.

The geometric parameters of magnets arrangement are calculated by formulas in the Table 5-1[79]:

Parameter	Circles	Squares
r_{outer}	$r(1+\sin(\frac{\pi}{n})$	$r(1+\sqrt{2}\theta(n))$
r_{inner}	$r(1-\sin(\frac{\pi}{n})$	$r(1-\sqrt{2}\theta(n))$
a	$2rsin(\frac{\pi}{n})$	$2r\theta(n)$

Table 5-1: The formulas use to calculate the geometric parameters.

Where:

$$\boldsymbol{\theta(n) = \frac{\cos\left(\frac{2\pi}{n}\right)-\sin\left(\frac{2\pi}{n}\right)-\sqrt{2}\sin\left(\frac{\pi}{4}-\frac{4\pi}{n}\right)}{2\cos\left(\frac{\pi}{4}-\frac{4\pi}{n}\right)+\sqrt{2}}} \quad (5\text{-}1)$$

5.2.2 Simulation

5.2.2.1 2-D simulation

In order to simulate and calculate the field strength and the homogeneity of magnetic field, the region of interest (ROI) in which the sample is detected need to be defined as it shows in the Figure 5-3.

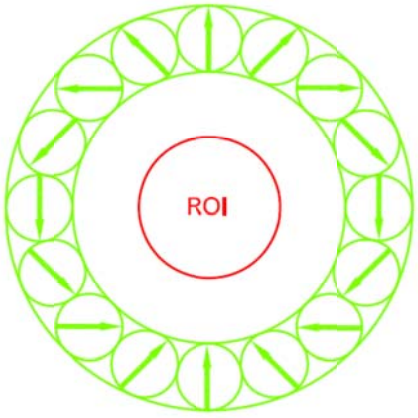

Figure 5-3: Region of interest (ROI), with radius of 25mm.

The number of mesh nodes in ROI was turned out for simulation and calculation of the homogeneity and the magnetic field respectively. The homogeneity and the magnetic field strength can be calculated by formulas (4-1) and (5-2):

$$\overline{\boldsymbol{B}} = \frac{\sum_i^n \boldsymbol{B_i}}{\boldsymbol{n}} \quad (5\text{-}2)$$

Where:

- B_i is the value of magnetic field varying in ROI.
- n is the number of mesh nodes in ROI.
- $\overline{B}$ is the mean value of magnetic field in ROI.

Four Mandhalas configurations made from n = 4, 8, 16, 32 in circle and square magnets are selected to simulate and calculate the homogeneity and field strength in 2D. For the special application, the inner radius (r_{inner}) of 50 mm was chosen. From 2D simulation, the properties of these configurations are compared together, then, we chose the best one for building prototype. The Figure 5-4-a, b, c, d show their directions of magnetization.

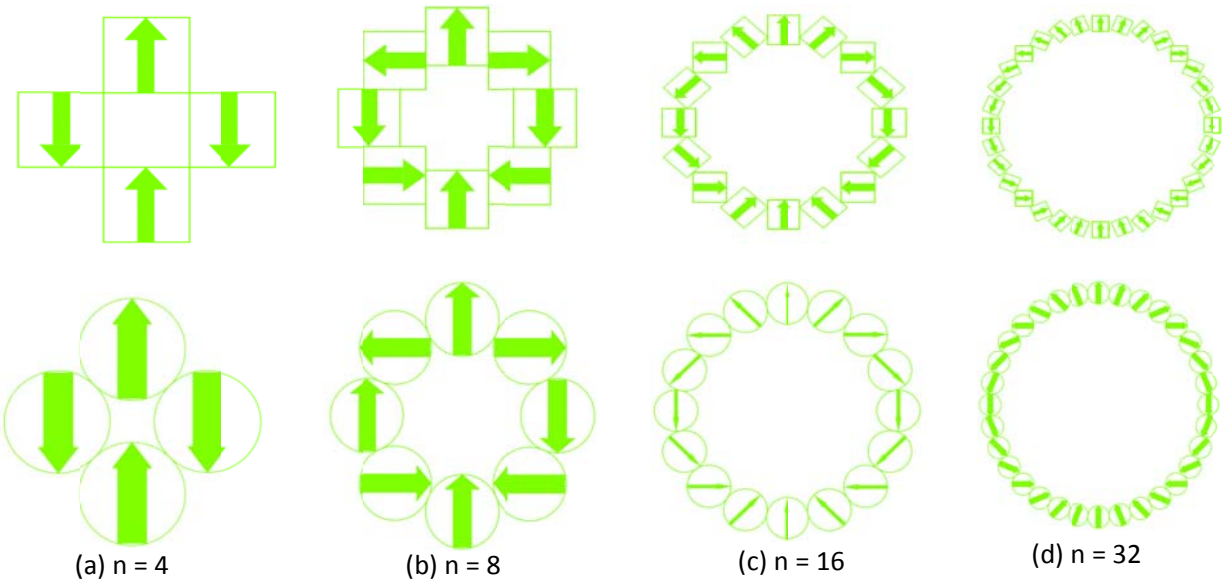

Figure 5-4: The direction of magnetization of four Mandhalas in circle and square magnets.

In order to compare our results, in the case of square shapes, to those obtained by Blümler *and coauthors* [74], for the 2D simulations, we choose the magnetic material FeNdB-37 (permeability μ = 1.049, coercively Hc = 911 kA/m).

The magnetic flux density simulated in 2D is shown on the Figure 5-5 and the direction of B_0 is defined in OY direction. The magnetic field concentrates in the center of Mandhalas and cancel in their outside.

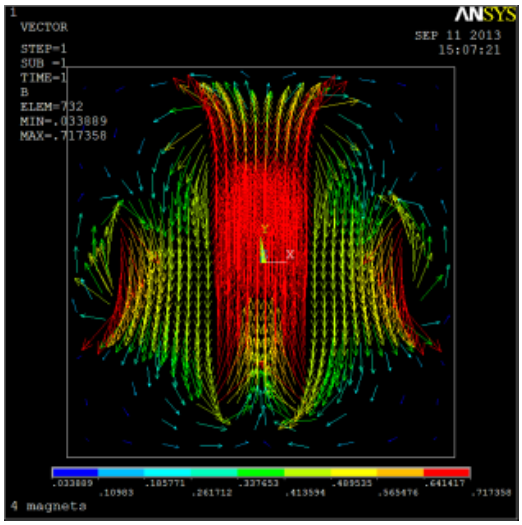

(a) n= 4

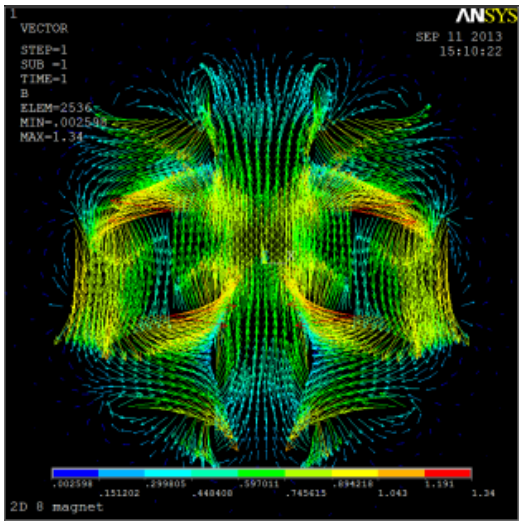

(b) n= 8

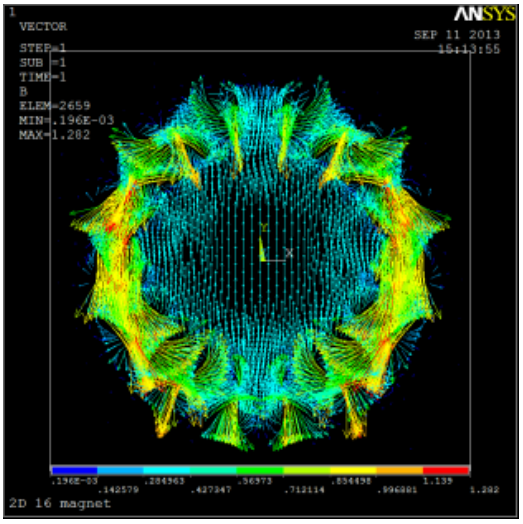

(c) n= 16

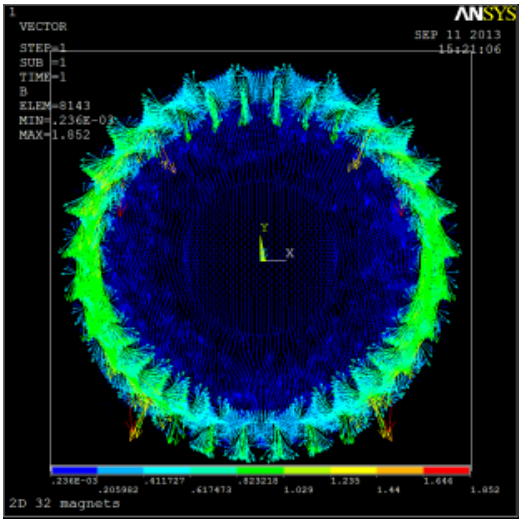

(d) n= 32

Figure 5-5: 2-D simulation with Mandhalas is made from cube magnets (vector plot).

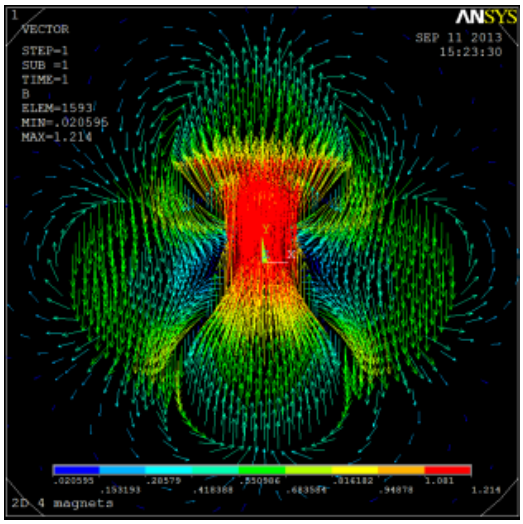

(a) n= 4

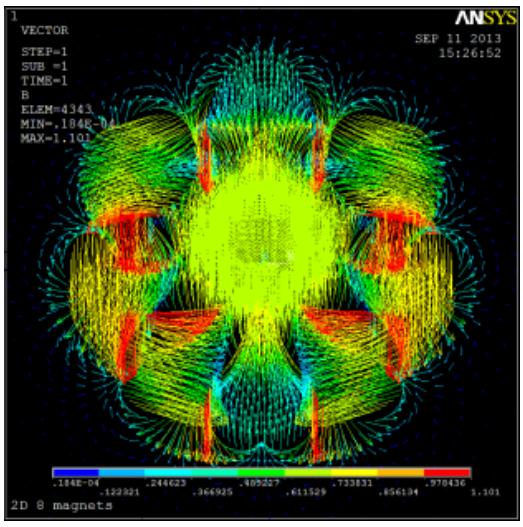

(b) n= 8

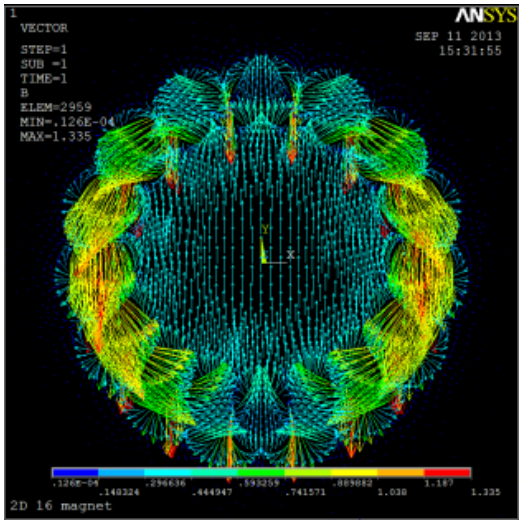

(c) n= 16

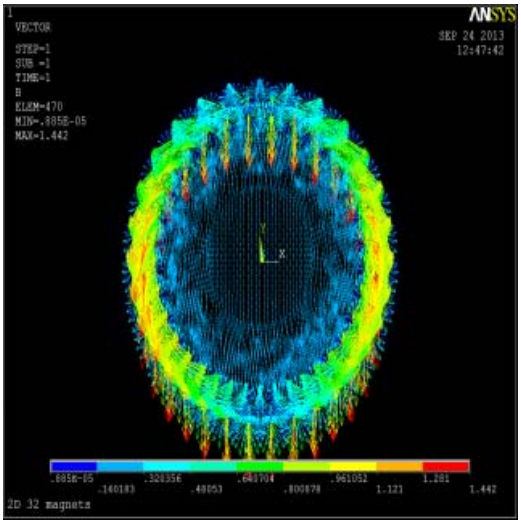

(d) n= 32

Figure 5-6: 2-D simulation with Mandhalas is made from cylindrical magnets (vector plot).

The Table 5-2 shows the summarization of 2D simulation results. The 2D simulation results obtained from Mandhalas made by square magnets are quite similar with those of reported by Blümer *et al* [74] both in magnetic field and homogeneity.

n	Squares (mm)		Circles (mm)		B(T)		Homogeneity* (ppm)		Weight (kg)	
	a	r	a	r	Squares	Circles	Squares	Circles	Squares	Circles
4	100	100	241.42	170.71	0.7014	1.1705	727	887456	90.24	412
8	70.71	100	61.99	80.99	0.7475	0.6853	3517	164	90.24	54
16	20.43	64.44	24.23	62.11	0.3011	0.3553	857	23	15.06	16.63
32	8.3	55.9	10.86	55.43	0.1348	0.1795	110	7	5.07	6.68

Table 5-2: The summary results of 2D simulations and geometric calculations.

*: The homogeneity is calculated in the region of radius 25mm.

The weights of Mandhalas are calculated by formula 5-3:

$$\mathbf{Weight(kg) = V.m.I} \tag{5-3}$$

Where:

- V is the volume of magnet (the length L=300mm).
- m is the mass density (mass density of material $\rho = 7{,}52 \frac{\text{g}}{\text{cm}^3}$)
- I is the number of magnet.

To compare the performance of Mandhalas in circle and square magnets, three coefficients proposed by H. Raich and P. Blümler [74] are defined. Then, the field strength related to homogeneity, mass and NMR sensitivity are calculated by formulas 5-4, 5-5 and 5-6 respectively.

$$\boldsymbol{f_B = \frac{\overline{B}}{\Delta B}} \tag{5-4}$$

$$\boldsymbol{f_A = \frac{\overline{B}}{\Delta B.A}} \tag{5-5}$$

$$\boldsymbol{f_\omega = \frac{\omega^{\frac{7}{4}}}{\Delta B.A} = \frac{(\gamma \overline{B})^{\frac{7}{4}}}{\Delta B.A}} \tag{5-6}$$

Where:

- $\overline{B}$ is the mean magnetic field strength value in ROI.
- ΔB is the homogeneity in ROI.
- γ is the gyromagnetic ratio.
- A is total areas of magnets.

Based on these factors, the Mandhalas made from circle magnets is better than that made from square magnets, except the case of n = 4. Although the case of n = 32 have a good homogeneity and light weight, its static magnetic field is quite small. On the other hand, n = 4 achieves a high magnetic field, its homogeneity and weight are unacceptable. Thus, the configurations of n = 16 cylindrical magnets were chosen for building the prototype. The Figure 5-7 shows the magnetic field distribution in the region of interest of 50 mm diameter with the case of n = 8. Obviously, the magnetic field of the circle magnets (Figure 5-7-a) is more homogeneous than that of square magnets (Figure 5-7-b).

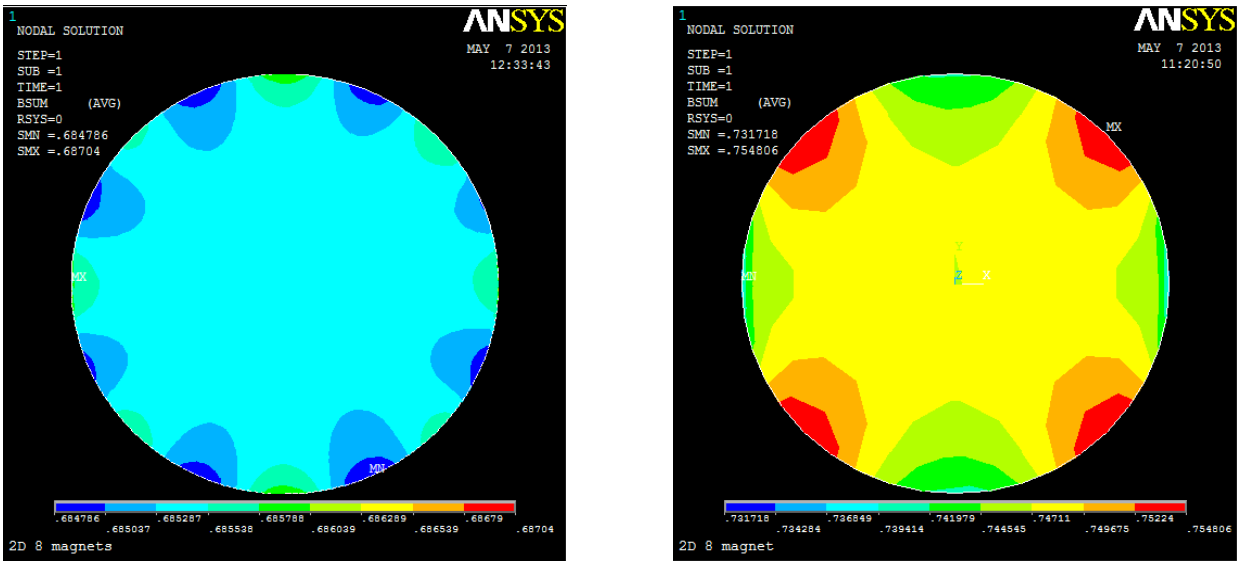

(a) Circle magnets (b) Square magnets

Figure 5-7: The field distribution in the region of interest 50mm diameter with n=8.

In theory, the magnetic field generated by an infinitely long magnet (2D) is perfectly homogeneous. However, in the 3D case, the field homogeneity for the finite-height magnet array is much smaller, apart from the fact that the absolute values are reduced by a factor of about 8 compared to the 2D case [79]. Therefore, to fully evaluate the properties of configuration, 3D

simulation must be done.

5.2.2.2 3-D simulation

For special application, the configuration with r_{inner}= 50 mm and 300 mm in length was chosen for 3D simulation. It has two rings placed in alignment to compensate the field outside of the rings; each ring has the length of 150 mm. These rings are separated by the gap G. The region of interest is expected in the middle length of the configuration as Figure 5-8. The magnetic material for simulation is NdFeB permanent magnets with coercively H_c = 870 kA/m.

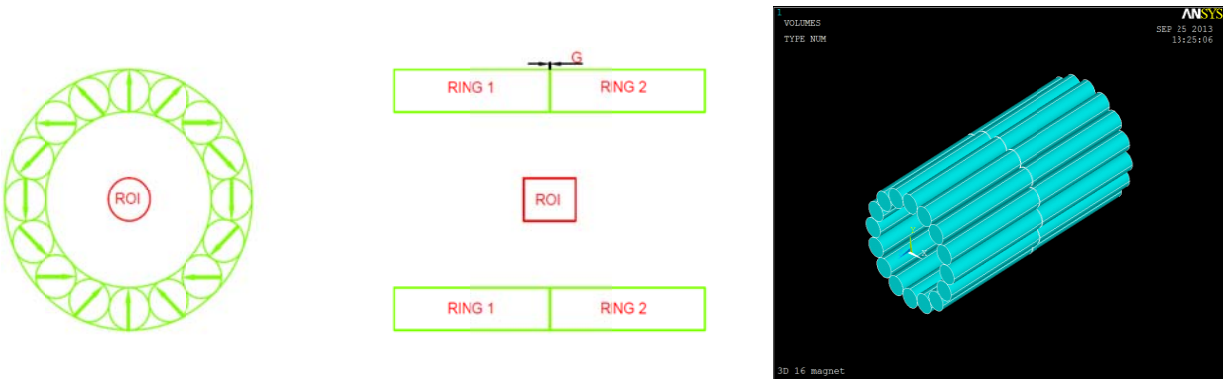

Figure 5-8: The Mandhalas consists of two rings of magnets and their direction of magnetization.

The results of 3D simulation show that the gap width G between two rings influences to the homogeneity of configuration. If the gap width is smaller than the optimum gap, the field profile in the longitudinal axis is a parabola down as shown Figure 5-9-a. In this case, the homogeneity of magnetic field remains on a short distance. The homogeneity is worst. In contrast, the field profile is a parabola up displayed on Figure 5-9-d. In this case, the magnetic field at the center gap significantly decreases along with the increase gap width. It means that there is only an optimum gap width which compensates the decay of magnetic field along configuration. Simulation shows that the magnetic field profile in longitudinal axis becomes more homogeneous at the gap of 1mm (Figure 5-9-c). It remains stability in the distance of 50 mm.

With the gap G=1mm, the magnetic field in OY direction varies nearly constant in the distance of 40 mm as shown on the magnetic field profile (Figure 5-10-a). The distribution of magnetic field in the plane of 40mm diameter which is perpendicular to the longitudinal axis of apparatus (XOY) is displayed on the Figure 5-10-b. In this region, the homogeneity calculated by formula 4-1 is 324 ppm.

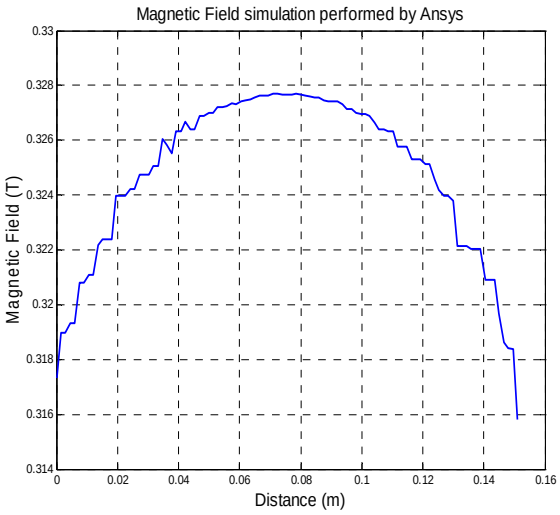

(a) G = 0mm

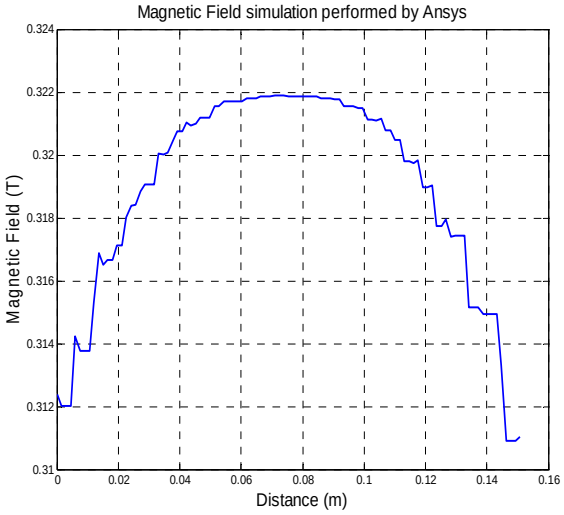

(b) G = 0.5mm

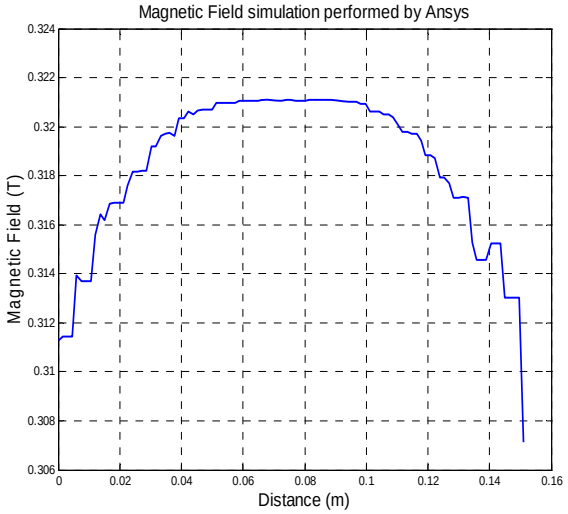

(c) G = 1mm

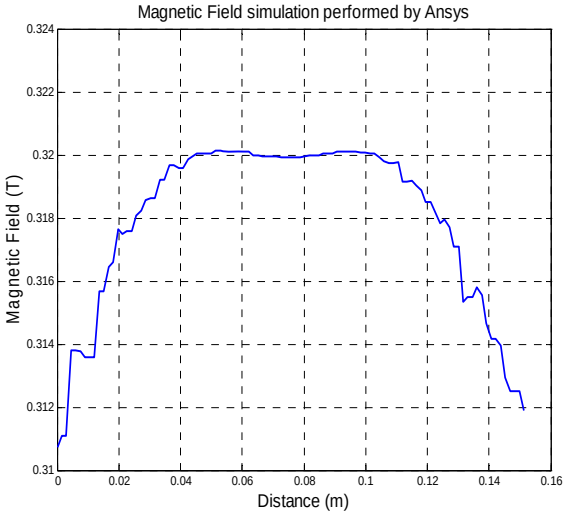

(d) G = 1.3mm

Figure 5-9: The variation of magnetic field in Z direction at different gaps of G.

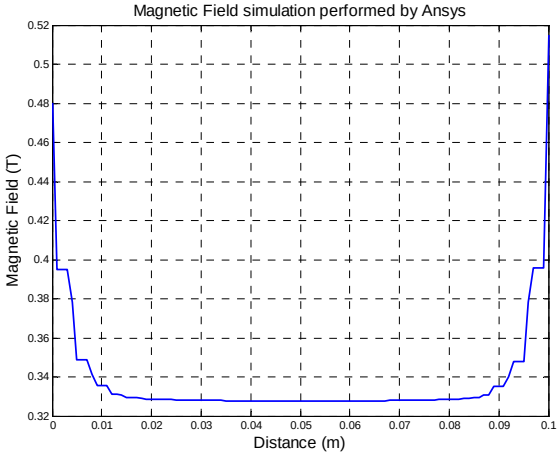

(a) Magnetic field profile in Oy axis

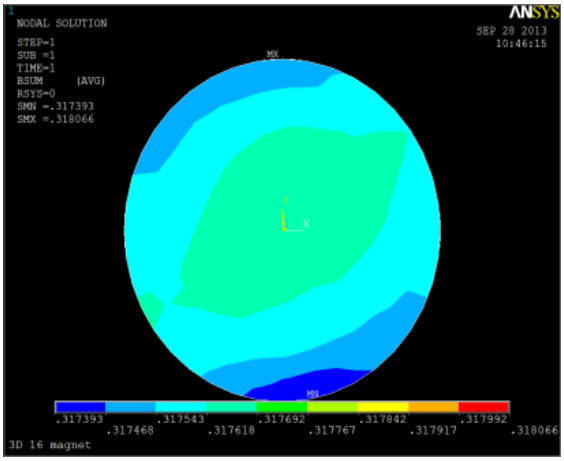

(b) Field distribution in the region of 40 mm diameter

Figure 5-10: The variation of magnetic field at the position 150.5mm from the left or right of configuration.

With the gap G = 1mm, the field variation is stable in the distance of nearly 50 mm along configuration and 40 mm in OY direction. This allows us to take into account the chosen sensitive volume of 40mm diameter and 50 mm length for calculation of magnetic field and homogeneity. In this region, the homogeneity is 638 ppm and the mean value of field strength is 0.32 T. The Figure 5-11-a shows the field map in the middle length of configuration with the size 40x50 mm in YOZ plane. The Figure 5-11-b shows the field distribution in the ROI of 40 mm diameter and 50 mm length in 3D.

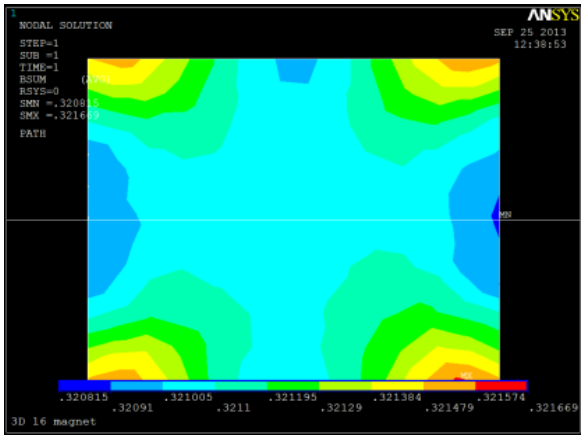

(a) Field distribution in the region of 40x50mm (YOZ) length.

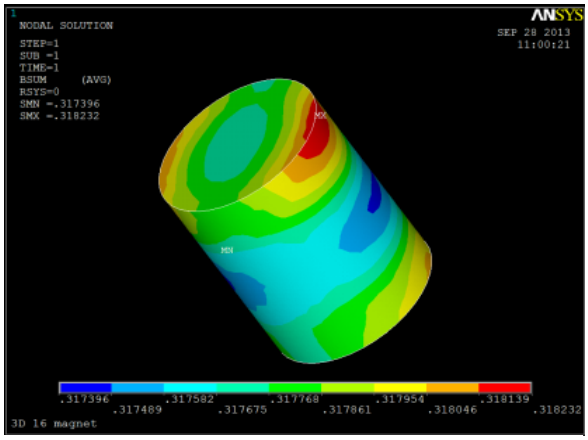

(b) The variation of magnetic field in the volume of 40mm diameter and 50mm. length

Figure 5-11: Geometric parameter of Mandhalas in circle and square magnets.

5.3 Improvement of magnetic field homogeneity

Although adjustment of the center gap is optimized in order to improve the homogeneity in the longitudinal axis, the homogeneity of magnetic field is not sufficient for high resolution NMR experiments. There are other affords to increase the homogeneity of magnetic field. The first method is that the Mandhalas are divided into many rings. These rings are stacked onto each other. By optimizing the gaps between these rings, the homogeneity of magnetic field in the longitudinal axis of configuration becomes more homogeneous [79]. However, this approach is too cumbersome. The second method is the use of shim magnets [77][81]. This approach is easier, faster, robust and more practical. The results of simulation show that the magnetic field is homogeneous at the center of the configuration and becomes worse toward at the end of configuration as in the Figure 5-12.

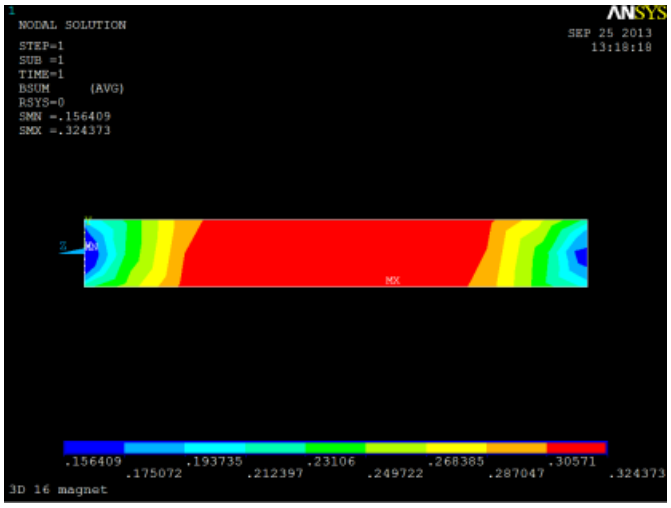

Figure 5-12: The field distribution in YOZ plane (region of 40 x 301mm).

In order to compensate these distortions, we use the shimming methods described in [77][81]. Two shim rings are placed in the bore of configuration. Each ring consists of eight small magnets as shown in Figure 5-13. “By setting the polarization of the shim unit opposite to that of the main field, the inhomogeneities of the last are corrected while the total field strength is maintained at an acceptable magnitude” [77]. Two shim rings are arranged on the circle with a radius of 40 mm. The gap between R_{outer} of the shim rings and R_{inner} of the main rings is 7 mm. This space is used for the cover of them. The geometric parameters with the shim magnets are displayed on Table 5-3. There are two variables that need to be optimized which are G and d. In order to keep the usable bore diameter as large as possible, the positions of shim magnets are optimized in one direction. Another reason is that this prototype consumes more magnetic material

than the prototype described in chapter 4. Thus, the optimization of the shim magnets in three dimensions is cumbersome because of the structure controlling them as in chapter 4. The optimized gap G here is different from the case without shim magnets due to the field addition of the shim magnets.

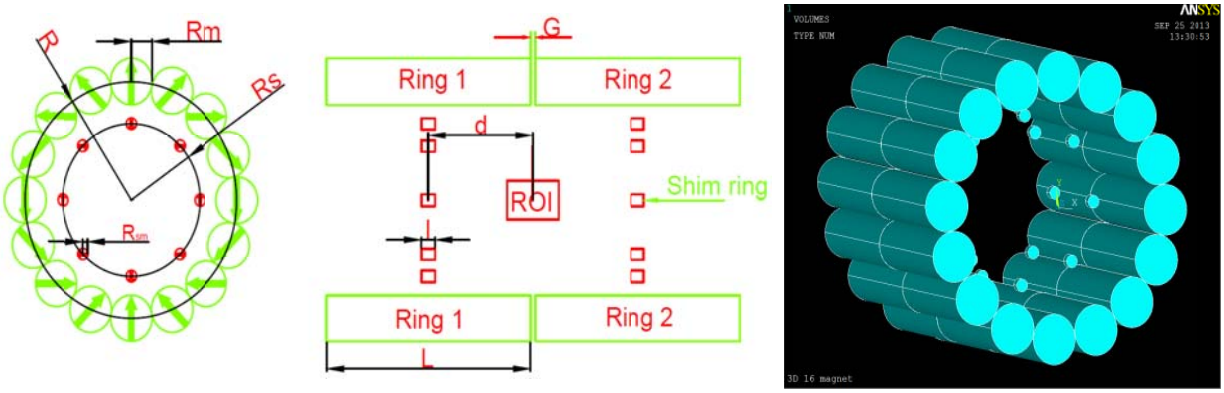

Figure 5-13: The Mandhalas with two shim ring magnets and their direction of magnetization.

Notations	Definitions	Dimensions (mm)
R	Radius of the main rings	62
Rs	Radius of the shim rings	40
Rm	Radius of the main magnets	12
Rsm	Radius of the shim magnets	3
L	The length of the main magnets	150
l	The length of the shim magnets	8
G	The gap between two main rings	To be optimized
d	The distance from the middle length of configuration to the middle length of shim ring	To be optimized

Table 5-3: The geometric parameters of configuration with shim magnets.

The aim of optimization is to find the values of d and G which achieve the highest homogeneity of magnetic field in the given volume (40mm in diameter and 50mm in length). G varies from 0.1mm to 1mm while d varies from 1mm to 150mm. Each step of increase of G and d is 0.1mm and 1mm respectively. The flow chart below (Figure 5-14) shows the optimum process.

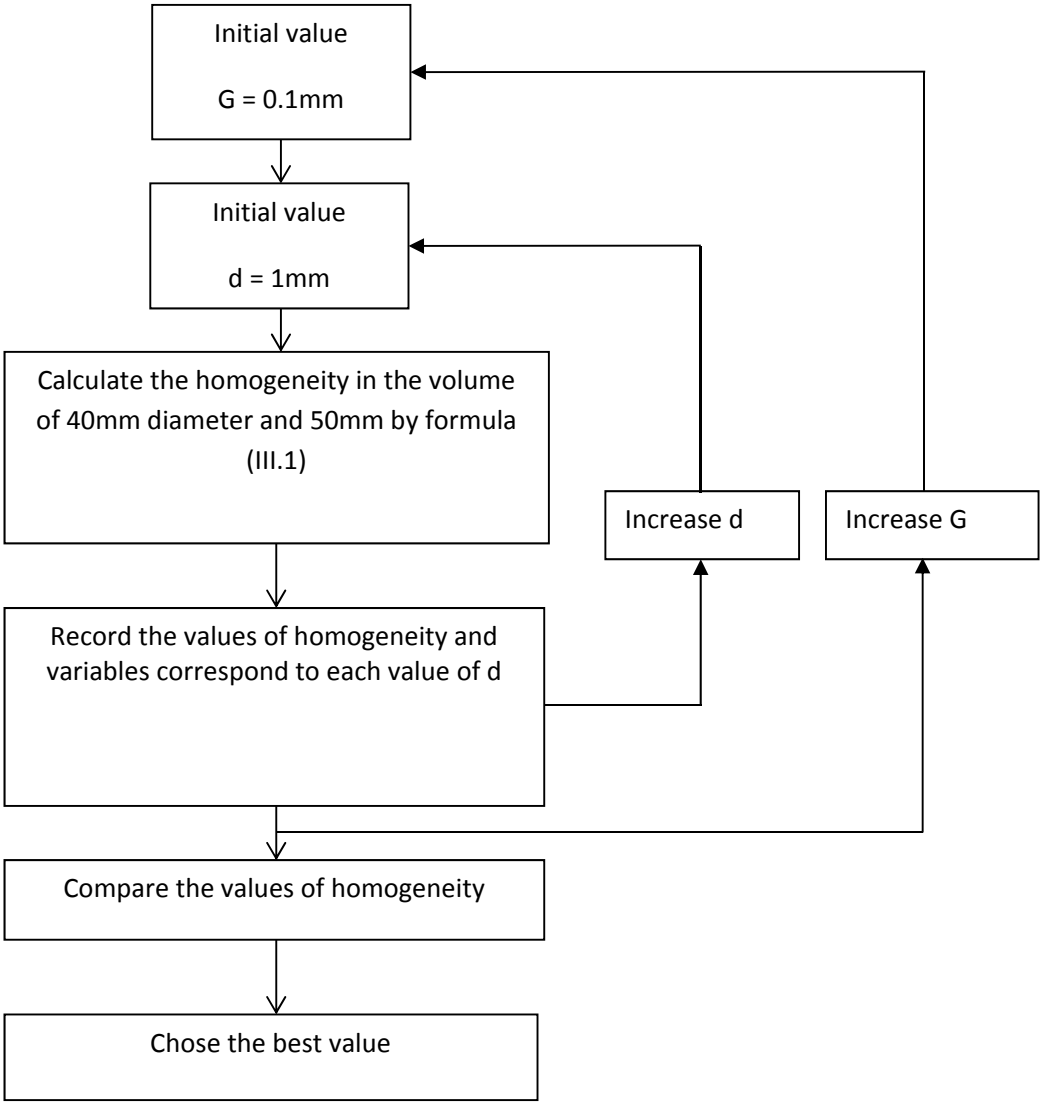

Figure 5-14: The flow chart describes the optimum process.

The results of optimum parameters are displayed on the table 5-4.

Parameters	Optimum values (mm)
G	0.5
d	54

Table 5-4: The results of optimization.

The results of optimization show significant improvement of magnetic field homogeneity. On the transverse plane (XOY), the homogeneity calculated on the circle of diameter 40 mm is 96

ppm while the correspondent value before shim is 324 ppm. This improvement is presented on the Figure 5-15.

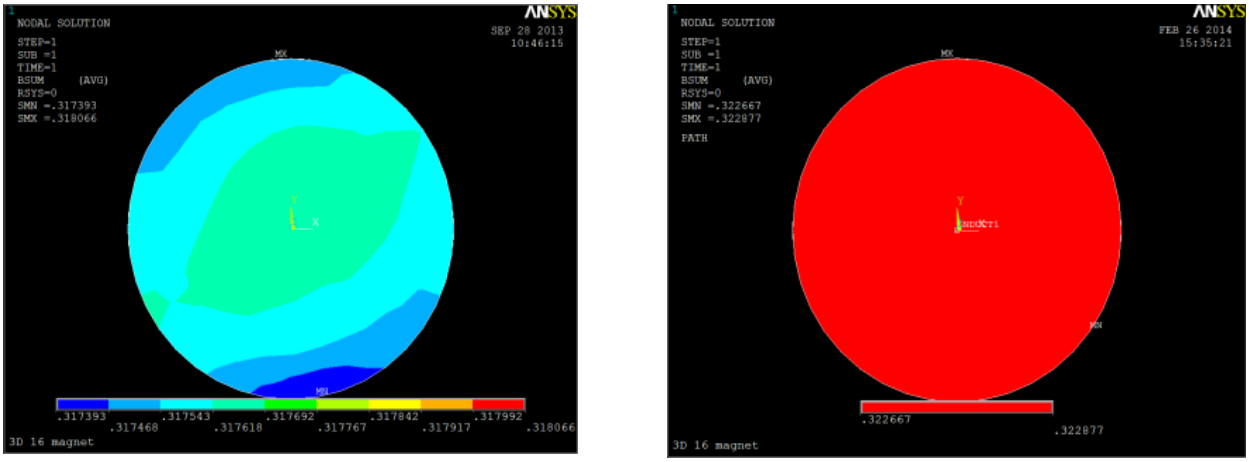

(a) Before shim (b) After shim

Figure 5-15: The variation of magnetic field in the plane 40 mm diameter at the position 150.5 mm from the left or right of configuration (XOY).

In the longitudinal axis, the homogeneous region extends over 2.5 times in comparison to that without shim magnets. This is confirmed by the magnetic field profile and field maps in the Figure 5-16 and Figure 5-17 respectively.

The homogeneity of magnetic field in the cylindrical volume 40 mm diameter and 50 mm length is 178 ppm while the correspondent value of the configuration without shim magnets is 638 ppm. It is approximate 3.5 times better than. Figure 5-18 shows the improvement of magnetic field homogeneity in the volume of 40 mm diameter, 90 mm length before shim and after shim.

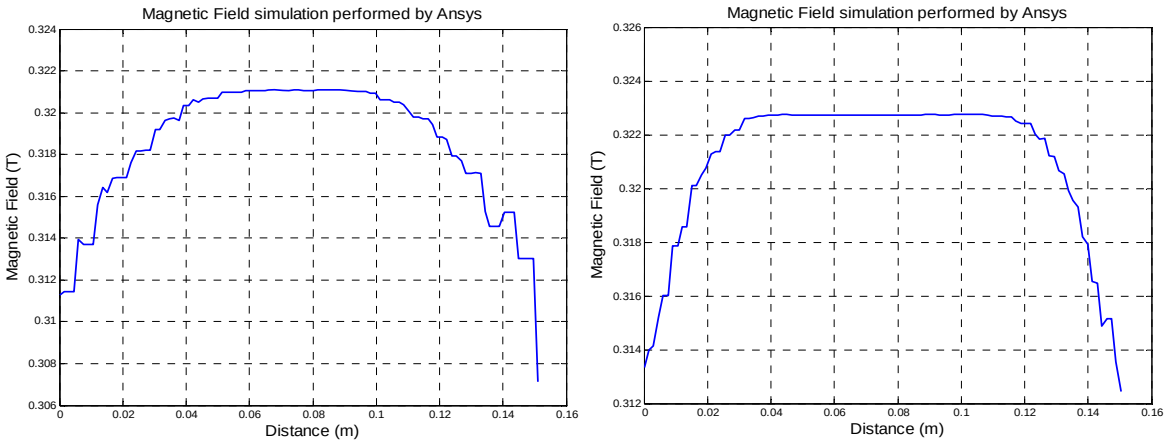

(a) Before shim (b) After shim

Figure 5-16: The magnetic field profile in Z direction (150mm in the middle length of configuration).

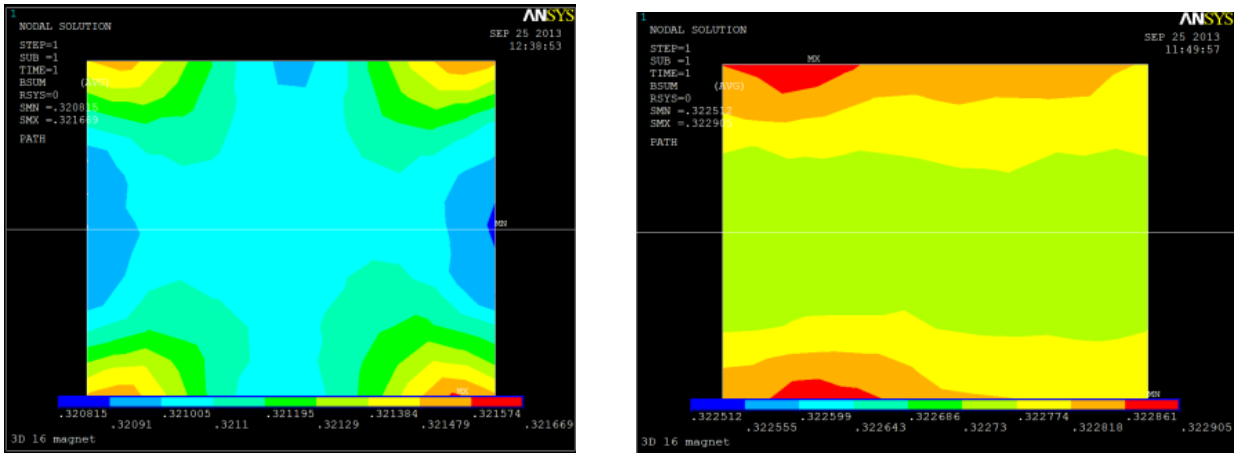

(a) Before shim (b) After shim

Figure 5-17: The field distribution in the region of 40x50mm (YOZ plane) at the middle length of configuration.

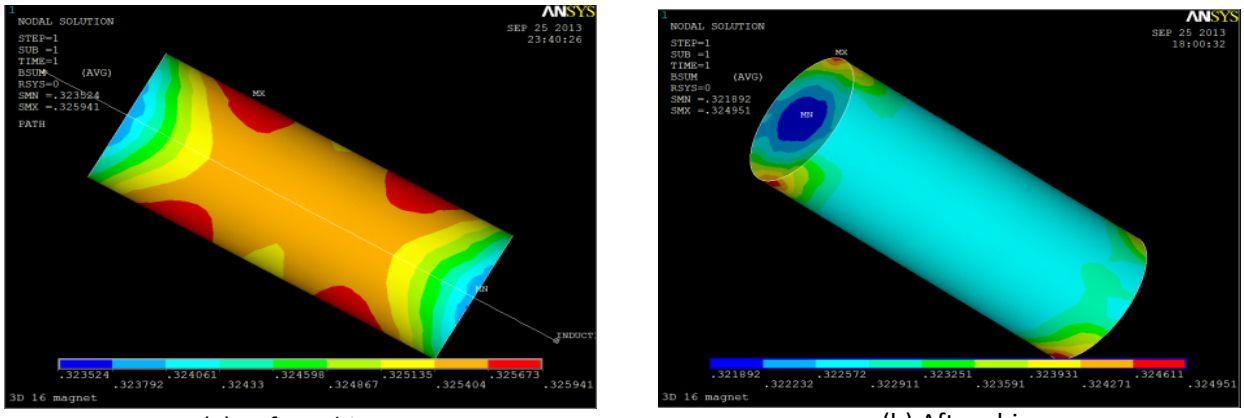

(a) Before shim (b) After shim

Figure 5-18: The field distribution in the volume 40 mm diameters and 90mm length.

5.4 Prototype design

We choose the commercial magnets made from NdFeB with coercively H_c=870kA/m. These magnets have the dimensions 24 mm for the diameter, 150mm for the length (2x16 magnets) arranged on a circle with radius of 62 mm.

This configuration consists of two rings separated by the gap of 0.5 mm shown on the Figure 5-19-a. Each ring has 16 magnets which are covered by two aluminum frames as shown in Figure 5-19-b. These magnets can rotate in the frame holes to find the position that generate the best homogeneity obtained by simulation. When these magnets achieve the desired position, they

are fixed by the screws. Two rings are assembled on eight axes. They can slide on these axes until achieve the optimized position given by simulation, and then fixed by the screws on the frame.

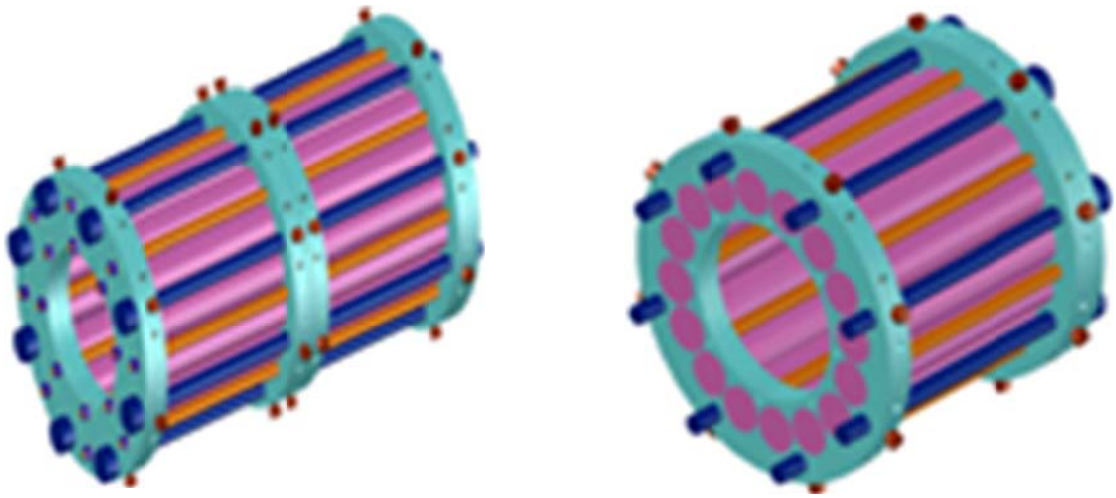

(a) Two rings slide on 8 axes

(b) One ring with its frame

Figure 5-19: the prototype consists of two rings.

5.5 Discussion and conclusions

One of the difficulties of Mandhalas made from cylindrical magnets is assembly due to they are lack of a geometric feature to identify the exact magnetization. Moreover, if the adjacent magnets touch each other, they cannot rotate to find the best position as simulation because of impulsive force. In order to overcome these difficulties, the diameter of the magnets are reduced a little to create the gaps between the neighbor magnets. These gaps allow the magnets easily rotate in the frame holes. That is the reason why the diameter of the magnets are 24 mm instead of 24.23mm as theory calculation shown on the Table 5-2. The gap between two neighbor magnets determined with the help of Autocad is 0.2 mm as in the Figure 5-20.

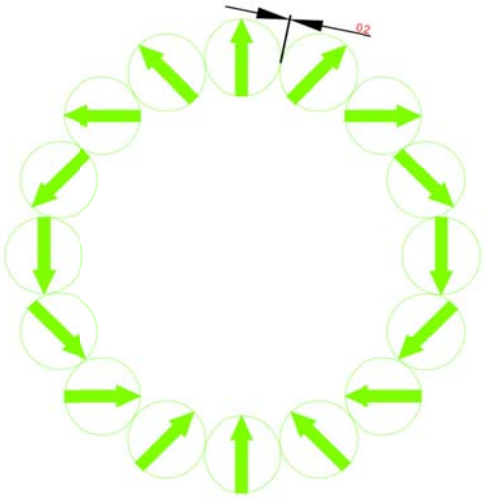

Figure 5-20: the gap between two neighbor magnets.

The Table 5-5 shows the comparison of performances of previous prototypes selected in state of the art to this works.

Reference	Resolution (ppm)	Mass (kg)	ROI size (mm)	Field strength (T)
Moresi and Magin [67]	20	4	3 o.d. x 5	0.6
Raich and Blümler [74]	700	11.4	18 x 18 x 30	0.3
Jachmann *et al* [81]	56	5	0.25 o.d. x 2	0.5
Danieli *et al* [77]	0.85	50	10 o.d. x 10	0.22
Hugon *et al* [72]	10	1.8	1.5 DSV	0.12
Windt *et al* [78]	200	3.1	5 DSV	0.57
Prototype in chapter 4	230	3	7 x 8 x 20	0.12
Prototype in chapter 5	178	20	40 o.d. x 50	0.32

Table 5-5: *The comparison of existing prototypes to this works.*

In conclusion, based on ANSYS® Multiphysics software, we introduce the new approach of simulation. This tool allows us to simulate the magnetic field and homogeneity of the different Mandhalas configurations with the number of magnets 4, 8, 16, 32 in cylindrical and square shapes respectively. The 2D simulation results, allowed us to perform a primarily comparison between these configurations based on three important criteria for NMR portable device: magnetic field strength, homogeneity, and weight. This comparative study has demonstrated that the configurations with n=16 magnets in cylindrical shape are suitable for building prototypes. Due to

the reduction of the field homogeneity with finite height magnet array, we calculate and simulate its field strength and homogeneity in 3D for fully analyses the properties of the configuration. Based on the results of 3D simulation, we propose the shim method to improve the homogeneity of magnetic field. The results of shim method show that the magnetic field homogeneity significantly improves. In the volume of 40 mm diameter and 50 mm length, the homogeneity of the configuration with shim magnets is 3.5 time better than that without shim magnets with 178 ppm and 638 ppm respectively. These impressive results motivate us design the prototype with two main rings and two shim rings. It has the length of 300 mm and 70 mm diameter in use separated by a gap of 0.5 mm. The total weight is approximate 20 kg. This mobile magnet generates magnetic field of 0.32 T and offers the homogeneity in the large sensitive volume 40 mm diameters, 50 mm length with 178 ppm. It is suitable for our NMR experiments on Biomedical and Agro alimentary applications.

Conclusion and perspectives

Based on the objective of application and the examination of previous works (chapter I), we have decided to choose the *in-situ* magnet for our applications. Our configurations are based on the Halbach type due to its homogeneity and ability to confine the field inside it. Before the simulation, we have figured out the properties of different families of magnetic materials. The advantages and drawbacks of magnetic materials are analyzed in order to give a comparison. Based on these analyses, we found that the family of neodymium iron boron magnets (NdFeB) is suitable for our works. This family of magnetic material has similar properties with another rare-earth magnetic material samarium cobalt (S_mC_o) while 30% to 40% cheaper than [29]. The numerical and simulation methods of the existing ideas also have been examined to find the best solution for our simulation and optimization. The finite element method which is the underlying procedure of many software packages was chosen. The process of simulation based on ANSYS software has been introduced in order to show progresses to be done.

The calculation and simulation are mainly based on ANSYS. The results of ANSYS will be verified to that of RADIA software. They are two different methods. The principle calculation of ANSYS is based on the finite element method while RADIA is based on boundary integral methods. The results of verification are impressive in both homogeneity and optimization. However, the magnetic field strength is quite different between two softwares due to the meshing. Another software used in our works is Matlab. This software is used to calculate the homogeneity with the mesh nodes turned out from ANSYS. Matlab is also used to plot and visualize the measurable field points. The measurement is carried on with the gaussmeter Hirst GM08 with the limit sensibility of 10^{-4}T. The micropositioner Signatone S-926 is used to control the movement of the probe in three dimensions.

Based on the simulation results, we realized a compact and light weight prototype with 24 identical rod magnets. Our prototype has two rings; each ring consists of 12 magnets. Each magnet has the length of 50mm and 8mm in diameter. The prototype generates the field B_0 in transverse plane with the field strength 0.12T. Its homogeneity is 4230ppm over a volume 7x8x20mm. It is obvious that this homogeneity is not enough for high resolution. In order to improve the homogeneity, we proposed the shim method with 8 small magnets placed in the bore of the prototype. By optimizing the positions of these magnets, we achieve the optimum configuration. The results of optimization show the great improvement of homogeneity. The homogeneity

achieved after shim is 18 times better than that of before shim with 230ppm in comparison to 4230ppm over a same volume 7x8x20mm. The measurement was carried out to verify the result of simulation. The magnetic field which varies in the longitudinal axis obtained by measurement is quite similar to the results of simulation. However, the homogeneity obtained by simulation and measurement is different due to the imperfection of the material.

We also proposed another configuration for biomedical and agroalimentary applications. This configuration is based on the idea of NMR Mandhalas (Magnetic Arrangement for Novel Discrete Halbach Layout) [74][79]. In order to choose the best configuration, two Halbach permanent magnet arrays with cube and cylindrical shape, respectively, were compared in criteria of average magnetic field strength, magnetic field homogeneity and material consumption. This comparison was performed by 2-D simulation with ANSYS software. It was found that the cylindrical shape magnet has better performance than the cube one; except for the case with n = 4. Based on the results of 2-D simulation, we chose the NMR Mandhalas with 16 cylidrical magnet for our design. 3-D simulation was carried out in order to fully evaluate the properties of this configuration. Then the field homogeneity optimization was performed by using the passive shim method. After optimization, the magnetic field homogeneity has been significantly improved in comparison to the case before using the shim magnets. The difficulties of assembly process have also been discussed and well compared to the previous works. These results laid a foundation for the design and manufacture of the NMR Mandhalas with cylindrical magnets.

Future work will be focused on two main parts

The first part is concentrated the correction of the misalignment of magnetic direction mentioned in chapter 4. We bought the magnets from “HKCM MAGNTES from STOCK”[107]. We will assembly the magnets and measure the magnetic field strength and homogeneity. The NMR experiments will be applied after this step.

The second part is machining and assembling accuracy the NMR Mandhalas to achieve high performance. Then this configuration will be used to carry out the NMR experiments in biomedical and agroalimentary field. Along with the micro antennas developed by our group, we can envision a wide development of our magnet systems for biomedical and agroalimentary application.

References

[1] H. Y. Carr, “Free precession techniques in nuclear magnetic resonance.,” 1953.

[2] P. C. Lauterbur, “Image Formation by Induced Local Interactions: Examples Employing Nuclear Magnetic Resonance,” *Nature*, vol. 242, no. 5394, pp. 190–191, Mar. 1973.

[3] I. I. Rabi, J. R. Zacharias, S. Millman, and P. Kusch, “A New Method of Measuring Nuclear Magnetic Moment,” *Phys. Rev.*, vol. 53, no. 4, pp. 318–318, Feb. 1938.

[4] George.R Coates, Lizhi Xiao, and Manfred G. Prammer, *NMR logging - Principles and Applications*. Houston: Halliburton Energy Services, 1999.

[5] Brian Cowan, *Nuclear Magnetic Resonance and Relaxation*. Cambridge University Press, 1997.

[6] “The Basics of MRI.” [Online]. Available: https://www.cis.rit.edu/htbooks/mri/inside.htm. [Accessed: 20-Feb-2014].

[7] R. R. Ernst and W. A. Anderson, “Application of Fourier Transform Spectroscopy to Magnetic Resonance,” *Rev. Sci. Instrum.*, vol. 37, no. 1, pp. 93–102, Jan. 1966.

[8] E. Odeblad, “Micro-NMR in high permanent magnetic fields. Theoretical and experimental investigations with an application to the secretions from single glandular units in the human uterine cervix,” *Acta Obstet. Gynecol. Scand.*, vol. 45, p. Suppl 2:1–188, 1966.

[9] D. I. Hoult and R. E. Richards, “The signal-to-noise ratio of the nuclear magnetic resonance experiment,” *J. Magn. Reson.*, vol. 213, no. 2, pp. 329–343, Dec. 2011.

[10] D. I. Hoult, “The NMR receiver: A description and analysis of design,” *Prog. Nucl. Magn. Reson. Spectrosc.*, vol. 12, no. 1, pp. 41–77, 1978.

[11] M. P. Augustine, D. M. TonThat, and J. Clarke, “SQUID detected NMR and NQR,” *Solid State Nucl. Magn. Reson.*, vol. 11, no. 1–2, pp. 139–156, Mar. 1998.

[12] R. McDermott, S. Lee, B. Ten Haken, A. H. Trabesinger, A. Pines, and J. Clarke, “Microtesla MRI with a superconducting quantum interference device,” *Proc. Natl. Acad. Sci. U. S. A.*, vol. 101, no. 21, pp. 7857–7861, 2004.

[13] M. Pannetier, C. Fermon, G. L. Goff, J. Simola, and E. Kerr, “Femtotesla Magnetic Field Measurement with Magnetoresistive Sensors,” *Science*, vol. 304, no. 5677, pp. 1648–1650, Jun. 2004.

[14] M. Pannetier, C. Fermon, G. Legoff, J. Simola, E. Kerr, M. Welling, and R. J. Wijngaarden, “Ultra-sensitive field sensors-an alternative to SQUIDs,” *Appl. Supercond. IEEE Trans. On*, vol. 15, no. 2, pp. 892–895, 2005.

[15] J. A. Sidles, “Noninductive detection of single-proton magnetic resonance,” *Appl. Phys. Lett.*, vol. 58, no. 24, pp. 2854–2856, Jun. 1991.

[16] C. L. Degen, M. Poggio, H. J. Mamin, C. T. Rettner, and D. Rugar, “Nanoscale magnetic resonance imaging,” *Proc. Natl. Acad. Sci.*, vol. 106, no. 5, pp. 1313–1317, 2009.

[17] E. K. Insko, M. A. Elliott, J. C. Schotland, and J. S. Leigh, “Generalized Reciprocity,” *J. Magn. Reson.*, vol. 131, no. 1, pp. 111–117, Mar. 1998.

[18] Malcolm H. Levitt, *Spin Dynamics - Basics of Nuclear Magnetic Resonance*, Second edition. John Wiley & Sons, Ltd.

[19] R. K. Wangsness and F. Bloch, “The Dynamical Theory of Nuclear Induction,” *Phys. Rev.*, vol. 89, no. 4, pp. 728–739, Feb. 1953.

[20] T. L. Peck, R. L. Magin, and P. C. Lauterbur, “Design and analysis of microcoils for NMR microscopy,” *J. Magn. Reson. B*, vol. 108, no. 2, pp. 114–124, Aug. 1995.

[21] TRUONG Cong Tien, “Optimisation par approche physique des micro-antennes RMN fabriquées par Techniques de Microélectroniques: Étude Théorique et Expérimentale,” Thèse doctorat, Institut national des sciences Appliquéees de Lyon.

[22] E. L. Hahn, “Spin echoes,” *Phys. Rev.*, vol. 80, no. 4, p. 580, 1950.

[23] M. Goldman, *Quantum Description of High-Resolution NMR in Liquids*. Oxford : New York: Oxford University Press, USA, 1991.

[24] H. Y. Carr and E. M. Purcell, “Effects of diffusion on free precession in nuclear magnetic resonance experiments,” *Phys. Rev.*, vol. 94, no. 3, p. 630, 1954.

[25] S. Meiboom and D. Gill, “Modified Spin-Echo Method for Measuring Nuclear Relaxation Times,” *Rev. Sci. Instrum.*, vol. 29, no. 8, p. 688, 1958.

[26] K.-J. Dunn, D. J. Bergman, and G. A. LaTorraca, *Nuclear Magnetic Resonance: Petrophysical and Logging Applications*. Elsevier, 2002.

[27] W. R. Hendee and E. R. Ritenour, *Medical Imaging Physics*. John Wiley & Sons, 2003.

[28] H. C. Torrey, “Bloch Equations with Diffusion Terms,” *Phys. Rev.*, vol. 104, no. 3, pp. 563–565, Nov. 1956.

[29] Cédric HUGON, “Aimants permanents pour la RMN et l’IRM,” Thèse doctorat, Université de Versailles Saint-Quentin-en-Yvelines, 2010.

[30] B. Blumich, *NMR Imaging of Materials*. Oxford University Press, 2003.

[31] F. A. Nelson and H. E. Weaver, “Nuclear Magnetic Resonance Spectroscopy in Superconducting Magnetic Fields,” *Science*, vol. 146, no. 3641, pp. 223–232, Oct. 1964.

[32] B. Blümich, J. Perlo, and F. Casanova, “Mobile single-sided NMR,” *Prog. Nucl. Magn. Reson. Spectrosc.*, vol. 52, no. 4, pp. 197–269, May 2008.

[33] V. R. H, “Apparatus and method for identifying substances,” US3395337 A, 30-Jul-1968.

[34] J. A. Jackson, L. J. Burnett, and J. F. Harmon, “Remote (inside-out) NMR. III. Detection of nuclear magnetic resonance in a remotely produced region of homogeneous magnetic field,” *J. Magn. Reson. 1969*, vol. 41, no. 3, pp. 411–421, Dec. 1980.

[35] R. L. Kleinberg, A. Sezginer, D. D. Griffin, and M. Fukuhara, “Novel NMR apparatus for investigating an external sample,” *J. Magn. Reson. 1969*, vol. 97, no. 3, pp. 466–485, May 1992.

[36] J. C. Goswami, A. Sezginer, and B. Luong, “On the design of NMR sensor for well-logging applications,” *IEEE Trans. Antennas Propag.*, vol. 48, no. 9, pp. 1393–1402, Sep. 2000.

[37] A. Reiderman, “Method and apparatus for high signal-to-noise ratio nmr well logging,” US20070222444 A1, 27-Sep-2007.

[38] E. W. Randall, “Stray-Field (STRAFI) NMR: Imaging in Large Field Gradients,” in *eMagRes*, John Wiley & Sons, Ltd, 2007.

[39] P. J. McDonald and B. Newling, “Stray field magnetic resonance imaging,” *Rep. Prog. Phys.*, vol. 61, no. 11, p. 1441, 1998.

[40] P. J. McDonald, “Stray field magnetic resonance imaging,” *Prog. Nucl. Magn. Reson. Spectrosc.*, vol. 30, no. 1–2, pp. 69–99, Mar. 1997.

[41] G. Eidmann, R. Savelsberg, P. Blümler, and B. Blümich, “The NMR MOUSE, a Mobile Universal Surface Explorer,” *J. Magn. Reson. A*, vol. 122, no. 1, pp. 104–109, Sep. 1996.

[42] B. Blümich, P. Blümler, G. Eidmann, A. Guthausen, R. Haken, U. Schmitz, K. Saito, and G. Zimmer, “The NMR-mouse: construction, excitation, and applications,” *Magn. Reson. Imaging*, vol. 16, no. 5, pp. 479–484, 1998.

[43] B. Blümich, V. Anferov, S. Anferova, M. Klein, R. Fechete, M. Adams, and F. Casanova, “Simple NMR-mouse with a bar magnet,” *Concepts Magn. Reson.*, vol. 15, no. 4, pp. 255–261, Dec. 2002.

[44] B. Blümich, F. Casanova, J. Perlo, S. Anferova, V. Anferov, K. Kremer, N. Goga, K. Kupferschläger, and M. Adams, “Advances of unilateral mobile NMR in nondestructive materials testing,” *Magn. Reson. Imaging*, vol. 23, no. 2, pp. 197–201, Feb. 2005.

[45] S. Anferova, V. Anferov, M. Adams, P. Blümler, N. Routley, K. Hailu, K. Kupferschläger,

M. j. d. Mallett, G. Schroeder, S. Sharma, and B. Blümich, “Construction of a NMR-MOUSE with short dead time,” *Concepts Magn. Reson.*, vol. 15, no. 1, pp. 15–25, Mar. 2002.

[46] P. J. Prado, “Single sided imaging sensor,” *Magn. Reson. Imaging*, vol. 21, no. 3–4, pp. 397–400, Apr. 2003.

[47] P. J. Prado, “NMR hand-held moisture sensor,” *Magn. Reson. Imaging*, vol. 19, no. 3–4, pp. 505–508, Apr. 2001.

[48] A. E. Marble, I. V. Mastikhin, B. G. Colpitts, and B. J. Balcom, “A constant gradient unilateral magnet for near-surface MRI profiling,” *J. Magn. Reson.*, vol. 183, no. 2, pp. 228–234, Dec. 2006.

[49] A. E. Marble, I. V. Mastikhin, B. G. Colpitts, and B. J. Balcom, “An analytical methodology for magnetic field control in unilateral NMR,” *J. Magn. Reson.*, vol. 174, no. 1, pp. 78–87, May 2005.

[50] W.-H. Chang, J.-H. Chen, and L.-P. Hwang, “Single-sided mobile NMR with a Halbach magnet,” *Magn. Reson. Imaging*, vol. 24, no. 8, pp. 1095–1102, Oct. 2006.

[51] W.-H. Chang, J.-H. Chen, and L.-P. Hwang, “Single-sided mobile NMR apparatus using the transverse flux of a single permanent magnet,” *Magn. Reson. Imaging*, vol. 28, no. 1, pp. 129–138, Jan. 2010.

[52] E. Fukushima and J. A. Jackson, “Unilateral magnet having a remote uniform field region for nuclear magnetic resonance,” US6489872 B1, 03-Dec-2002.

[53] B. Manz, A. Coy, R. Dykstra, C. D. Eccles, M. W. Hunter, B. J. Parkinson, and P. T. Callaghan, “A mobile one-sided NMR sensor with a homogeneous magnetic field: The NMR-MOLE,” *J. Magn. Reson.*, vol. 183, no. 1, pp. 25–31, Nov. 2006.

[54] A. E. Marble, I. V. Mastikhin, B. G. Colpitts, and B. J. Balcom, “A compact permanent magnet array with a remote homogeneous field,” *J. Magn. Reson.*, vol. 186, no. 1, pp. 100–104, May 2007.

[55] J. L. Paulsen, L. S. Bouchard, D. Graziani, B. Blümich, and A. Pines, “Volume-selective magnetic resonance imaging using an adjustable, single-sided, portable sensor,” *Proc. Natl. Acad. Sci.*, vol. 105, no. 52, pp. 20601–20604, 2008.

[56] J. Perlo, F. Casanova, and B. Blümich, “Profiles with microscopic resolution by single-sided NMR,” *J. Magn. Reson.*, vol. 176, no. 1, pp. 64–70, Sep. 2005.

[57] J. Perlo, F. Casanova, and B. Blümich, “3D imaging with a single-sided sensor: an open tomograph,” *J. Magn. Reson.*, vol. 166, no. 2, pp. 228–235, Feb. 2004.

[58] C. A. Meriles, D. Sakellariou, H. Heise, A. J. Moulé, and A. Pines, “Approach to High-Resolution ex Situ NMR Spectroscopy,” *Science*, vol. 293, no. 5527, pp. 82–85, Jul. 2001.

[59] J. Perlo, V. Demas, F. Casanova, C. A. Meriles, J. Reimer, A. Pines, and B. Blümich, “High-Resolution NMR Spectroscopy with a Portable Single-Sided Sensor,” *Science*, vol. 308, no. 5726, pp. 1279–1279, May 2005.

[60] J. Perlo, F. Casanova, and B. Blümich, “Single-sided sensor for high-resolution NMR spectroscopy,” *J. Magn. Reson.*, vol. 180, no. 2, pp. 274–279, Jun. 2006.

[61] J. Perlo, F. Casanova, and B. Blümich, “Ex Situ NMR in Highly Homogeneous Fields: 1H Spectroscopy,” *Science*, vol. 315, no. 5815, pp. 1110–1112, Feb. 2007.

[62] M. G. Abele, *Structures of permanent magnets: generation of uniform fields*. John Wiley, 1993.

[63] K. Halbach, “Design of permanent multipole magnets with oriented rare earth cobalt material,” *Nucl. Instrum. Methods*, vol. 169, no. 1, pp. 1–10, Feb. 1980.

[64] M. G. Abele, W. Tsui, and H. Rusinek, “Methodology of pole piece design in permanent magnets,” *J. Appl. Phys.*, vol. 99, no. 8, p. 08D903, Apr. 2006.

[65] A. McDowell and E. Fukushima, “Ultracompact NMR: 1H Spectroscopy in a Subkilogram Magnet,” *Appl. Magn. Reson.*, vol. 35, no. 1, pp. 185–195, Nov. 2008.

[66] M. G. Abele and H. A. Leupold, “A general method for flux confinement in permanent-magnet structures,” *J. Appl. Phys.*, vol. 64, no. 10, pp. 5988–5990, Nov. 1988.

[67] G. Moresi and R. Magin, “Miniature permanent magnet for table-top NMR,” *Concepts Magn. Reson.*, vol. 19B, no. 1, pp. 35–43, 2003.

[68] B. P. Hills, K. M. Wright, and D. G. Gillies, “A low-field, low-cost Halbach magnet array for open-access NMR,” *J. Magn. Reson.*, vol. 175, no. 2, pp. 336–339, Aug. 2005.

[69] X. Zhang, V. Mahesh, D. Ng, R. Hubbard, A. Ailiani, B. O’Hare, A. Benesi, and A. Webb, “Design, construction and NMR testing of a 1 tesla Halbach Permanent Magnet for Magnetic Resonance,” in *COMSOL Users Conference, Boston*, 2005.

[70] D. Sakellariou, C. Hugon, A. Guiga, G. Aubert, S. Cazaux, and P. Hardy, “Permanent magnet assembly producing a strong tilted homogeneous magnetic field: towards magic angle field spinning NMR and MRI,” *Magn. Reson. Chem.*, vol. 48, no. 12, pp. 903–908, Dec. 2010.

[71] C. Hugon, P. M. Aguiar, G. Aubert, and D. Sakellariou, “Design, fabrication and evaluation of a low-cost homogeneous portable permanent magnet for NMR and MRI,” *Comptes Rendus Chim.*, vol. 13, no. 4, pp. 388–393, Apr. 2010.

[72] C. Hugon, F. D'Amico, G. Aubert, and D. Sakellariou, "Design of arbitrarily homogeneous permanent magnet systems for NMR and MRI: Theory and experimental developments of a simple portable magnet," *J. Magn. Reson.*, vol. 205, no. 1, pp. 75–85, Jul. 2010.

[73] R. Ravaud, G. Lemarquand, and others undefined, "Magnetic field in MRI yokeless devices: Analytical approach," *PIER-Prog. Electromagn. Res.*, pp. 327–341, 2009.

[74] H. Raich and P. Blümler, "Design and construction of a dipolar Halbach array with a homogeneous field from identical bar magnets: NMR Mandhalas," *Concepts Magn. Reson. Part B Magn. Reson. Eng.*, vol. 23B, no. 1, pp. 16–25, Oct. 2004.

[75] S. Anferova, V. Anferov, J. Arnold, E. Talnishnikh, M. A. Voda, K. Kupferschläger, P. Blümler, C. Clauser, and B. Blümich, "Improved Halbach sensor for NMR scanning of drill cores," *Magn. Reson. Imaging*, vol. 25, no. 4, pp. 474–480, May 2007.

[76] S. Anferova, V. Anferov, D. G. Rata, B. Blümich, J. Arnold, C. Clauser, P. Blumler, and H. Raich, "A mobile NMR device for measurements of porosity and pore size distributions of drilled core samples," *Concepts Magn. Reson.*, vol. 23B, no. 1, pp. 26–32, Oct. 2004.

[77] E. Danieli, J. Mauler, J. Perlo, B. Blümich, and F. Casanova, "Mobile sensor for high resolution NMR spectroscopy and imaging," *J. Magn. Reson.*, vol. 198, no. 1, pp. 80–87, May 2009.

[78] C. W. Windt, H. Soltner, D. van Dusschoten, and P. Blümler, "A portable Halbach magnet that can be opened and closed without force: The NMR-CUFF," *J. Magn. Reson.*, vol. 208, no. 1, pp. 27–33, Jan. 2011.

[79] H. Soltner and P. Blümler, "Dipolar Halbach magnet stacks made from identically shaped permanent magnets for magnetic resonance," *Concepts Magn. Reson. Part A*, vol. 36A, no. 4, pp. 211–222, Jul. 2010.

[80] Q. Y. Chen, G. C. Zhang, Y. J. Xu, Y. Chang, H. Wang, and X. D. Yang, "Simulation and Optimization of an Octagonal Halbach Permanent Magnet Array for Small-Size NMR," *Appl. Mech. Mater.*, vol. 543–547, pp. 509–513, Mar. 2014.

[81] R. C. Jachmann, D. R. Trease, L.-S. Bouchard, D. Sakellariou, R. W. Martin, R. D. Schlueter, T. F. Budinger, and A. Pines, "Multipole shimming of permanent magnets using harmonic corrector rings," *Rev. Sci. Instrum.*, vol. 78, no. 3, p. 035115, Mar. 2007.

[82] R. Haken and B. Blümich, "Anisotropy in Tendon Investigated in Vivo by a Portable NMR Scanner, the NMR-MOUSE," *J. Magn. Reson.*, vol. 144, no. 2, pp. 195–199, Jun. 2000.

[83] G. Navon, U. Eliav, D. E. Demco, and B. Blümich, “Study of order and dynamic processes in tendon by NMR and MRI,” *J. Magn. Reson. Imaging*, vol. 25, no. 2, pp. 362–380, Feb. 2007.

[84] M. Dias, J. Hadgraft, P. M. Glover, and P. J. McDonald, “Stray field magnetic resonance imaging: a preliminary study of skin hydration,” *J. Phys. Appl. Phys.*, vol. 36, no. 4, pp. 364–368, 2003.

[85] L. Backhouse, M. Dias, J. P. Gorce, J. Hadgraft, P. J. McDonald, and J. W. Wiechers, “GARField magnetic resonance profiling of the ingress of model skin-care product ingredients into human skinin vitro,” *J. Pharm. Sci.*, vol. 93, no. 9, pp. 2274–2283, Sep. 2004.

[86] B. Blümich, S. Anferova, S. Sharma, A. L. Segre, and C. Federici, “Degradation of historical paper: nondestructive analysis by the NMR-MOUSE,” *J. Magn. Reson.*, vol. 161, no. 2, pp. 204–209, Apr. 2003.

[87] N. Proietti, D. Capitani, E. Pedemonte, B. Blümich, and A. L. Segre, “Monitoring degradation in paper: non-invasive analysis by unilateral NMR. Part II,” *J. Magn. Reson.*, vol. 170, no. 1, pp. 113–120, Sep. 2004.

[88] C. Casieri, S. Bubici, I. Viola, and F. De Luca, “A low-resolution non-invasive NMR characterization of ancient paper,” *Solid State Nucl. Magn. Reson.*, vol. 26, no. 2, pp. 65–73, Sep. 2004.

[89] F. J. Rühli, T. Böni, J. Perlo, F. Casanova, M. Baias, E. Egarter, and B. Blümich, “Non-invasive spatial tissue discrimination in ancient mummies and bones in situ by portable nuclear magnetic resonance,” *J. Cult. Herit.*, vol. 8, no. 3, pp. 257–263, Jul. 2007.

[90] H. Piepenbrink, J. Frahm, A. Haase, and D. Matthaei, “Nuclear magnetic resonance imaging of mummified corpses,” *Am. J. Phys. Anthropol.*, vol. 70, no. 1, pp. 27–28, May 1986.

[91] W. L. Rollwitz and G. A. Persyn, “On-stream NMR measurements and control,” *J. Am. Oil Chem. Soc.*, vol. 48, no. 2, pp. 59–66, Feb. 1971.

[92] K. Kopinga and L. Pel, “One-dimensional scanning of moisture in porous materials with NMR,” *Rev. Sci. Instrum.*, vol. 65, no. 12, pp. 3673–3681, Dec. 1994.

[93] L. Pel, K. Kopinga, G. Bertram, and G. Lang, “Water absorption in a fired-clay brick observed by NMR scanning,” *J. Phys. Appl. Phys.*, vol. 28, no. 4, p. 675, 1995.

[94] L. Pel, K. Hazrati, K. Kopinga, and J. Marchand, “Water absorption in mortar determined by NMR,” *Magn. Reson. Imaging*, vol. 16, no. 5–6, pp. 525–528, Jun. 1998.

[95] P. Blümler, C. W. Windt, and D. van Dusschoten, “Magnetic resonance of plants,” *Nova Acta Leopoldina*, vol. 357, pp. 17–30, 2009.

[96] H. . Pedersen, S. Ablett, D. . Martin, M. J. . Mallett, and S. . Engelsen, “Application of the NMR-MOUSE to food emulsions,” *J. Magn. Reson.*, vol. 165, no. 1, pp. 49–58, Nov. 2003.

[97] S.-M. Kim, P. Chen, M. J. McCarthy, and B. Zion, “Fruit Internal Quality Evaluation using On-line Nuclear Magnetic Resonance Sensors,” *J. Agric. Eng. Res.*, vol. 74, no. 3, pp. 293–301, Nov. 1999.

[98] P. Poulichet, L. Fakri-Bouchet, C. Delabie, L. Rousseau, A. Fakri, and A. Exertier, “Optimisation and realisation of a portable NMR apparatus and micro antenna for NMR,” in *Design, Test, Integration and Packaging of MEMS/MOEMS (DTIP), 2011 Symposium on*, 2011, pp. 193–196.

[99] A. E. Marble, I. V. Mastikhin, B. G. Colpitts, and B. J. Balcom, “Designing Static Fields for Unilateral Magnetic Resonance by a Scalar Potential Approach,” *IEEE Trans. Magn.*, vol. 43, no. 5, pp. 1903–1911, May 2007.

[100] “ANSYS - Simulation Driven Product Development.” [Online]. Available: http://www.ansys.com/. [Accessed: 13-Aug-2014].

[101] E. P. Furlani, *Permanent Magnet and Electromechanical Devices: Materials, Analysis, and Applications*, 1 edition. San Diego, Calif: Academic Press, 2001.

[102] J. M. D. Coey, *Magnetism and Magnetic Materials*. Cambridge: Cambridge University Press, 2010.

[103] D. C. Jiles, *Introduction to Magnetism and Magnetic Materials, Second Edition*. CRC Press, 1998.

[104] B. D. Cullity, *Introduction to Magnetic Materials*, 2 edition. Wiley-IEEE Press, 2010.

[105] V. Demas and P. J. Prado, “Compact magnets for magnetic resonance,” *Concepts Magn. Reson. Part A*, vol. 34A, no. 1, pp. 48–59, Jan. 2009.

[106] Peter Kohnke, *ANSYS, Inc. Theory Release 5.7*. SAS IP, Inc.

[107] “HKCM MAGNETS from STOCK, from FACTORY & MAGNETS ON DEMAND.” [Online]. Available: https://www.hkcm.de/expert.php. [Accessed: 11-Jul-2014].

[108] P. Poulichet, Hung Dang Phuc, Tien Truong Cong, Latifa Fakri-Bouchet, Abdennasser Fakri, and Christophe Delabie, “Simulation and optimisation of homogeneous permanent magnet for portable NMR applications,” *8th International Conference on Sensing Technology*, Liverpool, UK., 04-Sep-2014.

[109] B. D. Armstrong, M. D. Lingwood, E. R. McCarney, E. R. Brown, P. Blümler, and S. Han, "Portable X-band system for solution state dynamic nuclear polarization," *J. Magn. Reson.*, vol. 191, no. 2, pp. 273–281, Apr. 2008.

A. Publications

1. **Hung Dang Phuc**, Patrick Poulichet , Tien Truong Cong, Abdenasser Fakri, Christophe Delabie, and Latifa Fakri-Bouchet." Design and construction of light weight portable NMR Halbach magnet". *International Journal on smart sensing and intelligent system*. Vol. 7, No.4, December 2014. Page 1555-1578.
2. Patrick Poulichet , **Hung Dang Phuc**, Tien Truong Cong, Latifa Fakri-Bouchet , Abdenasser Fakri and Christophe Delabie. "Simulation and optimization of homogeneous permanent magnets for portable NMR applications". The proceeding of the 8th International conference on sensing and technology (ISTC) program. Page 401-406.
3. Tien Truong Cong, Josué Tréjo Rosillo, **Hung Dang Phuc**, Patrick Poulichet, Huy Hoang Pham, Abdennasser Fakri, and Latifa Fakri-Bouchet. **"**The inductance of the straight conductors and the planar coils of rectangular cross section"**.** Submitted to IEEE Transactions on Microwave Theory and Techniques. Submitted.
4. T. Truong-Cong, J.T. Rosillo, **Hung Dang Phuc**, P. Poulichet,.H. Pham, A. Fakri and L. Fakri-Bouchet. Analytical simulations for NMR microcoil performances improvement. Submitted à JMR.

B. Oral communications

1. **Hung Dang Phuc**, Patrick Poulichet , Tien Truong Cong, Abdenasser Fakri, Christophe Delabie, Huan Phan Dinh and Latifa Fakri-Bouchet. ." Homogeneous permanent magnet for portable NMR system: Modeling and optimization". ESMRMB**,** *The 30th annual scientific meeting, October 3-5, 2013, Toulouse. France.*
2. T. Cong Truong, J. Trejo Rosillo, **H. Phuc Dang**, H. Huy Pham, A. Fakri and L.Fakri-Bouchet. A method for improving the performance of implantable RF microcoil designed for MRI and MRS of murine brain at 4.7T. *8 ème*
   Journées Maghreb Europe Matériaux et Applications et Applications aux Dipositifs et Capteurs, MADICA Sousse (Tunisie), 2012.

C. Posters

1. Patrick Poulichet, **Hung Phuc Dang**, Tien Truong Cong, Latifa Fakri-Bouchet, Abdenasser Fakri and Christophe Delabie "Optimized modelisation of homogeneous permanent magnet for portable NMR system"**.** *9th International Symposium on Electric and Magnetic Fields (EMF 2013) – Bruges, Belgium.*
2. **Hung Dang Phuc**,Tien Truong Cong, Huan Phan Dinh, Abdennasser Fakri, Patrick Poulichet, and Latifa Fakri-Bouchet, "Mobile NMR system : Modeling and design of Mandhalas configuration magnets". *6ème Colloque Interdisciplinaire en Instrumentation, C2I101, Lyon-Villeurbanne, 29-30 Janvier 2013.*
3. T. Truong Cong, J.T. Rosillo, **H. Dang Phuc**, H.H. Pham, P. Poulichet, A. Fakri and L. Fakri-Bouchet. A method for improving the performance of implantable RFmicrocoil designed for MRI and MRS of murine brain at 4.7T. *6ème*
   Colloque Interdisciplinaire en Instrumentation, C2I101, Lyon-Villeurbanne, 29-30 Janvier 2013.

4. T. Truong Cong, J. T. Rosillo, **H. Dang Phuc**, H.H. Pham, P. Poulichet, A. Fakri and L. Fakri-Bouchet. A Numerical method for design of implantable RF microcoil for MRI and MRS 4.7T. *The International Conference on Advanced Materials forPhotonics, Sensing and Energy Conversion Applications* (AMPSECA 2012).
5. T. Cong Truong, J.T. Rosillo, **H. Phuc Dang**, H.H. Pham, A. Fakri, L. Fakri-Bouchet. A Numerical methods for improving the performance of implantable NMR microcoil. *4ème réunion de Institut Thématique multi-Organismes (ITMO) Technologiespour la Santé*, 8 et 9 octobre 2012 Lille.

DESIGN AND CONSTRUCTION OF LIGHT WEIGHT PORTABLE NMR HALBACH MAGNET

Hung Dang Phuc[1], Patrick Poulichet[2], Tien Truong Cong[1], Abdennasser Fakri[2], Christophe Delabie[2], Latifa Fakri-Bouchet[1]

Laboratoire CREATIS UMR CNRS 5220, INSERM U1044, INSA de Lyon, Universite de Lyon, Lyon 1
3, rue Victor-Grignard
69616 Villeurbanne, France[1]

ESIEE, 2 BD Blaise Pascal
93162 Noisy Le Grand, France[2]
Emails: hung@creatis-insa-lyon.fr, p.poulichet@esiee.fr, latifa.bouchet@univ-lyon1.fr

Submitted: Sep. 27, 2014 ***Accepted: Nov. 5, 2014*** ***Published: Dec. 1, 2014***

Abstract- A light weight, simple design NMR apparatus consists of 24 identical magnets arranged in Halbach array was designed and built. The homogeneity of the magnetic field B_0 can be improved by dividing a long magnets into several rings. The size of the useful volume depends on both the gap between each ring and some others shim magnets. Our aim is to enhance the sensitive volume and to maintain the highest magnetic static field (B_0). This apparatus generates a B_0 field strength of about 0.1 T. This work focuses on the magneto-static simulation of NdFeB magnets arrangement and on the comparison with the measurement of the magnetic field strength and homogeneity in three dimensions (3D). The homogeneity of the magnetic field B_0 is optimized with the help of CAD and mathematical software. Our results were also validated with a Finite Element Method (FEM). The simulation results of the strength and of the homogeneity of B_0 field were compared to those obtained with a digital gaussmeter. The homogeneity in the magnet longitudinal axis and the field B_0 strength are similar. However, the homogeneity in transverse plane differs from simulation and measurement because of the quality of the magnets. In order to improve the homogeneity, we propose a new shim method.

Index terms*:* Nuclear Magnetic Resonance (NMR); Low field; Portable Permanent Magnet; Halbach; Shim magnets; Homogeneity, Simulation, Finite Element Method (FEM).

I. INTRODUCTION

In recent years, NMR/MRI portable devices [1][2] have drawn attention of numerous researcher teams. They are used for variety of applications, from medical diagnosis [3] to archaeological analysis [4], nondestructive material testing [5], evaluation of water presence in building materials [6] and food emulsions [7]. Different magnets designs have been proposed by many groups of researchers. They can be divided into two groups: the magnets *ex-situ* [8][9] and the magnets *in-situ* [10][11]. The first group has the simple configuration with the sensitive volume near their surface and the samples under test are located outside the magnets. Thus, they can be used for the experimental investigation of objects with unlimited dimensions. Although the *ex-situ* magnets have simple shape and are light weight, they are difficult to achieve in terms of homogeneity of the magnetic field in the sensitive volume.

In comparison, the *in-situ* magnets have their static field reinforced inside their bore center and canceled outside of the structure. Thus, their magnetic field is homogeneous inside the structure. The *in-situ* magnets use Halbach [11] or Aubert Configurations [17].

Starting with the proposition of Klaus Halbach in 1980 [12], the Halbach ring consists of segments of permanent magnets put together in an array. This creates a homogeneous field in the transverse plane. Based on this principle, the Halbach structure with discrete magnets for portable NMR magnet known as NMR Mandhalas was given in 2004 by Raich and Blümler [13]. It is based on an arrangement of identical bar magnets, described by the analytical equations reported in literature [14]. This concept has been widely used for building prototypes due to their easy assembly and the accessibility of their region of interest. The homogeneity of Halbach type is poor compared to traditional magnets [15]. For measurement of the relaxation times T2 and T1 or the spectrum, the inhomogeneity should not be higher than 10 ppm. To insure the sufficient field homogeneity for NMR experiments, a popular method is to add shimming magnets. The concept of movable permanent magnets in the shim unit of a Halbach array was reported by Ernesto Danieli et al [16]. Another method of shimming, based on the spherical harmonic expansion, proposes a complete procedure for permanent magnet design, fabrication, and characterization [17][18]. The advantages of Halbach structure motivated us to choose it for building our prototype.

However, increasing homogeneity while maintaining high field strength is a challenge when building NMR portable devices. In this study, we propose a light weight magnet system for NMR applications. Such system consists of two rings of 12 magnets arranged in a Halbach configuration. Its homogeneity and its magnetic field strength B_0 are simulated and calculated by RADIA and Mathematica software, and confirmed by Finite Element software 'ANSYS multiphysics'. In order to improve its homogeneity, we used eight small shim magnets placed inside its bore. By optimizing the position of these magnets, we have reached a configuration with a significant increase in the homogeneous region. Based on the results of simulations, we designed and built a prototype. The magnetic field strength and homogeneity of our prototype were also

measured by a digital gaussmeter, and then compared to those obtained by simulation. Comparison shows that homogeneity in the longitudinal axis of apparatus and field strength B_0 are similar. However, the homogeneity in transverse plane differs from results of simulation and measurement. One explanation could be the real characteristics of the used magnets and their quality. This difference has been also discussed in this study.

II. MATERIALS AND METHODS

In most of the Halbach configurations, the static field B_0 is transverse to the cylindrical axis as shown in Figure 6-1. The direction of magnetization of each magnet is defined by two angles α_i and β_i.

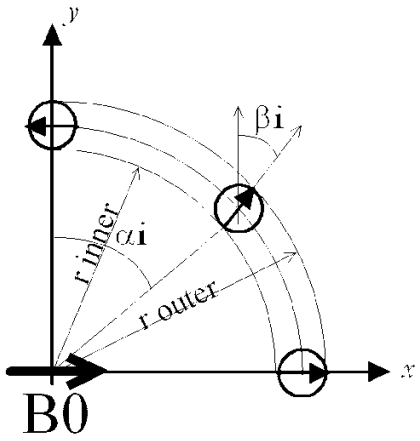

Figure 6-1: Geometric parameters of Halbach structure.

The i^{th} magnet is placed on a circle at an angle α_i as $\alpha_i = \frac{2\pi.i}{n}$ and its magnetization is defined by an angle β_i as $\beta_i = 2.\alpha_i$. Where n is the number of magnets (i = 0, 1, 2… n-1). Our configuration has 12 magnets placed on a circle of radius r0 = 30 mm. As shown in Figure 6-2-a, each magnet is placed at an angle $\alpha_i = i\frac{\pi}{6}$ and its magnetization is rotated by an angle $\beta_i = i\frac{\pi}{3}$. For compensation of the magnetic field outside of a ring, two others rings are placed in alignment as shown in Figure 6-2-b. The geometric parameters are depicted in Figure 6-2 and Figure 6-7.

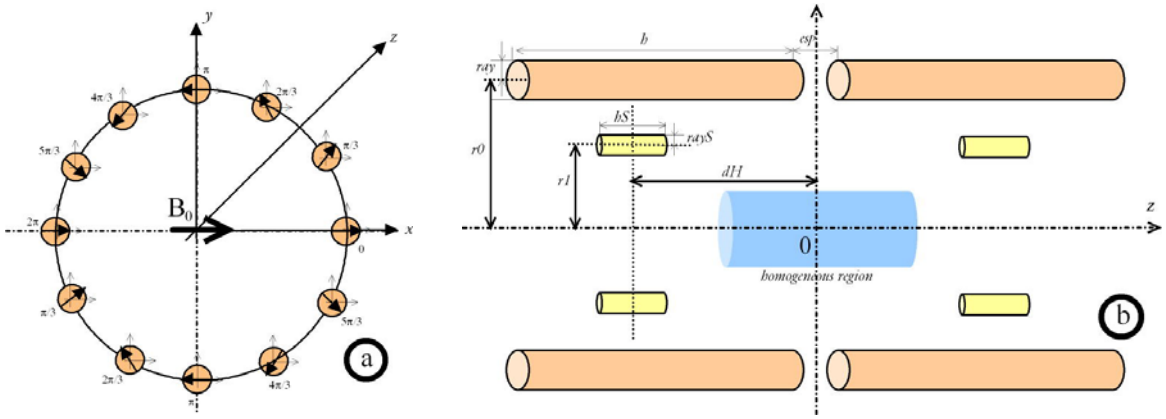

Figure 6-2: Position of magnets and the direction of their magnetization.

The geometric parameters are displayed in Table 6-1.

Table 6-1: Geometric parameters of our configuration.

Names of the parameter	Definitions	Dimensions
r0	Radius of the ring	30 mm
h	Height of the ring	50 mm
ray	Radius of magnets	4 mm
hS	Height of shim magnets	6 mm
rays	Radius of shim magnets	2 mm

To calculate the magnetic field of the magnet configuration, RADIA [19] and ANSYS [20] softwares were used. RADIA was developed to design the Insertion Devices for Synchrotron light sources. It uses boundary integral methods. Each volume created to represent the magnets is subdivided in a number of sub-elements to solve the general problem of magnetization. The solution is performed by building a large matrix with represents mutual interactions between the objects.

ANSYS is a multiphysics software using FEM modeling. Each volume is divided with sub-elements. Even the air between and around the magnets has to be meshed. The flux conditions have to be placed outside the global volume in order to apply parallel or normal condition. Usually, boundary integral method is considered faster than FEM. In our case, these two

complementary methods are implemented: RADIA allowing a faster simulation, is used for optimization and ANSYS is used for verification and validation of results. The size of the meshing is reduced until the simulation results do not change.

The properties of the material modeled magnets during simulation were chosen to represent magnets from "HKCM MAGNETS from STOCK" [21]. The magnet material is Neodymium NdFeB with the following characteristics:

- a saturation magnetization of 1.37 T,
- a coercivity Hc = 1000 kA/m,
- the diameter and the length of the magnets are respectively 8 mm and 50 mm,
- the maximal operating temperature is 120 °C,
- the temperature coefficient is 0.11 %.°C^{-1},
- and the magnetization is oriented along the diameter.

In order to calculate the homogeneity, the values for the magnetic field are selected in the homogeneous region and treated by Matlab Software. The homogeneity is calculated by the formula (1).

$$Homogeneity = \frac{\sum_i^n \frac{Abs\left(B_i - B\right)}{B} 10^6}{m} \quad (1)$$

Where,

- Bi is the value of magnetic field at the ith position in the homogeneous region,
- B is the magnetic field value at the center of the homogeneous region,
- m is the number of mesh nodes in the homogeneous region.

III. SIMULATION RESULTS

a. Optimization of the gap between two rings without shim results

Our NMR portable magnet model is constituted with 24 magnets, placed as displayed in Figure 6-7 and used for the simulations with ANSYS and RADIA. Considering the magnetic field B_0 oriented along Ox axis and the gap between two rings *esp* = 0, the maximum value of B_0 calculated with RADIA is about of 0.103 T and of 0.11 T obtained with ANSYS Analysis. The difference of calculation between RADIA and ANSYS is about 6.79 %. This difference can be accounted for by the problem of mesh size convergence. It means that the results obtained with

fine meshes are higher than those obtained with coarse meshes. Furthermore, the difference is acceptable.

Figure 6-3-a represents the variation of the magnetic field B_0 along the Ox axis. The value of the magnetic field is almost constant for 1.8mm < x < 4.2mm. Figure 6-3-b represents the variation of the magnetic field B_0 in the plane xOy. Each shades of color represent a variation of 50 ppm of the inhomogeneity $\frac{\Delta B_0}{B_0}$. In a rectangle of 5 × 6.4 mm^2, the inhomogeneity $\frac{\Delta B_0}{B_0}$ is larger than 450 ppm (RADIA) and 380 ppm (ANSYS). For an inhomogeneity lower than 100 ppm, the expected volume for experiment is 3 × 3 × 3 mm^3.

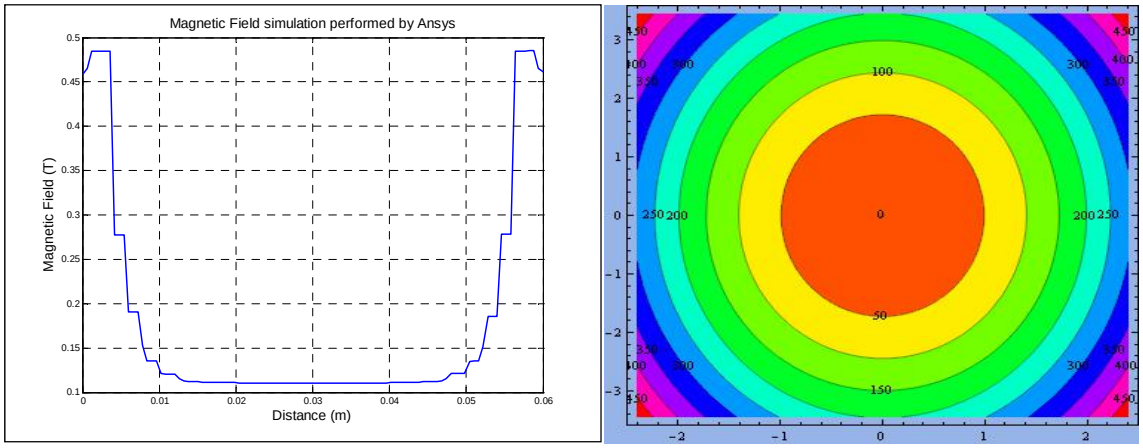

(a) Variation of magnetic field Bx versus x.

(b) Inhomogeneity of the magnetic field Bx versus x and y.

Figure 6-3: Magnetic Field Bx distribution at z = 0 (xOy plane).

The variation of the magnetic field Bx on the xOz plane is shown in Figure 6-4. The magnetic field homogeneity in a region of 5 x 6.4 mm² is about 300 ppm determined by RADIA, while ANSYS gives a result of 200 ppm.

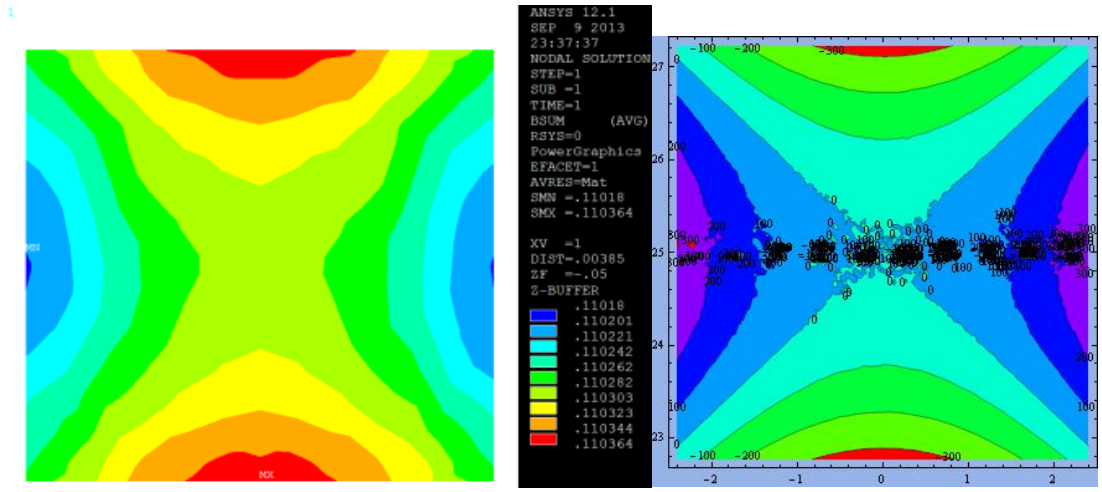

(a) ANSYS Result. (b) RADIA Result.

Figure 6-4: Magnetic Field Bx distribution in the region of 5 x 6.4 mm² in xOz plane.

The variation of profile of the magnetic field Bx along Oz axis depends on the *esp* gap between the two rings. To optimize this gap, we increased the value of *esp* by steps of 0.1mm. Figure 6-5 shows Bx profile for four values of *esp*. When *esp* = 0, the magnetic field outside one ring does not compensate exactly the one of the other ring. For *esp* = 0.9 mm, the compensation is optimum and the magnetic field at the center is almost constant.

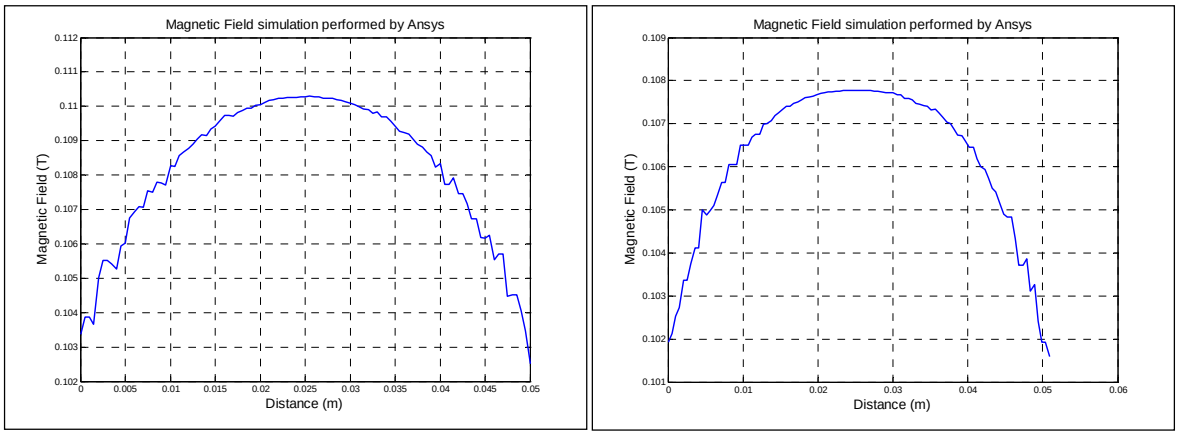

(a) *esp* = 0 mm. (b) *esp* = 0.5 mm.

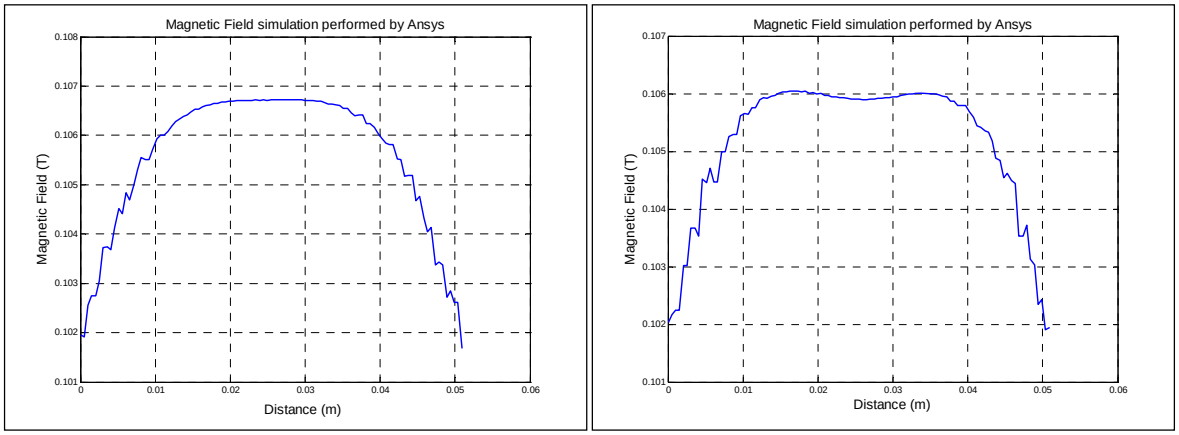

(c) *esp* = 0.9 mm. (d) *esp* = 1.3 mm.

Figure 6-5: The field profile for different values of the gap *esp* between the two rings.

The "useful" volume for NMR sample is determined from the coordinates (x,y,z) of the point where Bx is maximal. Then, the volume is calculated with the coordinates (x,y,z) that generate a variation of $\frac{\Delta B_0}{B_0}$ not higher than 100 ppm. The Figure 6-6 shows that the volume of the homogeneous region is a function of the *esp*. The optimal value of *esp* determined by RADIA is around 0.77 mm and the "useful" volume is about 2640 mm^3. When the spacing *esp* between the two rings is optimized, the "useful" volume is increased by a ratio of around 80. This is caused by the decrease of the magnetic field outside one ring, which is similar to the increase of the other ring. There's an optimum gap between the two rings where the sum of the variations of the magnetic field outside the rings are canceled.

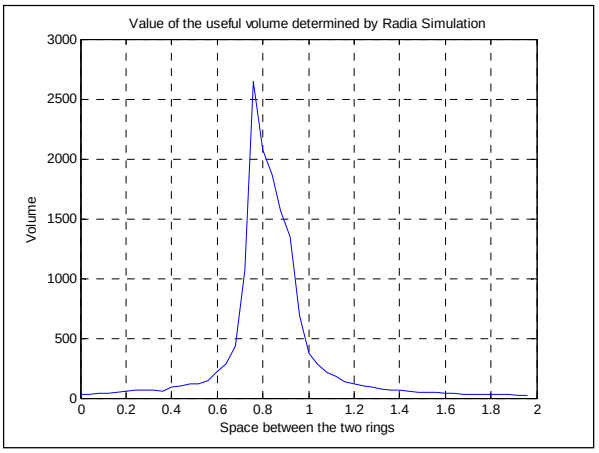

Figure 6-6: Volume (mm^3) for a variation of $\frac{\Delta B_0}{B_0}$ lower than 100 ppm is a function of the gap *esp*.

b. Optimization of the configuration with shim magnets

Although the magnetic field homogeneity increases by adjusting the gap *esp* between the two rings, the inhomogeneity of magnetic field also comes from magnetic material (dispersion of both the value and the orientation of the magnetization), from errors in fabrication process and positioning of the array magnets. These factors cannot be corrected only by adjustment of *esp*. To overcome these difficulties, the shim magnets are considered as a way to compensate for the inhomogeneity of the magnetic field [16][17][18]. In our case, we use eight small magnets placed inside the bore of the two rings as shown in the Figure 7.

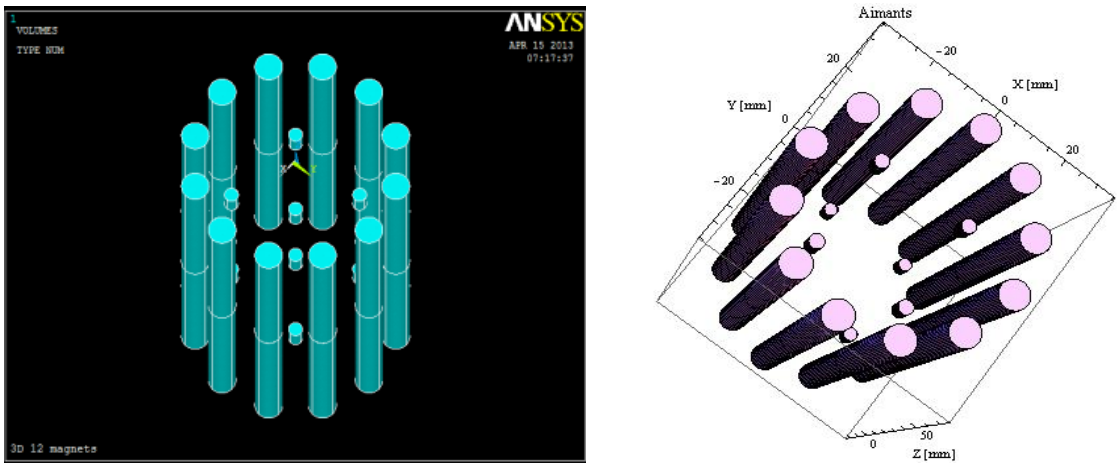

(a) With ANSYS. (b) With RADIA.

Figure 6-7: Halbach configuration with 24 magnets and 8 shim magnets, modeled with ANSYS and RADIA.

The direction of magnetization of the shim magnets is defined as shown in Figure 8.

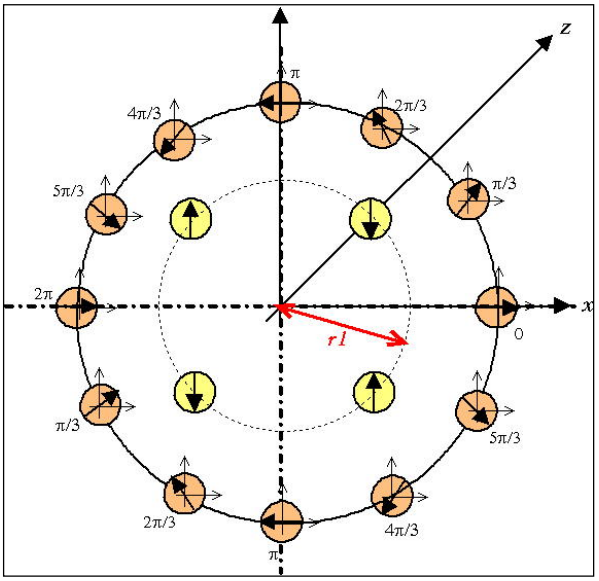

Figure 6-8: Direction of magnetization of the 8 shim magnets.

There are three variables that need to be optimized: *esp,* r1 and dH. The optimization objective is to determine the values for *esp*, r1 and dH that maximize the volume for an inhomogeneity of 100 ppm. The flow chart shown in Figure 9 describes the optimization process implemented with Mathematica software and the calculation of the magnetic field with RADIA software. To avoid the superposition of the main magnets and the shim magnets, we set the range of r1 from 15 to 23 mm and the one for *esp* ranging from 0.1 to 0.6 mm. The optimal value for *esp,* considered here, is different from the value considered before because of the presence of shim magnets.

Each step of increase of r1 is 1 mm while correspondent value of esp is 0.1 mm. Each possible values of r1 is placed in a matrix. The corresponding magnetic field and then the three coordinates (x,y,z) for an homogeneity lower than 100 ppm are also determined. For each value of r1, we have a value for the homogeneous volume. The value of r1 leading to the highest value of the volume will be saved. The same process is repeated with the others parameters *esp* and dH. After a variation of one parameter, the variation is refined around the best value previously obtained. It's very important to choose good initial conditions and started the variation of one parameter with reliable value for the others parameters. This method was preferred to the use of Mathematica software optimization functions, as FindMaximum.

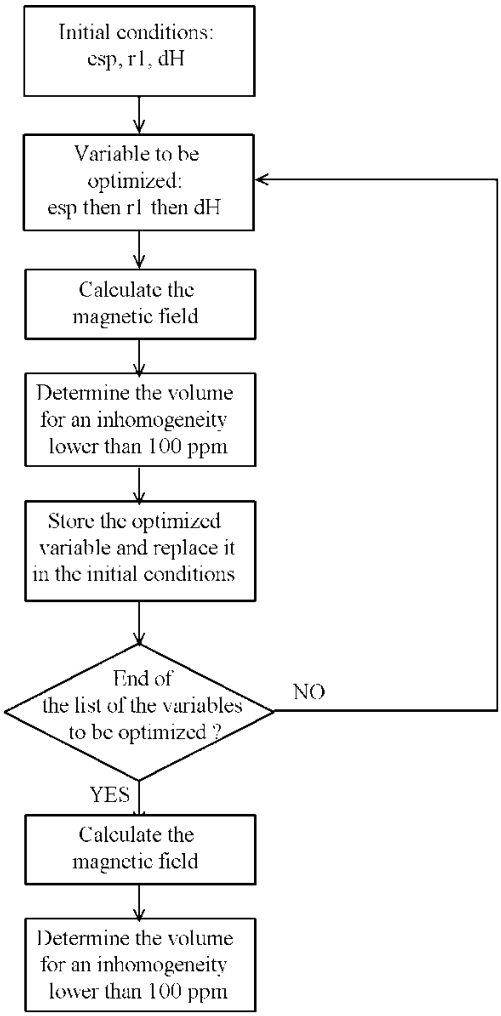

Figure 6-9: Flow chart of our configuration with 24 main magnets and 8 shim magnets.

The optimized parameters are presented in the Table 6-2.

Table 6-2: The geometric parameters of an optimal configuration.

Name of the parameter	Dimension
esp	0.2 mm
r1	20 mm
dH	26 mm

The optimizations results allow a great improvement of homogeneity, as it can be seen in Figure 6-10. It shows that the inhomogeneity of the magnetic field calculated in a 7 x 8 mm² region is 90 ppm after shimming while the value before shimming was 370 ppm.

The magnetic field inhomogeneity calculated by RADIA and by ANSYS is in good agreement. However, ANSYS gives always smaller useful volumes than those obtained by RADIA due to the method of calculation. This can be explained by the fact that RADIA result is the highest value at the region edge while ANSYS compute the mean value for the overall region.

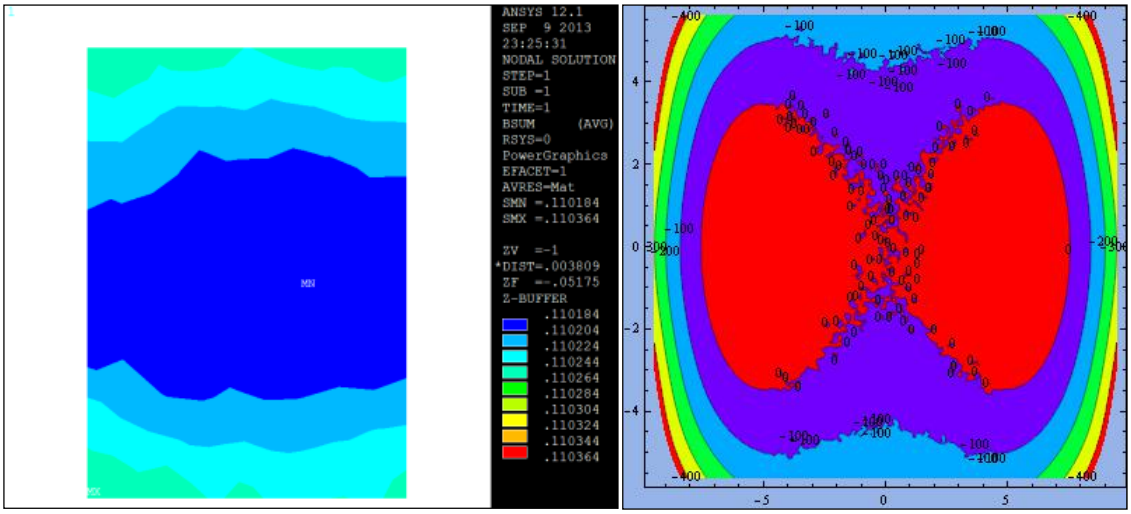

(a) Before shimming. (b) After shimming.

Figure 6-10: Magnetic field homogeneity in the xOy plane and z = 0.

The Figure 6-11 shows great improvement of homogeneity along Oz axis. The size of the homogeneous region increases drastically in length from 8 mm to 20 mm. This is confirmed by the stability of the magnetic field profile of the Figure 6-12.

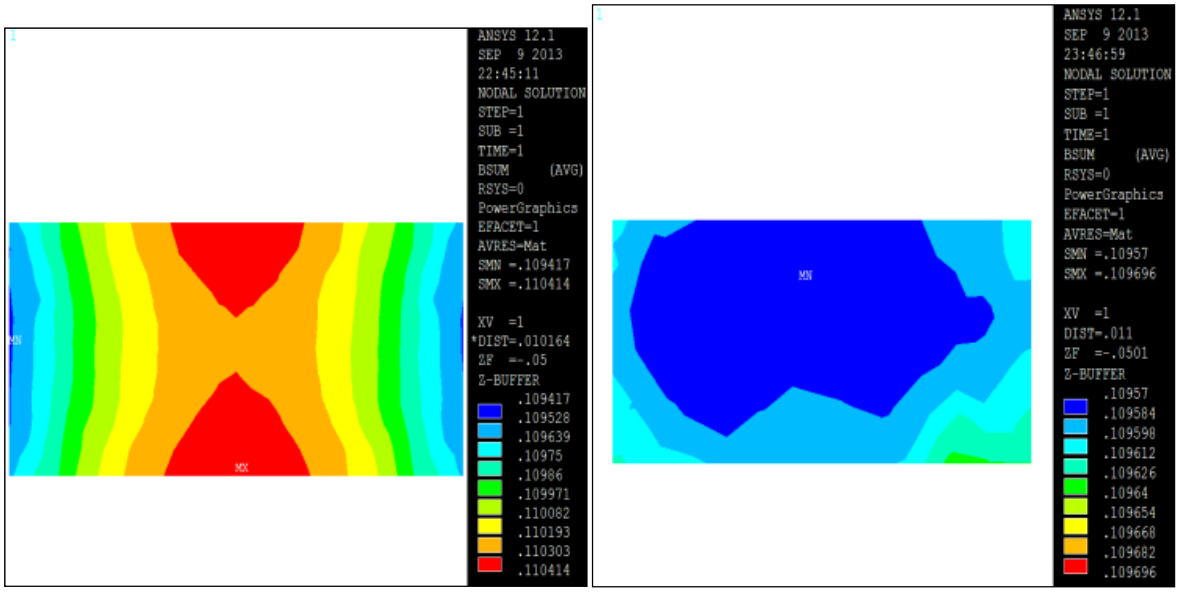

(a) Before shimming. (b) After shimming.

Figure 6-11: Magnetic field homogeneity in the region 8 x 20 mm^2 along Oz axis

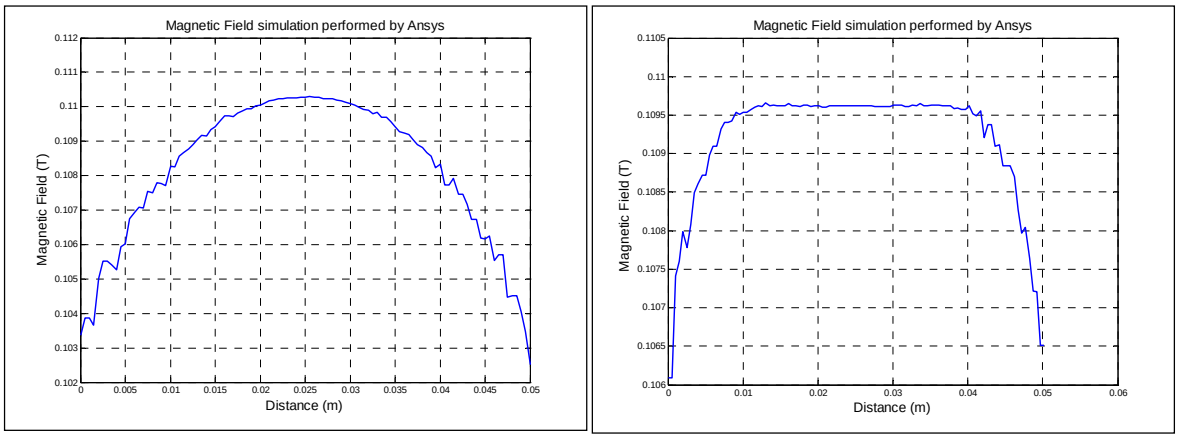

(a) Before shimming. (b) After shimming.

Figure 6-12: Magnetic field profiles at the center of our Halbach arrangement of magnets.

As shown in Figure 6-13, the inhomogeneity of magnetic field in a volume of 7 x 8 x 20 mm^3 is respectively 4320 ppm without shim magnets and of 230 ppm with the shim magnets.

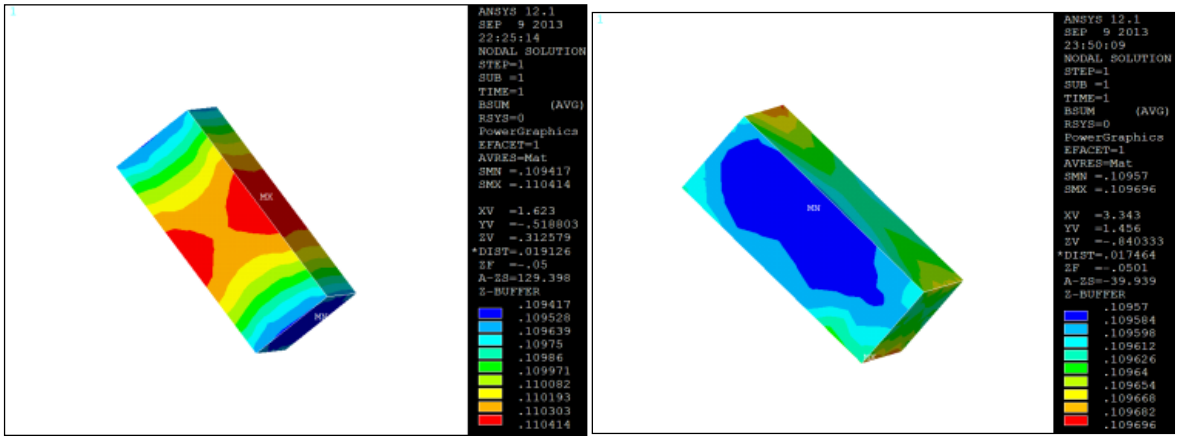

(a) Before shimming. (b) After shimming.

Figure 6-13: Magnetic field distribution in the 3D sensitive volume: 7 x 8 x 20 mm^3.

IV. PROTOTYPE DESIGN AND EXPERIMENTAL SET UP

a. Prototype design

The prototype consists of two rings of 12 magnets each one. These magnets are placed on a circle of 30 mm radius and inserted into the twelve holes of two aluminum frames. The two rings of the prototype, fixed by some screws on the aluminum frames, can slide on three rods, to achieve the desired position. The highest value of the magnetic field magnets measured at the center of the frame, allow us to determine their rotation angles and to fix them by the dedicated screws as shown on Figure 6-14.

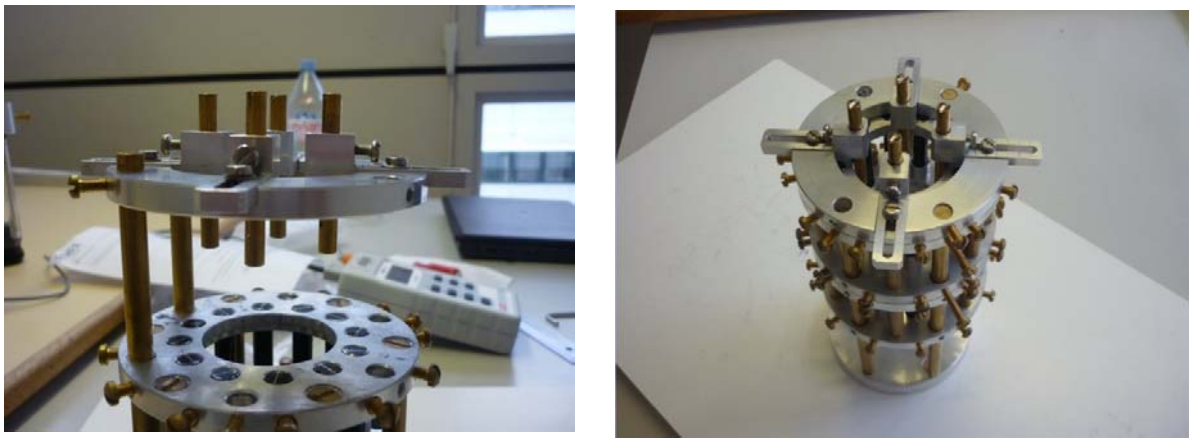

(a) Shim magnets that can move along three degrees of freedom. (b) Halbach prototype with the slide-blocks used to move the shim magnets in radial direction.

Figure 6-14: Picture of the prototype with shim magnets.

Each shim magnet shown on the Figure 6-14 is glued in a nonmagnetic cylinder. These cylinders can rotate, move along the longitudinal axis and slide along the radius of the prototype to find the optimal position of the shim magnets. These cylinders are placed in the holes of sliding-blocks moving on the four apertures of an aluminum frame concentric with the prototype.

b. Experimental setup

The magnetic field is measured by the digital gaussmeter Hirst GM08 with sensitivity limit of 10^{-4} T in the range 0 – 0.299 T. The micropositioner Signatone S-926 is used to control the probe movement in three directions as shown in the Figure 6-15. The resolution is 254 µm per knob revolution. Matlab software carries out the plotting of the measurable values.

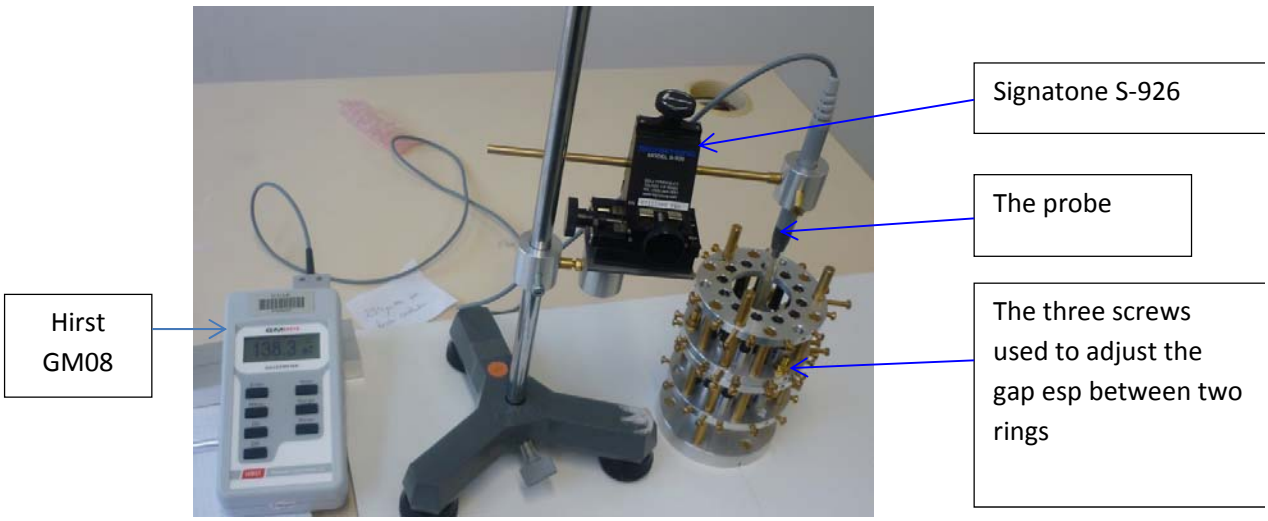

Figure 6-15: Measurement set-up of the magnetic field in the prototype.

V. EXPERIMENTAL RESULTS

a. Measurements before shimming

To optimize the gap *esp* between two rings, at the beginning, it was set at 0 mm, and was progressively increased by turning the screws on the frame of the device (Figure 6-15).

The Figure 6-16 shows the magnetic field profiles in Oz direction for four different gaps *esp* between the rings. The optimal gap is displayed in Figure 6-16-c where the magnetic strength is equal to 0.138 T and remains constant for the distance of 10 mm. The shapes of the curves plotted in the Figure 6-16 are similar to those obtained by simulation in the Figure 6-5.

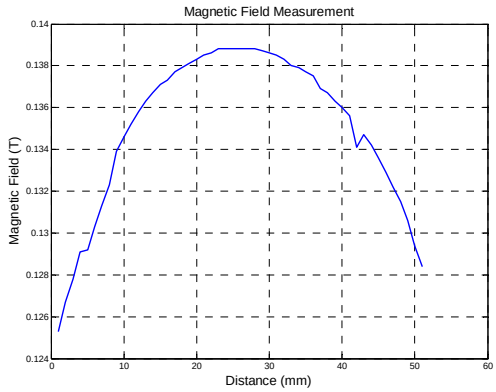

(c) *esp = 0.*

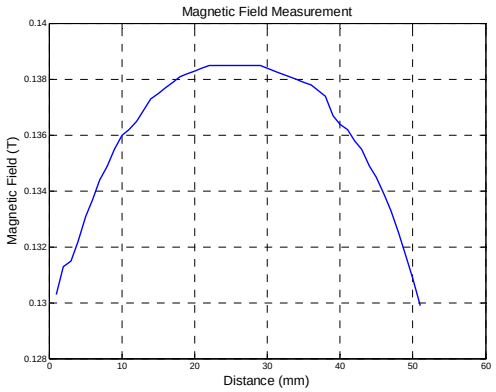

(b) *esp = 1.6 mm.*

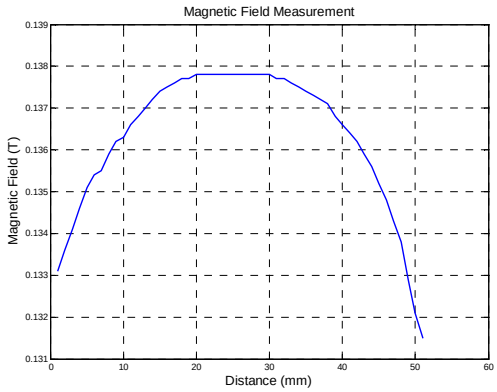

(c) *esp = 2.4 mm.*

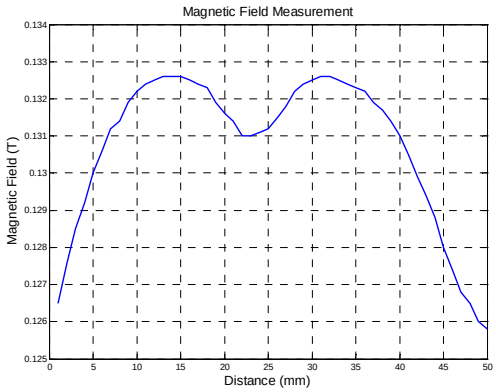

(d) *esp = 6.4 mm.*

Figure 6-16: Magnetic field profiles in Oz direction for different esp values.

The magnetic field distribution shown in Figure 6-17, is measured at z = 0, in the region 6 x 6.5

mm² (xOy). In this region, the homogeneity value is respectively 1399 ppm calculated by formula (1) and 380 ppm obtained by simulation. It means that the measurable homogeneity is approximately 3.5 times worse than that simulated (Figure 6-3-b).

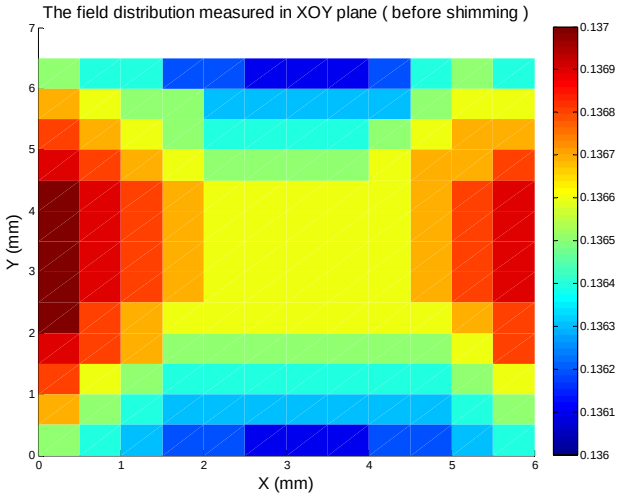

Figure 6-17: The magnetic field distribution in xOy plane obtained by measurement before shimming.

Figure 6-18 shows the magnetic field distribution measurement in xOz plane in the region of 7 x 20 mm². In this region the homogeneity calculated by formula (1) is equal to 1426 ppm. This homogeneity is of 4415 ppm in the volume of 6 x 7 x 20 mm^3.

The magnetic field distribution is similar to the simulation as shown in the Figure 6-4.

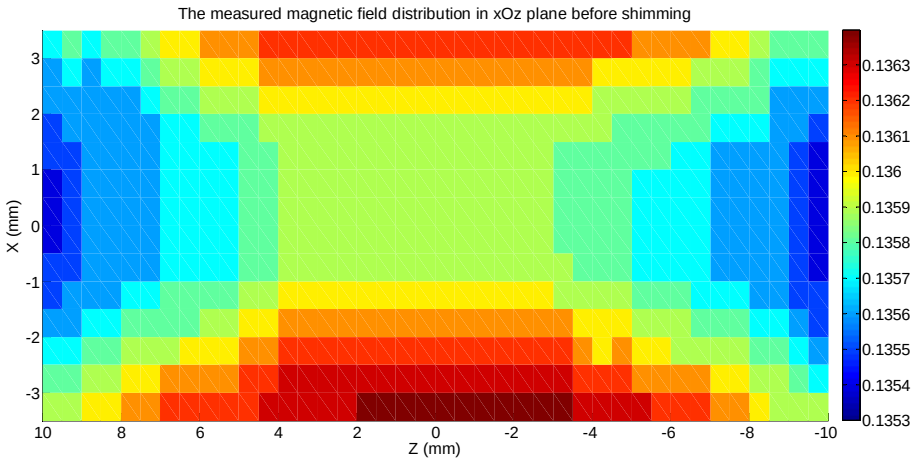

Figure 6-18: The measured magnetic field distribution in xOz plane before shimming.

b. Measurements after shimming

Figure 6-19 shows the improvement of the magnetic field homogeneity in xOy plane in the same region 6 x 6.5 mm². The homogeneity is respectively, 1399 ppm before shimming calculated by formula (1) and 817 ppm after shimming.

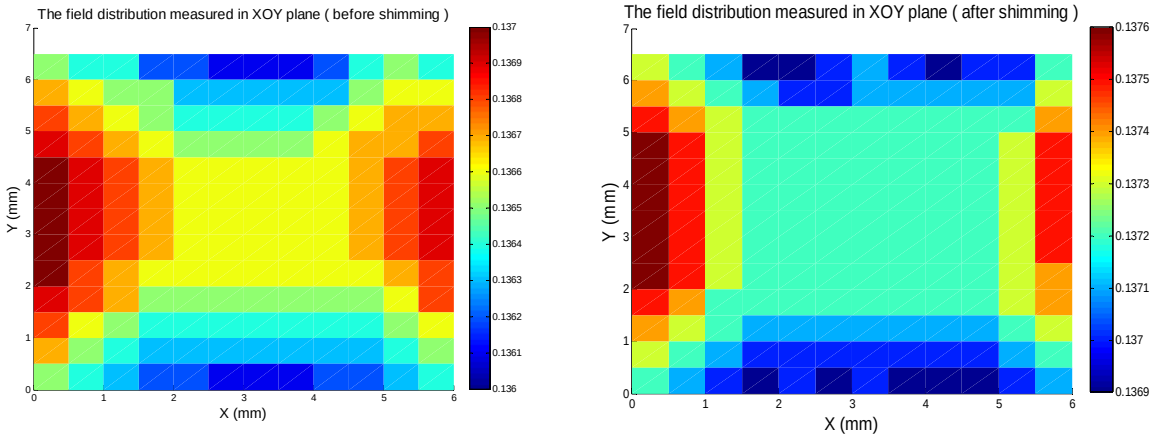

(a) Before shimming. (b) After shimming.

Figure 6-19: Magnetic field homogeneity at z = 0 in xOy plane.

In the region of 7 x 20 mm^2 (xOz plane), the homogeneity calculated by formula (1) is 894 ppm

while it is 1426 ppm without shim magnets. The magnetic field homogeneity with shim magnets shows in Figure 6-20, achieved in the volume 6 x 7 x 20 mm^3 is 1335 ppm in comparison to 4415 ppm obtained without shim magnets. The magnetic field homogeneity is 3.3 times better. Figure 6-20 shows the improvement of the homogeneity that is approximate 5.8 times worse than the simulated value. The measured and simulated field distribution in xOz plane are similar as shown in the Figure 6-4.

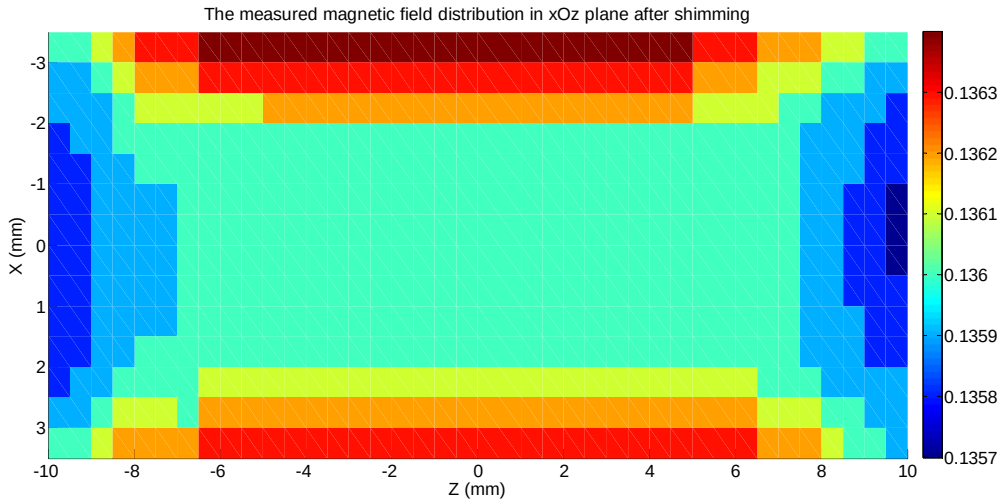

Figure 6-20: The magnetic field homogeneity in xOz plane after shimming.

VI. DISCUSSION

The difference between the simulated and measured values of the magnetic field homogeneity is due to the poor quality of the magnets. There is a large dispersion of the magnets properties. For our prototype we selected 24 magnets among 27 having a similar magnetic field strength and the magnets 5, 22 and 23 was rejected. This was done with the measurement of the magnetic field on each tip of the magnet cylinder. Table 6-3 shows the value of B_1 and B_2 for 27 magnets and the misalignment angle α. B_1 and B_2 are respectively the magnetic field in the vicinity of the two faces of the magnet cylinder as shown on the Figure 21. The average value of the magnetic field is around 27.3 mT. The misalignment angle represents the error of orientation of the radial direction of the magnetic field on each face. In ideal case, this angle value is zero but for some magnets this value can reach 17 degrees and the consequence, is an error of homogeneity of the magnetic field.

Table 6-3: Magnetic field and misalignment angle measured on each tip of the 27 magnets.

Magnet	**1**	**2**	**3**	**4**	**5**	**6**	**7**	**8**	**9**	**10**
B_1 (mT)	27.3	27.2	27.3	27.2	27.3	27.2	27.1	27.0	26.9	27.0
B_2 (mT)	27.2	27.1	27.5	27.1	27.0	27.1	27.2	26.9	27.0	27.2
α (degree)	0	0	8	9	17	8	0	0	0	12
Magnet	**11**	**12**	**13**	**14**	**15**	**16**	**17**	**18**	**19**	**20**
B_1 (mT)	27.4	27.2	27.2	27.2	27.3	27.3	27.3	27.4	27.4	27.4
B_2 (mT)	27.5	27.0	27.2	27.4	27.4	27.3	27.5	27.4	27.5	27.2
α (degree)	0	10	0	12	0	0	12	0	0	8
Magnet	**21**	**22**	**23**	**24**	**25**	**26**	**27**			
B_1 (mT)	27.3	27.2	27.6	27.3	27.4	27.4	27.3			
B_2 (mT)	27.3	27.5	27.5	27.4	27.3	27.5	27.4			
α (degree)	0	16	4	6	9	7	8			

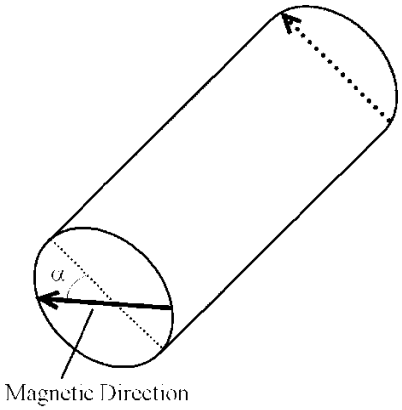

(a) Magnet cylinder with B_1 and B_2 the magnetic field in the vicinity of its two faces and the misalignment angle α.

(b) Picture of Magnet cylinder.

Figure 6-21: A prototype of Magnet cylinder.

In the following, we will study the impact of the error of the misalignment of magnetic directions and the reducing of the homogeneity. During the simulation, an angle error of 3 degrees of the magnetic field direction for four magnets is considered as shown in the Figure 6-22.

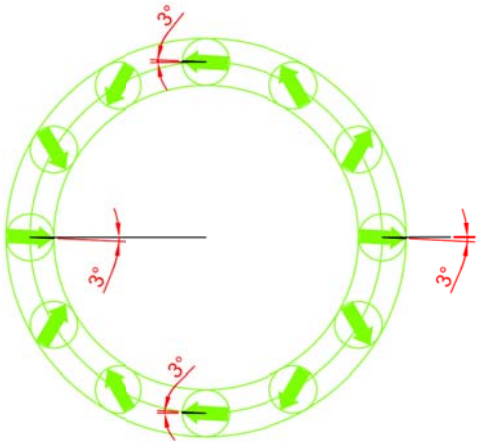

Figure 6-22: Misalignment of the magnetic direction for four magnets.

The results of simulation show that the inhomogeneity of magnetic field drastically increases to 2750 ppm in the region of 6 x 6.5 mm^2 (xOz plane) in comparison to 380 ppm, the value without misalignment error. As shown in the Figure 6-23, the magnetic field distribution is similar to the measurement.

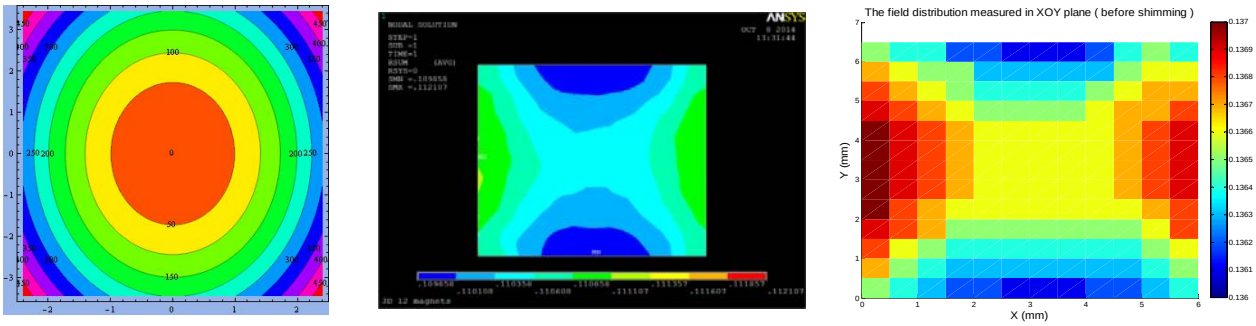

(a) Simulation without misalignment error of the direction of the magnetic field.

(b) Simulation with 3 degree misalignment error.

(c) Field distribution measurement of the prototype.

Figure 6-23: The magnetic field distribution in xOz plane, for ideal case and with error of misalignment of the direction of the magnetic field.

VII. CONCLUSION

The study presented here depicts two methods of simulation and the main measurement results of a light weight NMR portable Halbach type magnet. We described the optimization process of this permanent magnet designed with two rings of 12 magnets each one, that provide a magnetic field B_0 around 0.1 T. The simulation results have been published in [22]. The study describes the used based on the RADIA software process, for calculate and simulate the magnetic field B_0 and its homogeneity. We verified also those results with the finite element software ANSYS multiphysics. The obtained results with the two softwares are in good agreement. Based on the software analysis, we simulated the homogeneity of magnetic field and optimized the gap *esp* of the two consecutive rings to increase the size of the homogeneous region. The optimum gap length is around *esp*= 0.8 mm. The measurement of the magnetic field profile for different values of the gap *esp* between the two rings give a similar value of the optimal gap.

To compensate for the magnetic field inhomogeneity caused by the errors of fabrication process and the dispersion of the magnetic properties of the magnets, we used eight small shim magnets placed at the center of the device. By optimizing their position, the homogeneity had been significantly improved. The results of optimization show that the homogeneity for a given volume (7 x 8 x 20 mm^3) is improved 18 times in comparison to the same configuration without shim magnets. Thus the value of the homogeneity decreases from 4320 ppm to 230 ppm.

For a given volume of 6 x 7 x 20 mm^3, the measurement of the magnetic field variation, shows the

same homogeneity improvement, using the shim magnets. Thus the homogeneity is of 1335 ppm while it was of 4415 ppm for the case without shim magnets. The magnetic field homogeneity was enhanced of a 3.3 factor. However, there is still a difference between the simulation and the measurement, which could be explained by the poor quality of the magnets. For each used magnets for the NMR device design, the magnetic field on the tip of the cylindrical magnet and the misalignment angle of the radial magnetic field were measured. The misalignment angle could be as high as 17 degrees. The simulations with some misalignment angle error of 3 degree on four magnets were performed and the same shape of the magnetic field distribution was obtained. Thus we attribute the difference between the simulation and the measurement to the misalignment angle of the magnets.

Despite these results, there's a good agreement between the simulation results and the measurement.

REFERENCES

[1] S. Anferova, V. Anferov, M. Adams, P. Blümler, N. Routley, K. Hailu, K. Kupferschläger, M. j. d. Mallett, G. Schroeder, S. Sharma, and B. Blümich, "Construction of a NMR-MOUSE with short dead time," *Concepts Magn. Reson.*, vol. 15, no. 1, pp. 15–25, Mar. 2002.

[2] G. Moresi and R. Magin, "Miniature permanent magnet for table-top NMR," *Concepts Magn. Reson.*, vol. 19B, no. 1, pp. 35–43, 2003.

[3] G. Navon, U. Eliav, D. E. Demco, and B. Blümich, "Study of order and dynamic processes in tendon by NMR and MRI," *J. Magn. Reson. Imaging*, vol. 25, no. 2, pp. 362–380, Feb. 2007.

[4] F. J. Rühli, T. Böni, J. Perlo, F. Casanova, M. Baias, E. Egarter, and B. Blümich, "Non-invasive spatial tissue discrimination in ancient mummies and bones in situ by portable nuclear magnetic resonance," *J. Cult. Herit.*, vol. 8, no. 3, pp. 257–263, Jul. 2007.

[5] B. Blümich, F. Casanova, J. Perlo, S. Anferova, V. Anferov, K. Kremer, N. Goga, K. Kupferschläger, and M. Adams, "Advances of unilateral mobile NMR in nondestructive materials testing," *Magn. Reson. Imaging*, vol. 23, no. 2, pp. 197–201, Feb. 2005.

[6] T. Poli, L. Toniolo, M. Valentini, G. Bizzaro, R. Melzi, F. Tedoldi, and G. Cannazza, "A portable NMR device for the evaluation of water presence in building materials," *J. Cult. Herit.*, vol. 8, no. 2, pp. 134–140, Apr. 2007.

[7] H. Pedersen, S. Ablett, D. Martin, M. J. Mallett, and S. Engelsen, "Application of the NMR-MOUSE to food emulsions," *J. Magn. Reson.*, vol. 165, no. 1, pp. 49–58, Nov. 2003.

[8] B. Blümich, V. Anferov, S. Anferova, M. Klein, R. Fechete, M. Adams, and F. Casanova, "Simple NMR-mouse with a bar magnet," *Concepts Magn. Reson.*, vol. 15, no. 4, pp. 255–261, Dec. 2002.

[9] W.-H. Chang, J.-H. Chen, and L.-P. Hwang, "Single-sided mobile NMR with a Halbach magnet," *Magn. Reson. Imaging*, vol. 24, no. 8, pp. 1095–1102, Oct. 2006.

[10] C. W. Windt, H. Soltner, D. van Dusschoten, and P. Blümler, “A portable Halbach magnet that can be opened and closed without force: The NMR-CUFF,” *J. Magn. Reson.*, vol. 208, no. 1, pp. 27–33, Jan. 2011.
[11] X. Zhang, V. Mahesh, D. Ng, R. Hubbard, A. Ailiani, B. O’Hare, A. Benesi, and A. Webb, “Design, construction and NMR testing of a 1 tesla Halbach Permanent Magnet for Magnetic Resonance,” in *COMSOL Users Conference, Boston*, 2005.
[12] K. Halbach, “Design of permanent multipole magnets with oriented rare earth cobalt material,” *Nucl. Instrum. Methods*, vol. 169, no. 1, pp. 1–10, Feb. 1980.
[13] H. Raich and P. Blümler, “Design and construction of a dipolar Halbach array with a homogeneous field from identical bar magnets: NMR Mandhalas,” *Concepts Magn. Reson. Part B Magn. Reson. Eng.*, vol. 23B, no. 1, pp. 16–25, Oct. 2004.
[14] H. Soltner and P. Blümler, “Dipolar Halbach magnet stacks made from identically shaped permanent magnets for magnetic resonance,” *Concepts Magn. Reson. Part A*, vol. 36A, no. 4, pp. 211–222, Jul. 2010.
[15] B. P. Hills, K. M. Wright, and D. G. Gillies, “A low-field, low-cost Halbach magnet array for open-access NMR,” *J. Magn. Reson.*, vol. 175, no. 2, pp. 336–339, Aug. 2005.
[16] E. Danieli, J. Mauler, J. Perlo, B. Blümich, and F. Casanova, “Mobile sensor for high resolution NMR spectroscopy and imaging,” *J. Magn. Reson.*, vol. 198, no. 1, pp. 80–87, May 2009.
[17] C. Hugon, F. D’Amico, G. Aubert, and D. Sakellariou, “Design of arbitrarily homogeneous permanent magnet systems for NMR and MRI: Theory and experimental developments of a simple portable magnet,” *J. Magn. Reson.*, vol. 205, no. 1, pp. 75–85, Jul. 2010.
[18] R. C. Jachmann, D. R. Trease, L.-S. Bouchard, D. Sakellariou, R. W. Martin, R. D. Schlueter, T. F. Budinger, and A. Pines, “Multipole shimming of permanent magnets using harmonic corrector rings,” *Rev. Sci. Instrum.*, vol. 78, no. 3, p. 035115, Mar. 2007.
[19] " RADIA Introduction." [Online].
http://www.esrf.eu/Accelerators/Groups/InsertionDevices/Software/RADIA/Documentation/Introduction. [Accessed: 05-Oct-2014].
[20] “ANSYS - Simulation Driven Product Development.” [Online]. Available:
http://www.ansys.com/. [Accessed: 13-Aug-2014].
[21] “HKCM MAGNETS from STOCK, from FACTORY & MAGNETS ON DEMAND.” [Online]. Available: https://www.hkcm.de/expert.php. [Accessed: 11-Jul-2014].
[22] P. Poulichet, Hung Dang Phuc, Tien Truong Cong, Latifa Fakri-Bouchet, Abdennasser Fakri, and Christophe Delabie, “Simulation and optimisation of homogeneous permanent magnet for portable NMR applications,” *8th International Conference on Sensing Technology*, Liverpool, UK., 04-Sep-2014.

B_0: Static field

B_1: applied field

γ: gyromagnetic ratio of proton

M_0: Magnetization

f: Lamor frequency

T_1: spin lattice relaxation time

T_2: spin-spin lattice relaxation time

M_z: magnitude of magnetization along Z direction

θ: tip angle

FID: free induction decay

SNR: signal to noise ratio

ξ: electromotive force

V_N: thermal noise

G: field gradient

ppm: part per million

Φ_1: angular position of the magnets

Φ_2: angular orientation of magnetization

r_1: inner radius of the ring

r_2: outer radius of the ring

m: magnetic dipole moment

M: net magnetic dipole moment per unit volume

μ_0: permeability of free space

χ: susceptibility of the material

B: Flux density

H: magnetic field strength

J: magnetic polarization

μ_r: relative permeability

H_c: coercivity of a material

B_r: remanence of a material

r0: radius of the ring

h: height of the ring

ray: radius of magnets

hS: height of shim magnets

rays: radius of shim magnets

esp: gap between two rings

r1: radius of the shim ring

dH: Distance from the middle length of shim magnets to z = 0

f_B: field strength related to homogeneity

f_A: field strength related to mass

f_ω: field strength related to NMR sensitivity

The RADIA software

The RADIA software package was designed for solving physical and technical problems one encounters during the development of Insertion Devices for Synchrotron Light Sources. However, it can also be used in different branches of physics, where efficient solutions of 3D boundary problems of Magnetostatics are needed (Figure A- 1).

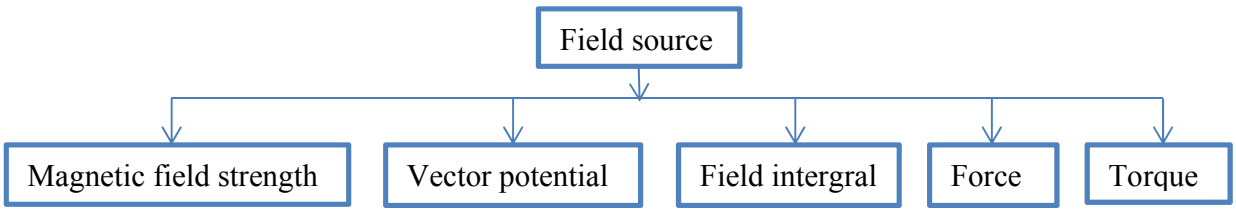

*Figure A- 1: General methods for field sources can be solved by **RADIA***

RADIA uses a boundary integral method to determine the 3D magnetic field created by an arbitrary set of coils, permanent magnets, and linear and nonlinear iron volumes. The method used in RADIA belongs to the category of boundary Integral Methods and differs strongly from the Finite Element Methods (FEM). Volume objects are created, material properties are applied to these objects. Each object can be subdivided into a number of smaller objects for which one tries to solve for the general problem in terms of the magnetization (Figure A- 2).

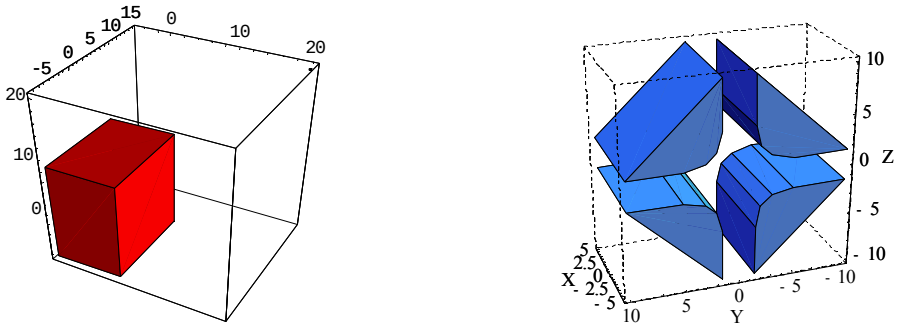

Figure A- 2: Volume objects are created and subdivided into a number of smaller objects

The solution is performed by building a large matrix in memory which represents mutual interactions between the objects. We call this an Interaction Matrix. The final magnetization in each small object is obtained iteratively, by a sequence of multiplications of the Interaction Matrix by instant magnetizations vector, taking into account the material properties. We call this a Relaxation procedure.

Normally, the process of magnetostatic calculations with RADIA includes the following steps:

(I) Describing the problem in *Mathematica Language* in terms of *RADIA* functions:

(I-a) creating initial objects - field sources prototypes;

(I-b) creating and applying appropriate magnetic materials to the objects created at (I-a);

(I-c) grouping objects by placing them in containers;

(I-d) creating and applying necessary transformations (boundary conditions);

(II) Solving the problem:

(II-a) applying any subdivision to the objects created;

(II-b) constructing an interaction matrix corresponding to the problem (I) and particular subdivision (II-a), and executing a relaxation procedure;

(II-c) computing any components (as field induction, field integrals along straight line, potentials or forces) of the magnetic field created by the "relaxed" objects;

3D magnetostatic problems solved by RADIA based on these equations:

Poisson equation for Scalar magnetic potential: ⟹

$$\nabla \mathbf{B} = 0,$$
$$\mathbf{B} = \mu_0 (\mathbf{H} + \mathbf{M}),$$
$$\mathbf{H} = -\nabla \varphi,$$
$$\Delta \varphi = \nabla \mathbf{M},$$

Solution through volume and surface integrals: ⟹

$$\varphi(\mathbf{r}) = \frac{-1}{4\pi} \iiint_{V'} \frac{\nabla \mathbf{M}}{|\mathbf{r}' - \mathbf{r}|} dV' + \frac{1}{4\pi} \oiint_{S'} \frac{\mathbf{M}\, \mathbf{n}_{S'}}{|\mathbf{r}' - \mathbf{r}|} dS',$$
$$\mathbf{H}(\mathbf{r}) = \frac{1}{4\pi} \iiint_{V'} \frac{(\mathbf{r}' - \mathbf{r})\, \nabla \mathbf{M}}{|\mathbf{r}' - \mathbf{r}|^3} dV' - \frac{1}{4\pi} \oiint_{S'} \frac{(\mathbf{r}' - \mathbf{r})\, \mathbf{M}\, \mathbf{n}_{S'}}{|\mathbf{r}' - \mathbf{r}|^3} dS',$$

Magnetic field created by uniformly magnetized volume: ⟹

Si $\mathbf{M} = \mathbf{const}$:

$$\mathbf{H}(\mathbf{r}) = \mathbf{Q}(\mathbf{r})\, \mathbf{M},$$
$$\mathbf{Q}(\mathbf{r}) = \frac{1}{4\pi} \oiint_{S'} \frac{(\mathbf{r} - \mathbf{r}') \otimes \mathbf{n}_{S'}}{|\mathbf{r} - \mathbf{r}'|^3} dS';$$

In this approach, one applies some kind of segmentation to the field-producing objects (typically iron) but, contrary to the FEM approach, one does not need to mesh the vacuum.

ANSYS Multiphysics software

ANSYS Multiphysics software is a comprehensive FEA analysis (finite element) tool for static and dynamic structural analysis (both linear and non-linear), heat transfer and fluid problems, as well as acoustic and electro-magnetic problems. The ANSYS Multiphysics software is a general-purpose analysis tool allowing a user to combine the effects of two or more different yet interrelated physics, within one unified simulation environment. Normally, ANSYS solves problems based on three steps as shown in the flowchart below (Figure B- 1)

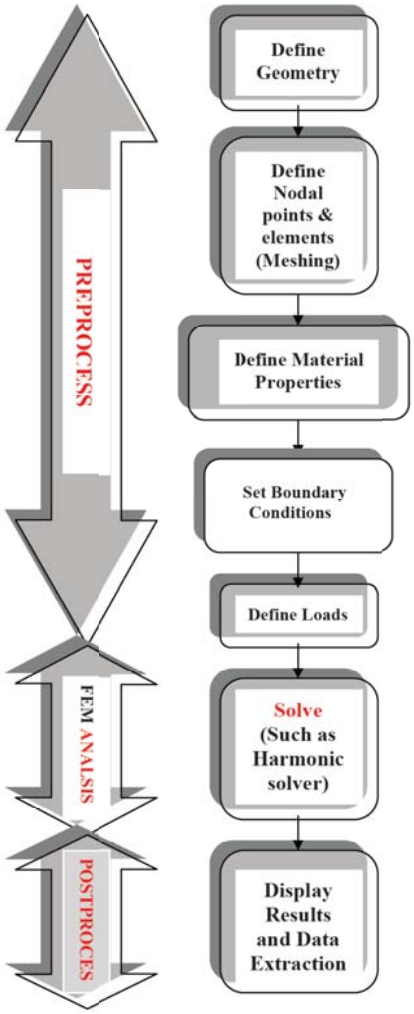

Figure B- 1: Flowchart for FEM analysis using ANSYS.

(I) Preprocess:

(I-a) geometry modeling

(I-b) setting up material properties (such as permeability…)

(I-c) meshing

- Selecting finite elements that suit the needs (from a predefined library)
- Defining the element density (may change significantly in regions, some regions high some regions probably low)

(I-d) Apply the loads and degrees of freedom and decide what forces act on which nodes and what boundary conditions have to be fulfilled.

(II) Numerical solving: This gives us the solution for every nodes or elements (discrete)

(III) Post processing: Visualization of element solution and data export.

In ANSYS, the values of H and B can be obtained by two solutions, which are the magnetic scalar potential and the magnetic vector potential.

The scalar potential method as implemented in SOLID5, SOLID96, SOLID98 for 3D magnetostatic field. Magnetosatic means that time varying effects are ignored. This reduces Maxwell's equations for magnetic field to:

$$\boldsymbol{\nabla x}\{\boldsymbol{H}\} = \{\boldsymbol{J_s}\} \tag{B- 1}$$

$$\boldsymbol{\nabla}.\{\boldsymbol{B}\} = \boldsymbol{0} \tag{B- 2}$$

The vector potential method as implemented in PLANE13, PLANE53 and SOLID97 for both 2D and 3D electromagnetic fields. Considering static and dynamic fields and neglecting displacement currents (quasi-stationary), the following subset of Maxwell's equations apply:

$$\boldsymbol{\nabla x}\{\boldsymbol{H}\} = \{\boldsymbol{J}\} \tag{B- 3}$$

$$\boldsymbol{\nabla x}\{\boldsymbol{E}\} = -\frac{\boldsymbol{\partial B}}{\boldsymbol{\partial t}} \tag{B- 4}$$

$$\boldsymbol{\nabla}.\{\boldsymbol{B}\} = \boldsymbol{0} \tag{B- 5}$$